Politecnico di Torino

Università degli Studi di Torino

Universitat Politècnica de Catalunya

Ph.D. in Bioengineering and Medical-Surgical Sciences

XXXVI Cycle

Design of a multi-functional, nanoparticles loaded supramolecular hydrogel to treat chronic wounds

Tutors:
Prof. Gianluca Ciardelli
Prof. Clara Mattu
Prof. Tzanov Tzanko
Prof. Monica Boffito

Candidate:
Giulia Crivello

Doctoral Examination Committee:

Prof. Ana Marina Ferreira Duarte, Newcastle University, United Kingdom, *Referee*
Prof. Jochen Salber, Ruhr-University Bochum, Germany, *Referee*
Prof. Chiara Tonda-Turo, Politecnico di Torino
Prof. Chiara Vitale Brovarone, Politecnico di Torino
Prof. Lorenza Draghi, Politecnico di Milano

"Nella vita non c'è nulla da temere, solo da capire"

Margherita Hack

"Research is the process of going up alleys to see if they are blind"

Marston Bates

Index of the thesis

Index of the thesis ***I***

Acknowledgements – Ringraziamenti ***V***

Brief curriculum vitae ***VII***

List of publications and congress ***VIII***

Publications **VIII**

Congress participation **VIII**

Prizes **VIII**

Abstract of the thesis ***IX***

List of acronyms ***XII***

1. General introduction and aim of the thesis ***1***

1.1. Wound healing and chronic wounds: definitions and current treatments **1**
1.1.1. Introduction 1
1.1.2. The wound-healing process 2
1.1.3. The impaired wound-healing process in chronic wounds 4
1.1.4. Management and treatment of CWs 5
1.1.5. Commercial dressings used in wound treatments 6
1.1.6. Multifunctional wound dressings – state of the art 8

1.2. Outline of the work **15**

1.3. References **19**

2. Development and optimization of a supramolecular hydrogel for treating CWs ***29***

2.1. Introduction **29**

2.2 Materials and Methods **36**
2.2.1. Materials and reagents 36
2.2.2. Poly(ether urethane) synthesis 36
2.2.2.1. The PEUs cytocompatibility 37
2.2.3. Preparation of the SM-Gel 37
2.2.4. Characterisation of the SM-Gel 37
2.2.4.1. Rheology 37
2.2.4.2. Water absorption into dry hydrogels 38
2.2.4.3. Bovine Serum Albumin (BSA) uptake in the SM-Gel 38
2.2.4.4. Gel stability 38
2.2.4.5. Gel cytocompatibility 39
2.2.5. Statistical analysis 39

2.3. Results and Discussion **39**
2.3.1. Polyurethane synthesis and characterization of SHF68 and CHP407-based SM-gels 39
2.3.1.1 Synthesis and characterization of CHP407 and SHF68 39
2.3.1.2. Cytocompatibility of CHP407 and SHF68 40
2.3.1.3. Rheological characterization of SHF68 and CHP407-based SM-gels 41
2.3.1.4. Cytocompatibility of CHP407 and SHF68-based hydrogels 47
2.3.1.5. Conclusion 48
2.3.2. Characterization and optimization of CHP407 and SHF68 blend SM-gels 48
2.3.2.1. Rheological characterization of SHF68 and CHP407-based SM-gels 48
2.3.2.2. SM-gel absorption capacities: protein uptake and medium absorption of freeze-dried gels 54

2.3.2.3. Cytocompatibility of the selected CHP407/SHF68 blend hydrogels 56
2.3.2.4. Stability of the selected CHP407/SHF68 blend hydrogels 56
2.4. Conclusion **57**
2.5. References **59**
3. Design of lignin-cobalt NPs- loaded SM-gel ***63***
3.1. Introduction **63**
3.2. Materials and methods **67**
3.2.1. Materials and reagents 67
3.2.2. Enzymatic Functionalization of Lig 68
3.2.3. Characterization of Lig-TA-LTH 68
3.2.3.1. ATR-FTIR Spectroscopy 68
3.2.3.2. Measurement of the Phenolic Content 68
3.2.3.3. Quantification of the LTH Content 68
3.2.4. Preparation of Cobalt/Lig Nanoparticles (CoLig NPs) 68
3.2.5. Characterization of CoLig NPs 69
3.2.5.1. Morphological Characterization and Cobalt Loading 69
3.2.5.2. MPO and MMP Inhibition Assays 69
3.2.5.3. Antioxidant activity of CoLig NPs 70
3.2.5.4. Antibacterial Activity of CoLig NPs 70
3.2.5.5. Cytotoxicity of CoLig NPs 71
3.2.6. Preparation and Characterization of a Supramolecular Hydrogel (SM-Gel) Embedded with CoLig NPs 71
3.2.6.1. Preparation of the SM-Gel Loaded with CoLig NPs 71
3.2.6.2. Stability of the SM-Gel Loaded with CoLig NPs 71
3.2.6.3. Rheological Tests 72
3.2.6.4. CryoSEM 72
3.2.6.5. CoLig NPs Interaction with SM-gel components 72
3.2.6.6. CoLig NPs' release from the SM-Gel 73
3.2.6.7. Cytocompatibility of the SM-Gel Containing CoLig NPs 73
3.2.6.8. Antioxidant activity of CoLig NPs released from the SM-gel. 74
3.2.6.9. Antibacterial Activity of the SM-Gel Containing CoLig NPs 74
3.2.7. Statistical Analysis 74
3.3. Results and discussion **74**
3.3.1. Synthesis and characterization of Lig-TA-LTH 74
3.3.2. Synthesis and characterization of CoLig NPs 75
3.3.2.1. Antioxidant and anti-inflammatory activity of CoLig NPs 76
3.3.2.2. Cytocompatibility of CoLig NPs 78
3.3.2.3. Antibacterial and antibiofilm activity of CoLig NPs 79
3.3.3. SM-gel loaded with CoLig NPs 81
3.3.3.1. Rheological properties of SM-gel loaded with CoLig NPs 81
3.3.3.2. Stability of SM-gel loaded with CoLig NPs 84
3.3.3.3. Release of CoLig NPs from SM-gel 86
3.3.3.4. Cytocompatibility of SM-gel loaded with CoLig NPs 87
3.3.3.5. Antioxidant capacity of the CoLig NPs released from the SM-gel 88
3.3.3.6. Antibacterial activity of the CoLig NPs released from the SM-gel 89
3.4. Conclusions **89**
3.5. References **91**
4. Strategies to impart antibiofilm features to NPs ***97***
4.1. Introduction **97**
4.2. Materials and methods **99**
4.2.1. Materials and reagents 99

4.2.2. Preparation and characterization NPs delivering NO 100
4.2.2.1. GSH S-nitrosylation to GSNO 100
4.2.2.2. Functionalization of amino cellulose with GSNO 100
4.2.2.3. Coating of CoLig NPs with AC-GSNO 101
4.2.2.4. Cytocompatibiltiy of NO-CoLig NPs 101
4.2.2.5. Antibacterial and anti-biofilm activity of NO-CoLig NPs 101
4.2.3. Preparation and characterization of CoPc-Lig NPs 101
4.2.3.1. Preparation of CoPc-Lig NPs 101
4.2.3.2. Cytocompatibility and cell internalization of CoPc-Lig NPs 102
4.2.3.3. Antioxidant activity of CoPc-Lig NPs 102
4.2.3.4. MMPs inhibitory assay 103
4.2.3.5. Antibacterial activity of CoPc-Lig NPs 103
4.2.3.6. Internalization of CoPc-Lig NPs into S. aureus and P. aeruginosa biofilms 103
4.2.3.7. Photothermal activity of CoPc-Lig NPs 103
4.2.3.8. Photoacoustic activity of CoPc-Lig NPs 104
4.2.4. Statistical Analysis 105

4.3. Results and discussion 105
4.3.1. Preparation and characterization of Nitric oxide delivering NPs 105
4.3.1.1. GSH S-nitrosylation to GSNO 105
4.3.1.2. Functionalization of amino cellulose with GSNO 106
4.3.1.3. Coating of CoLig NPs with AC-GSNO 107
4.3.1.4. Cytocompatibility of NO-CoLig NPs 107
4.3.1.5. Antibacterial and antibiofilm activity of NO-CoLig NPs 108
4.3.1.6. Consideration on NO-CoLig NPs 110
4.3.2. Synthesis and characterization of CoPc-Lig NPs 110
4.3.2.1. Optimization of the Lig-TA-LTH content in CoPc-Lig NPs 110
4.3.2.2. Optimization of the CoPc content in CoPc-Lig NPs 116
4.3.2.3. Morphological characterization of CoPc-Lig NPs through TEM 117
4.3.2.4. MMPs inhibitory activity of CoPc-Lig NPs 118
4.3.2.5. Cytocompatibility of CoPc-Lig NPs 118
4.3.2.6. Antibacterial activity 119
4.3.2.7. Photothermal activity 120
4.3.2.8. Photoacoustic activity 122
4.3.2.9. Considerations on CoPc-Lig NPs 124

4.4. Conclusions 124

4.5. Annex figures 126

4.6. References 130

5. Design of new SM-gels with antioxidant and anti-inflammatory properties and enhanced stability 135

5.1. Introduction 135

5.2. Materials and methods 136
5.2.1. Materials and reagents 136
5.2.2. Development of Lig-SHF68-based SM-gel 137
5.2.2.1. Enzymatic functionalization of lignin with TA and characterization (Lig-TA) 137
5.2.2.2. Enzymatic functionalization of SHF68 (Lig-SHF68) 138
5.2.2.3. Preparation and characterization of Lig-SHF68-based SM-gel 138
5.2.3. Development of photo-crosslinked SM-gel (UV-SM-gel) 140
5.2.3.1. PEG-DA synthesis and characterization 140
5.2.3.2. Preparation and optimization of an SM-gel combining PEG-DA and Lig-SHF68 140
5.2.3.3. Photorheology of the UV-SM-gel 141
5.2.3.4. Incorporation and release of various NPs and compounds 141
5.2.4. Statistical analysis 142

5.3. Results and discussion **142**
5.3.1. Enzymatic functionalization of lignin with TA and characterization 142
5.3.1.1. Lig-TA chemical characterization and phenolic content quantification 142
5.3.1.2. Lig-TA antioxidant and anti-inflammatory activity 143
5.3.2. Preparation and characterization of Lig-SHF68-based SM-gel 144
5.3.2.1. Lig-SHF68 chemical characterization and quantification of phenolic groups 144
5.3.2.2. Lig-SHF68 antioxidant and anti-inflammatory activity 145
5.3.2.3. Cytocompatibility of Lig-SHF68 145
5.3.2.4. Rheological properties of Lig-SHF68-based SM-gels (Lig-SHF68-SM-gels) 146
5.3.2.5. Stability of Lig-SHF68-SM-gels 151
5.3.2.6. The cytocompatibility of Lig-SHF68-based SM-gels 152
5.3.2.7. Antioxidant activity of the components released from the Lig-SHF68-based SM-gels 152
5.3.3. Development of photo-crosslinked SM-gels 154
5.3.3.1. Optimization of UV-stabilized Lig-SHF68-based SM-gels 154
5.3.3.2. Stability test of the selected UV-SM-gel 156
5.3.3.3. Photorheology of the UV-SM-gel 156
5.3.3.4. Rheological tests of the UV-SM-gel 157
5.3.3.5. Antioxidant activity of the components released from the UV-SM-gel 160
5.3.3.6. Release of NPs and compounds from the new gel formulation 161
5.4. Conclusions **162**
5.5. References **163**
6. General discussion ***165***
6.1. References **172**

Acknowledgements – Ringraziamenti

Questo dottorato è stato un percorso molto formativo e intenso, sia da un punto di vista professionale che personale. Vorrei ringraziare innanzitutto il prof. Gianluca Ciardelli, che mi ha proposto di lavorare a questo tema, mi ha affiancato lungo il percorso e sostenuto, quando necessario, sia scientificamente che umanamente.

Un sentito grazie anche alle prof.sse Clara Mattu a Monica Boffito, che hanno accompagnato con le loro osservazioni e i loro commenti i miei progressi scientifici. In particolare, a Clara per il suo rigore scientifico e la sua attenzione ai dettagli, e a Monica per la sua singolare dedizione e il suo sostegno morale.

Un'altra figura importante per la riuscita di questo progetto è quella del prof. Tzanko Tzanov dell'UPC di Barcellona, presso cui ho svolto un periodo di mobilità. La collaborazione instauratasi ha contribuito fortemente a dare una direzione al progetto e la sua totale disponibilità ha sostenuto attivamente la mia ricerca. Colgo qui anche l'occasione per ringraziare i colleghi con cui ho lavorato a Barcellona, in particolare Gala e Kristina, con cui ho strettamente collaborato durante gli esperimenti, e Antonio, che con la sua allegria ha saputo alleviare i momenti di stanchezza. E poi Garima, Alex, Guillem, Pol, Eva, Feifei, Ivan, Jennifer e Silvia con cui ho condiviso la vita in laboratorio e i momenti di svago.

Un'altra persona che ha avuto un ruolo significativo in questo progetto è Alessandro Torchio, sul cui lavoro ho basato lo sviluppo dell'idrogelo e dei materiali qui descritti. Il suo affiancamento nei primi mesi è stato fondamentale per capire i processi di sintesi e integrarmi al meglio nella vita di laboratorio.

Due altri gruppi di ricerca sono stati coinvolti in questo progetto e mi hanno fortemente sostenuto e aiutata durante gli esperimenti. Il primo è il gruppo della prof.ssa Letizia Fracchia dell'UPO di Novara, da cui sono stata ospite per le prove di caratterizzazione batterica. Lei, Chiara Ceresa e Andrea Sansotera sono state un aiuto concreto nel capire l'affascinante mondo dei trattamenti antibatterici. Il secondo è il gruppo di Luca Menichetti del CNR di Pisa, da cui sono andata per effettuare i test fototermici. In particolare, Paolo Armanetti e Claudia Catarinicchia che mi hanno seguita e aiutato durante gli esperimenti.

Facendo parte di un gruppo numeroso, diviso tra Alessandria e Torino, ho avuto modo di incontrare molte persone straordinarie che mi hanno aiutato nei momenti di sconforto e con cui abbiamo condiviso puri momenti di ilarità. Vorrei ringraziare in particolare Roberta Pappalardo per il sostegno durante gli ultimi mesi e la condivisione di letture, podcast e progetti di viaggio; il gruppo di nanoparticellisti di cui faccio parte insieme a Andrea Bezze, Carlotta Mattioda, Sara Muccio e Marialucia Rubicondo, con cui ho strettamente collaborato e che sono stati un sostegno scientifico e morale in molti momenti di questo percorso; e Elena Marcello che mi ha sopportato durante un catartico congresso in Corea del Sud e che stimo profondamente, sia scientificamente che umanamente. Un grazie sentito per il sostegno anche agli altri membri sia di Alessandria, Susanna Sartori, Rossella Laurano, Andrea Alliaud e Sara Pionato, che di Torino, Chiara Tonda-Turo, Irene Carmagnola, Alice Zoso, Michela Licciardello, Viola Sgarminato, Camilla Paoletti, Ines Hamouda, Maria Antonia Cassa, Letizia Nicoletti, Gerardina Ruocco, Mattia Spedicati, Giovanni Paolo Stola, Daniele Testore, Francesca Tivano, Cecilia Traldi, Matteo Bortolomeazzi e Martina Coletto. Un grazie sentito anche a Giuliana Orlandini e Matteo Felice Pezzuto che hanno svolto la loro tesi magistrale sotto la mia supervisione e che hanno contribuito attivamente con il loro lavoro ai risultati che sono qui riportati.

Non posso poi mancare nel ringraziare gli amici che ho incontrato in questi anni al di fuori dell'ambito lavorativo e che mi hanno sostenuto più o meno consapevolmente in questo percorso: i miei amici di una vita, Chiara, Martina, Roberta, Matteo, Tea e Betta, che mi confortano e appoggiano nonostante i miei difetti; gli amici del CUS arrampicata, Diego, Jacopo, Daniele, Antonio, Anna, Federico, Paola, Marco, Simona, Igor, Cristina, Andrea, Davide e Nani, con cui coltivo e condivido più di una semplice passione; gli amici di Casa Fools, Luigi, Michela, Andrea, Juliet, Annabelle, Jelena, Chiara, che hanno affrontato il pubblico insieme a me e sono diventati compagni di molte altre avventure; e le altre persone che conosco o che ho incontrato durante le mie permanenze fuori porto, Francesco, Andrea, Alessandro, Federica, Giulia, Michele, Marta, Asja, Elisa, Alice, Martina, Iolanda, Silvia, Laura, Anna, Adrian, Luca, Maxime, Eliya, Damian e Carme.

Volevo anche ringraziare la mia famiglia che è stata un profondo esempio di vita e mi ha sempre supportato materialmente ed emotivamente in tutto quello di cui avevo bisogno: mia mamma, per la sua decisione e la sua comprensione; mio papà, per il suo acume e la sua calma; mia sorella, per la sua perspicacia e i suoi consigli di stile; e le mie due nonne per il loro costante affetto.

Infine, un grazie profondo a Francesco, che è in grado di trovare soluzioni quando io non vedo che porte chiuse e che riesce ad ancorarmi alla terra quando sono persa nel mio mondo. Non è quantificabile l'importanza che tu hai avuto in questo percorso e che hai nella mia vita.

A tutti voi, grazie di cuore.

Giulia

Brief curriculum vitae

Giulia Crivello obtained a Bachelor's degree in Biomedical Engineering at Politecnico di Torino (Italy) in 2017 with a thesis on "Electrospun nanofiber for cell differentiation" under the supervision of Ph.D. Carmagnola (Politecnico di Torino, Italy) and Prof. Ciardelli (Politecnico di Torino, Italy). The same year, Giulia enrolled in the Master's course in Bioengineering at EPFL (Lausanne, Switzerland) obtaining the degree in 2020 with a specialization in Regenerative Medicine and Biotechnology. During her studies, she also worked in the research and development department of Abionic, a Swiss company developing microfluidic systems for rapid diagnostics. She performed her master's thesis under the supervision of Prof. Lutolf (EPFL, Switzerland) in prof. Barker's laboratory (A*star, Singapore) studying the effect of AQP5 in gastric cancer with mouse models and cancer cell lines. Since 2020, she enrolled in the PhD at Politecnico di Torino under the supervision of Prof. Ciardelli (Politecnico di Torino, Italy), Prof. Mattu (Politecnico di Torino, Italy) and Prof. Tzanov (UPC, Spain), where she is working on the development of polyfunctional nanoparticles to be integrated into supramolecular hydrogels for the treatment of chronic wounds. During her PhD, she collaborated with Prof. Tzanov's lab at UPC in Barcelona where she worked for 6 months. Giulia's research interests are highly multidisplinary and include biomaterial synthesis and functionalization, hydrogel-based drug delivery systems, hybrid metal-polymer nanoparticles, natural polyphenols, and *in vitro* tissue models for drug testing. She published a review article on *in vitro* models of bacteria biofilms, which was selected as an editor's choice article, and a research article on the development of a nanoparticles-loaded hydrogel for chronic wound treatment. She participated to various international congresses, including the World Biomaterial Congress 2024 in Daegu, South Korea, and the European Wound Management Association congress 2023 in Milan, Italy, where she was awarded the best e-poster prize.

List of publications and congress

Publications

G. Crivello, L. Fracchia, G. Ciardelli, M. Boffito, and C. Mattu. "In vitro models of bacterial biofilms: innovative tools to improve understanding and treatment of infections." Nanomaterials 13, no. 5 (2023): 904.

G. Crivello, G. Orlandini, A.G. Morena, A. Torchio, C. Mattu, M. Boffito, T. Tzanov, and G. Ciardelli. "Lignin–cobalt nano-enabled poly (pseudo) rotaxane supramolecular hydrogel for treating chronic wounds." Pharmaceutics 15, no. 6 (2023): 1717.

Congress participation

“Dual-function nanoparticles enzymatically conjugated with a custom-made polyurethane hydrogel for chronic wound treatment.” **G. Crivello**, G. Orlandini, A.G. Morena, C. Mattu, M. Boffito, T. Tzanov, and G. Ciardelli. Oral presentation at: ESIB 2022: European Summit Of Industrial Biotechnology, Graz (Austria), 14 - 15/11/2022.

“Dual-function nanoparticles loaded in a custom-made polyurethane hydrogel for chronic wound treatment”. **G. Crivello**, G. Orlandini, A.G. Morena, C. Mattu, M. Boffito, T. Tzanov, and G. Ciardelli. Oral presentation and e-poster at: EWMA 2023: The 33rd Conference Of The European Wound Management Association, Milan (Italy), 03 - 05/05/2023.

“Polyphenolic lignin-based material enzymatically conjugated with a custom-made polyurethane hydrogel for reducing inflammation in chronic wounds”. **G. Crivello**, C. Mattu, M. Boffito, T. Tzanov, and G. Ciardelli. Oral presentation at: SIB 2023 Congresso Nazionale Societa’ Italiana Biomateriali, Camerino (Italy), 03 -06/07/2023.

“Lignin-based nanoparticles with phthalocyanine functionality for photothermal treatment of bacterial biofilm”. **G. Crivello**, C. Mattu, M. Boffito, T. Tzanov, and G. Ciardelli. Poster at: WBC 2024: World Biomaterial Congress, Daegu (South Korea), 26 – 31/05/2024.

“Multi-functional supramolecular hydrogel based on custom-made polyurethanes for fighting inflammation by combined delivery of natural phenols and nitric oxide”. **G. Crivello**, C. Mattu, M. Boffito, T. Tzanov, and G. Ciardelli. Oral presentation at: WBC 2024: World Biomaterial Congress, Daegu (South Korea), 26 – 31/05/2024.

Prizes

E-POSTER PRIZE EWMA 2023 The E-Poster prize is awarded to an Electronic Poster that is: Visually appealing, is well laid out in a logical manner, has relevant and interesting content and clear conclusions (2023)

Editor's choice article. Certificate of publication for the article titled: 'In Vitro Models of Bacterial Biofilms: Innovative Tools to Improve Understanding and Treatment of Infections' (2023)

Abstract of the thesis

Chronic wounds (CWs) are defined as wounds that have failed to progress through a normal and timely healing process and may arise as a result of different pathologies including infections, tissue hypoxia, trauma, and chronic diseases, such as diabetes and cardiovascular ailments. These wounds represent a significant health concern as they may lead to severe tissue damage and even death. CWs are characterized by elevated levels of proinflammatory cytokines, reactive oxygen species (ROS), and enzymes (e.g., matrix metalloproteases, MMPs, and myeloperoxidase, MPO) which degrade the extracellular matrix (ECM) components and prevent wound closure. Additionally, bacteria in CWs secrete virulence factors that worsen the inflammatory condition. The aggregation of these pathogens into biofilms protects them from antibacterial treatments, preventing their eradication and enhancing the risk of antibiotic resistance. These factors together pose a substantial burden on healthcare systems, with patients necessitating long-term specialized care and repeated hospitalizations. Current treatments for CWs are largely inadequate, with no established gold standard, highlighting the need for innovative solutions that should be easy to handle and capable of combining multiple functions to address the multifactorial nature of CWs.

This PhD project responds to these needs by developing a multi-component dressing solution composed of an injectable hydrogel loaded with hybrid metal/organic nanoparticles (NPs) designed to reduce inflammation and control bacterial proliferation in CWs.

In **Chapter 2**, the development of an injectable, self-healing hydrogel is described. The hydrogel is based on a blend between two custom-made poly(ether urethane)s (PEUs), named CHP407 and SHF68, and α-cyclodextrins (αCDs), resulting in a self-assembled physical system. The two PEUs were synthesized from commercial amphiphilic block copolymers (Poloxamers®), used as macrodiols, and differ by the selection of the chain extender. For CHP407, a cyclic chain extender (1,4-cyclohexanedimethanol) was used, while SHF68 was synthesized with a chain extender containing pending BOC-protected amino groups (n-BOC serinol) and used after BOC-deprotection reaction. The use of custom-made synthetic polymers favors reproducibility and allows better control of the hydrogel properties. The initial tests focused on characterizing CHP407 and SHF68-based hydrogels at different PEUs content (1%, 3%, and 5% w/v) through reological tests and cytocompatibility. The results showed higher rheological performance for CHP407-based hydrogels, with maximum G’ and G’’ values of 6 kPa and 0.7 kPa respectively at 5% w/v, as compared to 2.5 kPa and 0.2 kPa respectively for SHF68-based hydrogels at the same concentration. However, SHF68-based hydrogels presented higher cytocompatibility with cell viability above 80% for all concentrations tested, while CHP407-based hydrogels presented cell viability above 80% only for the formulation at 1% w/v concentration. Given these premises, two blends (CHP407:SHF68 weight ratio 80:20 and 50:50) at different concentrations (1%, 3%, and 5% w/v) were tested to maximize their mechanical properties and cytocompatibility. These hydrogels were characterized in terms of rheological properties, stability in watery environments, cytocompatibility, and capability to rehydrate and absorb proteins from aqueous media mimicking exudate. The developed hydrogels showed injectability, and self-healing behavior, which allows the gel to comply with the wound shape and to withstand movements. The optimized system (3% w/v, CHP407:SHF68 weight ratio of 80:20) was a fully developed hydrogel, with values of G’ and G’’ around 10 kPa and 2 kPa, respectively. The optimized gel showed good cytocompatibility, with cell viability > 80% and stability for more than 24 h in conditions of high-medium turnover reproducing highly exudative wounds. The gel absorbed ≈ 30% of large proteins from aqueous media and rehydrated in a few seconds. These properties make the hydrogel a suitable dressing in CWs by virtue of its good cytocompatibility, stability, ability to absorb varying quantities of fluids, and

protein uptake. Thus, the optimized hydrogel was complemented with additional functionalities, either through combination with nanoparticles or through chemical modification or blending, as described in the following sections.

Chapter 3 describes the combination of the optimized hydrogel with hybrid polymer/inorganic NPs to obtain a dressing with antibacterial and antioxidative properties. To this aim, hybrid organic/inorganic NPs were obtained by combining the antibacterial properties of cobalt, with a lignin-based material (Lig-TA-LTH). Lig-TA-LTH was obtained by functionalizing lignin with the antioxidant tannic acid (TA) and L-tyrosine hydroxamate (LTH), an inhibitor of MMPs. The obtained Lig-TA-LTH is expected to enhance the antioxidant properties of Lig and to impart inhibitory activity against MMPs and MPO, two key enzymes involved in altering healing CWs. The obtained NPs (CoLig NPs) presented an irregular round shape with a size of around 200 nm. The incorporation of Lig-TA-LTH, with its polyphenolic nature, resulted in nearly 80% ROS scavenging activity at 2.5 mg/mL. Additionally, the NPs were able to inhibit more than 80% of the activity of MMPs and MPO. The presence of cobalt resulted in growth inhibition of S. aureus and P. aeruginosa at concentrations above 0.3 mg/mL and 0.6 mg/mL, respectively. Cytocompatibility tests indicated that cells could be treated with CoLig NPs at concentrations up to 0.6 mg/mL. Therefore, a concentration of CoLig NPs of 0.6 mg/mL was selected as the optimal condition to combine bacteria inhibition with high cytocompatibility and ROS scavenging ability. CoLig NPs were then integrated into the optimized hydrogel, resulting in enhanced stability (up to 48 h) and improved rheological properties, with a more than 50% increase of G’ and G’’. The nature of the interactions between the NPs and the hydrogel components was investigated through cryo-scanning electron microscopy (cryoSEM) and Attenuated Total Reflectance–Fourier Transformed Infrared (ATR-FTIR) spectroscopy demonstrating a 40% increase in the crosslinking of the hydrogel network through interactions between NPs and both, αCDs and SHF68. Additionally, the hydrogel allowed the sustained release of the NPs with a nearly zero-order release kinetics. The antibacterial and antioxidant properties of the components released from the hydrogel were also confirmed by observing bacterial membrane disruption and ROS scavenging activity, which was above 40% throughout the hydrogel life. The composite system demonstrated significant potential for CW treatment due to its ease of application and multifunctional therapeutic actions combining antioxidant, anti-inflammatory, and antibacterial properties.

In **Chapter 4**, CoLig NPs were modified to include anti-biofilm capabilities, as previous tests in Chapter 3 highlighted the absence of antibiofilm functionalities albeit a promising antibacterial effect. The presence of biofilms in CWs results in hampered healing and in the development of antibiotic resistance. Therefore, wound dressings with biofilm disruption capacity are highly needed. To achieve this, two strategies were implemented: the first based on CoLig NPs coating with a nitric oxide (NO) donor to obtain NO-CoLig NPs, and the second based on substituting bare cobalt with a complex of cobalt and the photo-excitable dye phthalocyanine, to obtain CoPc-Lig NPs to be used for photothermal biofilm disruption. NO delivery is known to alter the nitroxidative state, therefore inducing destabilization of biofilms, while promoting regeneration. The negatively-charged CoLig NPs were successfully coated with positively charged amino cellulose, which was conjugated with a NO donor (S-nitroso glutathione, GSNO). While the coating significantly improved the cytocompatibility of CoLig NPs, no antibiofilm effects were observed, suggesting scarce NO release from GSNO in the test conditions. The second approach proposed photothermal treatment of biofilms. CoPc-Lig-NPs presented ROS scavenging ability at 0.2 mg/mL and MMPs inhibition at 0.8 mg/mL. Additionally, they were cytocompatible up to 4 mg/mL, significantly improving the cytocompatibility of CoLig NPs. At 4 mg/ml CoPc-lig NPs presented 4.8 log reduction of S. aureus growth. They could be internalized into both S. aureus and P. aeruginosa biofilms and

produced a temperature increase of 7 °C upon near-infrared (NIR) light excitation. This temperature gradient led to a decrease in bacteria viability and a loss in biofilm integrity. Additionally, these NPs could be used in photoacoustic imaging responding to the need for monitoring CWs treatments. The photoacoustic signal was stable over time and could be detected in ex vivo phantoms. The developed CoPc-Lig NPs, combining antibacterial cobalt, antioxidant polyphenols, and photo-excitable phthalocyanines, deserve further investigation in CWs treatment.

In **Chapter 5**, SHF68 was functionalized with lig to obtain Lig-SHF68, through the enzymatic conjugation of Lig-TA to amino groups of SHF68, providing ROS-scavenging properties (> 80% at 12.5 mg/mL) and MMPs and MPO inhibitory activity (>50% at 10 mg/mL). The supramolecular hydrogel obtained by combining Lig-SHF68 at 5% w/v and αCDs maintained its antioxidant properties, with ROS scavenging activity above 80% in the first hours of release. Additionally, the weak interactions between lignin, αCDs and other hydrogel components extended the durability of the system. Indeed, at 5% w/v concentration, Lig-SHF68-based hydrogel was stable at 24 h and started to dissolve afterward, whereas SHF68-based hydrogel disassembled after 6 h. Interestingly, the rheological properties of Lig-SHF68 based-gel were lower compared to pristine SHF68 based gel, with G' and G'' values decreasing from 2400 Pa and 200 Pa in Lig-SHF68 hydrogel to 780 Pa and 75 Pa in SHF68-based system (at 5% w/v). To improve stability and rheological properties, Lig-SHF68 was blended with a photosensitive polymer (i.e., poly(ethylene glycol) diacrylate, PEG-DA) to provide additional chemical crosslinking through light irradiation at 365 nm and 10 mW/cm2 in presence of a catalytic amount of a photoinitiator. The modified hydrogel (5% w/v overall polymer concentration, Lig-SHF68:PEG-DA weight ratio 80:20) presented properties comparable to the hydrogel developed in Chapter 2 by blending CHP407 and SHF68 (3% w/v PEU content, CHP407:SHF68 weight ratio 80:20), showing injectability, self-healing capacity above 70%, and G' and G'' values of 9300 Pa and 2300 Pa, respectively. Additionally, the hydrogel maintained a good antioxidant activity (around 20% throughout its life) and displayed longer durability for over 7 days. The hydrogel was also able to sustain the release of CoPc-Lig NPs and of the antioxidant drug curcumin, with delivery mechanisms dependent on the nature of the encapsulated compound.

Overall, the innovative hydrogel/NP system developed in this PhD project represents a promising tool for CWs treatment. The hydrogel was injectable, granting the ability to adapt to the wound bed, and was able to absorb exudate and maintain moisture. The functionalization with Lig-TA provided MMPs and MPO inhibitory capacity and antioxidant properties. Blending with a photosensitive polymer produced light-mediate chemical crosslinking which improved stability, thus reducing dressing changes. CoLig NPs with broad-spectrum antibacterial activity, antioxidant properties, and capacity to inhibit MMPs and MPO were successfully obtained. CoPc-Lig NPs with photothermal and photoacoustic behavior were also successfully obtained. These particles were cytocompatible, antioxidant, antibacterial, and were able to enter bacteria biofilms. This work presents promising results which deserve further investigation. Future research should focus on finding the optimal combination between the developed solutions, e.g., combination of CoLig NPs with CoPc-lig NPs to find the optimal balance between broad-spectrum antibacterial activity and antibiofilm capacity. Investigation of the photoacoustic imaging potentialities and a deeper analysis of the tissue regeneration ability of the dressing should also be considered.

List of acronyms

^{1}H-NMR	Proton Nuclear Magnetic Resonance
2D	Two-dimensional
3D	Three-dimensional
ABTS	2,2’-azino-bis(3-ethylbenzothiazoline-6-sulfonic acid) diammonium salt
AC	Aminocellulose
ACl	Acryloyl Chloride
Ag	Silver
AMP	Antimicrobial Peptides
ATR-FTIR	Attenuated Total Reflectance–Fourier Transform Infrared
BSA	Bovine Serum Albumin
CDM	1,4-cyclohexanedimethanol
CDs	Cyclodextrins
CFU	Colony Formin Unit
CHP407	P407-based PEU with CDM as chain extender
CMT	Critical Micelle Temperature
CO	Carbon Monoxide
Co	Cobalt
CoPc	Cobalt (II) Phthalocyanines
CS	Chitosan
CWs	Chronic Wounds
DAPI	4’,6-diamidino-2-phenylindole
DBTDL	Dibutyltin Dilaurate
DCE	1,2-dichloroethane
DLS	Dynamic Light Scattering
DMEM	Dulbecco’s Modified Eagle’s Medium
DMSO	Dimethyl Sulfoxide
DNase I	Deoxyribonuclease I
DPPH	2,2-Diphenyl-1-picrylhydrazyl
DTNB	5,5’-dithiobis-(2-nitrobenzoic acid)
ECM	Extra Cellular Matrix
EDC	1-Ethyl-3-(3-dimethylaminopropyl)carbodiimide
EDTA	Ethylene Diamine Tetraacetic Acid
EDX	Energy Dispersive X-ray Spectrometry
EGF	Epidermal Growth Factor
EPS	Extracellular Polymeric Substances
F68	Poloxamer F68
FGF	Fibroblast Growth Factor
G'	Storage Modulus
G''	Loss Modulus
G*	Complex Shear Modulus
GA	Gallic Acid
GAE	GA Equivalents
GE	Glycine Equivalent

GSH	L-glutathione
GSNO	S-nitroso-L-glutathione
H_2O_2	Hydrogen Peroxide
HCl	Hydrochloric Acid
HDI	1,6-hexamethylene Diisocyanate
HOCl	Hypochlorous Acid
ICP-MS	Inductively Coupled Plasma Mass Spectrometry
IL-1	Interleukin-1
iNOS	Inducible Nitric Oxide Synthase
LAP	Lithium phenyl-2,4,6-trimethylbenzoylphosphinate
LCST	Lower Critical Solution Temperature
Lig	Lignin
LTH	L-tyrosine Hydroxamate
LVE	Linear Viscoelastic region
MIC	Minimum Inhibitory Concentration
MMPs	Matrix Metalloproteinase
Mn	Molecular Weight
MPO	Myeloperoxidase
MTT	3-(4,5-dimethylthiazol-2-yl)-2,5 diphenyl tetrazolium bromide
NB	Nutrient Broth
NBoc	N-boc Serinol
NHS	N-hydroxysuccinimide
NIR	Near Infrared
NLC	Nanostructured Lipid Carriers
NO	Nitric Oxide
NPs	Nanoaprticles
P407	Poloxamer P407
PA	Photoacoustic
PBS	Phosphate-buffered Saline
Pc	Phthalocyanines
PCL	Poly(caprolactone)
PDA	Polydopamine
PDGF	Platelet-Derived Growth Factor
PDI	Polydispersity Index
PDMS	Polydimethylsiloxane
PE	polyethylene
PEG-DA	Diacrylated PEG
PEO or PEG	Polyethylene oxide or Polyethylene glycol
PEUs	Poly(ether urethanes)
PGA	Poly(L-glutamic acid)
PHSt	Photostability
PLA	Poly(lactic acid)
PLGA	Polylactic-co-glycolic Acid
PPO	Poly(propylene oxide)
PPRs	Poly(pseudo)rotaxanes

PPT	Photothermal Therapy
PUs	Polyurethanes
PVA	Polyvinyl Alcohol
RNS	Reactive Nitrogen Species
ROI	Region Of Interest
ROS	Reactive Oxygen Species
SEC	Size Exclusion Chromatography
SEM	Scanning Electron Microscopy
SHF68	F68-based PEU with NBoc as chain extender
SLN	Solid-lipid NPs
SM	Supramolecular
SM-gel	Supramolecular hydrogel
SNP	Sodium Nitroprusside
TA	Tannic Acid
TEM	Transmission Electron Microscopy
TFA	Trifluoroacetic Acid
TGF-β	Transforming Growth Factor-beta
TIMPs	Tissue Inhibitors of Metalloproteinases
TNF-α	Tumour Necrosis Factor alpha
TPP	Sodium Tripolyphosphate
TSB	Tryptic Soy Broth
UCST	Upper Critical Solution Temperature
UV	Ulta Violet
VEGF	Vascular Endothelial Growth Factor
ZnO	Zinc Oxide
αCDs	α-cyclodextrins
τ_f	Flow point
τ_y	Yield point

1. General introduction and aim of the thesis

1.1. Wound healing and chronic wounds: definitions and current treatments

1.1.1. Introduction

Chronic wounds (CWs) are defined as "*wounds that have failed to proceed through an orderly and timely reparative process*" [1]. This condition causes significant discomfort and pain for patients, both physically and psychologically, and represents a serious health concern that can lead to severe tissue damage and, in extreme cases, even death [2].

Several factors, including local and systemic pathologies, contribute to the development of CWs. Local factors include infections, tissue hypoxia, repeated trauma, prolonged pressure, and necrosis [2]. Systemic factors involve conditions like cancer or chronic ailments such as diabetes mellitus, cardiovascular diseases, and cerebrovascular diseases [3], [4]. The most common CWs are vascular ulcers, diabetic ulcers, and pressure ulcers, which collectively represent about 70% of all CWs [5]. Vascular Ulcers predominantly involve the lower extremities and often occur in association with chronic cardiovascular diseases, such as venous hypertension, thrombosis, peripheral valve incompetence, and calf muscle dysfunction[3]. In diabetic patients, CWs often develop due to multiple synergistic factors. These include neuropathy which reduces pain sensation and delays wound detection, impaired capillary flow which causes ischemia and hypoxia [6], heightened susceptibility to infections, and aberrant neutrophil activity, which exacerbate the chronicity of wound [5]. Pressure ulcers can manifest in patients subjected to prolonged immobilization, such as those with spinal cord injuries. External pressure obstructs blood and lymphatic flow resulting in venous and arterial occlusion, tissue ischemia, and accumulation of toxic metabolites, which culminate in tissue necrosis and the formation of skin defects [3],[5].

Since CWs often arise in patients affected by long-term pathologies, they are also particularly challenging for the healthcare system, as they necessitate long-term nurse-administered treatments, extended hospital stays, readmissions, and specialized medical or surgical interventions [7], [8]. In 2005, the global incidence of skin and subcutaneous diseases was 492,883,000 cases, which rose to 605,036,000 cases in 2015 [9]. This trend is bound to grow further due to the progressive aging of the population in developed Countries, with rising healthcare costs and resource utilization. A hint on the economic size of this problem is given by the global market for advanced wound care products, valued at 10.6 billion US dollars in 2022 and projected to reach 16.2 billion US$ by 2030 [10].
Despite this worrying trend, comprehensive global data collection specific to CWs is still lacking, hindering the possibility of precisely estimating the cost and impact of this pathology. CWs are frequently managed in homecare settings, an aspect often overlooked in statistical reports. Additionally, the difficulty in obtaining information on CWs is exacerbated by discrepancies among studies in defining the wound types and in evaluating the healing process [11]. Such inconsistencies hinder cross-study comparison and the production of meta-analyses to correctly estimate the worldwide impact. Moreover, data from developing Countries are sporadic, resulting in an incomplete understanding of the geographical prevalence of CWs. Nevertheless, estimations suggest that the incidence of CWs ranges from 0.2% to 2% of the total population in developed Countries accounting for 1 to 4% of the total national healthcare budget [8], [12], [13], [14], [15].

The incidence of this pathology increases significantly when considering the elderly population, and is therefore expected to rise with the progressive extension of the population lifespan [8], [16].

An additional concern related to CWs is represented by infections. Unlike other infectious diseases with individual culpable pathogens, CW infections are usually polymicrobial. Open non-healing wounds are susceptible to microbial contamination, leading to infections that are challenging to eradicate and can develop resistance to conventional antibiotics [17]. On the other hand, Bacterial biofilms are arguably the most important factor that impairs healing. As the incidence of CWs continues to rise, there is an anticipated increase in the spread of antimicrobial-resistant infections, recognized by the World Health Organization as one of the foremost global public health threats [18].

1.1.2. The wound-healing process

Wound healing is a complex process that relies on the collaborative efforts of various cell types and enzymes, as well as on the precise regulation of the secretion of multiple growth factors and cytokines [2]. This intricate process can be divided into four phases: ***hemostasis, inflammation***, ***proliferation***, and ***remodeling*** (Figure 1.1). Each stage demands the activation of specific cell types and a sequence of interrelated processes, each with specific and well-defined time constraints. [19].

The initial phase, *hemostasis*, is triggered when the skin's integrity is compromised, initiating the coagulation cascade. Activated platelets release chemotactic factors, such as platelet-derived growth factor (PDGF) and transforming growth factor-beta (TGF-β), that are responsible for attracting macrophages, neutrophils, fibroblasts, endothelial cells, and smooth muscle cells which establish an immune barrier against the external environment [3].

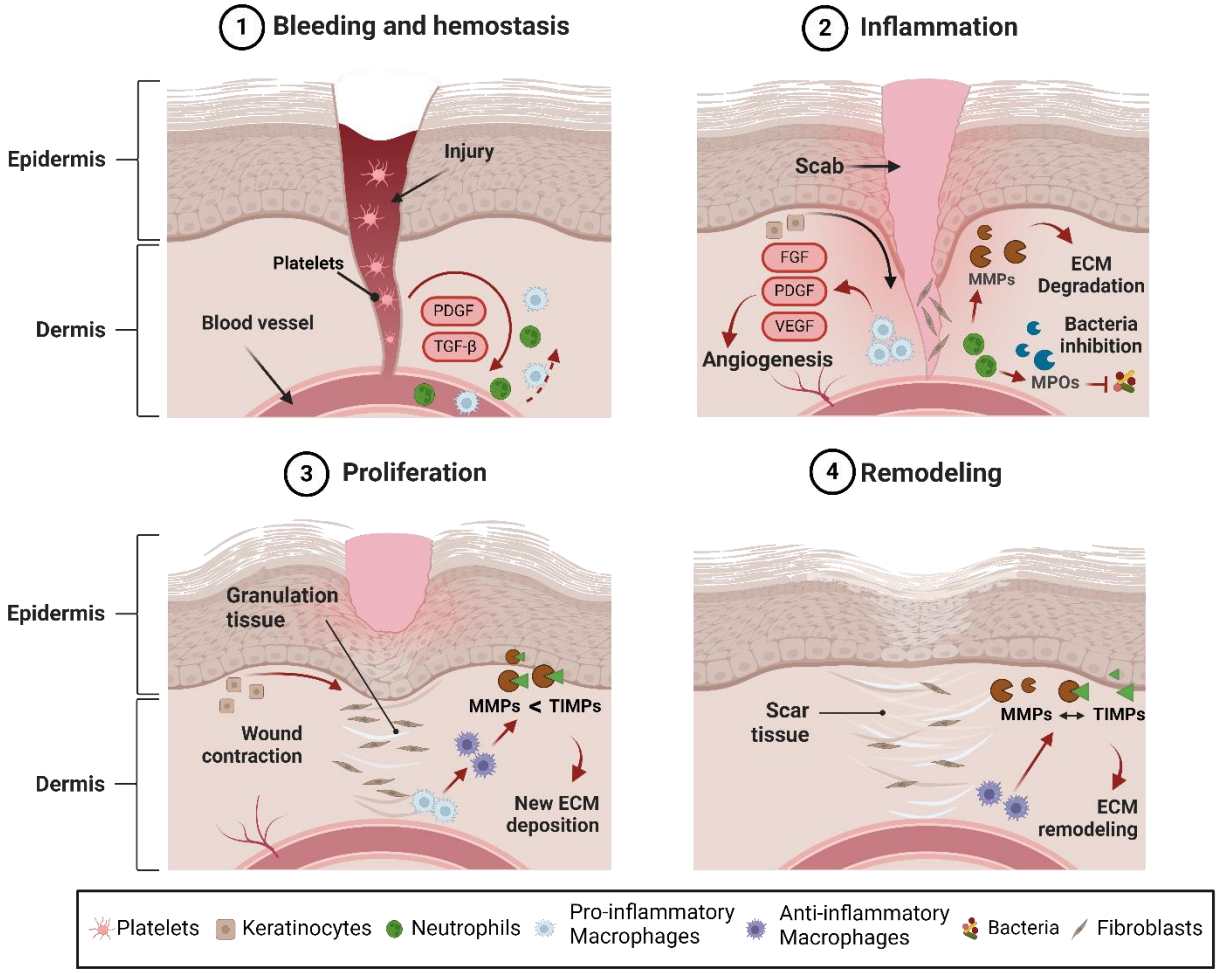


Figure 1.1. Schematic representation of the four main stages of the healing process.

In the *inflammatory phase*, a pivotal role is played by macrophages and neutrophils that eliminate pathogens and support regeneration [20]. Neutrophils are the first immune cells to accumulate at the wound site, where they remain for approximately 24 h before undergoing apoptosis. Their role is to eliminate foreign materials, damaged matrix components, and non-functional host cells, through the secretion of proteolytic enzymes, such as serine proteases and matrix metalloproteinases (MMPs) [2]. Moreover, they prevent infection insurgence by phagocytosing pathogens and secreting myeloperoxidase (MPO), an antimicrobial enzyme involved in the production of hypochlorous acid (HOCl) [21]. Macrophages arrive at the wound site 3-5 h post-injury and remain there for several weeks, undergoing phenotypic changes throughout the healing process. Initially, macrophages adopt a proinflammatory phenotype, also known as M1. M1 macrophages are primarily involved in clearing the wound site, by eliminating cellular debris, damaged extracellular matrix components, and microbes, as well as in the secretion of cytokines, such as interleukin-1 (IL-1), fibroblast growth factor (FGF), PDGF, and vascular endothelial growth factor (VEGF) [2]. These cytokines are essential for the mobilization of immune cells and for the proliferation of keratinocytes, fibroblasts, and epithelial cells, in turn stimulating the formation of granulation tissue and angiogenesis [22].

As fibroblasts and keratinocytes are progressively recruited and activated, the wound transitions from the inflammatory phase to the *proliferative state* [20]. Keratinocytes migrate into the wound bed through the fibrin matrix to close the wound, while fibroblasts produce new extracellular matrix (ECM) components, including collagen, elastin, glycosaminoglycans, and proteoglycans, as

well as MMPs, which degrade the old ECM to make room for the deposition of a new matrix [3]. During the formation of the new tissue, environmental cues prompt macrophages to shift to an anti-inflammatory state (M2) and secrete anti-inflammatory cytokines, such as TGF-β1, which promote ECM synthesis and facilitate wound contraction [22].
The final phase, the *remodeling*, can last weeks to years. In this stage, M2 macrophages exploit the synergistic action of MMPs and tissue inhibitors of metalloproteinases (TIMPs) to break down disorganized collagen and produce stronger type I collagen, rearranged along the tissue tension lines to give a stiffer network [2]. These macrophages also contribute to phagocytosing the remaining debris. The ultimate scar can regain up to 80% of the tensile strength of the non-wounded tissue [3].

1.1.3. The impaired wound-healing process in chronic wounds

The above paragraph describes how the process of wound healing progresses through distinct cellular and molecular events, meticulously orchestrated to culminate in tissue regeneration. Any disruption in these mechanisms can compromise wound healing, resulting in failed closure or excessive scarring and contracture [20]. CWs represent a common and widely studied example of disruption of this delicate equilibrium.
Despite their diverse origin, all CWs display the inability to progress beyond the inflammatory phase of the healing process, resulting in hampered proliferation, low matrix deposition, and incomplete wound closure [2].
CWs exhibit elevated levels of proinflammatory cytokines, reactive oxygen species (ROS), and proteases [22],[23] (e.g., MMPs), as well as reduced levels of TIMPs [19] (Figure 1.2). In normal wounds, macrophages support the healing process by phagocytosing apoptotic cells and neutrophils that have completed their function. However, in CWs macrophages exhibit reduced phagocytic activity, resulting in the accumulation of apoptotic cells and neutrophils [22]. The sustained activity of neutrophils is responsible for the continuous production of MMPs, which degrade cytokines and ECM components [2],[20]. Furthermore, neutrophils secrete MPO which contributes to the degradation of biological molecules, including TIMPs [24], [25]. The combination of MMPs overexpression and TIMPs inhibition leads to excessive ECM degradation, exacerbating the inflammatory state and impeding the healing process.
Additionally, macrophages in CWs fail to transition from the pro-inflammatory to the anti-inflammatory phenotype. M1 macrophages continue to secrete inflammatory mediators, including pro-inflammatory cytokines, ROS, and inducible nitric oxide synthase (iNOS) [22]. Excessive ROS disrupt the oxidant/antioxidant balance, leading to increased secretion of pro-inflammatory chemokines and MMPs, prompting premature fibroblast senescence [2]. Indeed, studies have shown that wound fluids from CWs inhibit the proliferation of fibroblasts and keratinocytes *in vitro* and that fibroblasts isolated from CWs possess signs of senescence and diminished mitogenic capacity [23].
Lastly, since the wound remains open for an extended period, it becomes susceptible to infections, therefore intensifying the inflammatory response and impeding healing [17]. In CWs, bacteria from different species can aggregate within a self-produced ECM to form *biofilms*. Bacteria communities within biofilms shift from an individual and proliferative state, known as the planktonic state, to a more organized and static condition, called the sessile state [26], and produce extracellular polymeric substances (EPS). These EPS, mainly exopolysaccharides, proteins, and DNA, form three-dimensional structures that improve intercellular communication and nutrient exchange among bacteria, while also providing protection against antibacterial treatments [27]. Indeed, bacteria embedded in biofilms exhibit resilience against both, the host immune system and conventional antibiotics [28]. The poor vascularization in CWs further worsens the situation by reducing immune

cell infiltration and hampering the accumulation of systemically administered antibiotics in the wound [29]. Therefore, antimicrobial treatments are administered over a long period, increasing the risk of developing antimicrobial resistance [30]. Furthermore, bacteria can manipulate the inflammatory environment in the wound by secreting virulence factors that upregulate pro-inflammatory cytokines, MMPs, and ROS [6]. Additionally, the presence of the biofilm impedes the formation of tight junctions between epithelial cells, which is critical for establishing a fluid-impermeable barrier for skin protection [17].

Collectively, these factors create a pro-inflammatory environment, which hinders the wound from progressing through the final phases of healing.

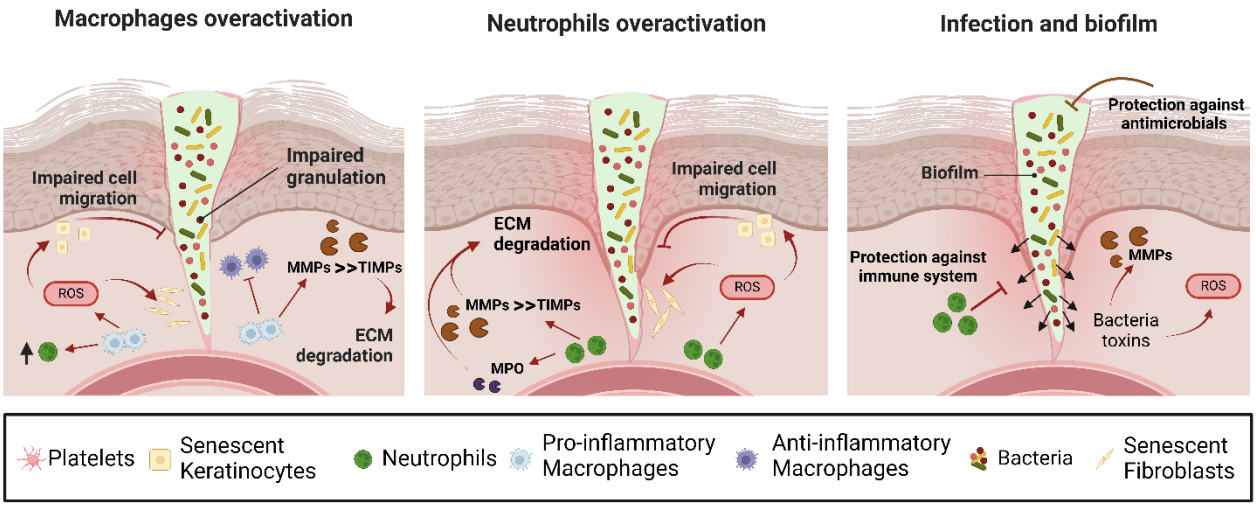


Figure 1.2. Inflammatory process in chronic wounds.

1.1.4. Management and treatment of CWs

CWs represent a complex pathological condition characterized by sustained inflammation. To address CWs, healthcare professionals have developed a guideline, known as TIME, which emphasizes four key aspects of CW management: *Tissue*, *Infection, Moisture imbalance*, and *Edge advancement* [29], [31].

Typically, the first step is to prepare the wound bed. TIME recommends maintaining a clean wound bed with a healthy granulating base [31]. To achieve this, the removal of necrotic and devitalized tissue is essential and can be performed through various methods, including physical, surgical, enzymatic, and biological debridement. In CWs, this preparation may need to be repeated regularly due to continuous debris production. Cleansing antimicrobial agents can also be applied during this process to reduce the bacterial burden on the wound bed [29].

The second aspect to be addressed is the presence of infections, which must be identified and evaluated. Infected wounds often exhibit malodor, pain, excessive exudate production, undermining borders, and friable tissue [17]. Thorough wound cleansing and targeted treatment of microbial organisms with appropriate antimicrobial agents, which can be either administered systemically or topically, are essential factors in reducing the persistence of infections in CWs [29]. To address the infection topically, dressings containing antimicrobial agents can be chosen. Their characteristics will be described in the following paragraphs [4].

The third critical aspect to manage is moisture imbalance. Maintaining optimal moisture levels involves reducing excessive exudate and preventing the wound bed from drying out. The selection

of suitable dressings is crucial for achieving this goal, with various options available that can absorb significant amounts of exudate while preserving moisture and restoring a healthy wound environment [31]. In acute wounds, the exudate is considered beneficial for the healing process since it contains biochemical factors that stimulate regeneration. Moreover, the presence of a moist environment assists cell migration and maintains pH, oxygen levels, and electrical gradients. Therefore, occlusive dressings are recommended for treating this type of wound [32]. However, in CWs, dressing selection is more complicated, as CW fluids contain compounds that may be detrimental to healing and should be eliminated [29]. Various dressing options are available depending on the quantity of exudate present and will be discussed in the following paragraphs.

Lastly, promoting wound edge advancement is essential for facilitating healing. This entails maintaining a healing-promoting environment by establishing a well-vascularized wound bed with sufficient oxygen and nutrient supply, and by managing systemic diseases such as diabetes mellitus, chronic venous insufficiency, or arterial disease [29]. To achieve this, different techniques are employed, such as the use of bioengineered dressings containing cells, growth factors, and ECM components mimicking the healthy skin architecture [31]. Hyperbaric oxygen therapy is also utilized to induce hyperoxia, which is known to stimulate wound healing by enhancing the production of growth factors and nitric oxide [29].

1.1.5. Commercial dressings used in wound treatments

Various dressings for CW treatment are available on the market and are classified into passive, active dressings, and bioengineered dressings (Figure 1.3). The selection is performed by the medical personnel mainly based on the wound condition but is also influenced by other factors, such as cost or patient preference and comfort [33].

Most dressings are passive dressings, meaning that they exert a passive action on the wound environment by controlling moisture and absorbing exudate. Depending on the amount of exudate produced, different solutions are available. For highly exudative wounds, the ideal dressing should possess strong fluid-retention properties [29], [33]. Polyurethane foams, such as Allevyn® (by Smith & Nephew), Biatain® (by Coloplast) and Tegaderm® (by 3M), or alginate dressings, such as Curasorb (by Covidien), SeaSorb (by Coloplast), and Sorbsan (by Unomedical) are particularly suited for this purpose since the material can absorb and retain a large quantity of fluids.
On the other hand, mildly exudating wounds can be treated with hydrocolloids, such as ranuflex® (by ConvaTec), and NU DERM® (by Systagenix) [34]. These occlusive dressings are composed of high molecular weight hydrophilic polymers capable of forming a gel when in contact with the moist wound surface [33].
Finally, hydrogels, such as ActiformCool® by Activa [35] - composed of a hydrophilic polymer carrying pendant sulphonyl groups - and Aquaflo® by Covidien [36]) - made of polyethylene glycol and propylene glycol - are used preferably on dry or low-exudating wounds by virtue of their ability to absorb a high amount of water [29], [31], [33].
The market also presents dressings capable of exerting an active function on wounds [7]. For instance, hydrocolloids and hydrogels can stimulate autolytic debridement, a process that stimulates wound regeneration by promoting the activity of endogenous proteolytic enzymes capable of eliminating damaged tissue [37]. Additionally, dressings can embed active compounds that are released on the wound site. For instance, local delivery of growth factors or platelet-enriched plasma showed improved healing in clinical trials, but meta-analyses highlighted the lack of high-quality evidence [38], [39]. As a result, these dressings failed to progress to the market. When infections are present, dressing can be loaded with broad-spectrum antimicrobials, such as iodine (e.g., doflex® by Smith & Nephew and Iodozyme® by Insense) or silver ions (e.g. Acticoat®

by Smith & Nephew and Urgosorb Silver® by Urgo) [33]. In particular, silver is considered a gold standard in the treatment of infected wounds due to its antibacterial activity and the low risk of stimulating antibiotic resistance [40]. Some dressings also use natural compounds such as honey to reduce the bacterial burden (e.g., Medihoney® by Medihoney and Activon Tulle® by Advancis). Despite the large choice of medicated dressings, several meta-analyses failed to observe significant differences in their healing capacity, mainly because the trials were small and poorly reported [33], [34], [41], [42], [43]. Moreover, in clinical trials, antimicrobial dressings failed to show a significant increase in the complete healing rate when compared to passive dressings [41], [42], [44]. This lack of significance can be partly attributed to the qualitative methods used by medical personnel for assessing the wound, which reduces the possibility of quantifying and comparing different dressings [33].

When standard solutions are insufficient to induce regeneration, allogenic skin grafts and bioengineered dressings are used [29]. These dressings comprise ECM components and/or human cells to better mimic the skin architecture. They can be divided into three categories: epidermal, dermal, and combined epidermal-dermal constructs. Epidermal substitutes are obtained by culturing the patient's keratinocytes in sheets that are applied to the wound site [45]. Several companies handle the entire process, from patient cell collection to expansion, and provide the final epidermal constructs. These services can be found on the market under the names Epicel® (by Genzyme Corporation), Cell Spray® (by Avita Medical), Myskin® (by Regenerys) and Epidex® (by EuroDerm Biotech & Aesthetics) [45]. This type of autograft has long been used in hospitals, especially for treating extensive burn wounds. However, it cannot be utilized steadily, since growing the cell sheets requires 16 to 21 days [29].
Dermal substitutes may include a synthetic matrix, human cells, and non-human ECM components to reproduce the dermal compartment and are applied on both, acute and chronic wounds [29]. For instance, OASIS® Matrix (by Smith & Nephew), a decellularised dermal matrix derived from porcine small intestinal submucosa, has been applied successfully for treating various acute and chronic wounds, such as full-thickness wounds, pressure ulcers, venous ulcers, diabetic ulcers, and surgical wounds [45]. Dermagraft® (by Organogenesis Inc), a dermal matrix composed of a biodegradable polyglycolic acid mesh, includes live human fibroblasts with the potential to produce cytokines and growth factors beneficial for regeneration [45]. However, when compared to OASIS® Matrix in a clinical trial, the treatment with Dermagraft® was more expensive and did not result in significantly improved outcomes [46], underlining the importance of conducting comparative trials to assess the effectiveness of new treatments.

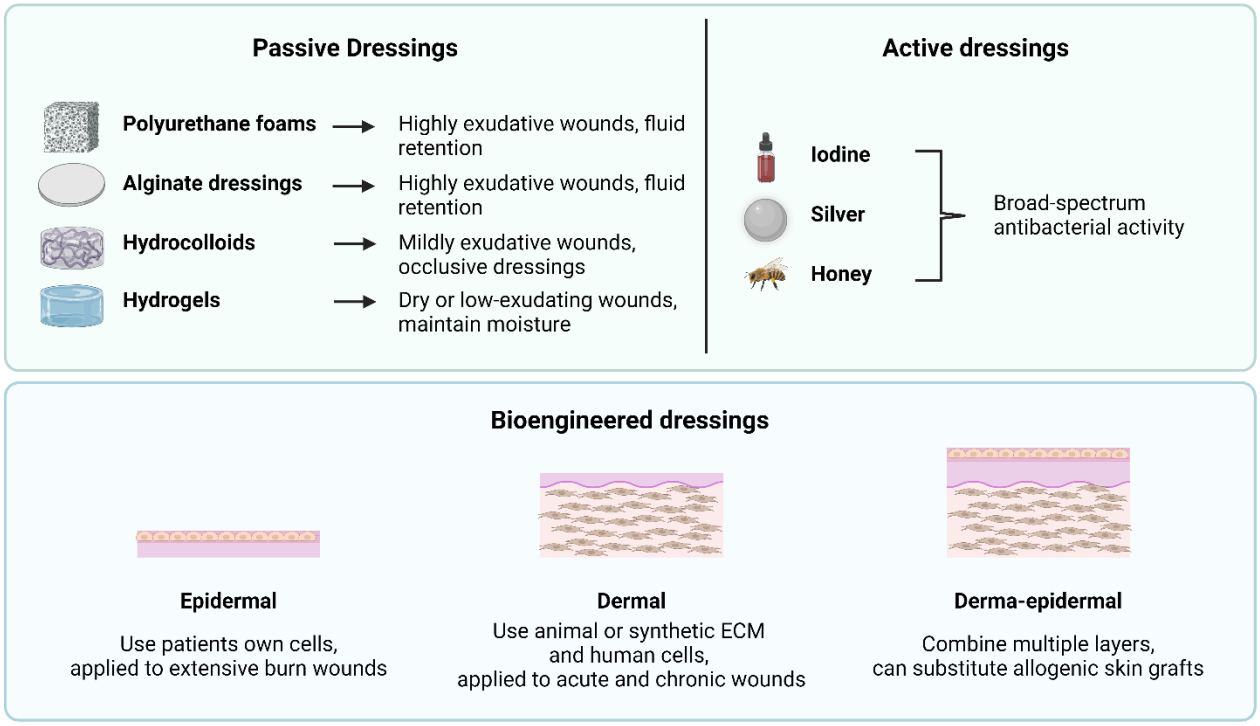


Figure 1.3. Types of dressings available on the market.

Finally, products that combine dermal and epidermal components in a single construct have the potential to better mimic the skin architecture. Apligraf® (by Organogenesis Inc) is composed of a bovine collagen matrix seeded with neonatal fibroblasts, mimicking the dermis, and a superficial layer of human keratinocytes, mimicking the epidermis. Different clinical trials confirmed the effectiveness of Apligraft® in promoting wound closure compared to patients treated with traditional dressings [47], [48]. Similarly, StrataGraft® (by Stratatech) combines a fully developed keratinocyte layer with neonatal fibroblast embedded in a murine collagen matrix to generate a stratified skin substitute [49]. In clinical trials, StrataGraft® emerged as a valid alternative to cadaveric allografts, showing comparable performances while reducing the risk of infections [50], [51]. A comprehensive meta-analysis comparing different clinical trials confirmed that using bioengineered dressings significantly improves the patient's clinical outcomes compared to traditional dressings [52]. However, their cost, storage requirements, and need for professional handling limit their applicability in home-based wound care settings and in developing Countries.

Despite the wide choice of dressings, the development of new solutions addressing all aspects of CWs remains a largely unmet clinical need and the definition of a golden standard for treating CWs is far from being achieved. Optimal dressings should be cheap and easy to handle, and capable of combining multiple functions, such as timely and orderly tissue regeneration with broad-spectrum antibacterial and anti-inflammatory action.

1.1.6. Multifunctional wound dressings – state of the art

In the last decade, research on CWs focused on exploiting biomaterials, including polymers and inorganic compounds, to develop novel multifunctional dressings capable of inducing regeneration while exerting a therapeutic effect [53]. This is achieved through the combination of macroscopic matrices, designed to support the regeneration process, with therapeutic compounds and/or nanoparticles (NPs), designed to mitigate the inflammatory response, stimulate angiogenesis, and manage local infections [54] (Figure 1.4).

Different macroscopic 3D matrices in the form of nanofibrous structures, scaffolds, or hydrogels have been proposed. These matrices should possess a porous structure that facilitates fluid and nutrient exchange, provide a cell-friendly environment for cell migration and tissue regeneration, protect the wound bed from external contamination, absorb the exudate, and host and release therapeutic compounds [55].

The matrix structure and its forming material are the most critical parameters affecting the performance of the dressing. For instance, polymers with cell-binding sites are used to recreate a cell-friendly environment [54]. Natural polymers, e.g., proteins, peptides, and polysaccharides (mainly chitosan and alginate) and hyaluronic acid), are particularly appealing in this regard, being also extremely biocompatible, biodegradable, and having low antigenicity. For instance, collagen is the main protein component of the ECM. Therefore, collagen and its derivative, gelatine, have been widely used in wound dressings to provide a biomimetic environment for cell colonization and tissue regeneration [56][57]. Other natural polymers possess antibacterial and/or hemostatic activity, useful in wound regeneration. For example, fibrin, a derivative of fibrinogen, silk fibroin, and alginate are used because of their adhesive and hemostatic properties [58] [59]. Intrinsically antibacterial polymers, such as chitosan, polyethyleneimine, and small cationic peptides, are appealing to reduce bacterial contamination in wounds [56], [60], [61]. Moreover, their antibacterial function can be further enhanced by functionalization with cations, such as quaternary ammonium [62].

Since natural polymers often display scarce mechanical properties and high batch-to-batch variability, they are often blended with, or substituted by, synthetic polymers, which possess more controllable and reproducible properties [54], [59]. Among synthetic polymers, polyesters (such as polylactic-co-glycolic acid (PLGA), poly(lactic acid) (PLA) and poly(caprolactone) (PCL)), polyethers and polyurethanes have found extensive application in wound healing. Polyethers, such as polyethylene oxide (PEO), are applied in wound healing because of their ability to retain water and maintain moisture [54]. Polyesters and polyester urethanes possess tunable mechanical properties that allow the modulation of their stiffness and processability [54].

These materials, alone or in combination, have been processed through different techniques to obtain films, hydrogels, and nanofibers for CW treatment [63][63], [64], [65], [66]. The final architecture of the matrix is essential for tissue regeneration. For example, nanofibrous 3D matrices composed of agglomerates of randomly distributed nanometric fibers, are excellent mimics of the skin ECM architecture, thereby facilitating new tissue growth [67] [37]. Moreover, their porosity can be largely tuned to allow gas/nutrient exchange that favors cell survival and the incorporation and release of therapeutics [54] [68]. On the other hand, hydrogels, which are 3D porous networks obtained by chemical or physical interactions, have the potential to absorb and retain large amounts of fluids and are useful in preventing wound dehydration and in maintaining a moist environment beneficial for healing [69]. Hydrogels also possess a controllable porous structure that facilitates the penetration of oxygen and the encapsulation of drugs and cells [70] [71] [72]. Moreover, hydrogels may also display self-healing properties, injectability, and self-assembly, which makes them ideal candidates for covering complex wound shapes and for the encapsulation of unstable and delicate compounds [71].

Macroscopic matrices should also exert a therapeutic action, for instance by sustaining the release of therapeutic compounds and NPs or through the intrinsic properties of its forming materials. The therapeutic activity can be the mitigation of the inflammatory response, the stimulation of hemostasis and angiogenesis, and the management of local infections [68] [58].

To reduce inflammation, ROS-scavenging compounds, such as natural polyphenols (e.g. polydopamine (PDA), lignin, gallic and tannic acid), are often included in dressings [37]. For instance, Kaparekar et al. [73] encapsulated gallic acid within chitosan NPs which were integrated into a collagen-fibrin scaffold, achieving faster wound contraction and epithelialization *in vivo.* In another study, Fu et al. [74] combined PDA NPs with ascorbic acid, observing an enhanced ROS scavenging capacity compared to pristine PDA NPs. These NPs were then incorporated into chitosan/dextran hydrogels, achieving antibacterial activity *in vitro* and improving wound healing *in vivo*. With a different approach, Morena et al. [75] combined lignin with tannic acid to produce NPs with antibacterial and antioxidant properties. These NPs were then utilized to induce the gelation of a solution containing silk fibroin and hyaluronic acid, producing a hydrogel that displayed antibacterial properties and inhibited MMPs and MPO activity. Curcumin, with its excellent antioxidant and anti-inflammatory properties, is an appealing compound for wound treatment, albeit suffering from low water solubility [76]. Numerous studies have demonstrated that the incorporation of curcumin into different matrices enhances its stability and bioavailability both *in vitro* and *in vivo* [77], [78], [79], [80], [81]. For instance, Karri et al. [79] produced curcumin-chitosan NPs through the ionotropic gelation method and loaded them into a collage-alginate hydrogel. The obtained system greatly improved wound contraction *in vivo* and full regeneration of the epithelial layer in histological assays. Using a different strategy, Chen et al. [82] encapsulated curcumin into lipidic carriers and loaded them into a Poloxamers®-based hydrogel. The system demonstrated a strong anti-inflammatory effect and increased curcumin penetration into the skin tissue.

Antioxidant compounds can also be entrapped in the porous mesh of nanofibrous systems. For example, Agarwal et al. [83] integrated curcumin into PCL/polyvinyl alcohol/silk fibroin nanofibers showing improved wound healing efficacy in diabetic mice and restoration of normal skin structure. Similarly, Adeli-Sardou et al. [84] combined PCL and gelatine to obtain electrospun nanofibers encapsulating lawsone, a naphthoquinone extracted from Henna leaves with antioxidant and antibacterial activity but poor water solubility. They demonstrated consistent release over 20 days, antibacterial activity *in vitro* and improved wound closure *in vivo*.

Antioxidant components can also be directly attached to the matrix material. For instance, Tang et al. [85] modified graphene oxide with anti-oxidant dopamine and used it in combination with chitosan and silk fibroin to obtain a hydrogel capable of reducing cellular oxidation and promoting wound healing. Qu et al. [86] combined N-carboxyethyl chitosan with oxidized hyaluronic acid grafted with aniline tetramer, a ROS scavenger, through the Schiff base chemistry. The obtained hydrogel demonstrated antioxidant properties and was able to accelerate wound healing rate by promoting tissue granulation, collagen disposition and angiogenesis in murine wound model.

To facilitate hemostasis, the wound should be isolated from the external environment [3]. Adhesive matrices can achieve this by sealing the wound bed and stimulating the coagulation cascade [69]. For instance, dopamine and polysaccharides such as dextran, chitosan and alginate, have well-known adhesive properties [69]. Moreover, adhesiveness can be achieved by incorporating functional groups, such as aldehydes and thiols, in the polymer chain. Interestingly, chitosan and its derivatives have also been shown to activate platelets and promote clotting, improving overall wound healing *in vivo* [87]. Nanostructured matrices can stimulate hemostasis by means of their 3D architecture. For instance, Zhang et al. [88] developed a chitosan/PVA nanofibrous sponge by expanding a two-dimensional (2D) nanofibrous film through a gas-foaming technique. The obtained 3D sponge accelerated hemostasis thanks to the increased interfacial interaction between the matrix and blood cells. Moreover, the 3D structure showed higher gas

permeability and fluid absorption, was able to promote cell adhesion *in vitro*, and accelerated wound healing while reducing scar formation *in vivo*. In another study, Chen et al.[89] used sequential electrospinning to obtain a three-layered nanofibrous membrane composed of chitosan, PVA and nanobioglass, each layer with a specific function. The chitosan sublayer aimed to promote hemostasis and reduce bacterial burden, the chitosan-PVA-based mid-layer retained moisture and absorbed exudates and the PVA-bioglass top-layer promoted tissue regeneration. *In vivo*, the system accelerated and enhanced wound healing by stimulating re-epithelialization and collagen alignment. Moreover, the 3D system could upregulate growth factors, such as VEGF and TGF-β, and downregulate inflammatory cytokines, such as tumor necrosis factor-alpha (TNF-α) and IL-1.

The promotion of angiogenesis is another fundamental step toward healing since it favors cell infiltration and nutrient accumulation at the wound site [37]. The most common strategy to achieve angiogenesis is by delivering cytokines and growth factors, such as VEGF [54], [68], [90]. Other than promoting angiogenesis, the delivery of growth factors and cytokines, such as VEGF, PDGF and epidermal growth factor (EGF), can stimulate tissue regeneration [68]. Unfortunately, these compounds are easily degraded in the CWs environment, rich in protein-degrading enzymes. Therefore, using appropriate systems for controlling, improving and protecting the delivery of these compounds is of utmost importance [91], [92]. For instance, Das et al. [93] encapsulated PDGF into liposomes modified with syndecan-4, a transmembrane proteoglycan involved in wound healing. These liposomes shielded the growth factor, while the presence of syndecan-4 augmented its activity. The NPs demonstrated improved wound closure and increased re-epithelialization and angiogenesis in diabetic mice models. Xie et al. [94] combined chitosan and PEO to obtain nanofibers for delivering VEGF and PDGF. The mesh was able to promote fibroblast proliferation *in vitro* and accelerate wound healing *in vivo.* Similarly, Garcia-Orue et al. [95] developed a PLGA fibrous system containing EGF and Aloe Vera extracts capable of accelerating wound closure and re-epithelialization. Similarly, Xie et al. [94] encapsulated PDGF and VEGF in PLGA NPs, loading them into chitosan–PEO electrospun nanofibers to promote angiogenesis and re-epithelialization *in vivo*. Nanogels, obtained through the physical or chemical crosslinking in the nanoscale range of polymers with amphiphilic properties, have also been proposed for the delivery of unstable compounds [54] [96]. Their high swelling capacity drives the release of their cargo by diffusion mechanisms coupled with network degradation, while their viscoelastic properties favor their injection through needles [96]. Kobayashi et al. [97] modified cholesterol with carbamate groups and conjugated it with pullulan. They then used the self-assembling capacity of cholesterol-bearing pullulan to produce nanogels encapsulating prostaglandin E1, which promoted epithelialization, angiogenesis, and wound closure in a rat wound model.

Hyperbaric oxygen therapy has been demonstrated to promote wound healing by alleviating the inadequate oxygen levels in CWs [69]. Therefore, systems controlling the delivery of oxygen have gained attention in recent years. Chen et al.[98] developed an oxygen-producing patch made of living algae, separated from the wound bed by a polytetrafluoroethylene membrane to allow gas permeation. Upon treatment with Near-infrared (NIR) light the patch was capable of releasing oxygen in the wound site, thereby increasing wound oxygenation, fibroblast proliferation, and angiogenesis in murine chronic wound models.

Finally, managing infections is a fundamental part of promoting wound healing. To address multi-species bacterial infections and biofilms, broad-spectrum antimicrobials, such as metals, essential oils, and antimicrobial peptides (AMPs), can be included in dressings [17]. Metal NPs represent the most studied antimicrobial agents for wound dressings by virtue of their broad-spectrum

antibacterial activity and low risk of inducing antimicrobial resistance [54]. Among them, Silver (Ag), gold (Au), and zinc oxide (ZnO) are the most widely employed [58]. Ag ions have been known for their antibacterial activity since ancient times and are broadly used in several dressings available on the market, such as Acticoat® by Smith & Nephew and Urgosorb Silver® by Urgo [33][33], [40], [44]. Because of the increasing concerns related to the toxicity of Ag ions to eukaryotic cells, several strategies have been proposed to better control Ag release. Keleştemur et al. [99] coated Ag NPs with oligonucleotides therefore improving their cytocompatibility and promoting wound healing. Polyphenolic compounds have also been proposed to encapsulate Ag, since Ag ions can be reduced by the catechols and phenols in polyphenolic materials, resulting in the formation of NPs [69]. For instance, Morena et al. [100] combined Ag and lignin to obtain NPs with antibacterial and antioxidant activity. These NPs were then integrated into a highly absorbent polyurethane foam that inhibited MPO and MMPs in wound exudates from patients. Sofi et al. [101] included Ag NPs in polyurethane nanofibers co-loaded with lavender oil. The system showed good antibacterial properties against both Gram-positive and Gram-negative bacteria. Other metal NPs, such as ZnO NPs, are studied as an alternative to Ag NPs. ZnO NPs have been integrated into different delivery systems [102] [103]. For example, Ahmed et al. [104] used chitosan and polyvinyl alcohol (PVA) to obtain electrospun fibers encapsulating zinc oxide (ZnO). The combined action of chitosan and ZnO enhanced the antibacterial activity and stimulated regeneration *in vivo*.

Essential oils and AMPs are also promising candidates in treating bacterial infections. Essential oils also possess antioxidant and anti-inflammatory activity [105], which makes them extremely appealing to concomitantly tackle several key aspects in wound regeneration. Nonetheless, their volatility and susceptibility to light necessitate proper encapsulation. Lipid NPs have been extensively utilized in various studies for this purpose [106], [107], [108] thanks to their capability of enhancing the bioavailability and tissue permeability of poorly soluble drugs and compounds [109]. For instance, Khezri et al. [110] encapsulated Rosmery essential oil into lipid nanocarriers and integrated them in a Carbopol® hydrogel. The gel reduced bacterial colonization and stimulated vascularization, fibroblast infiltration, re-epithelialization, and collagen production in a murine infected wound model. The essential oils have also been loaded directly within the dressing matrix. For example, García-Salinas et al. [111] developed PCL nanofibrous patches loaded with different essential oils: thymol, curcumin, cinnamaldehyde, carvacrol, squalene, tyrosol, and β-caryophyllene. They compared their action in inhibiting *Escherichia coli* and *S. aureus* and reducing inflammation in *in vitro* models, identifying thymol-loaded patches as the best for fulfilling both aspects.

AMPs are small peptides exerting antibacterial activity by physically disrupting the cellular membrane, therefore reducing the risk of developing resistance [112] [113]. However, they are also prone to degradation in the CW environment and require a protective system for their delivery. As an example, Ju et al. [114] obtained self-assembled NPs by conjugating chitosan, PEG, and AMPs, that were capable of penetrating the biofilm and inactivating Gram-negative *Pseudomonas aeruginosa*.

Nitric oxide (NO) delivery is also a studied solution in wound dressings since NO possesses broad-spectrum antibacterial activity and can promote biofilm dispersion [115], [116] Additionally, it is known to stimulate ECM deposition, cell proliferation, and angiogenesis [117] [90]. To target these properties, Nurhasni et al. [118] synthesized NO-enriched polyethyleneimine and combined it with PLGA to obtain NO-releasing NPs which showed controlled NO release over 6 days and antibacterial activity against methicillin-resistant *S. aureus* (MRSA) and *P. aeruginosa*.

Recent research is focusing on a new type of therapeutic matrices, in which the therapeutic action can be triggered in response to endogenous factors (such as variations in temperature, pH, ROS levels, ATP concentrations, enzyme activity, and blood glucose levels) or exogenous stimuli (such as light, magnetic and mechanical forces) [53], [69]. Hydrogels can be obtained with materials that present thermal sensitivity and are used to achieve gelation at temperatures below or close to the human body temperature. This property allows the preparation of a precursor solution that could be injected into the wound site, where it rapidly transitions to a more stable gel structure [119]. Poloxamers® are an excellent example of polymers presenting this property. They are a family of triblock amphiphilic polyether polymers consisting of poly(ethylene oxide) (PEO)/poly(ethylene glycol) (PEG) as the hydrophilic chain, and poly(propylene oxide) (PPO) as the hydrophobic block. [119]. For instance, Sivaraman et al. [120] and Khan et al. [121] exploited the thermosensitivity of Poloxamer-based hydrogels for transdermal delivery of different model drugs, using a microneedle system. They both demonstrated improved skin permeation and sustained delivery of the drugs in *ex vivo* porcine and human skin samples.

CWs possess an alkaline pH [122], while the pH in normal wounds varies with the wound stage. Therefore, responsiveness to pH levels has been exploited to trigger therapeutic actions in wound dressings. Oh et al. [123] obtained a hydrogel based on alginate and bentonite, a natural inorganic polymer, achieving increased drug release at alkaline pH. Similarly, Wang et al. [124] developed a calcium-alginate hydrogel loaded with hyaluronan, a compound capable of simulating endothelial cell proliferation and angiogenesis. The obtained hydrogel presented high swelling and network disruption in alkaline media, stimulating hyaluronan release and making the system an interesting candidate for treating CWs.

Light excitation in the NIR spectrum is another appealing strategy to trigger a therapeutic response [69]. Inorganic components at the nanoscale are particularly indicated thanks to their unique optical and magnetic properties [125], [126]. Indeed, nanoscaled inorganic compounds can be excited with NIR light to obtain local heat variations (photothermal effect) that can be exploited to treat bacteria and trigger local drug release [69], [127], [128]. For this reason, various inorganic NPs, such as metallic NPs (e.g. Ag NPs and Au NPs), carbon-based NPs (e.g. graphene oxide (GO) NPs), and ceramic NPs (e.g. silica NPs and titanium oxide NPs) have been used for promoting wound healing [125], [129]. For instance, Lin et al. [130] synthesized Ag-Au hollow NPs incorporating the photosensitizer Chlorin e6 (Ce6), which converts oxygen into ROS when excited by light. Upon NIR light irradiation, the NPs combined photothermal therapy, given by the presence of Ag and Au, with the production of ROS, mediated by Ce6. These combined effects exhibited antibacterial activity against wound-colonizing *S. aureus* and *E. coli* in a murine model, while also accelerating wound healing by promoting epithelial migration and vascularization. In another study, Wu et al. [131] produced copper-Au nano-assemblies that were able to generate heat upon NIR light irradiation, promoting biofilm disruption. Additionally, the temperature increase stimulated the disaggregation of the nano-assemblies into smaller particles favoring NPs penetration and copper ion release. Thanks to these effects, the NPs reduced bacterial burden and stimulated wound closure in MRSA-infected wounds in diabetic mice. Using a different approach, Shahnawaz et al. [132] developed GO nanoflakes exerting photothermal activity under NIR light irradiation. The NPs could eradicate different bacterial and fungal species *in vitro* and stimulate regeneration in a murine infected wound model. Additionally, organic compounds, such as dopamine, could also present photothermal properties. For instance, Gao et al. [133] developed an injectable hydrogel by combining antibiotic-loaded polydopamine NPs with amine-rich glycol chitosan through a Schiff base reaction. In the system, photothermal activity was achieved thanks to the presence of the polydopamine NPs. This NIR irradiation triggered the release of the

antibiotic, stimulating wound regeneration in *S. aureus*-infected wound models in mice. Similarly, Yuan et al. [134] used mesoporous polydopamine NPs loaded with a carbon monoxide (CO) donor that released bactericidal CO gas upon NIR irradiation. Additionally, the NPs were coated with deoxyribonuclease I (DNase I), capable of degrading the extracellular DNA present in biofilms. The final system successfully eliminated biofilms in an *in vivo* mice wound model through the synergic action of DNase I, CO release, and photothermal activity.

The stimuli-responsive matrices may also allow monitoring of the wound healing process, which is crucial for the timely therapy adjustment since parameters inside the wound are constantly changing during healing. In recent years, some dressings capable of giving real-time feedback on wound development have been proposed [69]. For instance, Mirani et al. [135] developed a hydrogel capable of changing color depending on pH variations, an important indicator of bacterial presence. Moreover, the dressing was loaded with an antibacterial agent to achieve the combined therapeutic and diagnostic effect. In another study, Zhu et al. [136] produced a zwitterionic hydrogel capable of simultaneously monitoring pH and glucose levels. The change of color of the dressing could be recorded by a smartphone that then analyzed the signal to quantify the wound parameters. Other approaches used patches with flexible electronics integrated with sensors that could transfer data on wound states, such as temperature and pH, to external devices. The electronics could also be programmed to trigger the on-demand delivery of therapeutic compounds [137], [138].

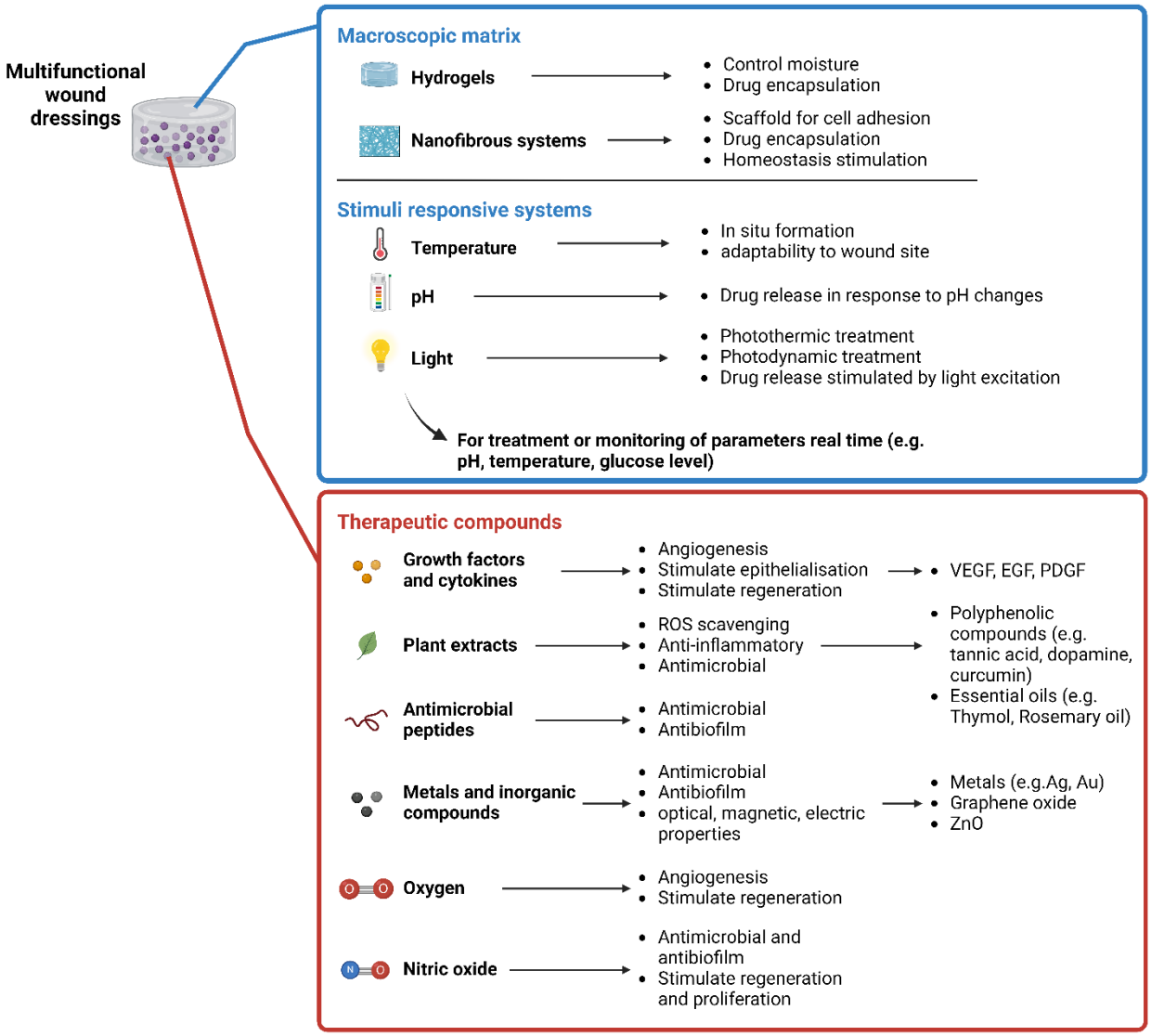


Figure 1.4. Strategies employed in literature for promoting wound healing. The blue box describes the types of matrices mainly used in the field and the approaches exploited to obtain responsive systems. The red box describes the type of therapeutic compounds used in literature and their function. VEGF: Vascular Endothelial Growth Factor; EGF: Epidermal Growth Factor; PDGF: Platelet-Derived Growth Factor; Ag: silver; Au: gold; ZnO: zinc oxide.

1.2. Outline of the work

As underlined in the previous paragraphs, new wound dressing solutions should be easy to handle and administer. In particular, injectable systems could be applied on the wound bed adapting to the wound shape and filling its cavity. At the same time, dressings should display multiple therapeutic functions. Firstly, restoring an appropriate moist environment is fundamental to favor regeneration. Chronic wounds tend to produce either a too-large amount of exudate, especially when infections are present, or a too-little quantity of exudate, such as in diabetic CWs, resulting in a dry environment that hinders cell proliferation. Therefore, an optimal dressing should adapt to the patient's exudative condition, absorbing the excess of exudate or providing moisture. The exudative state also impacts the frequency of wound change, which is higher for highly exudative wounds. Hence, a dressing that can control the moisture balance should have stability and degradation time that matches, and possibly reduces, the frequency of dressing renewal. Additionally, dressings should promote regeneration and exert antioxidant actions by scavenging

ROS and inhibiting the activity of harmful enzymes such as MMPs and MPO. Finally, the ideal dressing should limit the proliferation of multi-species bacteria, such as *P. aeruginosa* and *S. aureus*, prevent biofilm formation, and promote biofilm and infection eradication. Additionally, innovative dressings should include responsive moieties capable of providing information on the wound state and/or triggering a therapeutic action in response to endogenous or exogenous stimuli.

The rapidly expanding research in the field of wound healing proposed several approaches to obtain dressings combining multiple therapeutic actions. However, only a few of them were successfully translated into a commercial product, mainly due to the difficult scalability, cost, and complicated dressing design. Therefore, treatment and proper management of CWs remain an unsolved medical issue.

To address these needs, this PhD project aims at developing and optimizing an innovative hydrogel loaded with multifunctional nanoparticles capable of reducing the inflammatory state in CWs while also controlling bacterial proliferation. In detail, this two-component system is made of an injectable hydrogel with self-healing properties, capable of maintaining the moisture balance and absorbing harmful components from the exudate, in which hybrid organic/inorganic nanoparticles displaying antioxidant and antibacterial properties are incorporated (Figure 1.5).

Section 2 of this thesis is dedicated to the optimization of the injectable hydrogel, which is obtained through physical supramolecular interactions between custom-made poly(ether urethanes) (PEUs) and α-cyclodextrins (αCDs) [139], [140]. This combination was selected for several reasons. First, synthetic polymers provide the system with more reproducible and controllable properties compared to materials from natural origin. Additionally, the hydrogel gelation is based on physical interactions which provides injectability to the system and allows for its formation under mild conditions of temperature, reducing the risk of damaging therapeutic actives embedded within the system. Different hydrogel formulations were obtained by blending two custom-made PEUs at various ratios and concentrations. Rheological and stability tests provided information on the mechanical properties and durability of the hydrogels, while additional tests studied their capacity to interact with the external environment. These experiments allowed the selection of an optimal condition that achieved an appropriate balance among mechanical properties, durability, and responsivity to the external environment.

Section 3 details the development of dual-action NPs capable of reducing inflammation while also displaying an anti-bacterial effect. These nanoparticles were obtained by combining lignin and cobalt. Lignin, a readily available by-product of the paper industry and one of the most abundant biopolymers globally offers high interfacial activity and antioxidant capacity due to its polyphenolic nature. Cobalt was selected because of its wide range of therapeutic functions, including antibacterial and anticancer ability [141], [142] [143]and magnetic properties Despite their promising properties, cobalt and lignin are seldom used in biomedical applications, making their combination into nanoparticles an innovative approach. The resulting nanoparticles were evaluated for their antibacterial and antioxidant activity, cytotoxicity, and their ability to inhibit MPO and MMPs. The obtained NPs were then loaded into the hydrogel developed in Section 2, and the rheological properties, stability, and nanoparticle release ability from the obtained system were characterized. The principal results of Sections 2 and 3 are published in [144].

The subsequent two sections are dedicated to the modification of the hydrogel and the nanoparticles previously described with the attempt to enhance the number of functions that each component can perform.

Therefore, in Section 4, NPs were modified to achieve an anti-biofilm function in addition to the demonstrated anti-bacterial and antioxidant capacity. To achieve this, two strategies were explored. The first, investigated the possibility of coating NPs coating with a NO donor, capable of inducing biofilm dispersion since NO is known to stimulate bacteria apoptosis at high concentrations (μM) and induce biofilm dispersion at lower concentrations (nM) [61], [145]. The second method exploits the photothermal/photoacoustic effect of cobalt phthalocyanine (CoPc), which was included in the NPs. The modified NPs were then characterized in terms of biocompatibility, antibacterial, and antibiofilm activity.

In Section 5 the hydrogel was modified to incorporate antioxidant properties and to enhance its stability in aqueous environments. The custom-made PEU described in Section 2 was modified with lignin to incorporate anti-inflammatory properties and used to form a supramolecular hydrogel through the interaction with αCDs. Additionally, a photosensitive polymer was blended with the PEU to further stabilize the system via photo-crosslinking. The properties of the new hydrogel formulation were characterized by rheological, stability, and antioxidant tests, and its capacity to control the release of compounds is tested by incorporating the CoPc-based NPs described in Section 4. These results are commented also in a concluding chapter which highlights the most relevant findings of this work, discussing its potential in the treatment of CWs and its possible future developments.

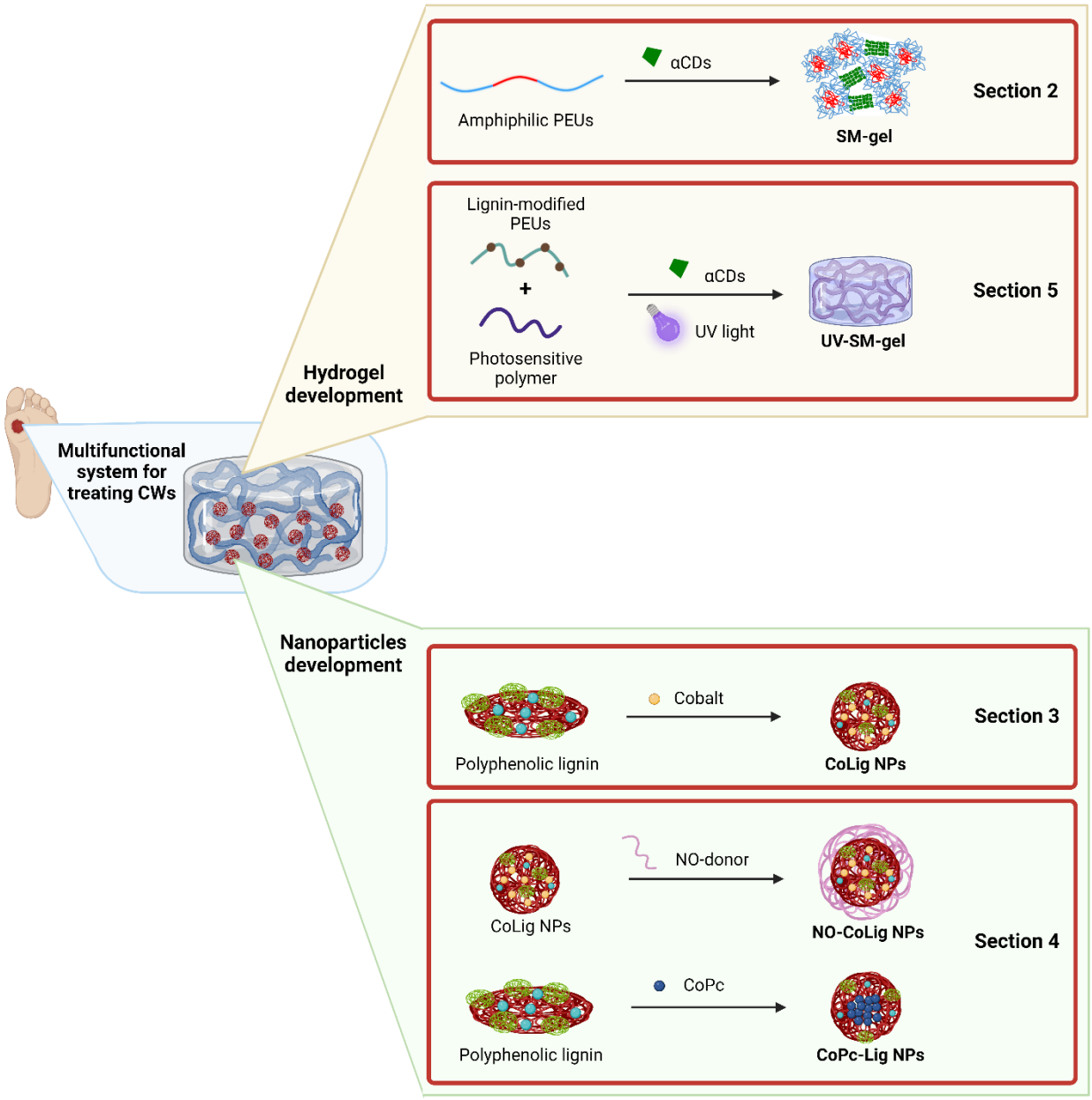


Figure 1.5. Graphical abstract of the PhD project. The work focused on developing supramolecular hydrogel in Section 2 and further improving its properties in Section 5. Additionally, a nanoparticle with antibacterial and antioxidant activity was developed in Section 3 and further modified in Section 4 to implement antibiofilm functionalities. PEU: poly(ether urethane); αCDs: α-cyclodextrins; UV: ultraviolet; SM: supramolecular; Lig: lignin; NO: nitric oxide; CoPc: cobalt phthalocyanine.

1.3. References

[1] C. K. Sen *et al.*, 'Human skin wounds: A major and snowballing threat to public health and the economy', *Wound Repair and Regeneration*, vol. 17, no. 6, pp. 763–771, 2009, doi: 10.1111/j.1524-475X.2009.00543.x.

[2] R. Zhao, H. Liang, E. Clarke, C. Jackson, and M. Xue, 'Inflammation in Chronic Wounds', *International Journal of Molecular Sciences*, vol. 17, no. 12, Art. no. 12, Dec. 2016, doi: 10.3390/ijms17122085.

[3] L. M. Morton and T. J. Phillips, 'Wound healing and treating wounds: Differential diagnosis and evaluation of chronic wounds', *Journal of the American Academy of Dermatology*, vol. 74, no. 4, pp. 589–605, Apr. 2016, doi: 10.1016/j.jaad.2015.08.068.

[4] P. G. Bowler, B. I. Duerden, and D. G. Armstrong, 'Wound Microbiology and Associated Approaches to Wound Management', *Clin Microbiol Rev*, vol. 14, no. 2, pp. 244–269, Apr. 2001, doi: 10.1128/CMR.14.2.244-269.2001.

[5] B. C. Nwomeh, D. R. Yager, and I. K. Cohen, 'Physiology of the Chronic Wound', *Clinics in Plastic Surgery*, vol. 25, no. 6, pp. 341–356, 1998.

[6] S. Noor, M. Zubair, and J. Ahmad, 'Diabetic foot ulcer—A review on pathophysiology, classification and microbial etiology', *Diabetes & Metabolic Syndrome: Clinical Research & Reviews*, vol. 9, no. 3, pp. 192–199, Jul. 2015, doi: 10.1016/j.dsx.2015.04.007.

[7] G. Han and R. Ceilley, 'Chronic Wound Healing: A Review of Current Management and Treatments', *Adv Ther*, vol. 34, no. 3, pp. 599–610, Mar. 2017, doi: 10.1007/s12325-017-0478-y.

[8] C. K. Sen, 'Human Wound and Its Burden: Updated 2020 Compendium of Estimates', *Adv Wound Care (New Rochelle)*, vol. 10, no. 5, pp. 281–292, May 2021, doi: 10.1089/wound.2021.0026.

[9] T. Vos *et al.*, 'Global, regional, and national incidence, prevalence, and years lived with disability for 310 diseases and injuries, 1990–2015: a systematic analysis for the Global Burden of Disease Study 2015', *The Lancet*, vol. 388, no. 10053, pp. 1545–1602, Oct. 2016, doi: 10.1016/S0140-6736(16)31678-6.

[10] 'Advanced Wound Care Products: A Global Industry Analysis', ReportLinker. Accessed: Feb. 06, 2024. [Online]. Available: https://www.reportlinker.com/p05961345/Global-Advanced-Wound-Care-Products-Industry.html

[11] L. Martinengo *et al.*, 'Prevalence of chronic wounds in the general population: systematic review and meta-analysis of observational studies', *Annals of Epidemiology*, vol. 29, pp. 8–15, Jan. 2019, doi: 10.1016/j.annepidem.2018.10.005.

[12] O. Nelzén, 'Prevalence of venous leg ulcer: The importance of the data collection method', *Phlebolymphology*, vol. 15, pp. 143–150, Jan. 2008.

[13] M. A. Fonder, G. S. Lazarus, D. A. Cowan, B. Aronson-Cook, A. R. Kohli, and A. J. Mamelak, 'Treating the chronic wound: A practical approach to the care of nonhealing wounds and wound care dressings', *Journal of the American Academy of Dermatology*, vol. 58, no. 2, pp. 185–206, Feb. 2008, doi: 10.1016/j.jaad.2007.08.048.

[14] N. Graves, C. J. Phillips, and K. Harding, 'A narrative review of the epidemiology and economics of chronic wounds', *British Journal of Dermatology*, vol. 187, no. 2, pp. 141–148, Aug. 2022, doi: 10.1111/bjd.20692.

[15] J. Posnett, F. Gottrup, H. Lundgren, and G. Saal, 'The resource impact of wounds on health-care providers in Europe', *J Wound Care*, vol. 18, no. 4, pp. 154–154, Apr. 2009, doi: 10.12968/jowc.2009.18.4.41607.

[16] S. R. Nussbaum *et al.*, 'An Economic Evaluation of the Impact, Cost, and Medicare Policy Implications of Chronic Nonhealing Wounds', *Value in Health*, vol. 21, no. 1, pp. 27–32, Jan. 2018, doi: 10.1016/j.jval.2017.07.007.

[17] D. Leaper, O. Assadian, and C. E. Edmiston, 'Approach to chronic wound infections', *British Journal of Dermatology*, vol. 173, no. 2, pp. 351–358, Aug. 2015, doi: 10.1111/bjd.13677.

[18] 'Antimicrobial resistance'. Accessed: Jan. 14, 2022. [Online]. Available: https://www.who.int/news-room/fact-sheets/detail/antimicrobial-resistance

[19] M. C. Robson, D. L. Steed, and M. G. Franz, 'Wound healing: Biologic features and approaches to maximize healing trajectories', *Current Problems in Surgery*, vol. 38, no. 2, pp. A1-140, Feb. 2001, doi: 10.1067/msg.2001.111167.

[20] R. Diegelmann F., 'Wound healing: an overview of acute, fibrotic and delayed healing', *Front Biosci*, vol. 9, no. 1–3, p. 283, 2004, doi: 10.2741/1184.

[21] K. C. Meyer, 'Neutrophils, myeloperoxidase, and bronchiectasis in cystic fibrosis: Green is not good', *Journal of Laboratory and Clinical Medicine*, vol. 144, no. 3, pp. 124–126, Sep. 2004, doi: 10.1016/j.lab.2004.05.014.

[22] J. Larouche, S. Sheoran, K. Maruyama, and M. Martino, 'Immune Regulation of Skin Wound Healing: Mechanisms and Novel Therapeutic Targets', *Advances in Wound Care*, vol. 7, Feb. 2018, doi: 10.1089/wound.2017.0761.

[23] R. G. Frykberg and J. Banks, 'Challenges in the Treatment of Chronic Wounds', *Advances in Wound Care*, vol. 4, no. 9, pp. 560–582, Sep. 2015, doi: 10.1089/wound.2015.0635.

[24] X. Fu, S. Y. Kassim, W. C. Parks, and J. W. Heinecke, 'Hypochlorous Acid Oxygenates the Cysteine Switch Domain of Pro-matrilysin (MMP-7): A Mechanism For Matrix Metalloproteinase Activation And Atherosclerotic Plaque Rupture By Myeloperoxidase*', *Journal of Biological Chemistry*, vol. 276, no. 44, pp. 41279–41287, Nov. 2001, doi: 10.1074/jbc.M106958200.

[25] J. Nève, N. Parij, and N. Moguilevsky, 'Inhibition of the myeloperoxidase chlorinating activity by non-steroidal anti-inflammatory drugs investigated with a human recombinant enzyme', *European Journal of Pharmacology*, vol. 417, no. 1, pp. 37–43, Apr. 2001, doi: 10.1016/S0014-2999(01)00895-0.

[26] I. Guzmán-Soto *et al.*, 'Mimicking biofilm formation and development: Recent progress in in vitro and in vivo biofilm models', *iScience*, vol. 24, no. 5, p. 102443, May 2021, doi: 10.1016/j.isci.2021.102443.

[27] H.-C. Flemming and J. Wingender, 'The biofilm matrix', *Nat Rev Microbiol*, vol. 8, no. 9, pp. 623–633, Sep. 2010, doi: 10.1038/nrmicro2415.

[28] G. Crivello, L. Fracchia, G. Ciardelli, M. Boffito, and C. Mattu, 'In Vitro Models of Bacterial Biofilms: Innovative Tools to Improve Understanding and Treatment of Infections', *Nanomaterials*, vol. 13, no. 5, Art. no. 5, Jan. 2023, doi: 10.3390/nano13050904.

[29] J. G. Powers, C. Higham, K. Broussard, and T. J. Phillips, 'Wound healing and treating wounds: Chronic wound care and management', *Journal of the American Academy of Dermatology*, vol. 74, no. 4, pp. 607–625, Apr. 2016, doi: 10.1016/j.jaad.2015.08.070.

[30] N. Høiby, T. Bjarnsholt, M. Givskov, S. Molin, and O. Ciofu, 'Antibiotic resistance of bacterial biofilms', *International Journal of Antimicrobial Agents*, vol. 35, no. 4, pp. 322–332, Apr. 2010, doi: 10.1016/j.ijantimicag.2009.12.011.

[31] G. S. Schultz *et al.*, 'Wound bed preparation: a systematic approach to wound management', *Wound Repair Regeneration*, vol. 11, no. s1, Mar. 2003, doi: 10.1046/j.1524-475X.11.s2.1.x.

[32] A. J. Nemeth, W. H. Eaglstein, J. R. Taylor, L. J. Peerson, and V. Falanga, 'Faster Healing and Less Pain in Skin Biopsy Sites Treated With an Occlusive Dressing', *Archives of Dermatology*, vol. 127, no. 11, pp. 1679–1683, Nov. 1991, doi: 10.1001/archderm.1991.01680100079008.

[33] L. Wu, G. Norman, J. C. Dumville, S. O'Meara, and S. E. Bell-Syer, 'Dressings for treating foot ulcers in people with diabetes: an overview of systematic reviews', *Cochrane Database of Systematic Reviews*, no. 7, 2015, doi: 10.1002/14651858.CD010471.pub2.

[34] J. C. Dumville, N. Stubbs, S. J. Keogh, R. M. Walker, and Z. Liu, 'Hydrogel dressings for treating pressure ulcers', *Cochrane Database of Systematic Reviews*, no. 2, 2015, doi: 10.1002/14651858.CD011226.pub2.

[35] H. S. Munro, 'Treatment of chronic ulcerous skin lesions', US20090148394A1, Jun. 11, 2009 Accessed: May 08, 2024. [Online]. Available: https://patents.google.com/patent/US20090148394A1/en

[36] E. Caló and V. V. Khutoryanskiy, 'Biomedical applications of hydrogels: A review of patents and commercial products', *European Polymer Journal*, vol. 65, pp. 252–267, Apr. 2015, doi: 10.1016/j.eurpolymj.2014.11.024.

[37] X. Zhang, W. Shu, Q. Yu, W. Qu, Y. Wang, and R. Li, 'Functional Biomaterials for Treatment of Chronic Wound', *Front Bioeng Biotechnol*, vol. 8, Jun. 2020, doi: 10.3389/fbioe.2020.00516.

[38] A. J. Martí-Carvajal *et al.*, 'Growth factors for treating diabetic foot ulcers', *Cochrane Database of Systematic Reviews*, no. 10, 2015, doi: 10.1002/14651858.CD008548.pub2.

[39] M. J. Martinez-Zapata *et al.*, 'Autologous platelet-rich plasma for treating chronic wounds', *Cochrane Database of Systematic Reviews*, no. 5, 2016, doi: 10.1002/14651858.CD006899.pub3.

[40] J. P. Sterling, 'Silver-resistance, allergy, and blue skin: Truth or urban legend?', *Burns*, vol. 40, pp. S19–S23, Dec. 2014, doi: 10.1016/j.burns.2014.10.007.

[41] A. B. Jull, N. Cullum, J. C. Dumville, M. J. Westby, S. Deshpande, and N. Walker, 'Honey as a topical treatment for wounds', *Cochrane Database of Systematic Reviews*, vol. 2015, no. 6, Mar. 2015, doi: 10.1002/14651858.CD005083.pub4.

[42] S. O'Meara, D. Al-Kurdi, Y. Ologun, L. G. Ovington, M. M.-S. James, and R. Richardson, 'Antibiotics and antiseptics for venous leg ulcers', *Cochrane Database of Systematic Reviews*, no. 1, 2014, doi: 10.1002/14651858.CD003557.pub5.

[43] J. C. Dumville, S. O'Meara, S. Deshpande, and K. Speak, 'Alginate dressings for healing diabetic foot ulcers', *Cochrane Database of Systematic Reviews*, no. 6, 2013, doi: 10.1002/14651858.CD009110.pub3.

[44] H. Vermeulen, J. M. van Hattem, M. N. Storm-Versloot, D. T. Ubbink, and S. J. Westerbos, 'Topical silver for treating infected wounds', *Cochrane Database of Systematic Reviews*, no. 1, 2007, doi: 10.1002/14651858.CD005486.pub2.

[45] C. Dai, S. Shih, and A. Khachemoune, 'Skin substitutes for acute and chronic wound healing: an updated review', *Journal of Dermatological Treatment*, vol. 31, no. 6, pp. 639–648, Aug. 2020, doi: 10.1080/09546634.2018.1530443.

[46] A. M. Gilligan, C. R. Waycaster, and A. L. Landsman, 'Wound closure in patients with DFU: a cost-effectiveness analysis of two cellular/tissue-derived products', *J Wound Care*, vol. 24, no. 3, pp. 149–156, Mar. 2015, doi: 10.12968/jowc.2015.24.3.149.

[47] V. Falanga and M. Sabolinski, 'A bilayered living skin construct (APLIGRAF®) accelerates complete closure of hard-to-heal venous ulcers', *Wound Repair and Regeneration*, vol. 7, no. 4, pp. 201–207, 1999, doi: 10.1046/j.1524-475X.1999.00201.x.

[48] A. Veves, V. Falanga, D. G. Armstrong, M. L. Sabolinski, and the Apligraf Diabetic Foot Ulcer Study, 'Graftskin, a Human Skin Equivalent, Is Effective in the Management of Noninfected Neuropathic Diabetic Foot Ulcers: A prospective randomized multicenter clinical trial', *Diabetes Care*, vol. 24, no. 2, pp. 290–295, Feb. 2001, doi: 10.2337/diacare.24.2.290.

[49] B. M. Steiglitz *et al.*, 'The viable bioengineered allogeneic cellularized construct StrataGraft® synthesizes, deposits, and organizes human extracellular matrix proteins into tissue type-

specific structures and secretes soluble factors associated with wound healing', *Burns*, vol. 50, no. 2, pp. 424–432, Mar. 2024, doi: 10.1016/j.burns.2023.06.001.

[50] M. J. Schurr *et al.*, 'Phase I/II Clinical Evaluation of StrataGraft: A Consistent, Pathogen-Free Human Skin Substitute', *Journal of Trauma: Injury, Infection & Critical Care*, vol. 66, no. 3, pp. 866–874, Mar. 2009, doi: 10.1097/TA.0b013e31819849d6.

[51] J. M. Centanni *et al.*, 'StrataGraft Skin Substitute Is Well-tolerated and Is Not Acutely Immunogenic in Patients With Traumatic Wounds: Results From a Prospective, Randomized, Controlled Dose Escalation Trial', *Annals of Surgery*, vol. 253, no. 4, pp. 672–683, Apr. 2011, doi: 10.1097/SLA.0b013e318210f3bd.

[52] T. B. Santema, P. P. Poyck, and D. T. Ubbink, 'Skin grafting and tissue replacement for treating foot ulcers in people with diabetes', *Cochrane Database of Systematic Reviews*, no. 2, 2016, doi: 10.1002/14651858.CD011255.pub2.

[53] T. Liu, Y. Lu, R. Zhan, W. Qian, and G. Luo, 'Nanomaterials and nanomaterials-based drug delivery to promote cutaneous wound healing', *Advanced Drug Delivery Reviews*, vol. 193, p. 114670, Feb. 2023, doi: 10.1016/j.addr.2022.114670.

[54] B. Blanco-Fernandez, O. Castaño, M. Á. Mateos-Timoneda, E. Engel, and S. Pérez-Amodio, 'Nanotechnology Approaches in Chronic Wound Healing', *Advances in Wound Care*, vol. 10, no. 5, pp. 234–256, May 2021, doi: 10.1089/wound.2019.1094.

[55] P. Kolimi, S. Narala, D. Nyavanandi, A. A. A. Youssef, and N. Dudhipala, 'Innovative Treatment Strategies to Accelerate Wound Healing: Trajectory and Recent Advancements', *Cells*, vol. 11, no. 15, Art. no. 15, Jan. 2022, doi: 10.3390/cells11152439.

[56] M. Naseri-Nosar and Z. M. Ziora, 'Wound dressings from naturally-occurring polymers: A review on homopolysaccharide-based composites', *Carbohydrate Polymers*, vol. 189, pp. 379–398, Jun. 2018, doi: 10.1016/j.carbpol.2018.02.003.

[57] A. Gaspar-Pintiliescu, A.-M. Stanciuc, and O. Craciunescu, 'Natural composite dressings based on collagen, gelatin and plant bioactive compounds for wound healing: A review', *International Journal of Biological Macromolecules*, vol. 138, pp. 854–865, Oct. 2019, doi: 10.1016/j.ijbiomac.2019.07.155.

[58] N. K. Rajendran, S. S. D. Kumar, N. N. Houreld, and H. Abrahamse, 'A review on nanoparticle based treatment for wound healing', *Journal of Drug Delivery Science and Technology*, vol. 44, pp. 421–430, Apr. 2018, doi: 10.1016/j.jddst.2018.01.009.

[59] G. D. Mogoşanu and A. M. Grumezescu, 'Natural and synthetic polymers for wounds and burns dressing', *International Journal of Pharmaceutics*, vol. 463, no. 2, pp. 127–136, Mar. 2014, doi: 10.1016/j.ijpharm.2013.12.015.

[60] S. Mizrahy and D. Peer, 'Polysaccharides as building blocks for nanotherapeutics', *Chem. Soc. Rev.*, vol. 41, no. 7, pp. 2623–2640, Mar. 2012, doi: 10.1039/C1CS15239D.

[61] A. Arora and A. Mishra, 'Antibacterial Polymers – A Mini Review', *Materials Today: Proceedings*, vol. 5, no. 9, pp. 17156–17161, 2018, doi: 10.1016/j.matpr.2018.04.124.

[62] J. Hoque, R. G. Prakash, K. Paramanandham, B. R. Shome, and J. Haldar, 'Biocompatible Injectable Hydrogel with Potent Wound Healing and Antibacterial Properties', *Mol. Pharmaceutics*, vol. 14, no. 4, pp. 1218–1230, Apr. 2017, doi: 10.1021/acs.molpharmaceut.6b01104.

[63] H. Tian, Z. Tang, X. Zhuang, X. Chen, and X. Jing, 'Biodegradable synthetic polymers: Preparation, functionalization and biomedical application', *Progress in Polymer Science*, vol. 37, no. 2, pp. 237–280, Feb. 2012, doi: 10.1016/j.progpolymsci.2011.06.004.

[64] M. Mir, N. Ahmed, and A. ur Rehman, 'Recent applications of PLGA based nanostructures in drug delivery', *Colloids and Surfaces B: Biointerfaces*, vol. 159, pp. 217–231, Nov. 2017, doi: 10.1016/j.colsurfb.2017.07.038.

[65] J. O. Akindoyo, M. D. H. Beg, S. Ghazali, M. R. Islam, N. Jeyaratnam, and A. R. Yuvaraj, 'Polyurethane types, synthesis and applications – a review', *RSC Adv.*, vol. 6, no. 115, pp. 114453–114482, Dec. 2016, doi: 10.1039/C6RA14525F.

[66] J. Joseph, R. M. Patel, A. Wenham, and J. R. Smith, 'Biomedical applications of polyurethane materials and coatings', *Transactions of the IMF*, vol. 96, no. 3, pp. 121–129, May 2018, doi: 10.1080/00202967.2018.1450209.

[67] A. D. Juncos Bombin, N. J. Dunne, and H. O. McCarthy, 'Electrospinning of natural polymers for the production of nanofibres for wound healing applications', *Materials Science and Engineering: C*, vol. 114, p. 110994, Sep. 2020, doi: 10.1016/j.msec.2020.110994.

[68] W. Wang, K. Lu, C. Yu, Q. Huang, and Y.-Z. Du, 'Nano-drug delivery systems in wound treatment and skin regeneration', *J Nanobiotechnol*, vol. 17, no. 1, p. 82, Dec. 2019, doi: 10.1186/s12951-019-0514-y.

[69] Y. Liang, J. He, and B. Guo, 'Functional Hydrogels as Wound Dressing to Enhance Wound Healing', *ACS Nano*, vol. 15, no. 8, pp. 12687–12722, Aug. 2021, doi: 10.1021/acsnano.1c04206.

[70] D. Stern and H. Cui, 'Crafting Polymeric and Peptidic Hydrogels for Improved Wound Healing', *Adv Healthcare Materials*, vol. 8, no. 9, p. 1900104, May 2019, doi: 10.1002/adhm.201900104.

[71] W. E. Hennink and C. F. Van Nostrum, 'Novel crosslinking methods to design hydrogels', *Advanced Drug Delivery Reviews*, vol. 64, pp. 223–236, Dec. 2012, doi: 10.1016/j.addr.2012.09.009.

[72] X. Ding and Y. Wang, 'Weak bond-based injectable and stimuli responsive hydrogels for biomedical applications', *Journal of Materials Chemistry B*, vol. 5, no. 5, pp. 887–906, 2017, doi: 10.1039/C6TB03052A.

[73] P. S. Kaparekar, S. Pathmanapan, and S. K. Anandasadagopan, 'Polymeric scaffold of Gallic acid loaded chitosan nanoparticles infused with collagen-fibrin for wound dressing application', *International Journal of Biological Macromolecules*, vol. 165, pp. 930–947, Dec. 2020, doi: 10.1016/j.ijbiomac.2020.09.212.

[74] Y. Fu *et al.*, 'Reduced polydopamine nanoparticles incorporated oxidized dextran/chitosan hybrid hydrogels with enhanced antioxidative and antibacterial properties for accelerated wound healing', *Carbohydrate Polymers*, vol. 257, p. 117598, Apr. 2021, doi: 10.1016/j.carbpol.2020.117598.

[75] A. G. Morena, S. Pérez-Rafael, and T. Tzanov, 'Lignin-Based Nanoparticles as Both Structural and Active Elements in Self-Assembling and Self-Healing Multifunctional Hydrogels for Chronic Wound Management', *Pharmaceutics*, vol. 14, no. 12, Art. no. 12, Dec. 2022, doi: 10.3390/pharmaceutics14122658.

[76] C. Mohanty and S. K. Sahoo, 'Curcumin and its topical formulations for wound healing applications', *Drug Discovery Today*, vol. 22, no. 10, pp. 1582–1592, Oct. 2017, doi: 10.1016/j.drudis.2017.07.001.

[77] H.-J. Lee, M. Jeong, Y.-G. Na, S.-J. Kim, H.-K. Lee, and C.-W. Cho, 'An EGF- and Curcumin-Co-Encapsulated Nanostructured Lipid Carrier Accelerates Chronic-Wound Healing in Diabetic Rats', *Molecules*, vol. 25, no. 20, Art. no. 20, Jan. 2020, doi: 10.3390/molecules25204610.

[78] V. Kakkar, S. Singh, D. Singla, and I. P. Kaur, 'Exploring solid lipid nanoparticles to enhance the oral bioavailability of curcumin', *Molecular Nutrition & Food Research*, vol. 55, no. 3, pp. 495–503, 2011, doi: 10.1002/mnfr.201000310.

[79] V. V. S. R. Karri *et al.*, 'Curcumin loaded chitosan nanoparticles impregnated into collagen-alginate scaffolds for diabetic wound healing', *International Journal of Biological Macromolecules*, vol. 93, pp. 1519–1529, Dec. 2016, doi: 10.1016/j.ijbiomac.2016.05.038.

[80] C. Gong *et al.*, 'A biodegradable hydrogel system containing curcumin encapsulated in micelles for cutaneous wound healing', *Biomaterials*, vol. 34, no. 27, pp. 6377–6387, Sep. 2013, doi: 10.1016/j.biomaterials.2013.05.005.

[81] A. Gupta *et al.*, 'Synthesis of Silver Nanoparticles Using Curcumin-Cyclodextrins Loaded into Bacterial Cellulose-Based Hydrogels for Wound Dressing Applications', *Biomacromolecules*, vol. 21, no. 5, pp. 1802–1811, May 2020, doi: 10.1021/acs.biomac.9b01724.

[82] P. Chen, H. Zhang, S. Cheng, G. Zhai, and C. Shen, 'Development of curcumin loaded nanostructured lipid carrier based thermosensitive in situ gel for dermal delivery', *Colloids and Surfaces A: Physicochemical and Engineering Aspects*, vol. 506, pp. 356–362, Oct. 2016, doi: 10.1016/j.colsurfa.2016.06.054.

[83] Y. Agarwal *et al.*, 'Curcumin loaded polycaprolactone-/polyvinyl alcohol-silk fibroin based electrospun nanofibrous mat for rapid healing of diabetic wound: An *in-vitro* and *in-vivo* studies', *International Journal of Biological Macromolecules*, vol. 176, pp. 376–386, Apr. 2021, doi: 10.1016/j.ijbiomac.2021.02.025.

[84] M. Adeli-Sardou, M. M. Yaghoobi, M. Torkzadeh-Mahani, and M. Dodel, 'Controlled release of lawsone from polycaprolactone/gelatin electrospun nano fibers for skin tissue regeneration', *International Journal of Biological Macromolecules*, vol. 124, pp. 478–491, Mar. 2019, doi: 10.1016/j.ijbiomac.2018.11.237.

[85] P. Tang *et al.*, 'Mussel-Inspired Electroactive and Antioxidative Scaffolds with Incorporation of Polydopamine-Reduced Graphene Oxide for Enhancing Skin Wound Healing', *ACS Appl. Mater. Interfaces*, vol. 11, no. 8, pp. 7703–7714, Feb. 2019, doi: 10.1021/acsami.8b18931.

[86] J. Qu, X. Zhao, Y. Liang, Y. Xu, P. X. Ma, and B. Guo, 'Degradable conductive injectable hydrogels as novel antibacterial, anti-oxidant wound dressings for wound healing', *Chemical Engineering Journal*, vol. 362, pp. 548–560, Apr. 2019, doi: 10.1016/j.cej.2019.01.028.

[87] X. Zhao, B. Guo, H. Wu, Y. Liang, and P. X. Ma, 'Injectable antibacterial conductive nanocomposite cryogels with rapid shape recovery for noncompressible hemorrhage and wound healing', *Nat Commun*, vol. 9, no. 1, p. 2784, Jul. 2018, doi: 10.1038/s41467-018-04998-9.

[88] K. Zhang *et al.*, 'Layered nanofiber sponge with an improved capacity for promoting blood coagulation and wound healing', *Biomaterials*, vol. 204, pp. 70–79, Jun. 2019, doi: 10.1016/j.biomaterials.2019.03.008.

[89] Q. Chen *et al.*, 'Electrospun chitosan/PVA/bioglass Nanofibrous membrane with spatially designed structure for accelerating chronic wound healing', *Materials Science and Engineering: C*, vol. 105, p. 110083, Dec. 2019, doi: 10.1016/j.msec.2019.110083.

[90] S. Hamdan *et al.*, 'Nanotechnology-Driven Therapeutic Interventions in Wound Healing: Potential Uses and Applications', *ACS Cent. Sci.*, vol. 3, no. 3, pp. 163–175, Mar. 2017, doi: 10.1021/acscentsci.6b00371.

[91] K. K. Chereddy, G. Vandermeulen, and V. Préat, 'PLGA based drug delivery systems: Promising carriers for wound healing activity', *Wound Repair Regeneration*, vol. 24, no. 2, pp. 223–236, Mar. 2016, doi: 10.1111/wrr.12404.

[92] G. Gainza *et al.*, 'A novel strategy for the treatment of chronic wounds based on the topical administration of rhEGF-loaded lipid nanoparticles: *In vitro* bioactivity and *in vivo* effectiveness in healing-impaired *db*/*db* mice', *Journal of Controlled Release*, vol. 185, pp. 51–61, Jul. 2014, doi: 10.1016/j.jconrel.2014.04.032.

[93] S. Das, M. Majid, and A. B. Baker, 'Syndecan-4 enhances PDGF-BB activity in diabetic wound healing', *Acta Biomaterialia*, vol. 42, pp. 56–65, Sep. 2016, doi: 10.1016/j.actbio.2016.07.001.

[94] Z. Xie *et al.*, 'Dual growth factor releasing multi-functional nanofibers for wound healing', *Acta Biomaterialia*, vol. 9, no. 12, pp. 9351–9359, Dec. 2013, doi: 10.1016/j.actbio.2013.07.030.

[95] I. Garcia-Orue *et al.*, 'Novel nanofibrous dressings containing rhEGF and *Aloe vera* for wound healing applications', *International Journal of Pharmaceutics*, vol. 523, no. 2, pp. 556–566, May 2017, doi: 10.1016/j.ijpharm.2016.11.006.

[96] F. Pinelli, Ó. F. Ortolà, P. Makvandi, G. Perale, and F. Rossi, '*In vivo* drug delivery applications of nanogels: a review', *Nanomedicine*, vol. 15, no. 27, pp. 2707–2727, Nov. 2020, doi: 10.2217/nnm-2020-0274.

[97] H. Kobayashi, O. Katakura, N. Morimoto, K. Akiyoshi, and S. Kasugai, 'Effects of cholesterol-bearing pullulan (CHP)-nanogels in combination with prostaglandin E1 on wound healing', *J Biomed Mater Res*, vol. 91B, no. 1, pp. 55–60, Oct. 2009, doi: 10.1002/jbm.b.31373.

[98] H. Chen *et al.*, 'Dissolved oxygen from microalgae-gel patch promotes chronic wound healing in diabetes', *Sci. Adv.*, vol. 6, no. 20, p. eaba4311, May 2020, doi: 10.1126/sciadv.aba4311.

[99] S. Keleştemur *et al.*, 'Wound healing properties of modified silver nanoparticles and their distribution in mouse organs after topical application', *Nano BioMed ENG*, vol. 4, no. 4, pp. 170–176, Nov. 2012, doi: 10.5101/nbe.v4i4.p170-176.

[100] A. G. Morena, I. Stefanov, K. Ivanova, S. Pérez-Rafael, M. Sánchez-Soto, and T. Tzanov, 'Antibacterial Polyurethane Foams with Incorporated Lignin-Capped Silver Nanoparticles for Chronic Wound Treatment', *Ind. Eng. Chem. Res.*, vol. 59, no. 10, pp. 4504–4514, Mar. 2020, doi: 10.1021/acs.iecr.9b06362.

[101] H. S. Sofi, T. Akram, A. H. Tamboli, A. Majeed, N. Shabir, and F. A. Sheikh, 'Novel lavender oil and silver nanoparticles simultaneously loaded onto polyurethane nanofibers for wound-healing applications', *International Journal of Pharmaceutics*, vol. 569, p. 118590, Oct. 2019, doi: 10.1016/j.ijpharm.2019.118590.

[102] O. R. Abbasabadi, M. R. Farahpour, and Z. G. Tabatabaei, 'Accelerative effect of nanohydrogels based on chitosan/ZnO incorporated with citral to heal the infected full-thickness wounds; an experimental study', *International Journal of Biological Macromolecules*, vol. 217, pp. 42–54, Sep. 2022, doi: 10.1016/j.ijbiomac.2022.07.038.

[103] P. C. Balaure *et al.*, '*In vitro* and *in vivo* studies of novel fabricated bioactive dressings based on collagen and zinc oxide 3D scaffolds', *International Journal of Pharmaceutics*, vol. 557, pp. 199–207, Feb. 2019, doi: 10.1016/j.ijpharm.2018.12.063.

[104] R. Ahmed *et al.*, 'Novel electrospun chitosan/polyvinyl alcohol/zinc oxide nanofibrous mats with antibacterial and antioxidant properties for diabetic wound healing', *International Journal of Biological Macromolecules*, vol. 120, pp. 385–393, Dec. 2018, doi: 10.1016/j.ijbiomac.2018.08.057.

[105] C. Turek and F. C. Stintzing, 'Stability of Essential Oils: A Review', *Comprehensive Reviews in Food Science and Food Safety*, vol. 12, no. 1, pp. 40–53, 2013, doi: https://doi.org/10.1111/1541-4337.12006.

[106] I. Usach *et al.*, 'Comparison between Citral and Pompia Essential Oil Loaded in Phospholipid Vesicles for the Treatment of Skin and Mucosal Infections', *Nanomaterials*, vol. 10, no. 2, Art. no. 2, Feb. 2020, doi: 10.3390/nano10020286.

[107] L. Risaliti *et al.*, 'Liposomes loaded with *Salvia triloba* and *Rosmarinus officinalis* essential oils: *In vitro* assessment of antioxidant, antiinflammatory and antibacterial activities', *Journal of Drug Delivery Science and Technology*, vol. 51, pp. 493–498, Jun. 2019, doi: 10.1016/j.jddst.2019.03.034.

[108] T. P. Pivetta, S. Simões, M. M. Araújo, T. Carvalho, C. Arruda, and P. D. Marcato, 'Development of nanoparticles from natural lipids for topical delivery of thymol: Investigation of its anti-inflammatory properties', *Colloids and Surfaces B: Biointerfaces*, vol. 164, pp. 281–290, Apr. 2018, doi: 10.1016/j.colsurfb.2018.01.053.
[109] A.-M. Matei *et al.*, 'Applications of Nanosized-Lipid-Based Drug Delivery Systems in Wound Care', *Applied Sciences*, vol. 11, no. 11, Art. no. 11, Jan. 2021, doi: 10.3390/app11114915.
[110] K. Khezri, M. R. Farahpour, and S. Mounesi Rad, 'Accelerated infected wound healing by topical application of encapsulated Rosemary essential oil into nanostructured lipid carriers', *Artificial Cells, Nanomedicine, and Biotechnology*, vol. 47, no. 1, pp. 980–988, Dec. 2019, doi: 10.1080/21691401.2019.1582539.
[111] S. García-Salinas *et al.*, 'Electrospun anti-inflammatory patch loaded with essential oils for wound healing', *International Journal of Pharmaceutics*, vol. 577, p. 119067, Mar. 2020, doi: 10.1016/j.ijpharm.2020.119067.
[112] J. Lei *et al.*, 'The antimicrobial peptides and their potential clinical applications', *Am J Transl Res*, vol. 11, no. 7, pp. 3919–3931, Jul. 2019.
[113] P. Tan, H. Fu, and X. Ma, 'Design, optimization, and nanotechnology of antimicrobial peptides: From exploration to applications', *Nano Today*, vol. 39, p. 101229, Aug. 2021, doi: 10.1016/j.nantod.2021.101229.
[114] X. Ju *et al.*, 'Combating Pseudomonas aeruginosa Biofilms by a Chitosan-PEG-Peptide Conjugate via Changes in Assembled Structure', *ACS Appl. Mater. Interfaces*, vol. 12, no. 12, pp. 13731–13738, Mar. 2020, doi: 10.1021/acsami.0c02034.
[115] C. Attinger and R. Wolcott, 'Clinically Addressing Biofilm in Chronic Wounds', *Advances in Wound Care*, vol. 1, no. 3, pp. 127–132, Jun. 2012, doi: 10.1089/wound.2011.0333.
[116] Z. Sadrearhami, T.-K. Nguyen, R. Namivandi-Zangeneh, K. Jung, E. H. H. Wong, and C. Boyer, 'Recent advances in nitric oxide delivery for antimicrobial applications using polymer-based systems', *J. Mater. Chem. B*, vol. 6, no. 19, pp. 2945–2959, May 2018, doi: 10.1039/C8TB00299A.
[117] M. J. Malone-Povolny, S. E. Maloney, and M. H. Schoenfisch, 'Nitric Oxide Therapy for Diabetic Wound Healing', *Advanced Healthcare Materials*, vol. 8, no. 12, p. 1801210, 2019, doi: https://doi.org/10.1002/adhm.201801210.
[118] H. Nurhasni *et al.*, 'Nitric oxide-releasing poly(lactic-co-glycolic acid)-polyethylenimine nanoparticles for prolonged nitric oxide release, antibacterial efficacy, and in vivo wound healing activity', *Int J Nanomedicine*, vol. 10, pp. 3065–3080, Apr. 2015, doi: 10.2147/IJN.S82199.
[119] E. Russo and C. Villa, 'Poloxamer Hydrogels for Biomedical Applications', *Pharmaceutics*, vol. 11, no. 12, Art. no. 12, Dec. 2019, doi: 10.3390/pharmaceutics11120671.
[120] A. Sivaraman and A. K. Banga, 'Novel in situ forming hydrogel microneedles for transdermal drug delivery', *Drug Deliv. and Transl. Res.*, vol. 7, no. 1, pp. 16–26, Feb. 2017, doi: 10.1007/s13346-016-0328-5.
[121] S. Khan, M. U. Minhas, I. A. Tekko, R. F. Donnelly, and R. R. S. Thakur, 'Evaluation of microneedles-assisted in situ depot forming poloxamer gels for sustained transdermal drug delivery', *Drug Deliv. and Transl. Res.*, vol. 9, no. 4, pp. 764–782, Aug. 2019, doi: 10.1007/s13346-019-00617-2.
[122] S. L. Percival, S. McCarty, J. A. Hunt, and E. J. Woods, 'The effects of pH on wound healing, biofilms, and antimicrobial efficacy', *Wound Repair Regeneration*, vol. 22, no. 2, pp. 174–186, Mar. 2014, doi: 10.1111/wrr.12125.

[123] S.-T. Oh, W.-R. Kim, S.-H. Kim, Y.-C. Chung, and J.-S. Park, 'The preparation of polyurethane foam combined with pH-sensitive alginate/bentonite hydrogel for wound dressings', *Fibers Polym*, vol. 12, no. 2, pp. 159–165, Apr. 2011, doi: 10.1007/s12221-011-0159-4.
[124] T. Wang, Y. Zheng, Y. Shi, and L. Zhao, 'pH-responsive calcium alginate hydrogel laden with protamine nanoparticles and hyaluronan oligosaccharide promotes diabetic wound healing by enhancing angiogenesis and antibacterial activity', *Drug Deliv. and Transl. Res.*, vol. 9, no. 1, pp. 227–239, Feb. 2019, doi: 10.1007/s13346-018-00609-8.
[125] S. Kumar Nethi, S. Das, C. Ranjan Patra, and S. Mukherjee, 'Recent advances in inorganic nanomaterials for wound-healing applications', *Biomaterials Science*, vol. 7, no. 7, pp. 2652–2674, 2019, doi: 10.1039/C9BM00423H.
[126] X. Wang, J. Chang, and C. Wu, 'Bioactive inorganic/organic nanocomposites for wound healing', *Applied Materials Today*, vol. 11, pp. 308–319, Jun. 2018, doi: 10.1016/j.apmt.2018.03.001.
[127] Y. Zhao *et al.*, 'Near-Infrared Light-Activated Thermosensitive Liposomes as Efficient Agents for Photothermal and Antibiotic Synergistic Therapy of Bacterial Biofilm', *ACS Appl. Mater. Interfaces*, vol. 10, no. 17, pp. 14426–14437, May 2018, doi: 10.1021/acsami.8b01327.
[128] W. He *et al.*, 'Highly efficient photothermal nanoparticles for the rapid eradication of bacterial biofilms', *Nanoscale*, vol. 13, no. 32, pp. 13610–13616, Aug. 2021, doi: 10.1039/D1NR03471E.
[129] Sonia, A. Singh, Shivangi, R. Kukreti, S. Kukreti, and M. Kaushik, 'Probing multifunctional azure B conjugated gold nanoparticles with serum protein binding properties for trimodal photothermal, photodynamic, and chemo therapy: Biophysical and photophysical investigations', *Biomaterials Advances*, vol. 134, p. 112678, Mar. 2022, doi: 10.1016/j.msec.2022.112678.
[130] S. Lin, H. Chen, R. Wang, T. Jiang, R. Wang, and F. Yu, 'Hollow silver–gold alloy nanoparticles for enhanced photothermal/photodynamic synergetic therapy against bacterial infection and acceleration of wound healing', *Biomater. Sci.*, vol. 11, no. 14, pp. 4874–4889, Jul. 2023, doi: 10.1039/D3BM00567D.
[131] X. Wu *et al.*, 'Temperature-Responsive Nanoassemblies for Self-Regulated Photothermal Therapy and Controlled Copper Release to Accelerate Chronic Wound Healing', *ACS Appl. Bio Mater.*, vol. 6, no. 5, pp. 2003–2013, May 2023, doi: 10.1021/acsabm.3c00267.
[132] M. Shahnawaz Khan, H. N. Abdelhamid, and H.-F. Wu, 'Near infrared (NIR) laser mediated surface activation of graphene oxide nanoflakes for efficient antibacterial, antifungal and wound healing treatment', *Colloids and Surfaces B: Biointerfaces*, vol. 127, pp. 281–291, Mar. 2015, doi: 10.1016/j.colsurfb.2014.12.049.
[133] G. Gao, Y.-W. Jiang, H.-R. Jia, and F.-G. Wu, 'Near-infrared light-controllable on-demand antibiotics release using thermo-sensitive hydrogel-based drug reservoir for combating bacterial infection', *Biomaterials*, vol. 188, pp. 83–95, Jan. 2019, doi: 10.1016/j.biomaterials.2018.09.045.
[134] Z. Yuan *et al.*, 'Near-Infrared Light-Activatable Dual-Action Nanoparticle Combats the Established Biofilms of Methicillin-Resistant Staphylococcus aureus and Its Accompanying Inflammation', *Small*, vol. 17, no. 13, p. 2007522, 2021, doi: 10.1002/smll.202007522.
[135] B. Mirani *et al.*, 'An Advanced Multifunctional Hydrogel-Based Dressing for Wound Monitoring and Drug Delivery', *Advanced Healthcare Materials*, vol. 6, no. 19, p. 1700718, 2017, doi: https://doi.org/10.1002/adhm.201700718.
[136] Y. Zhu *et al.*, 'A Multifunctional Pro-Healing Zwitterionic Hydrogel for Simultaneous Optical Monitoring of pH and Glucose in Diabetic Wound Treatment', *Adv Funct Materials*, vol. 30, no. 6, p. 1905493, Feb. 2020, doi: 10.1002/adfm.201905493.

[137] Q. Pang *et al.*, 'Smart Flexible Electronics-Integrated Wound Dressing for Real-Time Monitoring and On-Demand Treatment of Infected Wounds', *Advanced Science*, vol. 7, no. 6, p. 1902673, Mar. 2020, doi: 10.1002/advs.201902673.
[138] P. Mostafalu *et al.*, 'Smart Bandage for Monitoring and Treatment of Chronic Wounds', *Small*, vol. 14, no. 33, p. 1703509, Aug. 2018, doi: 10.1002/smll.201703509.
[139] A. Torchio, M. Boffito, A. Gallina, M. Lavella, C. Cassino, and G. Ciardelli, 'Supramolecular hydrogels based on custom-made poly(ether urethane)s and cyclodextrins as potential drug delivery vehicles: design and characterization', *J. Mater. Chem. B*, vol. 8, no. 34, pp. 7696–7712, Sep. 2020, doi: 10.1039/D0TB01261K.
[140] A. Torchio *et al.*, 'Injectable supramolecular hydrogels based on custom-made poly(ether urethane)s and α-cyclodextrins as efficient delivery vehicles of curcumin', *Materials Science and Engineering: C*, vol. 127, p. 112194, Aug. 2021, doi: 10.1016/j.msec.2021.112194.
[141] C. T. Anuradha and P. Raji, 'Effect of annealing temperature on antibacterial, antifungal and structural properties of bio-synthesized Co3O4 nanoparticles using Hibiscus Rosa-sinensis', *Mater. Res. Express*, vol. 6, no. 9, p. 095063, Jul. 2019, doi: 10.1088/2053-1591/ab2f9e.
[142] W. Anupong *et al.*, 'Cobalt nanoparticles synthesizing potential of orange peel aqueous extract and their antimicrobial and antioxidant activity', *Environmental Research*, vol. 216, p. 114594, Jan. 2023, doi: 10.1016/j.envres.2022.114594.
[143] S. Iravani and R. S. Varma, 'Sustainable synthesis of cobalt and cobalt oxide nanoparticles and their catalytic and biomedical applications', *Green Chem.*, vol. 22, no. 9, pp. 2643–2661, May 2020, doi: 10.1039/D0GC00885K.
[144] G. Crivello *et al.*, 'Lignin–Cobalt Nano-Enabled Poly(pseudo)rotaxane Supramolecular Hydrogel for Treating Chronic Wounds', *Pharmaceutics*, vol. 15, no. 6, Art. no. 6, Jun. 2023, doi: 10.3390/pharmaceutics15061717.
[145] D. McDougald, S. A. Rice, N. Barraud, P. D. Steinberg, and S. Kjelleberg, 'Should we stay or should we go: mechanisms and ecological consequences for biofilm dispersal', *Nature Reviews Microbiology*, vol. 10, no. 1, Art. no. 1, Jan. 2012, doi: 10.1038/nrmicro2695.

2. Development and optimization of a supramolecular hydrogel for treating CWs

Part of the results of this Section are published in **Crivello et al.** [46]

2.1. Introduction

Hydrogels have garnered increasing attention in the biomedical field serving as bioinks, fillers for porous matrices, carriers for cells, and tunable drug delivery systems. Tailoring their properties to specific applications involves the meticulous selection of the components and the type of interactions that govern gelation [1]. In particular, synthetic polymer-based hydrogels stand out for their reproducibility and tunability [2], [3].

Hydrogels can be divided into two main types: chemical and physical hydrogels [4]. Chemical hydrogels form through robust covalent bonds, driven by free radical or condensation reactions, resulting in a permanently cross-linked network. These structures exhibit excellent stability in aqueous environments over prolonged periods and possess significant mechanical strength. Moreover, the nature of these chemical bonds can provide the system with self-healing properties and tunable degradability [5], [6]. In the field of drug delivery systems for treating wounds, chemically crosslinked hydrogels have been used to obtain systems that could release their cargo over long periods of time. For instance, Champeau et al. [7] used the free radical crosslinking polymerization of acrylic acid to provide stability to an amphiphilic poloxamer-based hydrogel embedding a NO-donor. The controlled delivery of this therapeutic agent enhanced wound healing by promoting wound closure angiogenesis and organized collagen deposition in murine *in vivo* models. With a different approach, Anumolu et al. [8] used thiolated 8-arm PEG to obtain a hydrogel through the formation of reversible disulfide bonds. They then used it to encapsulate doxycycline, a drug presenting antimicrobial properties and acting as a MMPs inhibitor. The obtained system stimulated re-epithelialization and wound healing in *in vivo* mouse models.

In contrast, physical hydrogels rely on non-covalent interactions among their components for gelation, such as electrostatic, hydrophobic, and aromatic interactions, as well as Van der Waals forces [9]. These interactions lead to the formation of supramolecular (SM) structures, characterized by remarkable order, without the need for light irradiation or potentially toxic crosslinking agents. For instance, Zhang et al. [10] combined chitosan and polyvinyl alcohol (PVA) in a hydrogel based on weak hydrogen bond interactions and improved its mechanical properties by integrating lignin, a macromolecule containing different negatively charged groups, such as phenolic hydroxyl groups, hydroxyl groups, and sulfonic groups, that could interact with the positively charged amines of chitosan. The presence of lignin also promoted ROS scavenging and wound closure in *in vivo* murine models. Importantly, gelation in physical hydrogels does not release heat, minimizing the risk of denaturation or degradation of encapsulated drugs and biological compounds, such as growth factors [5]. For example, Lin et al. [11] developed a self-assembling hydrogel combining chitosan and Poloxamers®, an amphiphilic and thermosensitive triblock copolymer based on poly(ethylene oxide) (PEO) and poly(propylene oxide) (PPO). The mild gelation conditions allowed for the loading and protection of EGF without risks of denaturation. This compound was combined with Zinc gluconate showing antibacterial activity against *S. aureus* and *P. aeruginosa in vitro* and promoting fibroblast proliferation and collagen deposition in mouse models. The weak nature of the interactions within physical hydrogels, although reducing their stability, imparts them with self-healing properties and injectability, making them well-suited for minimally invasive applications. This unique combination of properties positions physical hydrogels

as ideal candidates for advanced drug delivery systems [12]. For instance, Poudel et al. [13] developed an injectable hydrogel exploiting the inclusion complexes forming between poly (ethylene glycol)-block-poly (lactic acid) (PEG-b-PLA) and cyclodextrins. The hydrogel could sustainedly release doxorubicin, a drug used as a model molecule. In this PhD thesis, a physical hydrogel was developed and adapted as a delivery system of nanoparticles to treat CWs. The hydrogel is composed of custom-made poly(ether urethane)s (PEUs) synthesized from Poloxamers® and the gelation is driven by the interaction of α-cyclodextrins (αCDs) with the PEO linear domains in the chain, which results in the formation of channel-like SM crystals known as poly(pseudo)rotaxanes (PPRs) [14]. Moreover, the amphiphilic nature of the PEU chains drives the organization into micelles, further strengthening the network.

Among the materials used for hydrogel production, poly(urethane)s (PUs) stand out for their versatility and tunability. PUs constitute a class of compounds characterized by the presence of urethane bonds along the polymer chains. Since their invention between 1930 and 1940, they have found extensive application in various industrial fields, serving as coatings, solid materials, or adhesives [15]. Their synthesis involves the reaction of an alcohol (typically a diol) with an isocyanate (usually a diisocyanate), which occurs in the presence of a catalyst, as schematized in *Figure 2.1*. Depending on the selection of diisocyanates and polyols, PUs with diverse properties can be obtained. For instance, the use of branched polyols or multi-functional isocyanates yields thermoset polymers, whereas linear reagents result in thermoplastic PUs. The latters are favored in biomedical applications due to their ease of manipulation and versatility [16].

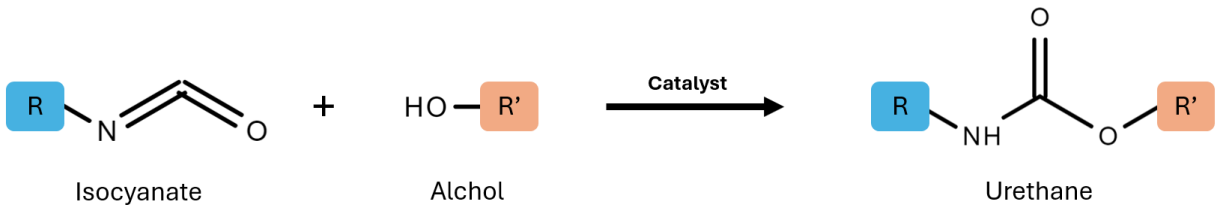


Figure 2.1. Reaction between an isocyanate and a hydroxyl group leading to a urethane bond.

Indeed, the synthesis of PUs enables precise control over the properties of the final polymer in a manner akin to assembling LEGO blocks. The careful selection of both the diisocyanate and the macrodiol (which can itself be a block co-polymer) enables the fine-tuning of polymer properties. Additionally, the PU synthesis may involve a step in which a low molecular weight diol or diamine, known as chain extender, is added to increase the polymer chain length and incorporate functional groups into the main polymeric backbone. The resulting polymer presents an alternation of soft and hard segments. The firsts are given by the long-chain diol which provides elasticity to the polymer. The seconds are the result of the reactions between diisocyanate and low molecular weight chain extenders, which give strength to the polymer and are responsible for the formation of crystalline regions in the PUs [15].

To obtain thermoplastic poly(urethane)s, different diols can be selected, with poly(ester)s and poly(ether)s being the two commonly involved families. PUs obtained from ether diols are known as poly(ether urethanes) (PEUs) and will be the family of polymers used in this PhD project. Among the poly(ether)s available, Poloxamers® stands out as an intriguing option for biomedical applications. This class of compounds constitutes a group of amphiphilic tri-block polymers consisting of poly(ethylene oxide) (PEO)/poly(ethylene glycol) (PEG) as the hydrophilic chain, and poly(propylene oxide) (PPO) as the hydrophobic block (*Figure 2.2*) [17].

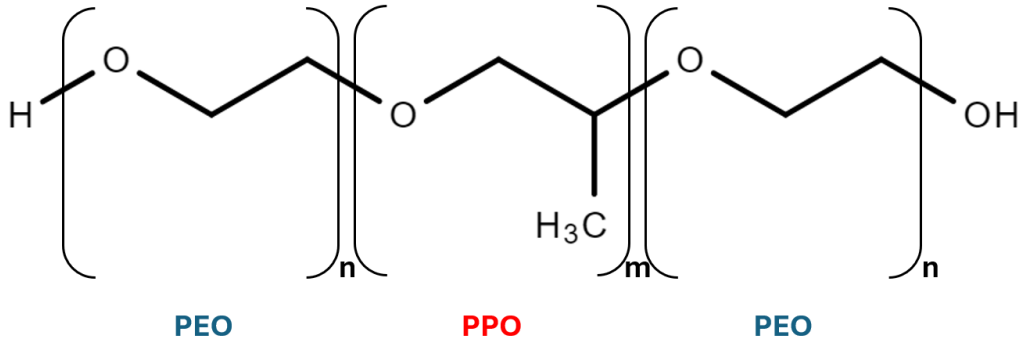


Figure 2.2. Chemical structure of Poloxamers®.

Aqueous solutions based on Poloxamers®, also known as Pluronics®, exhibit thermo-sensitive properties, that make them able to alter their supramolecular arrangement in response to thermal stimuli. There are two types of thermo-responsive polymeric systems. The first type, which also includes Poloxamers®, is characterized by a lower critical solution temperature (LCST), resulting in a polymeric solution that is liquid at low temperatures and forms a gel at high temperatures. Conversely, polymeric systems with an upper critical solution temperature (UCST) display the opposite behavior [18]. The first category holds particular interest in biomedical applications since materials with aqueous solutions show these characteristics can be easily manipulated as a solution at low temperatures and then transition to a gel state *in situ* upon contact with the body. The LCST nature of Poloxamers® stems from the amphiphilic nature of these polymers. In Poloxamers®-based aqueous solutions, gelation depends on the concentration of the polymer in the aqueous solution and the temperature of the system. With the increase in temperature, the PPO chain dehydrates, self-assembling into micelles with a PPO core and a PEO shell. The temperature required to induce micelles formation is known as critical micelle temperature (CMT). Higher polymeric concentrations result in lower CMT. When the Poloxamer® concentration is above a certain threshold, known as critical micelle concentration, the solution forms gels at a temperature higher than the sol-to-gel transition temperature [17]. As these interactions are weak, they are also reversible, making Poloxamer®-based gels injectable. Nevertheless, the absence of stronger bonds results in limited stability in water environments. Using Poloxamer® as a macrodiol in poly(urethane) production results in polymers that maintain the advantageous properties of self-assembling, thermo-sensitivity, and injectability, while improving the stability in water environments, mechanical performances and reducing the concentration and temperature required for gelation [19].

Diisocyanates are a family of compounds characterized by the presence of two -N=C=O end groups per molecule. They can be divided into aliphatic (e.g., 1,6-hexamethylene diisocyanate or 1,4-diisocyanatobutane) and aromatic (e.g., 4,4’-diphenylmethane diisocyanate) based on the nature of their domain. Aromatic diisocyanates exhibit higher reactivity compared to aliphatic counterparts, thanks to the electron stabilization given by the presence of the aromatic ring. However, PUs obtained with these isocyanates have lower oxidative and ultraviolet stabilities and produce degradation products that can pose toxicity risks to humans. Hence, aliphatic isocyanates are preferred in biomedical applications.

Chain extenders are small diols or diamine added during the PU polymerization to further modify the properties of the final polymer. For instance, 1,4-butanediol is a well-known compound used to provide the final PU with hard segments within the chain. Moreover, it has been applied for biomedical applications since its degradation product is non-toxic [20]. In other studies, the chain extender was selected to give responsivity to external stimuli. For example, Palumbo et al. [21] used L-glutathione oxidized as a chain extender to obtain a redox-sensitive PU, while Guan et al. [22] used a peptide-based diol to insert an elastase-sensitive segment.

In this PhD project, two FDA-approved Poloxamers® were selected for PEU synthesis, P407 and F68. The first is characterized by a number average molecular weight ($\overline{M_n}$) of 12600 Da and a 70% PEO content, while the second is smaller ($\overline{M_n}$ = 8400 Da) and has a higher PEO content (80%). These differences yield PEUs with distinct properties, with P407 offering greater stability and F68 giving higher responsiveness in water environments [23]. These macrodiols were combined with the non-toxic diisocyanate 1,6-hexamethylene diisocyanate (HDI) (*Figure 2.3*), also used in previous works [19], [24]. Additionally, the chain extenders selected were an amino acid-derived diol, N-boc serinol (NBoc), and an aliphatic cyclic diol, 1,4-cyclohexanedimethanol (CDM) (*Figure 2.4*). NBoc provided the final PU with primary amines upon Boc deprotection, which gives higher responsivity to the PU and could be utilized for further functionalization. On the other hand, the absence of pending lateral groups in CDM allowed better supramolecular interactions with α-cyclodextrins, as will be described in the following sections.



Figure 2.3. Chemical structure of 1,6-hexamethylene diisocyanate.

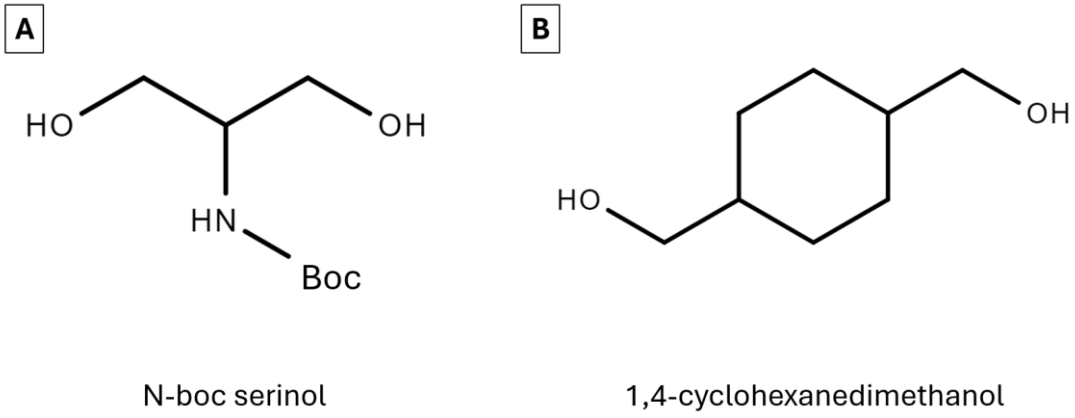


Figure 2.4. Chemical structure of (A) N-boc serinol and (B) 1,4-cyclohexanedimethanol.

Using these elements, two poly(ether urethane)s (PEUs) were synthesized (*Figure 2.5*). The first, designated as CHP407, based on P407 as macrodiol, HDI as diisocyanate, and CDM as chain extender. The second, named SHF68, comprised F68, HDI and deprotected NBoc along its polymer chains. The nomenclature assigned to these PEUs was based on the specific reagents utilized. The

prefixes "C", “N”, "S" and "H" denote the chain extender CDM, NBoc, deprotected NBoc, and diisocyanate HDI, respectively, while "P407" and "F68" identified the employed macrodiols.

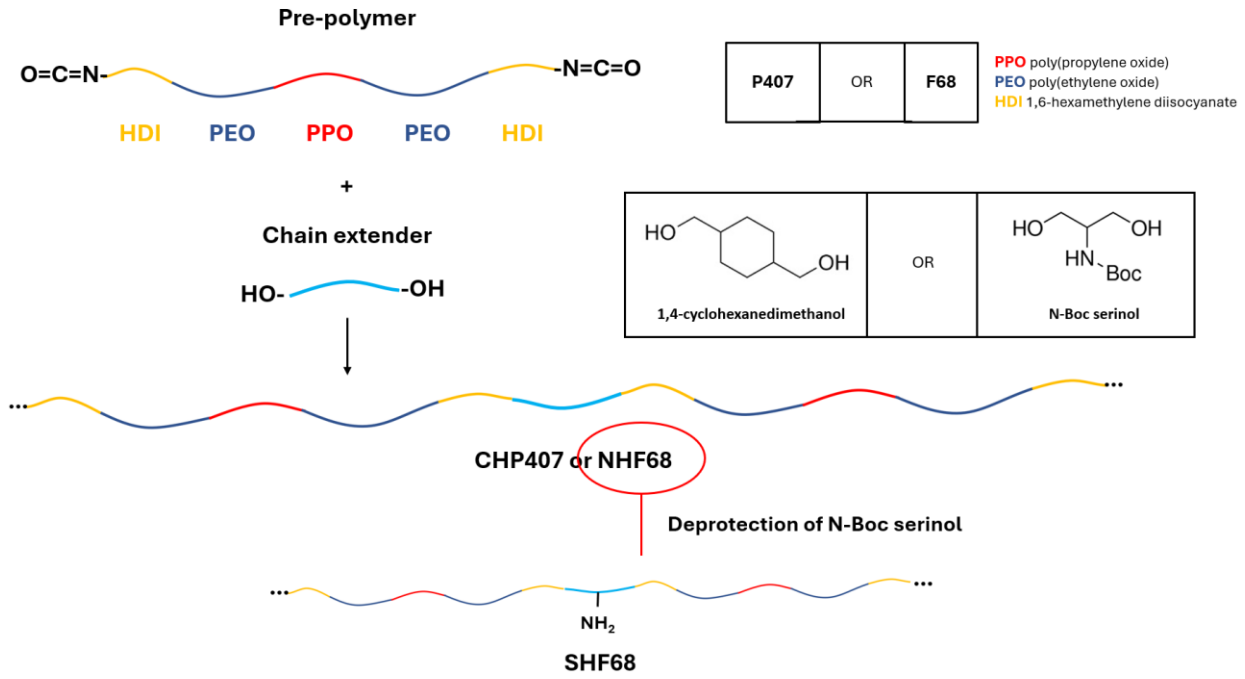
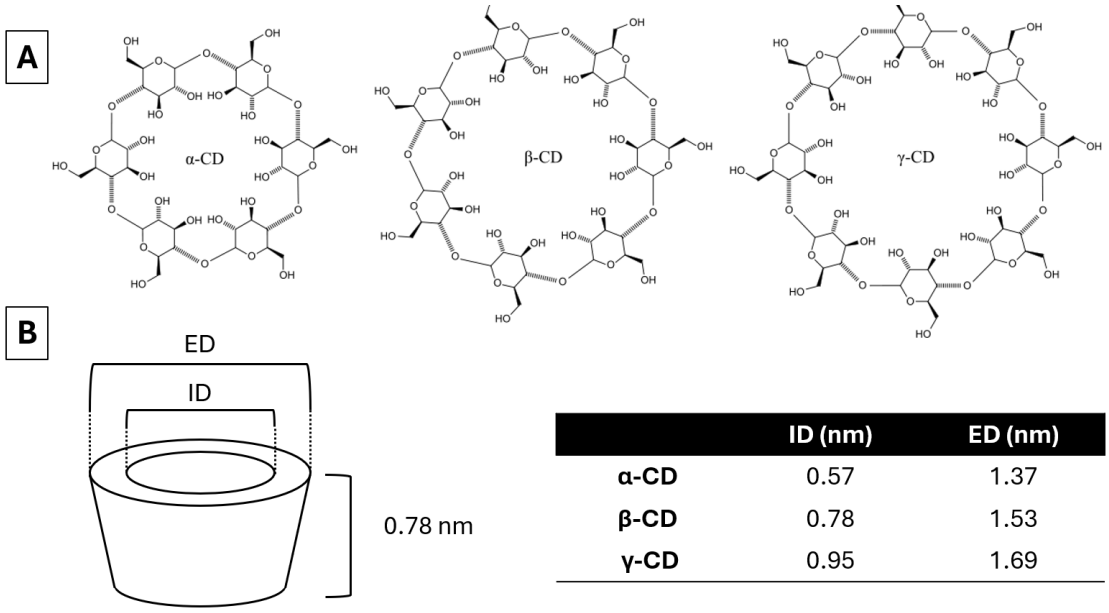


Figure 2.5. CHP407 and SHF68 synthesis.

To obtain a hydrogel, the synthesized PEUs were combined with αCDs. CDs are cyclic oligosaccharides composed of 6, 7, or 8 D-glucose units linked by α-1,4-linkages. They are named α-, β-, or γ-CDs based on the D-glucose unit number (*Figure 2.6*.A) [25]. In the 3D space, CDs take the conformation of a pierced truncated cone (*Figure 2.6*.B). The hydroxylic groups of the sugar residues are oriented on the cone exterior, making them available for interactions with other compounds, while the internal cavity exposes skeletal carbons and ethereal oxygens, which results in a hydrophobic environment [26]. The presence of this hydrophobic cavity makes CDs interesting to use for the delivery of poorly water-soluble compounds with low molecular weight. Indeed, CDs can be found as an excipient in various drug formulations present on the market [25]. Moreover, it is possible to modify the hydroxyl groups exposed on CDs external part with different aliphatic groups to give additional activity against various diseases such as cancer, sepsis, and infertility [26]. For example, Okamatsu et al. [27] developed a β-CD-based carrier, modified with folic acid capable of selectively targeting tumor cells and delivering doxorubicin, a well-known antitumor drug.



	ID (nm)	ED (nm)
α-CD	0.57	1.37
β-CD	0.78	1.53
γ-CD	0.95	1.69

Figure 2.6. Cyclodextrins structure. (A) chemical structure of α-, β- and γ-cyclodextrins. (B) Table summarizing the different cyclodextrins dimensions. ID: internal diameter; and ED: external diameter.

Another type of interaction that can be exploited in cyclodextrins-mediated drug delivery is the formation of host-guest interactions. Thanks to their hydrophobic cavities, CDs can interact with different small moieties forming complexes that can be responsive to stimuli, such as temperature, pH, and light [28], [29]. The most studied host-guest interaction is the one occurring between β-CDs and adamantane that exhibits a high binding constant. This kind of host-guest interaction has been exploited both in the development of nanoparticles for targeted drug release and in the formation of hydrogels which gelation is driven by β-CDs/adamantane association. For instance, Quan et al. [30] synthesized an α/β-CDs dimer and combined it with two polymers, one exposing adamantane and the other presenting phenolic groups. They successfully obtained NPs through the adamantane/β-CDs and phenols/αCDs interactions. Moreover, the NPs exposed a target ligand in acidic environments, thanks to the presence of pH-sensitive groups. Therefore, antitumor drugs turned out to be selectively delivered to tumor cells through the internalization of the NPs at the reduced pH of malignant environments. With a similar approach, Loebel et al. [31] modified hyaluronic acid with either adamantane or β-CDs and used the host-guest interaction between the obtained polymers to produce a hydrogel with shear-thinning and self-healing properties. This gel was injected into the kidneys of mice with chronic kidney disease and delivered cytokines for treating this pathology over 28 days. Apart from adamantane, other small moieties could be used to obtain host-guest complexes with CDs. For example, Wang et al. [32] exploited the interaction between αCDs and azobenzene to form poly(acrylic acid)-based hydrogels. Interestingly, the αCDs/azobenzene complex was sensitive to UV-light exposure and the gel that formed in dark conditions could be reversed to a liquid upon UV irradiation.

Finally, CDs can also be exploited to form necklace-like supramolecular structures when interacting with linear polymers, the so-called PPRs [28]. The formation of these inclusion complexes depends on the type of polymer and CDs involved since there is a correlation between the sizes of the CD cavity and the cross-sectional areas of the polymers [33]. For instance, αCDs are known to form PPRs with PEO or PCL, β-CD with PPO or PCL, and γ-CD with poly(dimethylsilane)s or two PEO chains simultaneously [34]. PPRs have been used in the medical field to obtain hydrogels of various natures that could encapsulate and sustain the release of drugs and molecules. For example, γ-CDs have been combined with PEG to obtain a hydrogel that could be injected subcutaneously to

release insulin and increase its permanence in blood circulation [35]. The interaction between PEG chains and αCDs to form PPRs has been particularly exploited in the biomedical field [14]. Some works investigated the integration of stimuli-responsiveness in PEO/αCDs hydrogels. In Chen et al. [36], pH responsivity was obtained by exploiting the micellization properties of the PEO/poly(L-glutamic acid) (PGA) copolymer. At normal pH, the polymers could undergo micellization with PGA as its core, leaving the PEO component available for interaction with αCDs, which drove the gelation. Reversely, at alkaline pH, PEO/αCDs complexes formed driving the formation of micelles with PEO as their core. Reducing then the pH, a hydrogel could form by the interaction among PGA chains. The different gelation processes affected the hydrogel stability, mechanical properties, and drug loading capacity. In another study, redox-sensitive hydrogels were achieved by combining PEG with poly(amido amine) presenting disulfide bonds [37]. In this system, the gelation was driven by the interaction of PEG with αCDs, while the rupture of disulfide bonds in reducing environments stimulated the hydrogel dissolution and the release of its cargo. Although these studies are promising, stimuli-responsive hydrogels are still in their initial phase of development and few investigations are implementing these systems *in vivo*. Among the PEO-containing polymers, Poloxamers® are particularly interesting since they present a variety of dimensions and PEO content. Indeed, several works combined these polymers with CDs to obtain formulations suitable for the delivery of active substances, such as antimicrobials [38], [39], or genetic material [40].

To conclude, in this PhD work, different PEUs were synthesized starting from Poloxamers® macrodiols, obtaining polymers with improved mechanical properties that could form hydrogels with enhanced durability in aqueous environments, compared to commercial Poloxamers® [19], [41]. The presence of selected chain extenders could add tailored properties to the system. Moreover, the amphiphilic nature of Poloxamers® allows for the protection and encapsulation of both hydrophilic and hydrophobic compounds. To further improve the hydrogel properties, the interaction between αCDs and PEO chains in the synthesized PEUs was exploited to obtain SM hydrogels at low polymeric content, which minimizes cytotoxic effects (*Figure 2.7*). Different hydrogel formulations were tested for their rheological properties, cytocompatibility, interaction with aqueous environments, and stability. The aim was to select the best formulation for applications in chronic wounds treatment. In particular, the desired hydrogel properties were:

- Injectability at low shear stress values (< 1kPa) [42], compatible with the force that can be applied on a syringe plunger
- Rheological properties that match skin derivatives such as gelatin (G' values 2-10kPa) [43], to achieve better biomimetic properties
- Absorption of proteins from external media simulating exudate
- Durability matching the dressing change frequency (from 24 h for highly exudative wounds to 7 days for wounds with limited or no exudate) [44].

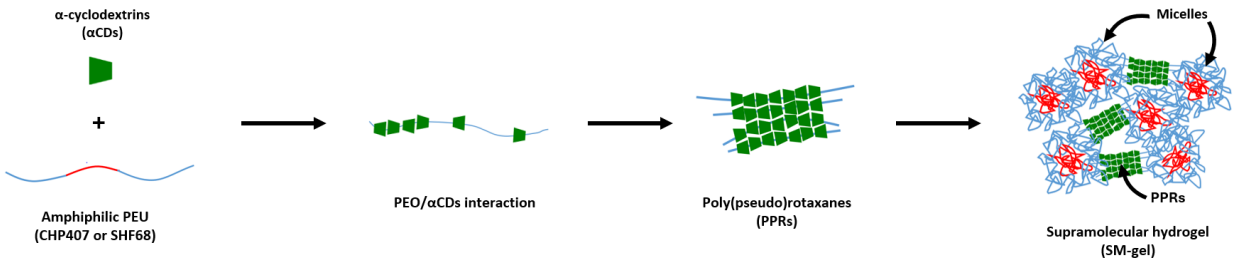


Figure 2.7. Scheme of SM-gel gelation mechanism. The PEO chain of the synthesized PEUs interact with αCDs forming PPRs, which drive the gelation. The amphiphilic nature of the PEUs allows the formation of micelles that contribute to the gelation process.

2.2 Materials and Methods

2.2.1. Materials and reagents

Poloxamer® 407 (P407, $\overline{M_n}$ 12,600 Da) and Pluronic® F68 (F68, $\overline{M_n}$ 8,400 Da); 1,6-hexamethylene diisocyanate (HDI) (168.2 Da); 1,4-cyclohexanedimethanol (CDM) (144.2 Da); N-Boc serinol (NBoc) (191.2 Da); dibutyltin dilaurate (catalyst, DBTDL); 3-(trimethylsilyl)propionic-2,2,3,3-d 4 acid sodium salt (TSP); and trifluoroacetic acid (TFA) were purchased from Merck (Milan, Italy). α-cyclodextrins (αCDs) were purchased from TCI Chemicals Europe (Zwijndrecht, Belgium). Polyethersulfone membranes 0.22 µm filters and Penicillin/Streptomycin were purchased from Carlo Erba Reagents (Milan, Italy). Dulbecco's modified Eagle's medium (DMEM 11960044, high glucose, no glutamine, without sodium pyruvate, sterile filtered) and bovine calf serum were purchased from ThermoFisher Scientific (Milan, Italy). CellTiterBlue cell viability assay was purchased from Promega (Milan, Italy). NIH-3T3 murine fibroblasts (ATCC® CRL-1658) were purchased from ATCC® (USA). All solvents used for poly(ether urethane) synthesis, which were purchased from Carlo Erba Reagents (Milan, Italy), were of analytic grade and used as received, except for 1,2-dichloroethane (DCE), which was dehydrated over activated (overnight drying at 120 °C, atmospheric pressure) molecular sieves at 4 Å (Sigma Aldrich, Milan, Italy) overnight under N_2 atmosphere before PEU synthesis. All other reagents required for the synthesis of the polymers were dried according to the protocol reported by Boffito et al. [19]. The water used in all experiments was purified using the Milli-Qplus system (Millipore) with 18.2 MΩ cm resistivity before its use.

2.2.2. Poly(ether urethane) synthesis

In this study, two custom-made poly(ether urethane)s (PEUs) named SHF68 and CHP407 were employed. Their synthesis and characterization have been detailed in previous literature [23], [24], [45]. Briefly, the synthesis process comprised two stages conducted under nitrogen atmosphere. Initially, a pre-polymerization step involved the reaction of the macrodiol (P407 or F68 at 20% w/v in anhydrous DCE) with HDI (at 2:1 M ratio relative to macrodiol) for 2.5 hours at 80 °C with DBTDL catalyst (0.1% wt with respect to macrodiol). Subsequently, the chain extender (CDM for P407 or NBoc for F68, at a 1:1 M ratio relative to macrodiol, solubilized in anhydrous DCE at a 3% w/v concentration) was added to the pre-polymer solution, and the reaction proceeded at 60 °C for 90 minutes. Methanol was added afterward to deactivate any unreacted isocyanate groups. The resulting PEU solution was then precipitated in petroleum ether (in a 4:1 weight ratio relative to the total DCE volume), dried overnight, and purified by solubilization in DCE and precipitation in a diethyl ether–methanol mixture (in a 98:2 v/v ratio, at a 5:1 weight ratio relative to DCE) to eliminate any unreacted reagents, by-products, and residual catalyst. After drying overnight under the fume hood, the obtained materials were stored at 4 °C under vacuum. Additionally, the PEU containing the NBoc chain extender underwent a deprotection reaction to remove the Boc caging groups and expose primary amines. This deprotection process involved an acid treatment using trifluoroacetic acid (TFA), as previously described [23], [24], [45]. Briefly, the PEU containing the NBoc chain extender was solubilized in chloroform (CF) at room temperature. Then, trifluoroacetic acid (TFA) was added at a final concentration of 4% w/v with a CF/TFA weight ratio of 90:10 and the reaction proceeded for 1 hour under stirring at 250 rpm. The resulting solution was concentrated using a rotary evaporator (RII Rotavapor, Buchi) at 60 °C and washed twice with CF. The concentrated solution was then diluted in demineralized water overnight under vigorous stirring and dialyzed (cellulose membrane, cut-off 10-12 kDa, Sigma Aldrich, Italy) for 48 hours

against distilled water at 3 °C, to remove residual traces of TFA and CF. The de-protected PEU was freeze-dried (Martin Christ ALPHA 2-4 LSC, Germany) and stored under vacuum at 3 °C until use.

The acronyms CHP407 and SHF68 were assigned based on the utilized reagents, where "C," "S," and "H" represent CDM, deprotected NBoc, and HDI, respectively, while P407 and F68 denote the macrodiols used for synthesis. The achievement of PEU synthesis was evaluated through Attenuated Total Reflectance–Fourier Transform Infrared (ATR-FTIR) spectroscopy, Proton Nuclear Magnetic Resonance (^{1}H-NMR) spectroscopy, and Size Exclusion Chromatography (SEC), as documented in earlier publications [23], [24], [42].

2.2.2.1. The PEUs cytocompatibility

The PEUs cytocompatibility was tested on the murine NIH/3T3 cell line (passage below 10th). Briefly, cells were seeded in a 96-well plate (7,500 cells per well) in 100 µL of DMEM (11960044) supplemented with 1% penicillin, and 10% (v/v) bovine calf serum. After 24 h of incubation at 37 °C in a humidified atmosphere with 5% CO_2, PEUs solubilized in the medium were filtered with 0.22 µm syringe filters and added at different concentrations to the cell culture. After 24 h of culture, cell viability was determined using the CellTiterBlue assay. The medium was discarded, and 100 µL of new medium added with 20 µL of CellTiterBlue reagent were added. After 3 h of incubation, the fluorescence at $\lambda_{ex/em}$ = 560/590 nm was measured. Cells incubated without PEUs were used as a growth control (100% cell viability).

2.2.3. Preparation of the SM-Gel

The supramolecular gel (SM-gel) was composed of α-cyclodextrins (αCDs) and SHF68 and CHP407 either alone or in blend. Briefly, SHF68 and CHP407 were first solubilized in phosphate buffer saline (PBS) at 4 °C; then, αCDs at 14% w/v concentration in PBS were added to the polymeric solutions to obtain a final formulation with 10% w/v αCDs concentration and different PEUs concentrations (1%, 3%, 5% w/v). The solutions were vortexed for 20 s and incubated at room temperature to allow gelation and obtain SM-gels composed of one of the two PEUs. Alternatively, the two PEUs solutions with αCDs were mixed at different weight ratios of CHP407:SHF68 (80:20 and 50:50), and then incubated at room temperature to allow gelation.

2.2.4. Characterisation of the SM-Gel

2.2.4.1. Rheology

The rheological properties of SM-gels with varying PEU concentrations (1%, 3%, 5% w/v) and different CHP407:SHF68 weight ratios (50:50 and 80:20) were examined using a stress-controlled rheometer (MCR302, Anton Paar GmbH, Graz, Austria) with a 25 mm parallel plate setup. Before gelation, the hydrogel was prepared and loaded into a syringe for easier placement onto the rheological plate. Each experiment utilized approximately 0.4 mL of SM-gel, with a set sample thickness of 0.6 mm and no applied normal force. Strain sweep tests were conducted at 37 °C, employing an angular frequency of 1 rad s^{-1} and a strain range of 0.01–500%. After a 15-minute interval, tests were repeated to evaluate the hydrogels' mechanical property recovery. Frequency sweep tests were carried out within the linear viscoelastic region (0.1% strain) at temperatures of 25 and 37 °C, by varying angular frequency between 100 and 0.1 rad s^{-1}. To assess the self-healing ability of SM-gels, self-healing strain tests were performed at a frequency of 1 Hz, subjecting the gels to cyclic deformations. Each cycle consisted of a recovery phase at low deformation (0.1%, 120 s) followed by a rupture phase at high deformation (100%, 60 s). After three cycles, the initial recovery phase was reinstated to evaluate residual mechanical properties.

2.2.4.2. Water absorption into dry hydrogels

The ability of the dried SM-gels to absorb aqueous solutions was tested in two ways. The hydrogels were completely dried through lyophilization. Then different volumes of PBS were progressively added to the dried matrices to evaluate the maximal PBS uptake. In parallel, the dried gels were put in contact with a tissue soaked in water, and the capacity to regain hydrogel-like characteristics was empirically assessed through imaging.

2.2.4.3. Bovine Serum Albumin (BSA) uptake in the SM-Gel

To evaluate the ability of SM-gels to absorb proteins from aqueous media, the gel's capacity to absorb BSA (Bovine Serum Albumin) was tested. BSA was chosen since it presents a size similar to the MMPs enzymes' size(50-90 kDa) [46]. The uptake of these enzymes inside the gel can facilitate the action of actives loaded within it. SM-gels were prepared following the previously outlined method, utilizing a 10% w/v concentration of αCD, and varying the CHP407:SHF68 weight ratio (50:50, 80:20) and PEUs overall concentration (1%, 3%, 5% w/v). Subsequently, 500 µL of each formulation was poured into vials and allowed to form SM-gels. After 48 hours, 500 µL of a 1 mg/mL BSA solution in PBS was added and incubated at 37 °C. At specific time intervals (i.e., 1, 3, 6, 24, 48, and 72 hours), supernatants were collected and analyzed spectrophotometrically at 280 nm to quantify the remaining BSA using a UV-Vis spectrophotometer (Perkin Elmer Lambda 25 UV/Vis spectrometer, Waltham, MA, USA). Results (A_f) were compared to the initial BSA concentration using a calibration curve established with BSA in PBS (A_i) (Equation 1). Following the removal of supernatants, the hydrogel in the vials was weighed ($W_{gel,f}$), freeze-dried (Telstar LyoAlfa 15, Telstar, Milano, Italy), and weighed again (W_{dry}). The hydrogel dissolution (weight loss %)and the PBS uptake % were calculated using Equations (2) and (3) respectively, with a control lyophilized before incubation serving as a reference.

$$\text{BSA uptake \%} = \left(1 - \frac{A_f}{A_i}\right)100 \quad (1)$$

$$\text{Residual weight \%} = \left(1 - \frac{W_{dry} - W_{dry,cntr}}{W_{dry,cntr}}\right)100 \quad (2)$$

$$\text{PBS uptake \%} = \frac{W_{gel,f} - W_{gel,i}}{W_{gel,f}}100 \quad (3)$$

2.2.4.4. Gel stability

The SM-gel, composed of a 3% w/v PEU overall concentration and varying CHP407:SHF68 weight ratios (50:50, 80:20), was prepared following the previously established procedure. Subsequently, 500 µL of the solution was dispensed into vials before gelation and incubated for 48 hours at room temperature to ensure complete development of the SM-gel network. Following gelation, the vials were weighed ($W_{gel,\,i}$), after which 500 µL of phosphate buffer saline (PBS) was added, and the vials were further incubated at 37 °C. At specified time intervals (6, 24, 48, and 72 hours), samples were collected, weighed following the removal of residual PBS ($W_{gel,f}$), subjected to lyophilization, and weighed again (W_{dry}). In contrast to the BSA uptake test procedure, wherein PBS was not renewed, in this case, PBS renewal occurred for all samples at each time point to mimic exudate renewal. Hydrogel dissolution (weight loss %) was calculated using Equation (2), employing a control lyophilized before PBS incubation as a reference ($W_{dry,cntr}$). The variation in wet weight (wet weight %) were calculated as per Equation (4), while the swelling ratio was measured as in Equation (5):

$$\text{Wet weight \%} = \frac{W_{gel,i} - W_{gel,f}}{W_{gel,i}}100 \quad (4)$$

$$\text{Swelling ratio} = \frac{W_{gel,f} - W_{dry}}{W_{dry}} \quad (5)$$

2.2.4.5. Gel cytocompatibility

Cytocompatibility assessment of the SM-gel followed ISO 10993:5 recommendations. Vials containing 100 mg of SM-gel, composed of a 3% w/v PEUs concentration at the two CHP407:SHF68 weight ratios, were prepared. Subsequently, 1 mL of cell culture medium was introduced into each vial. After a 24-hour incubation period at 37 °C, hydrogel extracts were obtained and filtered through a 0.22 µm syringe filter. Concurrently, NIH/3T3 cells were cultured for 24 hours. Following incubation, 100 µL of the filtered samples was added to each well containing cultured cells and incubated for additional 24 hours. Cell viability was assessed using the CellTiterBlue assay, as previously outlined.

2.2.5. Statistical analysis

The tests are conducted in triplicates and the results are reported as mean ± standard deviation. Statistical analysis was performed through Microsoft Excel for Windows 10. To compare results, one-way ANOVA analyses were performed, followed by Bonferroni's multiple comparison test. Statistical significance was assessed as follows: n.d.—non-significant difference, * $p < 0.05$, ** $p < 0.01$, and *** $p < 0.001$

2.3. Results and Discussion

2.3.1. Polyurethane synthesis and characterization of SHF68 and CHP407-based SM-gels

2.3.1.1 Synthesis and characterization of CHP407 and SHF68

SHF68 and CHP407 were obtained following previously optimized protocols [23], [24]. The synthesis process has been deeply studied and fine-tuned, therefore ATR-FTIR spectroscopy and SEC analysis were performed as a quality control to confirm the synthesis success. SEC results indicated a relevant increase in the polymers' number average molecular weight ($\overline{M_n}$) compared to the macrodiols (*Figure 2.8*), while ATR-FTIR spectra showed the appearance of bands characteristic of urethane bond formation (*Figure 2.9*).

A

	$\overline{M_n}$ (Da)	$\overline{M_w}$ (Da)	D
P407	9630	10900	1.1
CHP407	23800	40400	1.7
F68	7230	7500	1.0
SHF68	24500	41200	1.7

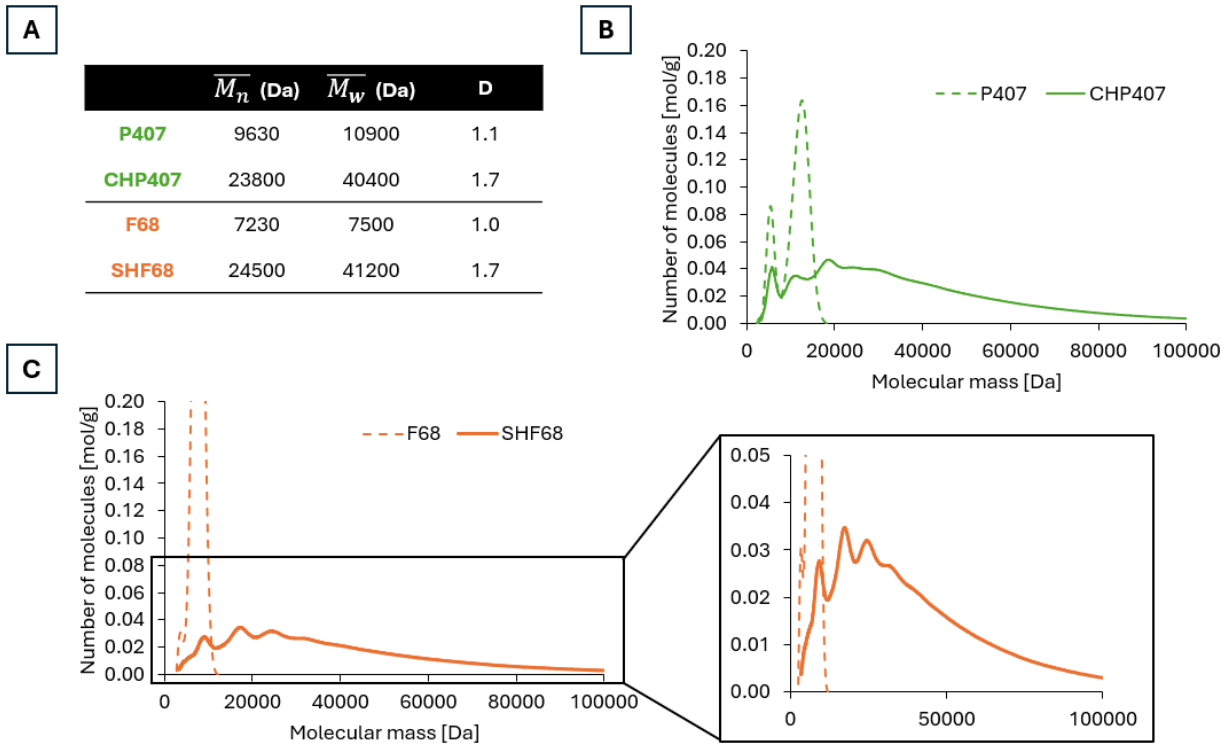


Figure 2.8. SEC analysis. (A) Summary of the polymer characteristics. $\overline{M_n}$: Number average molecular weight, $\overline{M_w}$: Weight average molecular weight, D: polydispersity index. (B-C) SEC graphs for F68, SHF68, P407 and CHP407.

A

Wavenumber [cm^{-1}]	Bond type
3350	N-H stretching
1720	C=O stretching
1530	C-N stretching and N-H bending

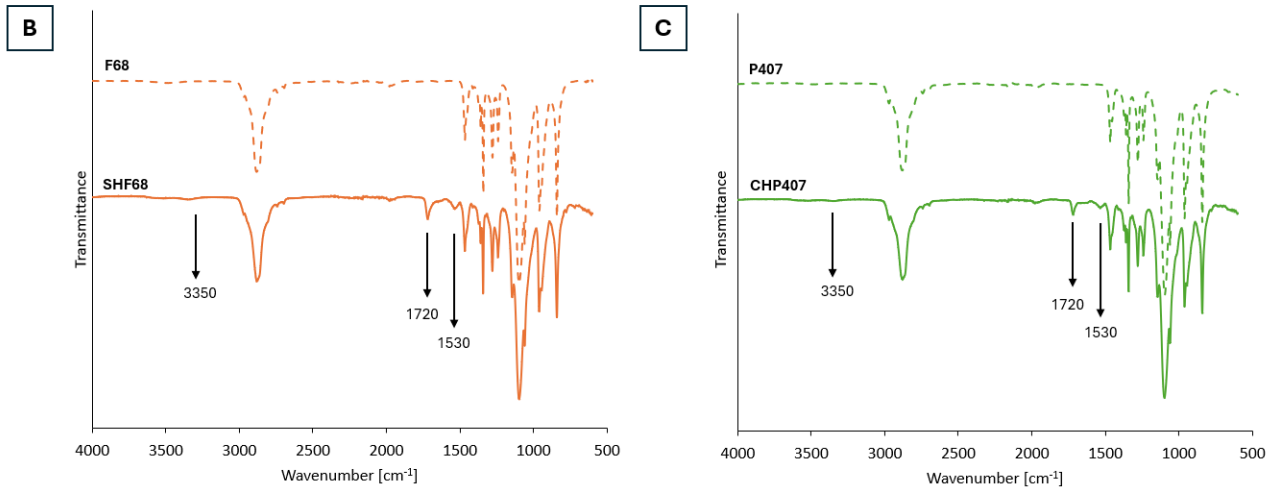


Figure 2.9. ATR-FTIR analysis. (A) Table summarizing the bands referred to the urethane domains. (B-C) ATR-FTIR spectra for F68, SHF68, P407 and CHP407.

2.3.1.2. Cytocompatibility of CHP407 and SHF68

To better investigate the applicability of the synthesized PEUs in the biomedical field, the cytocompatibility of the two polymers, solubilized at different concentrations in aqueous medium, was tested. SHF68 showed cytocompatibility at higher concentrations than CHP407. This difference could be related to the characteristics of F68 which present reduced molecular weight, higher PEO

content, shorter PPO chains, and, consequently, a lower tendency to form potentially cytotoxic micelles, which could interfere with cell membranes (*Table 2.1*). Additionally, the hard hydrophobic segment formed by the urethane bonds and the chain extender may cause some cytotoxic effects. If this is the case, the presence of N-boc serinol, a chain extender presenting hydrophilic pending groups, may reduce the hydrophobicity of the segment, thus improving the overall cytocompatibility. Finally, SHF68 undergoes a deprotection process including a dialysis step, which could purify the PEU further by eliminating possibly toxic small residues from the synthesis. Further tests are required to verify these hypotheses. This initial test suggested that a hydrogel based on SHF68 should be preferred in biomedical applications. In the following section, CHP407 and SHF68 were used in combination with αCDs to obtain supramolecular hydrogels, whose properties were characterized through rheological and biocompatibility tests.

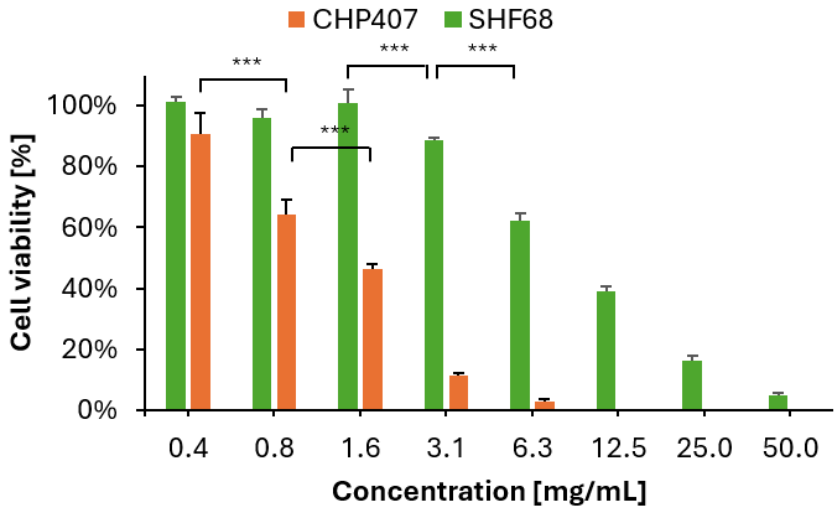


Figure 2.10. Cytocompatibility of CHP407 and SHF68 PEUs dissolved in the medium at different concentrations.

Table 2.1. Characteristics of P407 and F68 provided by the producer.

	P407	F68
$\overline{M_n}$ (Da)	12600	8400
PEO content	70%	80%
PPO $\overline{M_n}$ (Da)	4000	1800

2.3.1.3. Rheological characterization of SHF68 and CHP407-based SM-gels

SHF68 and CHP407 were combined with αCDs at 10 % w/v concentration to form SM-gels with PEU content of 1%, 3% and 5% w/v. A complete set of rheological tests was performed on both CHP407 and SHF68-based hydrogels to better investigate the contribution of these polymers on the formation of SM-gels. Moreover, rheological tests are essential to assess if a system presents the mechanical characteristics required for biomedical applications. The SM-gels developed in this work aimed to be used as a drug delivery system in the topical treatment of wounds. Therefore, it should be a completely developed hydrogel with no phase separation and good values of complex shear modulus (G*), which grants integrity to the system during application. Moreover, injectability and self-healing properties should be preferred to facilitate application on irregular wound beds and adapt to the patient's movements.

To characterize the rheological properties of SHF68 and CHP407-based hydrogels, strain sweep, frequency sweep, and strain test were performed and the results were summarized in *Table 2.2*. Strain sweep tests assess the hydrogels' capacity to withstand loads and self-heal. Moreover, it allows to identify essential parameters for interpreting the system properties:

- the **linear viscoelastic region (LVE)**, in which the sample can be solicited without destroying its structure.
- the **yield point (τ_y)**, or yield stress, which indicates the shear stress at the limit of the LVE region.
- the **flow point (τ_f)**, or flow stress, which is the shear stress at the crossover point where the storage (G') and loss modulus (G'') are equal.
- The **flow transition index**, calculated as the ratio τ_f/τ_y and indicating how the system fractures. The closer the index is to 1, the higher the tendency to brittle fracturing.

Figure 2.11 reports the trends of G' and G'' as registered through the strain sweep test. For all the conditions tested, excluding the SHF68 at 1% w/v, G' values were between 2 kPa and 10 kPa, which is comparable to the values of gelatin matrices extracted from the skin of different sources [43]. Additionally, it was possible to identify an LVE region in which G' values were higher than G'' and independent over applied strain, indicating that, at low shear stress, the SM-gels displayed a solid structure and could be identified as viscoelastic solid. Once reached the τ_y value, G' values started to decrease and G'' to increase until they crossed in the τ_f. After that point, the samples displayed a fluid structure and could be termed as viscoelastic liquids. In this region, G'' values were higher than G' due to the complete rupture of the gel network rather than to a system transition from gel to sol state. This type of behavior is an essential characteristic of injectable systems, which should be capable of flowing when they are subjected to high shear stress, such as the passage through needles or nozzles, but should regain their solid structure once the shear ceases. Therefore, all tested formulations showed rheological properties suggesting injectability potential. However, CHP407-based gels presented lower τ_f, indicating that a lower shear stress is required to reach the flowing state. Moreover, they also displayed lower τ_y values and flow transition indexes which suggest a stiffer and more brittle network. CHP407-based gels also showed superior mechanical properties, with higher values of G' and G'' within the LVE region. This could indicate a better interaction between CHP407 and αCDs in the PPRs formation, leading to a more developed gel network. Indeed, the presence of primary amines in SHF68 could interfere with the PPRs assembly. Additionally, a direct correlation between PEU content and G' values in the LVE region was identified. This was expected since at higher polymeric content, more interactions among the chains can occur and the network can develop better. Interestingly, the differences in G' value between the 3% and 5% w/v concentrated formulations were not too pronounced. An explanation of this behavior was given by Torchio et al. [24] that first studied these systems. The gelation of these hydrogels is driven by a combination of two mechanisms: PPRs assembly, given by the interaction between PEO chains and αCDs, and micelles formation, thanks to the amphiphilic nature of Poloxamers®. At low polymer content, the gelation is dominated by the PPRs formation mechanism, while, at high PEU content, micelle formation prevails. At 3% w/v concentration, these two mechanisms synergically contribute to the network formation and result in improved mechanical properties. This synergy can also be inferred by observing the flow transition index, which is lower at 3% w/v concentration. This result suggests that the network is susceptible to brittle rupture, which could be related to higher interactions within the hydrogel components both as PPRs and micelles. Conversely, at 1% w/v concentration, PPRs probably played the main role in determining gel network formation, while at 5% w/v micelle contribution was prevalent over PPRs.

Strain sweep tests were also performed to assess the self-healing capacities of these systems by repeating the test on the same sample after 15 minutes of recovery in quiescence at 37 °C. *Figure 2.12* displays the trends of G' and G'' for each formulation before and after the first rupture. For all samples, no major differences were observed in τ_y and τ_f values after the recovery period. A slight reduction of G' values in the LVE region was observed but the overall G' recovery percentage was above 80% for most of the samples. Interestingly, CHP407-based hydrogels showed a higher self-healing capacity. Moreover, the higher the PEUs content, the lower the G' recovery percentage. This further supports what was previously observed. PPRs-based networks present high self-healing capacity since they allow the polymer chains to flow through the CDs while maintaining fixed nodes composed of CDs aggregates [14]. Indeed, in this experiment, the best self-healing capacity was observed in the formulations that are supposedly more capable of forming PPRs-based networks. CHP407 is better suited than SHF68 to interact with αCDs since it does not present pending groups in the chain backbone. Moreover, in hydrogels with higher PEUs content, the contribution of PPRs in the gelation is shadowed by the mechanism of micelles formation.

Table 2.2. Summary of the rheological characteristics of SHF68 and CHP407 extracted from the strain sweep test.

PEU content [% w/v]		τ_y (Pa)	τ_f (Pa)	Flow transition index	G'_{LVE} (Pa)	G''_{LVE} (Pa)	G'_{LVE} recovery (Pa)	G''_{LVE} recovery (Pa)	G' recovery (%)
SHF68	**1%**	2.30	6.94	**3.02**	343	22	295	18	**86%**
	3%	6.18	12.90	**2.09**	2319	250	1870	169	**81%**
	5%	16.20	83.30	**5.14**	2402	228	1775	155	**74%**
CHP407	**1%**	3.35	6.91	**2.06**	3178	278	2905	245	**91%**
	3%	3.58	6.25	**1.74**	5324	640	4894	518	**92%**
	5%	2.23	12.35	**5.54**	6202	738	5402	666	**87%**

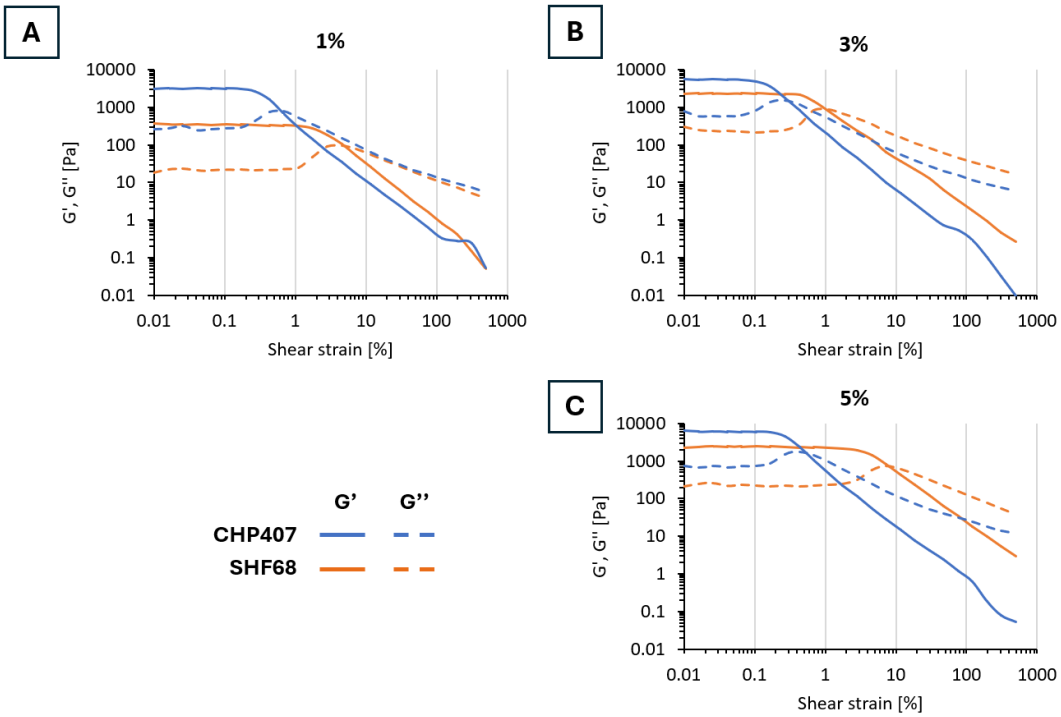


Figure 2.11. Rheology: strain sweep test for CHP407 and SHF68 hydrogels. Trends of G' (continuous line) and G'' (dashed line) for CHP407 (blue) and SHF68 (orange) at (A) 1%, (B) 3% and (C) 5% w/v PEU concentration.

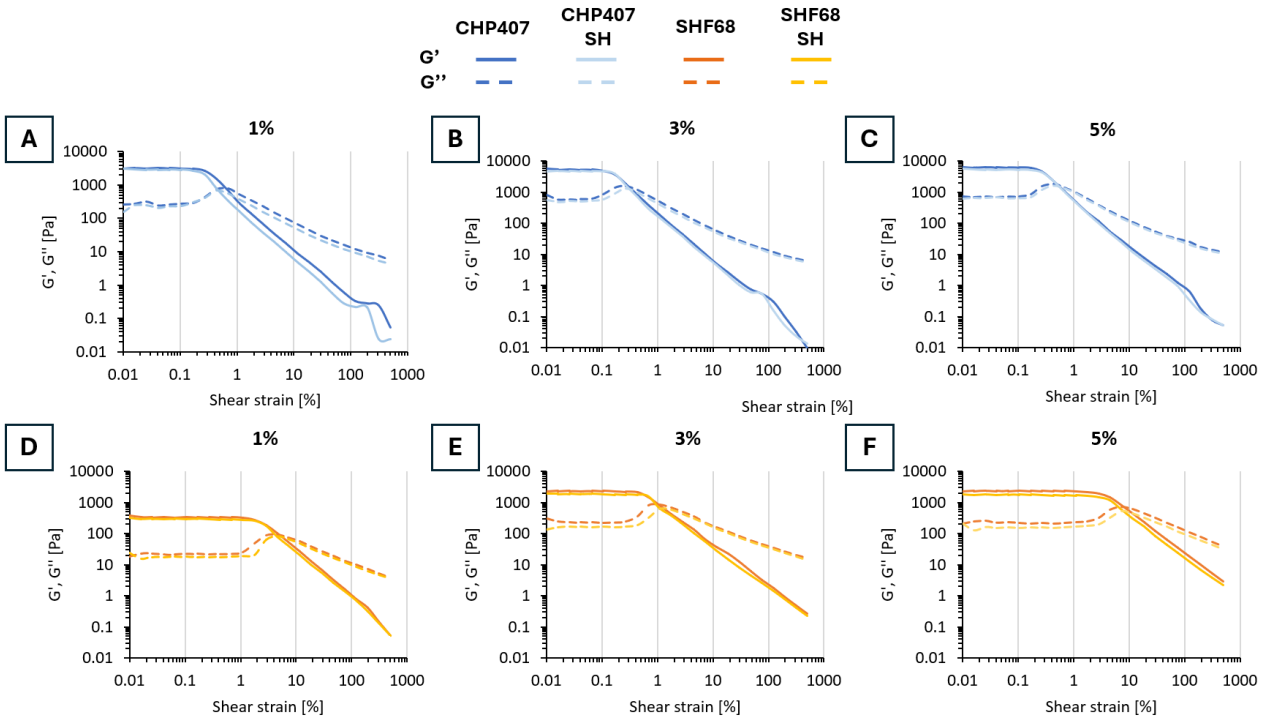


Figure 2.12. Rheology: strain sweep test for SHF68 and CHP407 hydrogels. Trends of G' (continuous line) and G'' (dashed line) at (A, D) 1%, (B, E) 3%, and (C, F) 5% w/v concentration for (A-C) CHP407 systems before (blue) and after 15 min recovery (SH) (light blue), and (D-E) SHF68 hydrogels before (orange) and after 15 min recovery (SH) (yellow).

Frequency sweep tests were performed to assess the attainment of fully developed SM-gels. The various formulations were tested at different frequencies under a constant shear strain within the LVE region. The test was repeated at three different temperatures (25 °C, 30 °C, and 37 °C) to assess the responsivity of the SM-gels to thermal changes. *Figure 2.13* and *Table 2.3* evidence that for

all the frequencies and temperatures tested, G’ was higher than G’’ and the curves were parallel, implying that the SM-gels were fully developed and characterized by a marked gel state. Interestingly, no major differences were observed when comparing G’ and G’’ values at different temperatures. This result indicates that, although SHF68 and CHP407 present a marked responsivity to thermic changes, once they interact with αCDs the obtained SM-gels can maintain their properties upon temperature variation. Since the temperature of the wound bed can change depending on various endogenous or exogenous factors, a dressing realized with this material could maintain its characteristics throughout the treatment. Additionally, CHP407 and SHF68 SM-gels at different PEUs contents were compared in *Figure 2.14* and showed trends of G’ and G’’ in accordance with the results obtained from the strain sweep test. Indeed, CHP407-based gels present higher G’ and G’’ values, and the increase in PEU content matched with an increase in the system stiffness.

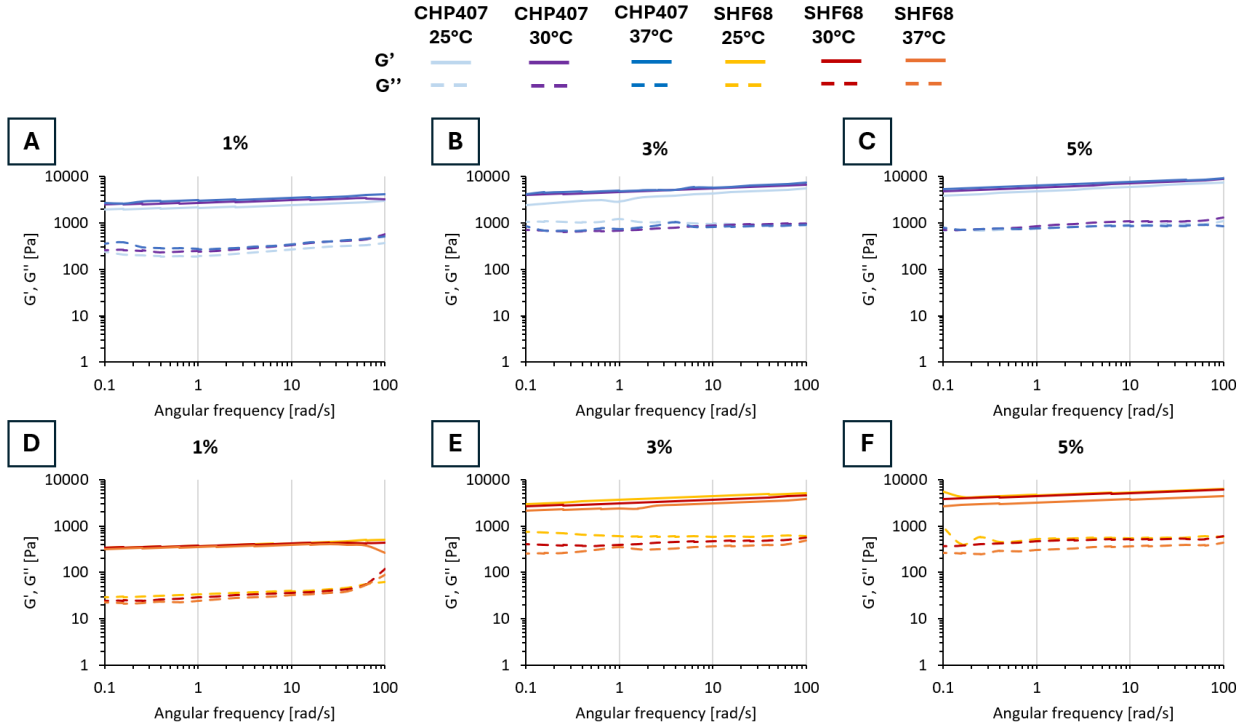


Figure 2.13. Rheology: Frequency sweep test for SHF68 and CHP4047 gels. Trends of G’ (continuous line) and G’’ (dashed line) at (A, D) 1%, (B, E) 3%, and (C, F) 5% w/v concentration for (A-C) CHP407 at 25 °C (light blue), 30 °C (purple) and 37 °C (blue), and (D-E) SHF68 at 25 °C (yellow), 30 °C (red) and 37 °C (orange).

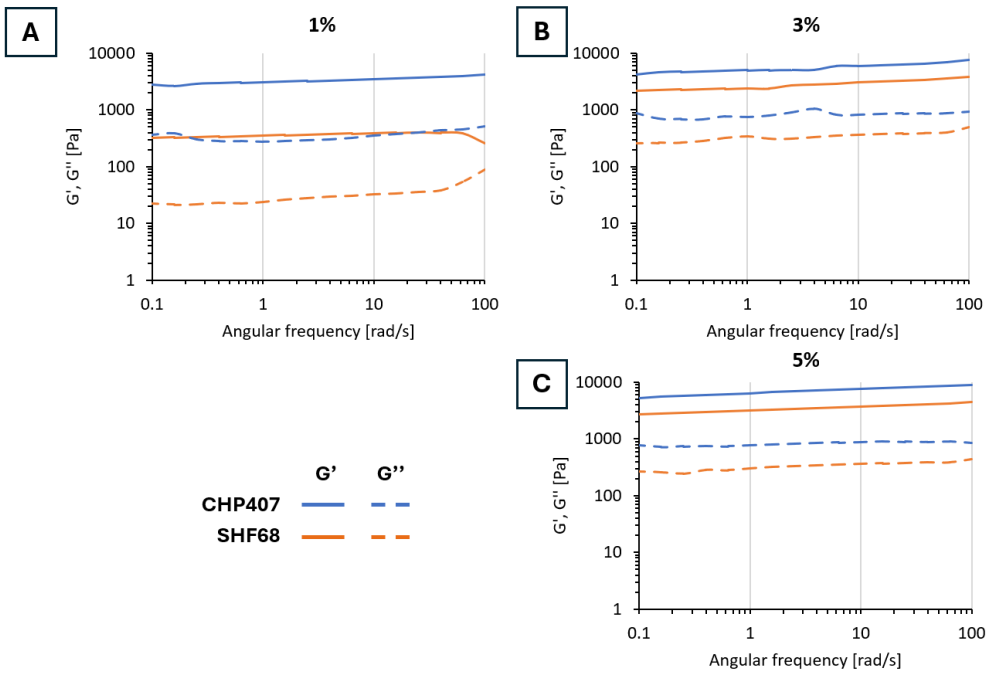


Figure 2.14. Rheology: Frequency sweep test performed at 37 °C for SHF68 and CHP407 formulations. Trends of G' (continuous line) and G'' (dashed line) for CHP407 (blue) and SHF68 (orange) hydrogels at (A) 1%, (B) 3% and (C) 5% w/v concentration.

Table 2.3. Summary of rheological characteristics for CHP407 and SHF68 hydrogels extracted from frequency sweep test.

PEU content [% w/v]		G' at 1 rad/s 25°C (Pa)	G' at 1 rad/s 30°C (Pa)	G' at 1 rad/s 37°C (Pa)
SHF68	**1%**	375	375	353
	3%	3680	3080	2410
	5%	4670	4450	3220
CHP407	**1%**	2150	2760	3110
	3%	2880	4650	5030
	5%	4820	5780	6440

Finally, shear tests were performed to assess the self-healing capacity of the SM-gels under repeated cycles of rupture. Values of G' and G'' were recorded while the samples underwent three cycles of rupture followed by a recovery period. The initial and final values of G' during the resting period were compared and for all tested conditions high percentages of G' recovery were reported (*Table 2.4*). In accordance with what was observed in the strain sweep test, CHP407-based gels showed higher self-healing properties with percentages of G' recovery above 90%. The G' values for CHP407 and SHF68 gels at different PEU contents were also completely in accordance with what was previously observed (*Figure 2.15*).

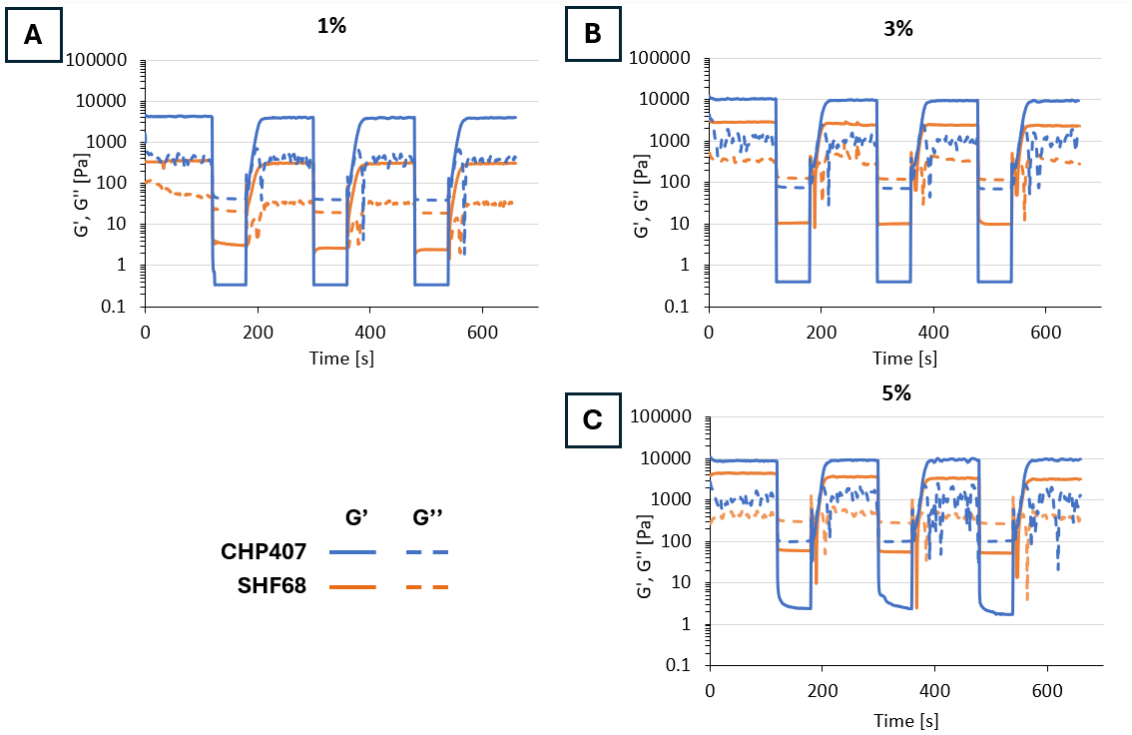


Figure 2.15. Rheology: Self-healing test for CHP407 and SHF68 formulations. Trends of G' (continuous line) and G'' (dashed line) for CHP407 (blue) and SHF68 (orange) hydrogels at (A) 1%, (B) 3%, and (C) 5% w/v concentration.

Table 2.4. Summary of G' recovery percentages for CHP407 and SHF68 gels extracted from strain test.

PEU content [% w/v]	SHF68	CHP407
1%	81%	68%
3%	72%	46%
5%	72%	106%

2.3.1.4. Cytocompatibility of CHP407 and SHF68-based hydrogels

To explore the applicability of the developed SM-gels in the biomedical field, the cytocompatibility of CHP407 and SHF68-based SM-gels was tested by incubating the NIH/3T3 cell lines with SM-gel extracts according to ISO 10993:5 guidelines. *Figure 2.16* reports a reduction in cytocompatibility with the increase in PEUs content. This is particularly severe for CHP407-based gels that showed a progressive reduction of cell viability. This result followed what was observed when testing the cytocompatibility of the PEUs as such and suggested that this cytotoxicity is related to the PEU chemical composition and its concentration.

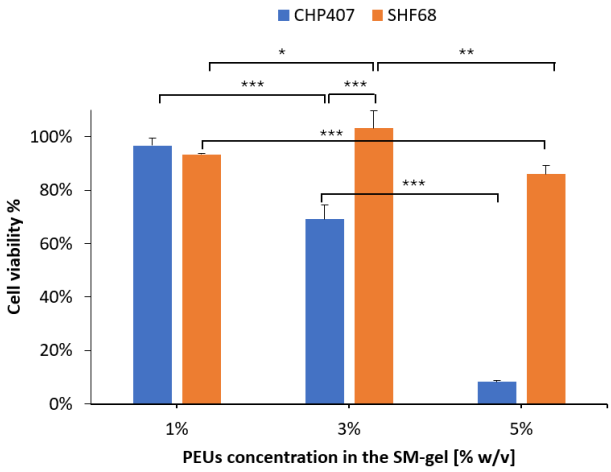


Figure 2.16. Cytocompatibility of CHP407 and SHF68-based SM-gels at different PEU content.

2.3.1.5. Preliminary conclusions on the CHP407 and SHF68-based hydrogels

The screening of the properties of CHP407 and SHF68-based hydrogels showed that the latter had higher cytocompatibility, while CHP407-based gels presented better rheological properties with higher stiffness and better self-healing capacity. The ideal hydrogel should have good cytocompatibility while maintaining satisfying mechanical properties. Therefore, the next section will explore the possibility of combining these two PEUs in a blend SM-gel. The cytocompatibility and rheological properties of the obtained hydrogels will be further characterized, and additional properties will be investigated.

2.3.2. Characterization and optimization of CHP407 and SHF68 blend SM-gels

To optimize the hydrogel formulation towards its final application, SHF68 and CHP407 were blended together at CHP407:SHF68 weight ratio of 80:20 and 50:50, and tested at PEUs content of 1%, 3% and 5% w/v. These blend ratios were selected since preliminary tests suggested increasing the CHP407 content above 80% of the weight ratio could pose some cytocompatibility issues while increasing the SHF68 content above 50% of the weight ratio could reduce significantly the hydrogel mechanical properties. Intermedial weight ratios (such as 70:30 or 60:40) should present properties close to the 80:20 and 50:50 weight ratios, respectively, and could be explored in future studies. The different compositions were tested for their rheological properties and for their capacity to interact with external medium and absorb large proteins. From these results, some conditions were selected for cytocompatibility and additional stability tests.

2.3.2.1. Rheological characterization of SHF68 and CHP407-based SM-gels

Rheological tests were performed following the same procedures described previously. Firstly, strain sweep tests were used to assess the hydrogel stiffness and self-healing capacity. *Figure 2.17* shows that G' and G'' curves presented the same trends of the CHP407 and SHF68-based gels. It was possible to identify an LVE region in which G' was higher than G'' and constant, then the samples began to rupture until they reached the τ_f where the hydrogels started to behave as viscoelastic liquids. The blend with a CHP407:SHF68 ratio of 80:20 presented higher values of τ_y than the 50:50 blend, but similar τ_f, resulting in lower flow transition indexes (

Table 2.5). This suggests that the 80:20 blend network was more brittle although it required the same shear stress to start behaving like a viscoelastic liquid. Comparing these results with the one obtained previously from hydrogels based on CHP407 and SHF68 as such, it could be inferred that the increased rigidity was probably provided by the CHP407 counterpart, while SHF68 was responsible for the observed plasticity upon rupture. Interestingly, the 80:20 blend presented the highest G' values within the LVE region for both 3% and 5% w/v PEUs content. This suggests that mixing the two polymers produces a synergy that improves the mechanical properties which may be related to the mechanism of micelles formations. Indeed, this was not observed at 1% w/v concentration, where the gelation driving force was the PPRs formation. At this low concentration, the G' values for both blends were lower than 2 kPa, set as the limit of acceptability (2-10 kPa [43]), thus suggesting that higher polymeric concentrations are preferable for applications in the wound healing field. Additionally, for each sample, the test was repeated after recovery of 15 minutes at 37 °C. *Figure 2.18* evidences that the values of G' and G'' before and after recovery were similar with a slight decrease in τ_f and the percentage of G 'recovery was above 80% in all cases. The highest recovery values were observed for the formulations at 80:20 ratio and are probably related to the increased CHP407 quantity in the blend. Similarly to what was previously observed, also for the blends the percentage of G' recovery decreased with the increase of PEUs content, underlining the importance of the contribution of PPRs in the self-healing process.

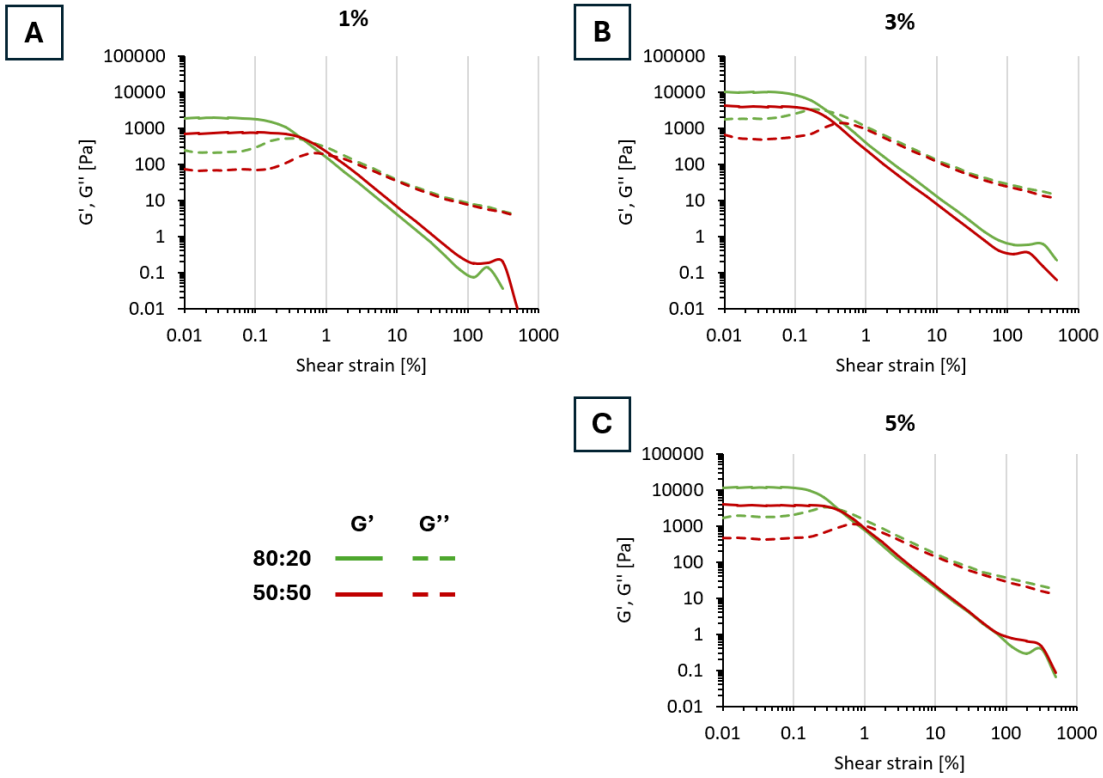


Figure 2.17. Rheology: strain sweep test for CHP407:SHF68 blend formulations. Trends of G' (continuous line) and G'' (dashed line) for CHP407:SHF68 blends at 80:20 (green) and 50:50 (red) ratio, at (A) 1%, (B) 3% and (C) 5% w/v overall PEU concentration.

Table 2.5. Summary of the rheological characteristics extracted from the strain sweep test of CHP407:SHF68 blends compared to CHP407 and SHF68 hydrogels.

CHP407: SHF68	PEU content [% w/v]	τ_y (Pa)	τ_f (Pa)	Flow transition index	G'_{LVE} (Pa)	G''_{LVE} (Pa)	G'_{LVE} recovery (Pa)	G''_{LVE} recovery (Pa)	G' recovery (%)
100:0	1%	3.35	6.91	**2.06**	3178	278	2905	245	**91%**
	3%	3.58	6.25	**1.74**	5324	640	4894	518	**92%**
	5%	2.23	12.35	**5.54**	6202	738	5402	666	**87%**
80:20	1%	1.92	3.23	**1.68**	1902	235	1892	224	**99%**
	3%	6.51	11.95	**1.84**	10100	1'840	10233	1'136	**101%**
	5%	7.94	17.60	**2.22**	12025	1'827	10800	1'458	**90%**
50:50	1%	1.91	3.01	**1.58**	749	70	768	63	**102%**
	3%	2.97	10.70	**3.60**	4492	524	3980	493	**89%**
	5%	4.02	13.40	**3.33**	3825	4'61	3248	330	**85%**
0:100	1%	2.30	6.94	**3.02**	343	22	295	18	**86%**
	3%	6.18	12.90	**2.09**	2319	250	1870	169	**81%**
	5%	16.20	83.30	**5.14**	2402	228	1775	155	**74%**

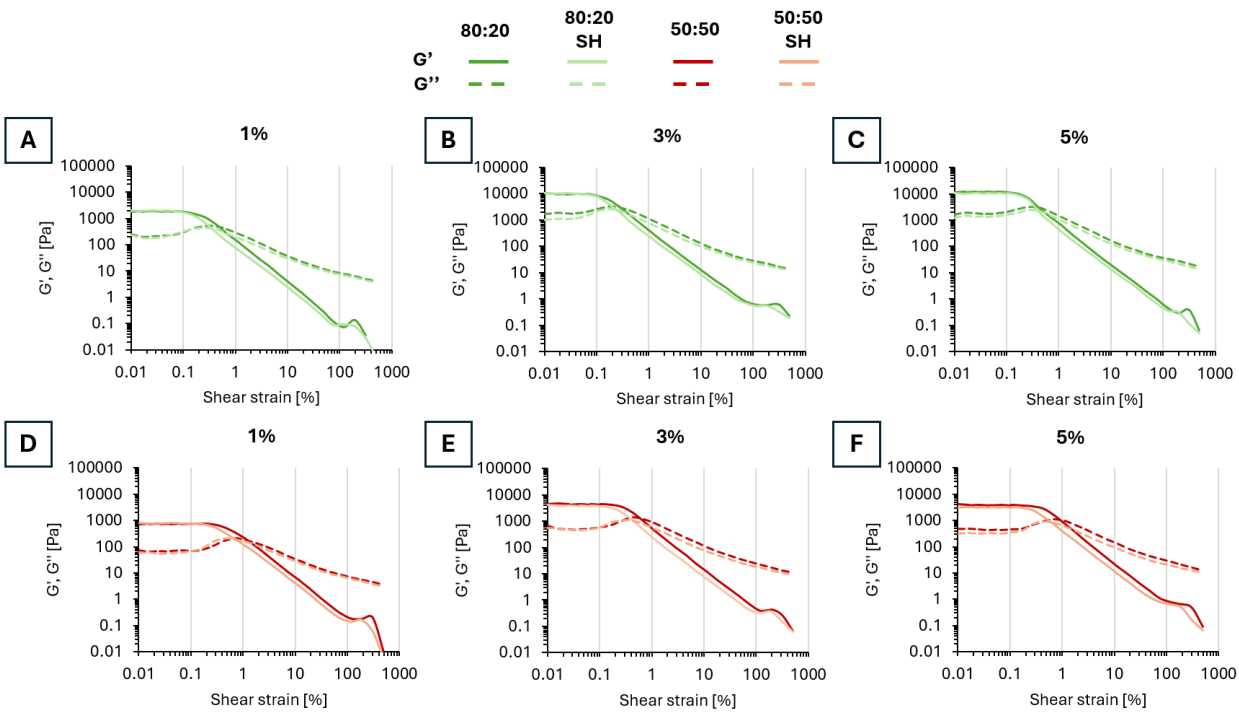


Figure 2.18. Rheology: strain sweep test for SHF68 and CHP407-based blend hydrogels. Trends of G' (continuous line) and G'' (dashed line) at (A, D) 1%, (B, E) 3% and (C, F) 5% w/v concentration for (A-C) CHP407:SHF68 80:20 ratio before (green) and after 15 min recovery (SH) (light green), and (D-E) CHP407:SHF68 50:50 ratio before (red) and after 15 min recovery (SH) (orange).

Frequency sweep tests were also performed within the LVE region to assess the hydrogel network development at three different temperatures. *Figure 2.19* highlights that the registered G' and G'' curves were parallel throughout all the frequencies tested and independent over applied frequency, indicating a fully developed gel network. As observed previously in the tests performed on formulations based on CHP407 and SHF68 as such, the differences between G' values at different temperatures were minor, indicating that the obtained network was not thermosensitive. Moreover, the values of G' and G'' were comparable to the ones obtained in the LVE region of the strain sweep test, further confirming the trend observed previously with the 80:20 blend having the highest G' values (*Figure 2.20* and *Table 2.6*).

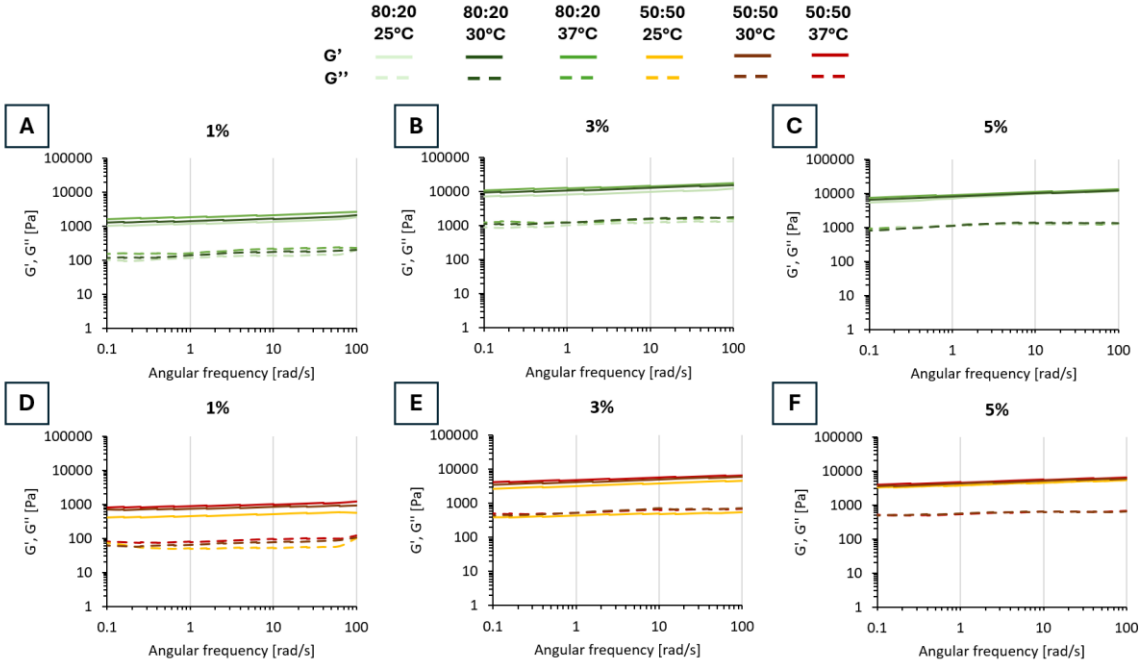


Figure 2.19. Rheology: Frequency sweep test for SHF68 and CHP407-based blend hydrogels. Trends of G' (continuous line) and G'' (dashed line) at (A, D) 1%, (B, E) 3%, and (C, F) 5% w/v concentration for (A-C) CHP407:SHF68 80:20 ratio at 25 °C (light green), 30 °C (dark green) and 37 °C (green), and (D-E) CHP407:SHF68 50:50 ratio at 25 °C (yellow), 30 °C (brown) and 37 °C (red).

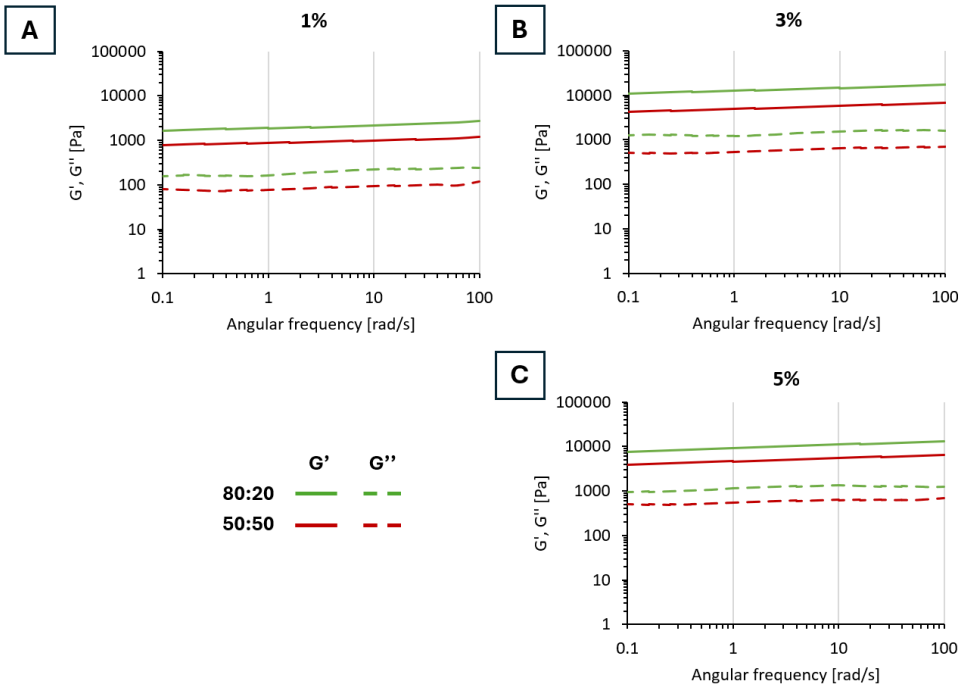


Figure 2.20. Rheology: frequency sweep test performed at 37 °C for SHF68 and CHP407-based blend hydrogels. Trends of G' (continuous line) and G'' (dashed line) for CHP407:SHF68 80:20 ratio (green) and CHP407:SHF68 50:50 ratio (red) at (A) 1%, (B) 3% and (C) 5% w/v overall PEU concentration.

Table 2.6. Summary of the rheological characteristics extracted from the frequency sweep tests of CHP407:SHF68 blends compared to CHP407 and SHF68 hydrogels.

CHP407: SHF68	PEU content [% w/v]	G' at 1 rad/s 25°C (Pa)	G' at 1 rad/s 30°C (Pa)	G' at 1 rad/s 37°C (Pa)
100:0	**1%**	2150	2760	3110
	3%	2880	4650	5030
	5%	4820	5780	6440
80:20	**1%**	1190	1450	1890
	3%	8200	10800	12700
	5%	7230	7980	9070
50:50	**1%**	448	742	879
	3%	3240	4200	4920
	5%	3830	4260	4650
0:100	**1%**	375	375	353
	3%	3680	3080	2410
	5%	4670	4450	3220

Finally, the strain test was performed to assess the self-healing capacity of the hydrogels subjected to multiple rupture cycles. Similarly to what was observed in the strain sweep test, the percentage of G' recovery was above 80% for almost all conditions. Surprisingly, except for the formulation at 3% PEUs concentration and CHP407:SHF68 80:20 ratio, the self-healing was higher for the 50:50 blend. Nevertheless, the percentages of G' recoveries were high for all conditions which confirmed the high self-healing properties of this type of network.

Overall, the blends showed improved mechanical properties and self-healing capacity compared to the gels based on CHP407 and SHF68 as such. In particular, the formulation at 80:20 ratio and 3% w/v PEUs content showed the best properties for applications in wound healing since it presented high G' and G'' values in the LVE region, corresponding to a good capacity to withstand loads; low τ_f which allows injectability under lower shear forces; and high percentage of G' recovery indicating high self-healing.

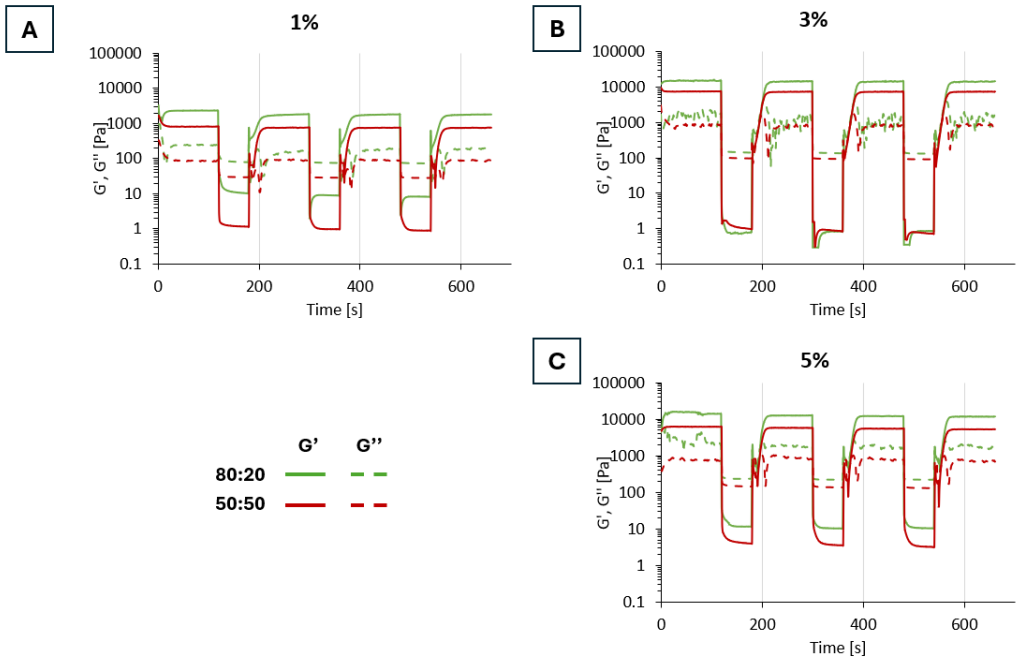


Figure 22.21. Rheology: strain test performed at 37 °C for SHF68 and CHP407-based blend hydrogels. Trends of G' (continuous line) and G'' (dashed line) for blend hydrogels at CHP407:SHF68 80:20 ratio (green) and CHP407:SHF68 50:50 ratio (red), at (A) 1%, (B) 3%, and (C) 5% w/v PEU concentration.

Table 2.7. Summary of the percentages of G' recovery extracted from the strain tests of hydrogels based on CHP407:SHF68 blends compared to formulations based on CHP407 and SHF68 as such.

PEU content [% w/v] \ CHP407:SHF68 weight ratio	100:0	80:20	50:50	0:100
1%	92%	77%	98%	86%
3%	90%	94%	85%	81%
5%	106%	80%	101%	72%

2.3.2.2. SM-gel absorption capacities: protein uptake and medium absorption of freeze-dried gels

The SM-gels underwent further characterization to assess their capacity to absorb external medium and compounds into their network. This capability is promising in the field of chronic wound healing since such wounds often present exudates abundant in components like MMPs, which prolong the inflammatory state [47], [48]. Effective management of wound exudate is thus pivotal for the healing process. Furthermore, the absorption of these components into the hydrogel network could facilitate interactions with loaded actives. Two approaches were used to study the absorption capacity of the SM-gels.

Firstly, the hydrogels were dried and put in contact with an aqueous medium. It was possible to observe that the dried matrix quickly absorbed the surrounding aqueous medium, increasing its weight up to 10 times its dry weight and regaining a hydrogel-like texture (*Figure 2.22*). This property is interesting for applications in highly exudative wounds. Indeed, the dried matrix applied to the wound could absorb and trap the exudate making it interact directly with loaded anti-inflammatory and antibacterial compounds.

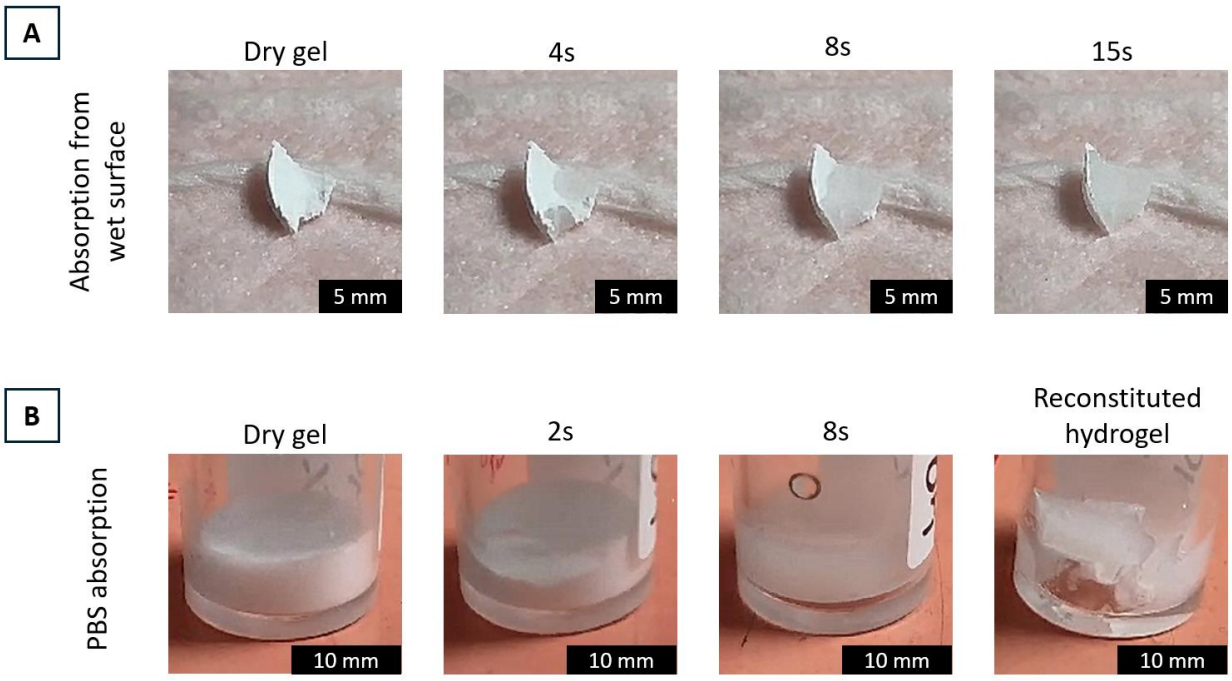


Figure 2.22. Dry SM-gel absorption capacity. (A) Water absorption from a wet surface, and (B) rehydration of the hydrogel with 0.5 mL of PBS.

On the other hand, the second approach aimed at investigating the capacity of the hydrogel matrix to absorb large proteins, such as enzymes present in the wound bed. This property is important in CWs treatments since sequestering harmful enzymes, such as MMPs and MPO, could help reduce the inflammatory state. Therefore, the ideal hydrogel should absorb the highest possible quantity of proteins from fluids. In this case, BSA served as a model protein, given its size (66 kDa) matching the range of MMPs' dimensions (50–70 kDa) [46]. *Figure 2.23* and *Figure 2.24* summarize the results obtained for the hydrogel put in contact with a PBS solution with 1 mg/mL BSA. Throughout the experiment, the SM-gels exhibited minimal variations in their wet weight and in the volume of the extracted solutions, suggesting minimal medium uptake (*Figure 2.23*.B and D). However, a progressive reduction in hydrogel constituents was observed by measuring their dry weight (*Figure 2.23*.A and C). Even if no swelling was perceived, these observations suggest an active exchange of materials between the SM-gels and the added medium occurred, with the hydrogels releasing part of their

constituents while absorbing the medium. The percentage of BSA absorbed into the gels was further proof of this process. Indeed, it progressively increased until reaching a plateau (*Figure 2.24*.A and B). Moreover, the percentage of BSA absorbed depended on the PEU content, with statistically significant differences observed between the three formulations ($p < 0.001$). Interestingly, the highest uptake was observed for the CHP407:SHF68 80:20 blend with 1% w/v PEU concentration (around 50%), while at 5% w/v PEU content, only 30% of the BSA was absorbed. For the CHP407:SHF68 50:50 blends, the trend was similar, but the BSA absorbed was lower for all conditions. The unique characteristics of these hydrogel systems can explain these results. Previous studies [23] have demonstrated that at low polymer concentrations, the networks of SM-gels exhibit a more pronounced SM character, enhancing their ability to maintain shape while interacting strongly with the surrounding environment. Additionally, at low polymeric content, the hydrogels are less crosslinked, favoring the diffusion of molecules within their networks. This likely accounts for the enhanced capacity to absorb BSA in the gel with 1% w/v PEU content and in the blends at CHP407:SHF68 80:20 ratio which presented a higher quantity of CHP407 that was more capable of interacting with αCDs forming PPRs.

The outcome of this experiment suggested that the hydrogels at low PEUs content behaved better in contact with aqueous solutions, such as exudates. However, the rheological tests indicated better mechanical properties for hydrogels at higher PEUs content, with G' values above 2 kPa (acceptability range 2-10 kPa [43]). Therefore, the formulation at 3% w/v PEU concentration was selected for further experiments, representing the best compromise between the two observed trends.

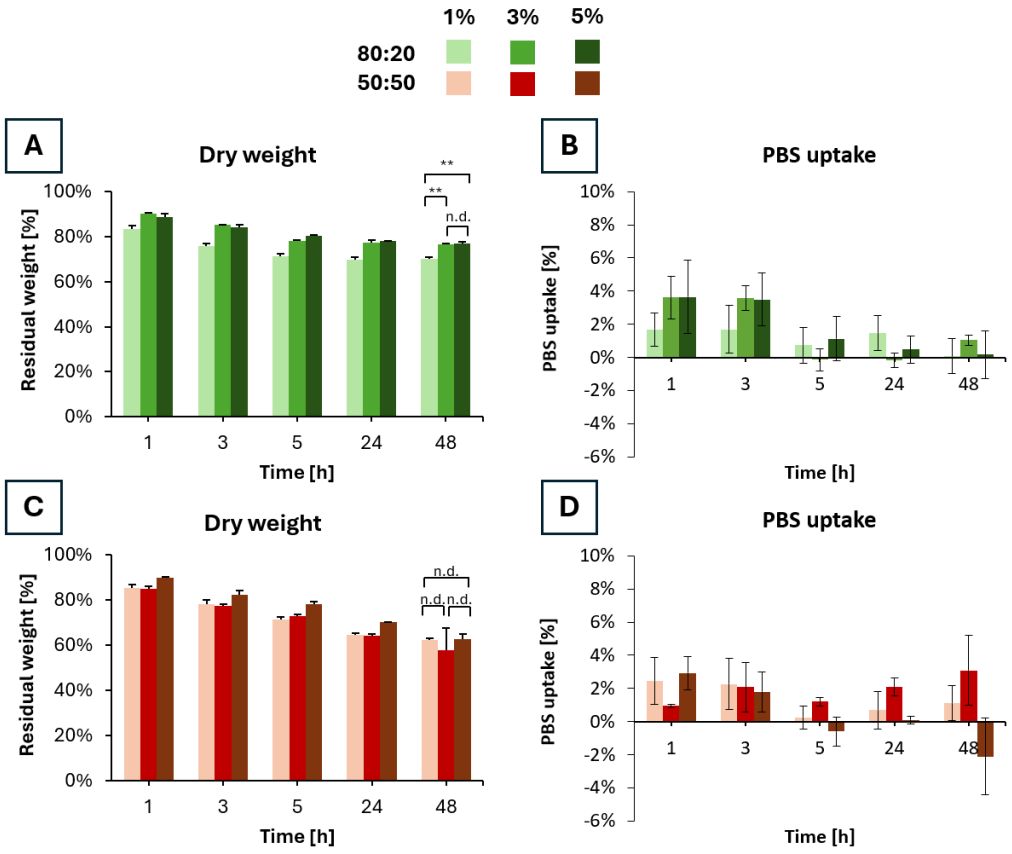


Figure 2.23. BSA absorption in the SM-gels. Comparison between the hydrogel dissolution and the BSA absorption. (A-B) Results of the test for the SM-gels at 80:20 ratios and 1% (light green), 3% (green), and 5% w/v (dark green) PEU content showing (A) the dry weight loss and (B) the PBS uptake at the different time point. (C-D) Results of the test for the SM-gels at 50:50 ratios and 1% (light red), 3% (red) and 5% w/v (dark red) PEU content showing (C) the dry weight loss and (D) the PBS uptake at the different time point.

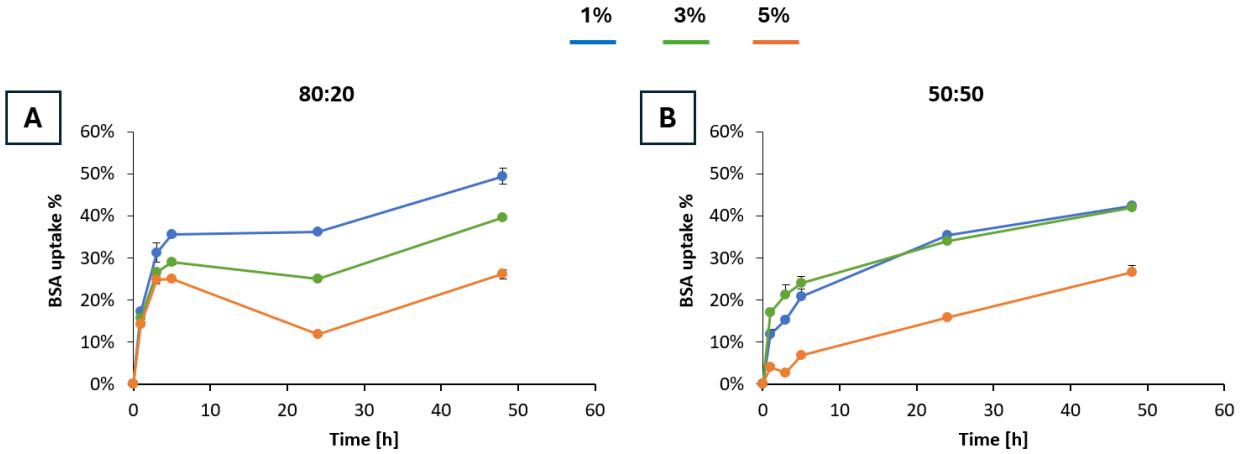


Figure 2.24. Percentage of BSA absorption in the SM-gels, comparing the two weight ratios studied ((A) 80:20 and (B) 50:50) and the three different PEUs concentrations (1% (blue), 3% (green) and 5% w/v (orange)).

2.3.2.3. Cytocompatibility of the selected CHP407/SHF68 blend hydrogels

The cytocompatibility of the blends at 3% w/v PEU concentration was tested according to the ISO 10993:5 guidelines to understand if the developed formulations could be applied in the medical field. In accordance with what was previously observed (*Figure 2.16*), the cytocompatibility increased with the increase of SHF68 content (*Figure 2.25*). Nevertheless, both the blends presented an acceptable cytocompatibility with cell viability higher than 75%.

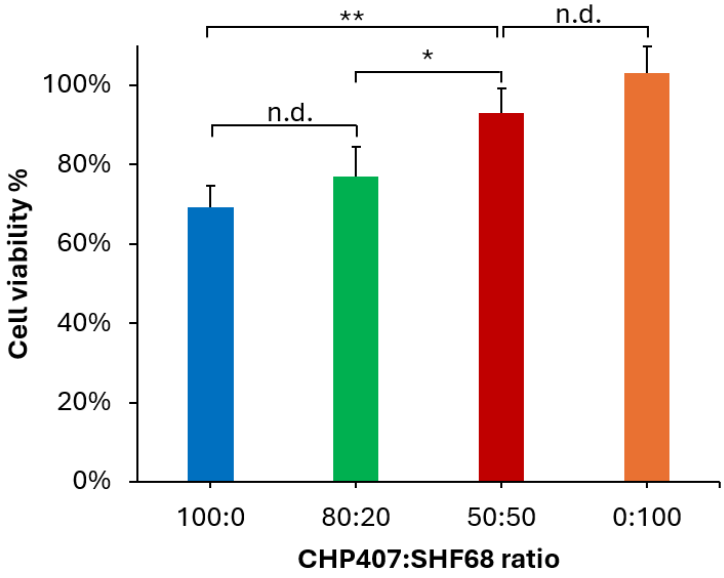


Figure 2.25. Cytocompatibility test for the blends at 3% w/v PEU content and CHP407:SHF68 80:20 and 50:50 ratio.

2.3.2.4. Stability of the selected CHP407/SHF68 blend hydrogels

To further evaluate the hydrogel applicability, the stability of the selected systems at 3% w/v PEU concentration was investigated. In this type of test, the SM-gels were put into contact with an aqueous medium (PBS) which was refreshed at each time point. This high medium turnover simulated what could happen in moderately to highly exudative wounds, such as infected CWs, and could be considered as the less conservative condition. Therefore, the SM-gels exposed to lower exudate turnover could present extended stability. *Figure 2.26*.A shows that the dry weight of

the two SM-gels was progressively lost, while no variation in wet weight was observed until the very last time points in which the SM-gels started losing their integrity (*Figure 2.26*.B). This is particularly evident for the blend at CHP407:SHF68 80:20 ratio which can lose more than 40% of its components while maintaining a stable hydrogel network. Conversely, the network of the 50:50 blend was too unstable to withstand the harsh dissolutive forces of the test and were unable to persist for more than 24 hours in aqueous environments. This is related to the higher presence of SHF68 which provided the hydrogel with higher responsivity to aqueous environments and was less capable of forming PPR networks compared to CHP407. This was also confirmed by the swelling ratio, which combines the contribution of water and hydrogel's components indicating the network responsivity. In the case of the CHP407:SHF68 50:50 blend, at 6h of incubation, the swelling ratio was higher than for the blends at 80:20 ratio (*Figure 2.26*.C).

At 80:20 CHP407:SHF68 ratio, the system appeared as a stable gel up to 24 hours of incubation and then completely dissolved at 48 hours. The frequency of wound dressing change depends greatly on the type of wound and the dressing chosen. Very exudative wounds may require daily dressing changes, moderately exudative wounds require bandage changes every 2-3 days, while dressings on wounds with limited or no exudate could stay in place for up to a week [44]. In the stability test, the conditions selected tackle moderately to highly exudative wounds, whose dressings are changed every 24-48 hours. Therefore, the stability of the developed system can be considered sufficient. Nevertheless, it could be useful to extend the SM-gel durability over 72h, to have a system that could reduce the current frequency of dressing change. This topic will be addressed in Section 5.

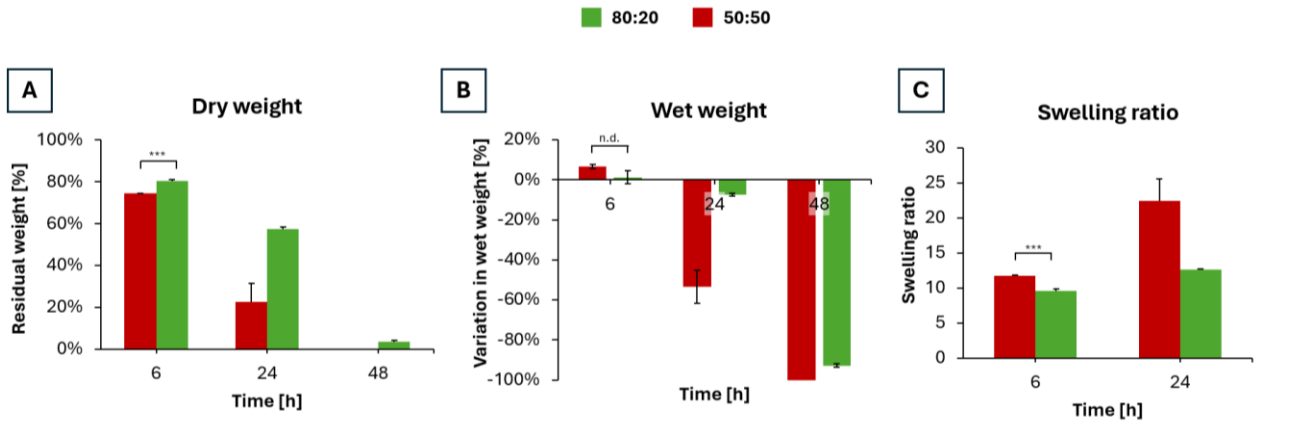


Figure 2.26. Stability of the hydrogels at 3% w/v PEU concentration and different CHP407:SHF68 ratio (80:20 in green and 50:50 in red). (A) Dry weight loss, (B) Wet weight and (C) swelling ratio at the different time point.

2.4. Conclusion

The SM-gel composition was optimized to better suit wound healing applications. Two PEUs were combined with αCDs to obtain SM hydrogels and their properties were characterized through rheology and cytocompatibility tests. The results of these tests proved that both PEUs could form completely developed hydrogels with self-healing properties and injectability. However, CHP407 provided better mechanical properties to the SM-gels while SHF68-based gels were more cytocompatible. To find a compromise between mechanical properties and cytocompatibility, CHP407:SHF68 blends at 80:20 and 50:50 ratios were tested. The rheological tests confirmed that higher CHP407 content provides higher rigidity to the network and a better capacity to withstand loads. The condition at CHP407:SHF68 80:20 ratio and 3% w/v PEUs content presented the best rheological characteristics having marked self-healing and G' value around 10 kPa, within the range

of values observed for skin-derived gelatin hydrogels. Additionally, this condition seemed promising when analyzing the hydrogel's capacity to interact with and absorb external medium and molecules. These tests highlighted that the total PEU content impacted the absorption of large proteins into the hydrogel. At low PEU content SM-gels presented a network mostly based on PPR interactions, which favored the exchange of materials with the external environment. Indeed, a higher BSA absorption was observed at low PEU content compared to hydrogels at higher PEU concentrations. Therefore, the condition at 3% w/v PEU concentration could grant good mechanical properties and high absorption of external compounds. This condition was thus selected for further analysis proving good cytocompatibility. Finally, stability tests confirmed the formulation at CHP407:SHF68 80:20 ratio and 3% w/v PEUs content as the best one in terms of durability in aqueous environments, maintaining 24 h stability under conditions of high medium turnover. This setup simulates highly exudative wounds whose dressings are changed daily [44]. For moderately and minimally exudative wounds, the durability of the SM-gel is expected to increase, aligning with the less frequent need for dressing changes. When dressings are changed after the SM-gel has dissolved, the exudate retention properties of the hydrogel are lost. However, the active compounds within the hydrogel should still be effective, and the dissolved hydrogel should be easier to remove without causing damage to the healing wound bed. The selected hydrogel is a promising candidate for delivering drugs and compounds to treat wounds. It can be injected at shear stress compatible with the force applied on syringe plungers, adapting to the wound bed, while its high self-healing allows for compliance in patient movements. Moreover, its absorption capacity allows for adaptability to the patient's needs. If a highly exudative wound is present, the dried hydrogel could be applied to absorb the excess exudate, while in the case of little exudate, the wet hydrogel could restore the moisture in the wound bed. Given these properties, this formulation was selected to encapsulate, protect, and control the release of newly developed multi-functional nanoparticles. Section 3 will focus on the development and characterization of these NPs and their encapsulation into the SM-gel.

2.5. References

[1] H. Chang, C. Li, R. Huang, R. Su, W. Qi, and Z. He, 'Amphiphilic hydrogels for biomedical applications', J. Mater. Chem. B, vol. 7, no. 18, pp. 2899–2910, May 2019, doi: 10.1039/C9TB00073A.

[2] B. Blanco-Fernandez, O. Castaño, M. Á. Mateos-Timoneda, E. Engel, and S. Pérez-Amodio, 'Nanotechnology Approaches in Chronic Wound Healing', Advances in Wound Care, vol. 10, no. 5, pp. 234–256, May 2021, doi: 10.1089/wound.2019.1094.

[3] G. D. Mogoşanu and A. M. Grumezescu, 'Natural and synthetic polymers for wounds and burns dressing', International Journal of Pharmaceutics, vol. 463, no. 2, pp. 127–136, Mar. 2014, doi: 10.1016/j.ijpharm.2013.12.015.

[4] E. Caló and V. V. Khutoryanskiy, 'Biomedical applications of hydrogels: A review of patents and commercial products', European Polymer Journal, vol. 65, pp. 252–267, Apr. 2015, doi: 10.1016/j.eurpolymj.2014.11.024.

[5] J. H. Lee, 'Injectable hydrogels delivering therapeutic agents for disease treatment and tissue engineering', Biomaterials Research, vol. 22, no. 1, p. 27, Sep. 2018, doi: 10.1186/s40824-018-0138-6.

[6] R. Eelkema and A. Pich, 'Pros and Cons: Supramolecular or Macromolecular: What Is Best for Functional Hydrogels with Advanced Properties?', Adv. Mater., vol. 32, no. 20, p. 1906012, May 2020, doi: 10.1002/adma.201906012.

[7] M. Champeau et al., 'Supramolecular poly(acrylic acid)/F127 hydrogel with hydration-controlled nitric oxide release for enhancing wound healing', Acta Biomaterialia, vol. 74, pp. 312–325, Jul. 2018, doi: 10.1016/j.actbio.2018.05.025.

[8] S. S. Anumolu, 'Doxycycline hydrogels with reversible disulfide crosslinks for dermal wound healing of mustard injuries', 2011.

[9] D. A. Gyles, L. D. Castro, J. O. C. Silva, and R. M. Ribeiro-Costa, 'A review of the designs and prominent biomedical advances of natural and synthetic hydrogel formulations', European Polymer Journal, vol. 88, pp. 373–392, Mar. 2017, doi: 10.1016/j.eurpolymj.2017.01.027.

[10] Y. Zhang et al., 'Novel lignin–chitosan–PVA composite hydrogel for wound dressing', Materials Science and Engineering: C, vol. 104, p. 110002, Nov. 2019, doi: 10.1016/j.msec.2019.110002.

[11] S. Lin et al., 'Chitosan-poloxamer-based thermosensitive hydrogels containing zinc gluconate/recombinant human epidermal growth factor benefit for antibacterial and wound healing', Materials Science and Engineering: C, vol. 130, p. 112450, Nov. 2021, doi: 10.1016/j.msec.2021.112450.

[12] M. Mahinroosta, Z. Jomeh Farsangi, A. Allahverdi, and Z. Shakoori, 'Hydrogels as intelligent materials: A brief review of synthesis, properties and applications', Materials Today Chemistry, vol. 8, pp. 42–55, Jun. 2018, doi: 10.1016/j.mtchem.2018.02.004.

[13] A. J. Poudel, F. He, L. Huang, L. Xiao, and G. Yang, 'Supramolecular hydrogels based on poly (ethylene glycol)-poly (lactic acid) block copolymer micelles and α-cyclodextrin for potential injectable drug delivery system', Carbohydrate Polymers, vol. 194, pp. 69–79, Aug. 2018, doi: 10.1016/j.carbpol.2018.04.035.

[14] A. Domiński, T. Konieczny, and P. Kurcok, 'α-Cyclodextrin-Based Polypseudorotaxane Hydrogels', Materials, vol. 13, no. 1, Art. no. 1, Jan. 2020, doi: 10.3390/ma13010133.

[15] J. O. Akindoyo, M. D. H. Beg, S. Ghazali, M. R. Islam, N. Jeyaratnam, and A. R. Yuvaraj, 'Polyurethane types, synthesis and applications – a review', RSC Adv., vol. 6, no. 115, pp. 114453–114482, Dec. 2016, doi: 10.1039/C6RA14525F.

[16] J. Joseph, R. M. Patel, A. Wenham, and J. R. Smith, 'Biomedical applications of polyurethane materials and coatings', Transactions of the IMF, vol. 96, no. 3, pp. 121–129, May 2018, doi: 10.1080/00202967.2018.1450209.
[17] P. Zarrintaj et al., 'Poloxamer: A versatile tri-block copolymer for biomedical applications', Acta Biomaterialia, vol. 110, pp. 37–67, Jul. 2020, doi: 10.1016/j.actbio.2020.04.028.
[18] M. A. Ward and T. K. Georgiou, 'Thermoresponsive Polymers for Biomedical Applications', Polymers, vol. 3, no. 3, Art. no. 3, Sep. 2011, doi: 10.3390/polym3031215.
[19] M. Boffito et al., 'Novel polyurethane-based thermosensitive hydrogels as drug release and tissue engineering platforms: design and in vitro characterization', Polymer International, vol. 65, no. 7, pp. 756–769, 2016, doi: 10.1002/pi.5080.
[20] S. Sartori et al., 'Synthesis and structure–property relationship of polyester-urethanes and their evaluation for the regeneration of contractile tissues', Reactive and Functional Polymers, vol. 73, no. 10, pp. 1366–1376, Oct. 2013, doi: 10.1016/j.reactfunctpolym.2013.01.006.
[21] F. S. Palumbo, S. Federico, G. Pitarresi, C. Fiorica, and G. Giammona, 'Synthesis and characterization of redox-sensitive polyurethanes based on l-glutathione oxidized and poly(ether ester) triblock copolymers', Reactive and Functional Polymers, vol. 166, p. 104986, Sep. 2021, doi: 10.1016/j.reactfunctpolym.2021.104986.
[22] J. Guan and W. R. Wagner, 'Synthesis, Characterization and Cytocompatibility of Polyurethaneurea Elastomers with Designed Elastase Sensitivity', Biomacromolecules, vol. 6, no. 5, pp. 2833–2842, Sep. 2005, doi: 10.1021/bm0503322.
[23] A. Torchio et al., 'Injectable supramolecular hydrogels based on custom-made poly(ether urethane)s and α-cyclodextrins as efficient delivery vehicles of curcumin', Materials Science and Engineering: C, vol. 127, p. 112194, Aug. 2021, doi: 10.1016/j.msec.2021.112194.
[24] A. Torchio, M. Boffito, A. Gallina, M. Lavella, C. Cassino, and G. Ciardelli, 'Supramolecular hydrogels based on custom-made poly(ether urethane)s and cyclodextrins as potential drug delivery vehicles: design and characterization', J. Mater. Chem. B, vol. 8, no. 34, pp. 7696–7712, Sep. 2020, doi: 10.1039/D0TB01261K.
[25] M. E. Brewster and T. Loftsson, 'Cyclodextrins as pharmaceutical solubilizers', Advanced Drug Delivery Reviews, vol. 59, no. 7, pp. 645–666, Jul. 2007, doi: 10.1016/j.addr.2007.05.012.
[26] H. Arima, Y. Hayashi, T. Higashi, and K. Motoyama, 'Recent advances in cyclodextrin delivery techniques', Expert Opinion on Drug Delivery, vol. 12, no. 9, pp. 1425–1441, Sep. 2015, doi: 10.1517/17425247.2015.1026893.
[27] A. Okamatsu et al., 'Folate-Appended β-Cyclodextrin as a Promising Tumor Targeting Carrier for Antitumor Drugs in Vitro and in Vivo', Bioconjugate Chem., vol. 24, no. 4, pp. 724–733, Apr. 2013, doi: 10.1021/bc400015r.
[28] G. Liu, Q. Yuan, G. Hollett, W. Zhao, Y. Kang, and J. Wu, 'Cyclodextrin-based host–guest supramolecular hydrogel and its application in biomedical fields', Polym. Chem., vol. 9, no. 25, pp. 3436–3449, Jun. 2018, doi: 10.1039/C8PY00730F.
[29] S. Tan, K. Ladewig, Q. Fu, A. Blencowe, and G. G. Qiao, 'Cyclodextrin-Based Supramolecular Assemblies and Hydrogels: Recent Advances and Future Perspectives', Macromolecular Rapid Communications, vol. 35, no. 13, pp. 1166–1184, 2014, doi: 10.1002/marc.201400080.
[30] C.-Y. Quan et al., 'Core−Shell Nanosized Assemblies Mediated by the α−β Cyclodextrin Dimer with a Tumor-Triggered Targeting Property', ACS Nano, vol. 4, no. 7, pp. 4211–4219, Jul. 2010, doi: 10.1021/nn100534q.

[31] C. Loebel, C. B. Rodell, M. H. Chen, and J. A. Burdick, ‘Shear-thinning and self-healing hydrogels as injectable therapeutics and for 3D-printing’, Nat Protoc, vol. 12, no. 8, pp. 1521–1541, Aug. 2017, doi: 10.1038/nprot.2017.053.
[32] M. Wang et al., ‘Photo-Reversible Supramolecular Hydrogels Assembled by α-Cyclodextrin and Azobenzene Substituted Poly(acrylic acid)s: Effect of Substitution Degree, Concentration, and Tethered Chain Length’, Macromolecular Materials and Engineering, vol. 301, no. 2, pp. 191–198, 2016, doi: 10.1002/mame.201500295.
[33] A. Harada, Y. Takashima, and H. Yamaguchi, ‘Cyclodextrin-based supramolecular polymers’, Chem. Soc. Rev., vol. 38, no. 4, pp. 875–882, Mar. 2009, doi: 10.1039/B705458K.
[34] A. Harada, T. Nishiyama, Y. Kawaguchi, M. Okada, and M. Kamachi, ‘Preparation and Characterization of Inclusion Complexes of Aliphatic Polyesters with Cyclodextrins’, Macromolecules, vol. 30, no. 23, pp. 7115–7118, Nov. 1997, doi: 10.1021/ma970680z.
[35] I. I. Abu Hashim et al., ‘Potential use of γ-cyclodextrin polypseudorotaxane hydrogels as an injectable sustained release system for insulin’, International Journal of Pharmaceutics, vol. 392, no. 1, pp. 83–91, Jun. 2010, doi: 10.1016/j.ijpharm.2010.03.026.
[36] Y. Chen, X.-H. Pang, and C.-M. Dong, ‘Dual Stimuli-Responsive Supramolecular Polypeptide-Based Hydrogel and Reverse Micellar Hydrogel Mediated by Host–Guest Chemistry’, Advanced Functional Materials, vol. 20, no. 4, pp. 579–586, 2010, doi: 10.1002/adfm.200901400.
[37] J. Yu, H. Fan, J. Huang, and J. Chen, ‘Fabrication and evaluation of reduction-sensitive supramolecular hydrogel based on cyclodextrin / polymer inclusion for injectable drug - carrier application’, Soft Matter, vol. 7, no. 16, pp. 7386–7394, 2011, doi: 10.1039/C1SM05426K.
[38] X. Marcos, S. Pérez-Casas, J. Llovo, A. Concheiro, and C. Alvarez-Lorenzo, ‘Poloxamer-hydroxyethyl cellulose-α-cyclodextrin supramolecular gels for sustained release of griseofulvin’, International Journal of Pharmaceutics, vol. 500, no. 1–2, pp. 11–19, Mar. 2016, doi: 10.1016/j.ijpharm.2016.01.015.
[39] S. M. N. Simões et al., ‘Syringeable Pluronic–α-cyclodextrin supramolecular gels for sustained delivery of vancomycin’, European Journal of Pharmaceutics and Biopharmaceutics, vol. 80, no. 1, pp. 103–112, Jan. 2012, doi: 10.1016/j.ejpb.2011.09.017.
[40] C. Yang, X. Wang, H. Li, J. Ling Ding, D. Yun Wang, and J. Li, ‘A supramolecular gene carrier composed of multiple cationic α-cyclodextrins threaded on a PPO–PEO–PPO triblock polymer’, Polymer, vol. 50, no. 6, pp. 1378–1388, Mar. 2009, doi: 10.1016/j.polymer.2009.01.010.
[41] M. Boffito, C. Pontremoli, S. Fiorilli, R. Laurano, G. Ciardelli, and C. Vitale-Brovarone, ‘Injectable Thermosensitive Formulation Based on Polyurethane Hydrogel/Mesoporous Glasses for Sustained Co-Delivery of Functional Ions and Drugs’, Pharmaceutics, vol. 11, no. 10, Art. no. 10, Oct. 2019, doi: 10.3390/pharmaceutics11100501.
[42] A. Vo, M. Doumit, and G. Rockwell, ‘The Biomechanics and Optimization of the Needle-Syringe System for Injecting Triamcinolone Acetonide into Keloids’, Journal of Medical Engineering, vol. 2016, 2016, doi: 10.1155/2016/5162394.
[43] G. Boran, S. j. Mulvaney, and J. m. Regenstein, ‘Rheological Properties of Gelatin from Silver Carp Skin Compared to Commercially Available Gelatins from Different Sources’, Journal of Food Science, vol. 75, no. 8, pp. E565–E571, 2010, doi: 10.1111/j.1750-3841.2010.01543.x.
[44] G. S. Schultz et al., ‘Wound bed preparation: a systematic approach to wound management’, Wound Repair Regeneration, vol. 11, no. s1, Mar. 2003, doi: 10.1046/j.1524-475X.11.s2.1.x.

[45] G. Crivello et al., ‘Lignin–Cobalt Nano-Enabled Poly(pseudo)rotaxane Supramolecular Hydrogel for Treating Chronic Wounds’, Pharmaceutics, vol. 15, no. 6, Art. no. 6, Jun. 2023, doi: 10.3390/pharmaceutics15061717.
[46] T. Klein and R. Bischoff, ‘Physiology and pathophysiology of matrix metalloproteases’, Amino Acids, vol. 41, no. 2, pp. 271–290, 2011, doi: 10.1007/s00726-010-0689-x.
[47] K. F. Cutting, ‘Wound exudate: composition and functions’, Br J Community Nurs, vol. 8, no. Sup3, pp. S4–S9, Sep. 2003, doi: 10.12968/bjcn.2003.8.Sup3.11577.
[48] U. J. Adderley, ‘Managing wound exudate and promoting healing’, Br J Community Nurs, vol. 15, no. Sup1, pp. S15–S20, Mar. 2010, doi: 10.12968/bjcn.2010.15.Sup1.46907.

3. Design of lignin-cobalt NPs- loaded SM-gel

Part of the results of this Section are published in **Crivello et al.** [65]

3.1. Introduction

The objective of the work described in this section, is to synthesize and characterize metal-organic nanoparticles (NPs) combining antibacterial and anti-inflammatory activity. To this aim, a polyphenolic Lignin (Lig)-based compound was synthesized and used to reduce cobalt ions to form NPs, which were then loaded in the SM gel developed and described in Section 2.

As previously discussed, NPs represent a promising asset in the treatment of CWs due to their ability to interact with tissues at the cellular level, to protect sensitive molecules from the degradative wound microenvironment, and to control their delivery in time and space in response to endogenous or exogenous stimuli [1], [2], [3]. Additionally, NPs have the potential to concomitantly exert more than one therapeutic action, thereby favoring the transition from traditional dressings to multi-functional dressings, capable of addressing the complicated multi-factorial nature of CWs [3].

Due to their enormous potential, NPs-based drug delivery systems in the form of polymer/lipid carriers, inorganic NPs, or combinations thereof, have been proposed for CWs treatment [4], [5], [6], [7], [8]. For instance, Li et al. [9] developed a tannic acid (TA) loaded microparticle combining corn starch and chitosan through inverse emulsion and surface cross-linking reaction method. The obtained NPs inhibited the growth of *S. aureus* and *E. coli in vitro*, thanks to the combined effect of chitosan and tannic acid. In an *in vivo* mouse model, the particles also promoted hemostasis thanks to the hydrophilicity of starch. In another study, Khezri et al. [10] encapsulated Rosmery essential oil into lipid nanocarriers and delivered them topically in an infected wound model in mice. The wide spectrum therapeutic activity of the rosemary essential oil reduced bacterial colonization and enhanced vascularization, fibroblast infiltration, re-epithelialization, and collagen production.

Inorganic, metal-based NPs have also been proposed for the treatment of CWs, primarily by virtue of their broad-spectrum antibacterial properties and minimal risk of promoting bacterial resistance [11], [12]. In particular, Ag has been widely exploited to obtain NPs., Gupta et al. [13] combined curcumin and βCDs into complexes capable of reducing Ag ions, thereby obtaining NPs. The presence of curcumin provided antioxidant properties, while Ag conferred antibacterial activity, as demonstrated against *P. aeruginosa* and *S. aureus in vitro*. In another study, Orlowski et al. [14] combined TA and Ag into NPs presenting antibacterial activity against *P. aeruginosa, S. aureus,* and *E. coli in vitro.* Additionally, the presence of TA stimulated wound closure, epithelialization, angiogenesis, and formation of the granulation tissue in murine *in vivo* models. Copper is another metal investigated in CWs thanks to its combined antimicrobial and pro-angiogenic effect [15]. Paterson et al. [16] integrated copper ions into mesoporous bioactive glass NPs. The combination of these two components promoted angiogenesis in e*x vivo* assays, while copper ions also exerted antibacterial function against *S. aureus* and *P. aeruginosa* in an infected *in vitro* 3D skin model.

Cobalt (Co) is also emerging as a promising candidate in the treatment of CWs by virtue of its antibacterial activity [17], [18]. Additionally, studies have shown that Co can stimulate angiogenesis and erythropoietin production, beneficial in conditions of tissue hypoxia [19] such as CWs. Furthermore, its magnetic properties make Co a promising candidate in applications such as local sensors, imaging, and hyperthermia [20]. Unfortunately, toxicity of Co has also been reported [19], [21]. The mechanism of cobalt toxicity is not fully understood. However, Co is known to have affinity for sulfhydryl groups and ion centres in metal enzymes, resulting in the inhibition of the

activity of enzymes involved in key cellular processes, such as mitochondrial respiration [19]. Additionally, Co interacts with Ca^{2+}, inhibiting its signaling by competing for binding to intracellular proteins, and generates ROS, resulting in oxidative damage to DNA, proteins, and lipids [22]. Therefore, controlled delivery of this metal is important to achieve a therapeutic action against bacteria and cellular targets, while avoiding side effects.
Different physicochemical methods have been developed for producing cobalt and cobalt oxide NPs, such as hydrothermal and solvothermal reactions, pulsed laser deposition and solution combustion [23], [24], [25], [26]. However, these approaches are energy and time-consuming and require specialized equipment and reagents that can be toxic to the environment [20]. To solve these issues, in recent years, green synthesis approaches have emerged for obtaining Co and Co oxide NPs. These processes use simple, non-hazardous methods that reduce operational costs. Additionally, these methods avoid toxic solvents thus improving environmental safety [20]. In these processes, polyphenolic compounds extracted from different plants, such as hibiscus [17], orange peel [18] and Sageretia thea [27], have been used to reduce Cobalt ions and obtain NPs with antioxidant and antibacterial activity. based on the above, in the present work, the phenolic groups in Lignin (Lig) and tannic acid (TA) were exploited for producing cobalt-based NPs.

Lignin (Figure 3.1.A), an aromatic biopolymer derived from the paper industry, stands as one of the most abundant and cheap biopolymers globally, yet its potential remains largely untapped in the biomedical field because of its limited solubility in water. Lignin presents phenolic and aliphatic hydroxyl groups which provide antioxidant properties, ROS-scavenging and anti-inflammatory activity [28], [29], [30]. Therefore, lignin has been proposed as a novel biomaterial for NPs or scaffold preparation [31], [32]. For instance, lignin has been combined with other polymers to form hydrogels with promising properties in the field of wound healing [33], [34], [35], [36]. An example is the composite hydrogel developed by Zhang et al. [33] by combining lignin, chitosan, and polyvinyl alcohol (PVA), which displayed antibacterial, antioxidant, and wound healing activity *in vivo*. Similarly, Xu et al. [36] incorporate lignin into a polyurethane hydrogel, demonstrating its ROS scavenging and inflammation reduction ability, as well as improved wound healing *in vivo*. Lignin has also been exploited in the formation of NPs for the delivery of various compounds, such as anti-tumor drugs, natural antioxidants, and ibuprofen [31], [37], [38]. Lig-based metal NPs have also been proposed, by exploiting lignin capacity to reduce metal ions, such as silver [39], [40], [41] and tellurium. For instance, Yang et al. [42] prepared a PVA-based hydrogel incorporating cellulose nanocrystals and silver-lignin NPs by chemical crosslinking in the presence of glutaraldehyde. The obtained gel presented ROS scavenging activity and promoted wound closure. In another work, Morena et al. [43] combined lignin and tellurium to obtain antibacterial NPs with demonstrated activity against Gram-negative bacteria. The above results demonstrated the potential of lignin as antioxidant compound in wound healing, confirming also its potential in the preparation of antibacterial metal NPs.

Tannic acid (TA) (Figure 3.1.B) is a naturally occurring polyphenol found in grapes and green tea, with known anti-inflammatory and anti-oxidative activity [44]. Its structure, characterized by gallol and catechol groups containing multiple hydroxyl moieties, endows TA with potent antioxidant capabilities, such as ROS and reactive nitrogen species (RNS) scavenging activity. Furthermore, TA demonstrated efficacy in inhibiting inflammatory cytokines, such as IL-1 and TNF-α, and of MPO and MMPs in wound exudates. Through these mechanisms, TA diminishes neutrophil recruitment and infiltration of inflammatory cells, representing a promising therapeutic compound in skin wound healing [45], [46]. Additionally, TA presents numerous multiple binding sites that allow the formation of electrostatic interactions, hydrophobic coordination, and hydrogen or ion bonds with various macromolecules [47]. Therefore, numerous studies explored TA in conjunction with

synthetic or natural polymers for developing drug delivery systems, such as hydrogels [48], [49], nanofibers [50], sponges [51], films [52], nanogels [46] and nanoparticles [14], [53], [54]. In hydrogels, TA can act both as a therapeutic agent and a structural reinforcement of the network. For instance, He et al. [55] combined TA with silk fibroin and chitosan to obtain a hydrogel exerting antioxidant and antibacterial properties, that was able to stimulate wound closure *in-vivo*. Additionally, they demonstrated that the adhesiveness of the hydrogel and its stiffness increased with the TA content, suggesting an active role of TA in network stabilization. The high reactivity of TA has also been exploited in the formation of nano and microparticles with promising results. For example, Li et al. [9] used TA as a crosslinker of hyaluronic acid, chitosan, and corn starch to form microparticles capable of promoting hemostasis and stimulating wound healing *in vivo*. Interestingly, the microparticles could interact with proteins and cells present in the wound fluid forming a secondary crosslinked network on the wound surface which rapidly stopped hemorrhage and stimulated regeneration.

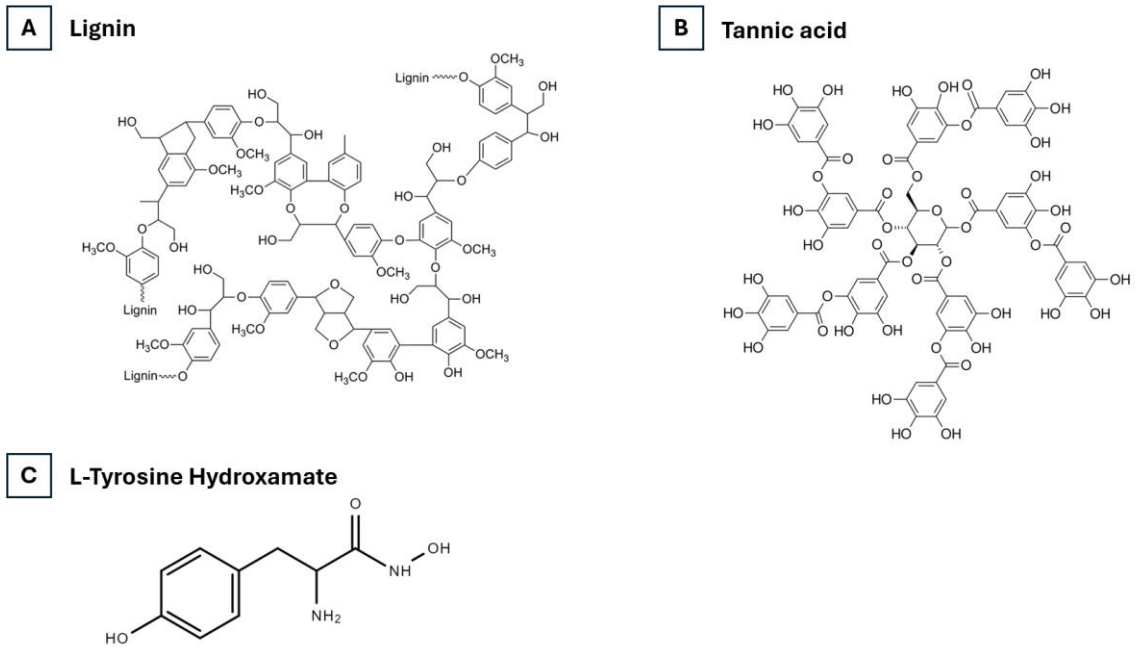


Figure 3.1.Chemical structure of (A) Lig, (B) TA and (C) LTH.

Previous studies by Morena et al. [41], [56] combined Lig and TA to increase the phenolic group content of Lig and enhance its interface reactivity. This new biomaterial was then used to obtain NPs that could interact with silk fibroin and hyaluronic acid to form a hydrogel, in which the NPs acted as a therapeutic and structural component. Indeed, hydrogels did not form in the absence of Lig NPs and the presence of Lig granted antioxidant activity and inhibition of MPO and MMPs, which are overexpressed in CWs [56]. In another study by the same authors, the enhanced interfacial activity of the Lig-TA biomaterial was exploited to reduce silver [41], thereby obtaining silver NPs with broad-spectrum antibacterial activity, that were incorporated in polyurethane foams. The system reduced the bacterial burden and inhibited MPO activity in *ex vivo* wound exudates.

Based on these findings, the work described in this chapter focuses on the combination of Lig, TA and L-tyrosine hydroxamate (LTH) through an enzyme-mediated green synthesis process, and in the application of the material as a reductive agent of Co to form NPs (CoLig NPs). The aim is to obtain a multifunctional NP capable of inhibiting the bacterial growth of both Gram-positive and Gram-negative bacteria, such as *S. aureus* and *P. aeruginosa* respectively, while reducing the

inflammatory state and promoting the passage into the proliferative phase of wound healing. To achieve this, three inflammatory processes were selected to be inhibited: the unbalance in ROS and the overexpression of MMPs and MPO, enzymes involved in ECM and proteins degradation.

In detail, Lig and TA were combined to increase the total phenolic and hydroxyl content of lignin and maximize its capacity to reduce cobalt. To do so, a green process exploiting the enzymatic activity of laccase was used [57]. Laccase is a member of the multicopper protein family, with the ability to oxidize its substrate, producing radicals, while simultaneously reducing molecular oxygen to water. These radicals are unstable and can undergo further reactions. This process is particularly interesting for phenol-containing polymers, such as Lig, since the radicals resulting from their oxidation can cross-react to form covalent bonds [58]. This mechanism was exploited to graft TA to lignin, as depicted in Figure 3.2.

L-tyrosine hydroxamate (LTH) (Figure 3.1.C) was added to increase the material's ability to inhibit MMPs. Hydroxamic acids, such as LTH, are organic compounds characterized by the presence of the RCONOHR' functional group, with the potential to inhibit metalloenzymes [59], [60]. Hydroxamic acids are known for their role as MMPs inhibitors by virtue of their strong affinity toward the zinc ion present in their active sites [61], [62]. Additionally, they are known to interact with other regions of the enzyme backbone through hydrogen bonding [63]. Since MMPs are overexpressed in CWs, active molecules presenting hydroxamic groups could be beneficial in reducing inflammation. However, the release of these compounds should be regulated to avoid unwanted side effects and achieve long-lasting MMP regulation *in situ*. Therefore, some studies proposed the incorporation of hydroxamic acid into hydrogels and other drug delivery systems. For instance, Liang et al. [64] conjugated hydroxamic groups to methacrylate collagen through carbodiimide chemistry. The resulting material was used to produce a hydrogel with inhibitory activity against different MMPs.

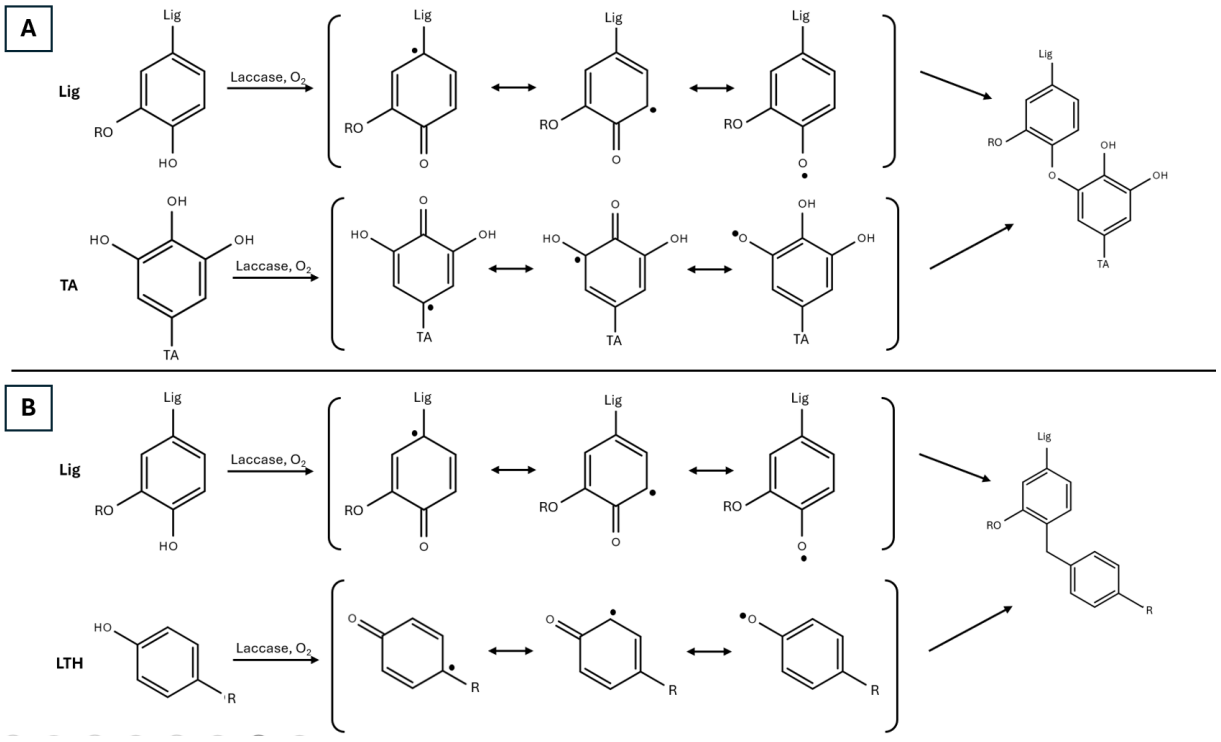


Figure 3.2. Enzymatic conjugation of lignin and TA through the action of the enzyme laccase. Image modified from Morena et al. [57]. (A) Scheme of the conjugation reaction between Lig and TA. Laccase oxidates phenolic groups on Lig, and TA, forming radicals that can then interact with each other producing covalent bonds. (B) Scheme of the conjugation reaction between Lig and LTH. The same reaction can take place between LTH and TA.

Here, the synthesized Lig-TA-LTH was then used to reduce cobalt and obtain NPs (CoLig NPs), which underwent comprehensive characterization, including the assessment of their antioxidant properties, ability to inhibit MPO and MMPs, antibacterial activity and cytotoxicity. Subsequently, these NPs were incorporated as active component into the SM-gel developed in Section 2 and the interactions between the gel and NPs were examined using microscopy, rheology, and stability tests in aqueous media at 37°C. The release kinetics of NPs from the hydrogel were also investigated. The resulting system exhibited injectability, self-healing, enhanced mechanical properties and stability as compared to the pristine SM-gel, which were attributed to the interactions between the gel material and NPs. These findings highlighted the potential of the system for treating CWs and were published in [65].

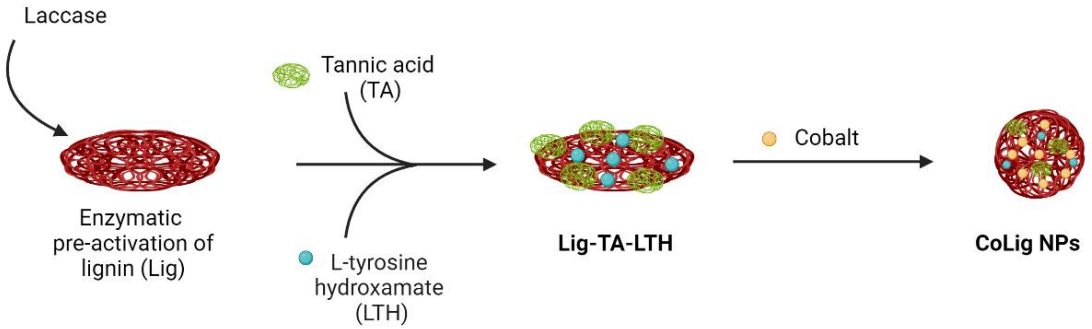


Figure 3.3. CoLig nanoparticle preparation. Firstly, Lig-TA-LTH is obtained by conjugating TA and LTH with Lig through the action of laccase. Then, CoLig NPs are obtained by reducing cobalt ions with the phenolic groups of Lig-TA-LTH.

3.2. Materials and methods

3.2.1. Materials and reagents

Protobind 6000 sulfur-free Lig powder was acquired from Green Value (Switzerland). Gallic acid, tannic acid, L-tyrosine hydroxamate, 3',5'-dimethoxy-4'hydroxyacetophenone (97%) (acetosyringone), guaiacol, hydrogen peroxide (H2O2), 2,2'-azino-bis(3-ethylbenzothiazoline-6-sulfonic acid) diammonium salt (ABTS), phosphate-buffered saline (PBS), Folin–Ciocalteu phenol reagent, sodium carbonate, fluorescamine, dimethyl sulfoxide (DMSO), cobalt(II) nitrate hexahydrate, nutrient broth (NB), Baird–Parker agar, cetrimide agar, and Dulbecco's modified Eagle's medium (DMEM) were obtained from Sigma-Aldrich (Madrid, Spain and Milan, Italy). Alpha-cyclodextrins (αCDs) were purchased from TCI Chemicals Europe (Zwijndrecht, Belgium). AlamarBlue cell viability reagent, myeloperoxidase, and EnzChek™ Gelatinase/Collagenase Assay Kit were supplied by Invitrogen, Life Technologies Corporation (Madrid, Spain). Novozym 51003 laccase from Miceliophtora termophila was provided by Novozymes (Bagsvaerd, Denmark). The laccase exhibited an enzymatic activity of 179 U/mL, defined as the quantity of enzyme needed to convert 1 µmol of ABTS to its cation radical (ε436 = 29,300 M−1 cm−1) in 5 mM Britton Robinson buffer (pH 5) at 40 °C. Bacterial strains (Staphylococcus aureus ATCC 25923 and Pseudomonas aeruginosa ATCC 10145) and human cell lines (fibroblasts ATCC-CRL-4001, BJ-5ta, and keratinocytes HaCaT cell line) were purchased from the American Type Culture Collection (ATCC LGC Standards, Spain). The water utilized throughout the experiments was purified via the Milli-Q plus system (Millipore) with a resistivity of 18.2 MΩ cm before application.

3.2.2. Enzymatic Functionalization of Lig

Protobind 6000 Lig was functionalized with TA and LTH by modifying a previously outlined procedure [41]. Briefly, Lig (10 mg/mL) was soaked in sodium acetate buffer (50 mM, pH 5) at 50 °C containing acetosyringone, one of the most efficient natural enhancers in laccase-mediated oxidation [66], at a concentration of 1.5 mg/mL. Subsequently, laccase (1% v/v) was introduced into the Lig solution for 1 h at 50 °C under stirring to initiate the oxidative reaction. Finally, TA (10 mg/mL) and LTH (0.5 mg/mL) were incorporated into the solution, and the reaction continued under stirring for 2 h at 50 °C. Unreacted TA and LTH were separated from the resulting material by centrifugation at 4750 rpm at 4 °C for 15 minutes. The resulting powder, designated as Lig-TA-LTH, was then freeze-dried and stored for further characterization.

3.2.3. Characterization of Lig-TA-LTH

Successful conjugation of TA and LTH to Lig was investigated with attenuated total reflectance–Fourier transform infrared (ATR-FTIR) spectroscopy. Variations in the phenolic content were assessed by using Folin–Ciocalteu reagent to confirm the presence of TA. The LTH content was evaluated using fluorescamine fluorimetric assay.

3.2.3.1. ATR-FTIR Spectroscopy

For characterization of the functionalized Lig, ATR-FTIR analysis was conducted on Lig-TA-LTH utilizing a PerkinElmer Spectrum 100 FTIR spectrometer (PerkinElmer, Waltham, MA, USA). Spectra were generated by averaging 32 scans over the spectral range from 4000 to 600 cm^{-1} at a resolution of 1 cm^{-1}. All analyses were carried out at room temperature. Spectra of Lig, TA, and LTH were also obtained for comparative purposes.

3.2.3.2. Measurement of the Phenolic Content

The phenolic content of Lig-TA-LTH was determined spectrophotometrically using Folin–Ciocalteu reagent. Briefly, 20 µL of a water solution containing Lig-TA-LTH (1 mg/mL) was combined with 100 µL of 20% w/v sodium carbonate (Na2CO3) and 80 µL of 0.2 N Folin–Ciocalteu phenol reagent. The resulting mixture was incubated for 10 minutes in the dark. Then, the absorbance at 765 nm was measured using an Infinite M200 spectrophotometer (TECAN). Gallic acid (GA) was used to obtain a calibration curve (0.1–1 mg/mL). All samples were measured in triplicate, and the results are expressed in GA equivalents (GAE) per g of material.

3.2.3.3. Quantification of the LTH Content

The primary amine of LTH was utilized for quantifying the LTH content in the Lig-TA-LTH conjugates through fluorescamine fluorimetric assay. In brief, 75 µL of the LTH, previously solubilized in water at 1 mg/mL, were mixed with 25 µL of fluorescamine reagent (3 mg/mL in DMSO). The plate was incubated at room temperature for 10 minutes and read using an Infinite M200 spectrophotometer (TECAN) at λex/em = 390/470 nm. A calibration curve was constructed using LTH. All samples were measured in triplicate.

3.2.4. Preparation of Cobalt/Lig Nanoparticles (CoLig NPs)

CoLig NPs were synthesized by adapting the protocol by Morena et al. [41]. Lig-TA-LTH was dissolved in water at a concentration of 5 mg/mL, and the pH was adjusted to 8.5. Subsequently, 30 mL of this solution was combined with 20 mL of cobalt(II) nitrate hexahydrate solution (4 mg/mL in water) and incubated for 2 hours at 60 °C at 250 rpm. The resulting nanoparticles (NPs) were purified via centrifugation at 18,000 rpm for 20 minutes. The pellet obtained was then resuspended in water and subjected to sonication for 30 seconds using a Bandelin Sonopuls HD

2070 sonicator (operating at 50% amplitude and 20 kHz) to disaggregate the NPs. Final purification was achieved through centrifugation at 1200 rpm for 5 minutes to eliminate aggregated NPs and residual Lig-TA-LTH.

As a control, NPs containing Lig-TA-LTH but lacking cobalt were prepared as previously described [56]. Initially, Lig (10 mg/mL) was soaked in a sodium acetate buffer (50 mM, pH 5) containing 1.5 mg/mL acetosyringone at 50 °C under stirring (250 rpm). Laccase (1% v/v) was then added to the Lig solution and incubated for 1 hour at 50 °C under stirring to initiate the oxidative reaction. Subsequently, TA (10 mg/mL) and LTH (0.5 mg/mL) were introduced to the solution, and the reaction proceeded under sonication (20 kHz, 50% amplitude) for 2 hours at 50 °C using a VCX 750 ultrasonic processor (Sonics, Oklahoma City, OK, USA). The solution was then centrifuged at 25,000× g for 15 minutes at 4 °C to remove unreacted TA and LTH in the supernatant. The resulting NPs (referred to as Lig NPs) were suspended in water via sonication for 30 seconds (at 50%, 20 kHz) and centrifuged at 500× g for 5 minutes to eliminate larger NPs and undissolved Lig.

3.2.5. Characterization of CoLig NPs

3.2.5.1. Morphological Characterization and Cobalt Loading

The size, size distribution, polydispersity index (PDI), and ζ-potential of the CoLig NPs were assessed using dynamic light scattering (DLS) analysis with a Zetasizer Nano Z (Malvern Instruments Inc., Malvern, UK). Additionally, scanning electron microscopy (SEM) (Merlin Zeiss, Oberkochen, Germany) was used to determine both the size and the morphology of the NPs, with SEM images analyzed using ImageJ software (version 1.53t). Quantification of cobalt content within the CoLig NPs was carried out via inductively coupled plasma mass spectrometry (ICP-MS) (ICP-MS 7800, Agilent Technologies, Santa Clara, CA, USA). Calibration was performed using an internal standard with 45Rh and a standard curve of 59Co. Before analysis, samples were digested with 20% (v/v) HNO3 at 100 ◦C for 3 h, then diluted to a final concentration of HNO3 of 2% v/v and filtered through a 0.2 µm filter.

3.2.5.2. MPO and MMP Inhibition Assays

The MPO inhibition capacity of CoLig NPs was evaluated using guaiacol as a substrate. Samples were dispersed at 2 mg/mL in 0.1 M sodium phosphate buffer with pH adjusted to 7.5 by adding 0.1 M sodium phosphate monobasic. Subsequently, 152 µL of each sample were combined with 32 µL of MPO (90 U/mL, diluted 1:20 in Milli-Q water) and 96 µL of guaiacol solution (16 mM in the prepared buffer). The mixtures were then incubated at 37°C for 90 minutes. Following incubation, 190 µL of the mixture were transferred to a 96-well plate, and 10 µL of 10 mM H2O2 were added to initiate the reaction. The absorbance at 476 nm was recorded over time, and the slopes of the curves within the first 150 seconds were compared. The percentage of MPO inhibition was calculated assuming that control values (MPO without NPs) represented 100% activity.

The MMP inhibition capacity of CoLig NPs was determined using the EnzCheck Gelatinase/Collagenase Assay Kit, with some modifications. Initially, samples were dispersed at 2 mg/mL in buffer (80% of 1 M Tris HCl buffer at pH 7.1 and 20% 1 M $CaCl_2$). Subsequently, 5 µL of 500 U/mL collagenase type IV from Clostridium histolyticum were added to achieve a final concentration of 5 U/mL. The solution was then incubated at 37°C for 24 hours. After incubation, 100 µL of the sample were mixed with 80 µL of buffer and 20 µL of fluorescein-conjugated gelatine (100 µg/mL in Milli-Q water). The plate was incubated for 20 minutes in darkness at room temperature, and fluorescence was measured at λex/em = 493/528 nm. Collagenase activity was determined as a percentage of enzyme inhibition compared to the control (a reaction mixture with enzyme and substrate but without NPs).

The CoLig NPs capacity to inhibit MMPs in wound exudate was also quantified using the EnzChek Gelatinase/Collagenase Assay Kit. Wound exudate was extracted from the dressing (UrgoCleans, Urgo Medical) of patients with venous leg ulcers (Hospital de Terrassa, Spain). After removing the dressing from patients' limbs, 1 g specimen containing the exudate, was soaked in 5 mL Milli-Q water for 10 min. After that, the mixture was vortexed for 3 min and centrifuged for 5 min at 10000 rpm. The extracted liquid was collected and centrifuged once again for 5 min at 10000 rpm to remove residues from the wound dressing and stored at 4 °C for further use. The MMPs presence was calculated using the EnzChek Gelatinase/Collagenase Assay Kit. Briefly, the exudate was diluted 10 times in Buffer (80ml 1 M Tris HCl buffer pH7.1 and 20 mL 1 M CaCl2). Then, 100 µL of the exudate were mixed with 80 µL of Buffer and 20 µL of fluorescein-conjugated gelatin (50 µg/mL in MilliQ water) in a 96well plate. The plate fluorescence was measured over time at λex/em = 493/528 nm. Once the presence of MMPs was confirmed, the ability of CoLig NPs to inhibit MMPs was evaluated by dissolving the NPs (1 mg/mL) in Buffer (80 mL 1 M Tris HCl buffer pH 7.1 and 20 mL 1 M $CaCl_2$). The NPs suspensions (170 µL) were then mixed with 10 µL of wound exudate and incubated at 37 °C for 24 h. Then, 20 µL of fluorescein-conjugated gelatin (50 µg/mL in MilliQ water) was added and the plate fluorescence was measured over time at λex/em = 493/528 nm.

3.2.5.3. Antioxidant activity of CoLig NPs

The antioxidant activity of CoLig NPs was assessed through 2,2-Diphenyl-1-picrylhydrazyl (DPPH) radical scavenging assay. Briefly, 25 µl of sample suspension (0.1-5 mg/mL in MilliQ water) and 75 µl of DPPH solution (0.1 mM in pure ethanol) were mixed and incubated for 30 min at room temperature. After incubation, the samples were centrifuged at 10000 rpm for 5 min to eliminate the suspended materials and the absorbance at 517 nm was measured. Samples mixed with ethanol were used as background, while DPPH mixed with MilliQ water represented the 100% DPPH signal. Each sample was analyzed in triplicate.

3.2.5.4. Antibacterial Activity of CoLig NPs

The susceptibility of *S. aureus* and *P. aeruginosa* to CoLig NPs was assessed using the broth dilution method in 96-well microtiter plates, following a previously established protocol [43]. Different dilutions of CoLig NPs (0.1-2.4 mg/mL) were incubated with bacterial suspensions (5×10^5 CFU/mL) in Nutrient broth at 37°C. After 24 hours, the optical density at 600 nm was measured using the Ultramark Microplate Imaging System (Bio-Rad Laboratories S.r.l., Segrate, Italy) to determine the minimum inhibitory concentration (MIC). Lig NPs were employed as a control and the test was performed in triplicate.

The morphology of S. aureus and P. aeruginosa treated with CoLig NPs was examined using scanning electron microscopy (SEM) (Merlin Zeiss, operated at 1 kV). Bacteria were cultured overnight in Nutrient broth and then diluted to an optical density at 600 nm (OD600) of 0.01. The bacterial suspension was mixed with CoLig NPs to achieve a final concentration of 2.4 mg/mL and transferred to a 48-well plate containing silicon wafers. After 24 hours at 37°C, the liquid was removed, and the bacteria remaining on the wafers were fixed overnight in a 2% paraformaldehyde solution. Subsequently, the bacteria were dehydrated by incubating the wafers in increasing concentrations of ethanol, each for 1 hour (25%, 50%, 75%, and 100%). The same procedure was repeated for untreated bacteria.

The NPs capability to eradicate preformed biofilm was tested. Briefly, *S. aureus* and *P. aeruginosa* were grown overnight at 37°C in appropriate medium (Tryptic Soy Broth (TSB) for *S. aureus* and Brain Heart Infusion (BHI) medium for *P. aeruginosa* both additionated with 1% glucose). Then, 50

µL of medium and 50 µL bacteria inoculum (OD600 = 0.01, ~105-106 CFU/mL) were mixed and incubated at 37 °C. After 24 h, the non-adherent bacteria were eliminated by two washes with PBS and the NPs resuspended in TBS were added to the formed biofilms. After incubation for 24 h, non-adherent bacteria were eliminated by washing and the biofilms were stained using crystal violet assay to assess the biofilm matrix quantity. Briefly, the samples were fixed by drying at 60 °C for 2 h. Then, the residual matrices were stained for 10 min with 0.1% crystal violet solution, washed twice with deionized water and dried at 60°C. To dissolve the crystal violet, acetic acid at 30% v/v was added and incubated for 15 min at room temperature. Finally, the absorbance at 595 nm was measured and the variation in biofilm biomass was calculated as follows:

$$\text{Biofilm biomass \%} = \frac{Absorbance\ treatment}{\text{Absorbance control}} 100 \qquad (1)$$

3.2.5.5. Cytotoxicity of CoLig NPs

The cytotoxicity of CoLig NPs was assessed on human cell lines (fibroblasts, BJ-5ta, keratinocytes, HaCaT) following previously established methods [43]. Cells were seeded in a 96-well tissue-culture-treated polystyrene plate at a density of 60,000 cells per well in 100 µL of DMEM supplemented with 200 mM of L-glutamine, 1% penicillin, and 10% (v/v) fetal bovine serum. After 24 hours of incubation at 37 °C in a humidified atmosphere with 5% CO_2, CoLig NPs dispersed in medium were added at various concentrations. Following an additional 24-hour incubation period, cell viability was assessed using the AlamarBlue assay. The medium was replaced with 100 µL of fresh medium containing AlamarBlue reagent (dilution 1:10), and fluorescence at λex/em = 560/590 nm was measured after 4 hours of incubation. Cells cultured without CoLig NPs served as a growth control (representing 100% cell viability). The concentration that inhibited 50% of the cells (IC_{50}) was calculated using GraphPad Prism 9.

3.2.6. Preparation and Characterization of a Supramolecular Hydrogel (SM-Gel) Embedded with CoLig NPs

3.2.6.1. Preparation of the SM-Gel Loaded with CoLig NPs

The SM-gel was composed of α-cyclodextrins (αCDs) and a mix of two custom-made poly(ether urethane)s (PEUs), SHF68 and CHP407. Both these polymers were synthesized and characterized as reported in Section 2 The SM-gel loaded with CoLig NPs was prepared by adapting the protocol described in Section 2. Briefly, SHF68 and CHP407 were first solubilized in PBS at 4 °C; then, αCDs (14% w/v in PBS) containing CoLig NPs were added to the polymer solutions to obtain a final formulation with 3% w/v PEUs, 2.5 mg/mL CoLig NPs, and 10% w/v αCDs. The samples were vortexed for 20 s, mixed at a weight ratio of CHP407:SHF68 80:20, and then incubated at room temperature to allow gelation. As a control, the same procedure was repeated without the addition of the nanoparticles.

3.2.6.2. Stability of the SM-Gel Loaded with CoLig NPs

The SM-gel was prepared at a 3% w/v PEU concentration, as described previously; then, 500 µL of the solution was incubated for 48 h at room temperature to allow for the complete development of the SM-gel network. Afterward, stability tests were carried out as described in Section 2. Briefly, the vials were weighed ($W_{gel,\,i}$), after which 500 µL of phosphate buffer saline (PBS) was added, and the vials were further incubated at 37 °C. At specified time intervals (6, 24, 48, and 72 hours), samples were collected, weighed following the removal of residual PBS ($W_{gel,f}$), subjected to lyophilization, and weighed again (W_{dry}). PBS renewal occurred for all samples at each time point to mimic exudate renewal. Hydrogel dissolution (weight loss %) was calculated using Equation (2), employing a control lyophilized before PBS incubation as a reference ($W_{dry,cntr}$). The variation in wet

weight (wet weight %) were calculated as per Equation (3), while the swelling ratio was measured as in Equation (4):

$$\text{Residual weight \%} = \left(1 - \frac{W_{dry} - W_{dry,cntr}}{W_{dry,cntr}}\right)100 \quad (2)$$

$$\text{Wet weight \%} = \frac{W_{gel,i} - W_{gel,f}}{W_{gel,i}}100 \quad (3)$$

$$\text{Swelling ratio} = \frac{W_{gel,f} - W_{dry}}{W_{dry}} \quad (4)$$

3.2.6.3. Rheological Tests

The mechanical properties of the SM-gels (3% w/v PEU concentration, with and without NPs) were studied through rheological strain sweep, frequency sweep and strain tests as described in Section 2 using a stress-controlled rheometer (MCR302, Anton Paar GmbH, Graz, Austria) with a 25 mm parallel plate setup. Before gelation, the hydrogel was prepared and loaded into a syringe for easier placement onto the rheological plate. Each experiment utilized approximately 0.4 mL of SM-gel, with a set sample thickness of 0.6 mm and no applied normal force. Strain sweep tests were conducted at 37 °C, employing an angular frequency of 1 rad s−1 and a strain range of 0.01–500%. After a 15-minute interval, tests were repeated to evaluate the hydrogels' mechanical property recovery. Frequency sweep tests were carried out within the linear viscoelastic region (0.1% strain) at temperatures of 25 and 37 °C, by varying angular frequency between 100 and 0.1 rad s−1. To assess the self-healing ability of SM-gels, self-healing strain tests were performed at a frequency of 1 Hz, subjecting the gels to cyclic deformations. Each cycle consisted of a recovery phase at low deformation (0.1%, 120 s) followed by a rupture phase at high deformation (100%, 60 s). After three cycles, the initial recovery phase was reinstated to evaluate residual mechanical properties.

3.2.6.4. CryoSEM

The SM-gels, with and without CoLig NPs, were loaded onto cryoSEM stubs. Analysis was conducted using a Hitachi S-3500N scanning electron microscope (Hitachi High-Tech Co., Tokyo, Japan) at the Institute of Marine Sciences of the Spanish Research Council. The gels were mounted on aluminum stubs and rapidly cooled in liquid nitrogen. Once frozen, they were transferred under vacuum conditions to a cryo-preparation chamber, the Quorum PP3000T (Quorum Technologies, Ltd., Lewes, UK). Within the preparation chamber, maintained under high vacuum, a cold stage allowed for the fracturing of the frozen samples. Subsequently, they were subjected to sublimation at −90 °C for 4 minutes, sputter-coated with platinum, and then transferred to another cold stage within the microscope chamber. The samples remained at −130 °C during observation, which was conducted at an acceleration voltage of 5 kV. The number of branches, indicating the level of crosslinking, was counted using the Skeleton tool of ImageJ, which identifies nodes and connections present in a network and calculates their total number.

3.2.6.5. CoLig NPs Interaction with SM-gel components

The interactions of CoLig NPs with SHF68 and αCDs were investigated through ATR-FTIR spectroscopy. Initially, 5 mg of SHF68 or 25 mg αCDs were dissolved in 500 µL of distilled water, while 5 mg of CoLig NPs were suspended in another 500 µL of distilled water. The two solutions were combined and allowed to interact at 37 °C overnight. Subsequently, the mixture was freeze-dried, and the resulting sample was analyzed using ATR-FTIR spectroscopy, following previously described protocols. The interaction between CHP407 and CoLig NPs was not investigated since CHP407 does not present reactive groups, and is therefore not expected to interact with NPs.

3.2.6.6. CoLig NPs' release from the SM-Gel

The SM-gels containing CoLig NPs were prepared as described above. Afterward, 500 µL of PBS were added to each vial, and the samples were further incubated at 37 °C. At specified time intervals (6, 24, 48, and 72 hours), the supernatant was collected, its volume measured, and fresh PBS was added to the vials. The collected release solutions were subjected to analysis using ICP-MS and fluorescence to quantify Co and Lig content, respectively. For Co content determination, samples were prepared for ICP-MS analysis as per standard protocols. For fluorescence analysis, 100 µL of each release solution were transferred to a 96-well plate, and fluorescence was measured at λex/em = 480/610 nm. A calibration curve was constructed using CoLig NPs. All measurements were performed in triplicate, and results are reported as mean ± standard deviation. The release rate was calculated using Equation (5):

$$\text{Release rate} = \frac{Mi}{\Delta t} \quad (5)$$

Where Mi represents the quantity of released CoLig NPs in mg at a defined time step i, and Δt denotes the duration of the time step in hours.

To elucidate the release kinetics, the Korsmeyer–Peppas model (Power law) was applied to the release data collected within the first 24 hours. Specifically, Equation (6) was employed to determine the release exponent, n:

$$\frac{Mt}{M\infty} = Kt^n \; ; \; Log(\frac{Mt}{M\infty}) = nLog(t) + Log(K) \quad (6)$$

Where Mt identifies the mass of released CoLig NPs at a defined time step t, M∞ denotes the total encapsulated payload, and K represents the dissolution rate constant. For cylindrical samples, n values of 0.45 and 0.89 correspond to release mechanisms based on diffusion or swelling, respectively. Values falling between 0.45 and 0.89 suggest anomalous transport, a combination of diffusion and swelling phenomena. n values exceeding 0.89 indicate a mode of transport characterized by tension within the hydrogel network generated via solvent uptake and significant mass exchange with the external environment [67], [68].

3.2.6.7. Cytocompatibility of the SM-Gel Containing CoLig NPs

The cytocompatibility of the SM-gel was assessed following ISO 10993:5 recommendations. Initially, 100 mg of SM-gel loaded with CoLig NPs were prepared in sterile glass vials under sterile conditions. Subsequently, 1 mL of cell culture medium was added to each vial to ensure contact with the hydrogel. The samples were then incubated for 24 hours at 37 °C, and hydrogel extracts were collected. The same procedure was repeated for the SM-gel without CoLig NPs to serve as a control. Human fibroblasts (BJ-5tα) and keratinocytes (HaCaT) cell lines were cultured for 24 hours in the same medium as described previously. Following incubation, 100 µL of the collected hydrogel extracts were added to each well containing the cells and incubated for additional 24 hours. The AlamarBlue test was performed to evaluate the impact of the SM-gel with CoLig NPs on cell viability.

Confirmation of cell viability was performed using fluorescence microscopy with the Live/Dead Viability/Cytotoxicity Kit (Thermo Fisher Scientific, Waltham, MA, USA). Cells were prepared as previously described and then incubated with CoLig NPs at various concentrations for 24 hours. Following incubation, the medium was aspirated, and the cells were stained for 20 minutes with a PBS solution containing 0.1% v/v calcein acetoxymethyl and 0.1% v/v ethidium homodimer 1. Fluorescence microscopy (Nikon/Eclipse Ti-S, The Netherlands) was used to observe the stained

cells, with calcein acetoxymethyl fluorescence detected at λex/em = 494/517 nm and ethidium homodimer-1 fluorescence detected at λex/em = 517/617 nm.

3.2.6.8. Antioxidant activity of CoLig NPs released from the SM-gel.

The antioxidant activity of the CoLig NPs released from the SM-gel was assessed through DPPH assay as described in *3.2.5.3. Antioxidant activity of CoLig* NPs. The release solutions from SM-gel were collected as described previously and mixed with DPPH using the same proportion as previously indicated. The release from the SM-gel without NPs was also collected as a control.

3.2.6.9. Antibacterial Activity of the SM-Gel Containing CoLig NPs

The antibacterial efficacy of the SM-gel incorporating CoLig NPs was evaluated by morphological changes in *S. aureus* and *P. aeruginosa*, assessed by SEM. Initially, 500 mg of SM-gel loaded with CoLig NPs were prepared in sterile glass vials under aseptic conditions in a biological safety cabinet to maintain sterility. Sterile PBS was utilized throughout the process to ensure the gel's sterility. Following gel preparation, 0.5 mL of Nutrient Broth (NB) were added to the vials, in contact with the SM-gel with or without CoLig NPs. The samples were then incubated for 24 hours at 37 °C, and hydrogel extracts were collected. Concurrently, bacteria were cultured overnight in NB and then diluted to an optical density of OD600 = 0.01. The bacterial suspension was combined with the hydrogel extract and transferred to a 48-well plate containing silicon wafers. After further incubation for 24 hours at 37 °C, the liquid was removed, and the remaining bacteria on the wafers were fixed overnight in a 2% paraformaldehyde solution. Subsequently, bacteria were dehydrated by incubations with increasing concentrations of ethanol (25%, 50%, 75%, and 100%). Each for 1 hour. This process was also performed on untreated bacteria controls. The samples were subjected to SEM analysis, following previously established protocols.

3.2.7. Statistical Analysis

Results are reported as mean ± standard deviation. Statistical analysis was performed through Microsoft Excel for Windows 10. To compare results, one-way ANOVA analyses were performed, followed by Bonferroni's multiple comparison test. Statistical significance was assessed as follows: n.d.—non-significant difference, * $p < 0.05$, ** $p < 0.01$, and *** $p < 0.001$.

3.3. Results and discussion

3.3.1. Synthesis and characterization of Lig-TA-LTH

Lig-TA-LTH was successfully synthesized through the enzymatic conjugation of LTH and TA to Lig. The successful grafting of LTH was confirmed by the quantification of primary amines present in Lig-TA-LTH, which was 2.4 ± 0.2 µg LTH per mg of Lig-TA-LTH conjugate. Phenolated Lig showed an increase to 150 ± 7 µg GAE per mg of conjugate compared to the initial 120 ± 2 µg GAE per mg of pristine Lig ($p = 0.013$), therefore confirming the presence of TA.

Analysis of the ATR-FTIR spectrum of Lig-TA-LTH (shown in Figure 3.4) further confirmed the TA conjugation. In the analyzed ATR-FTIR spectra, peaks at 2920 cm^{-1} and 2840 cm^{-1} were characteristics of C-H stretching of methyl groups typical of lignin. The peaks at 1700 cm^{-1} were attributed to the C=O stretching vibration of unconjugated carbonyl groups [69] present both on Lig and TA. The increase in the intensity if this signal in Lig-TA-LTH, compared to the small shoulder observed in pristine Lig, confirmed the presence of TA. Furthermore, a shift in the band around 3400 cm^{-1} was observed in Lig-TA-LTH (from 3290 cm^{-1} to 3360 cm^{-1}), indicative of the stretching of the OH- bond on the aromatic ring [70], [71]. This shift suggests that the cross-linking reaction between Lig and tannic acid occurred during laccase-assisted phenolation [57].

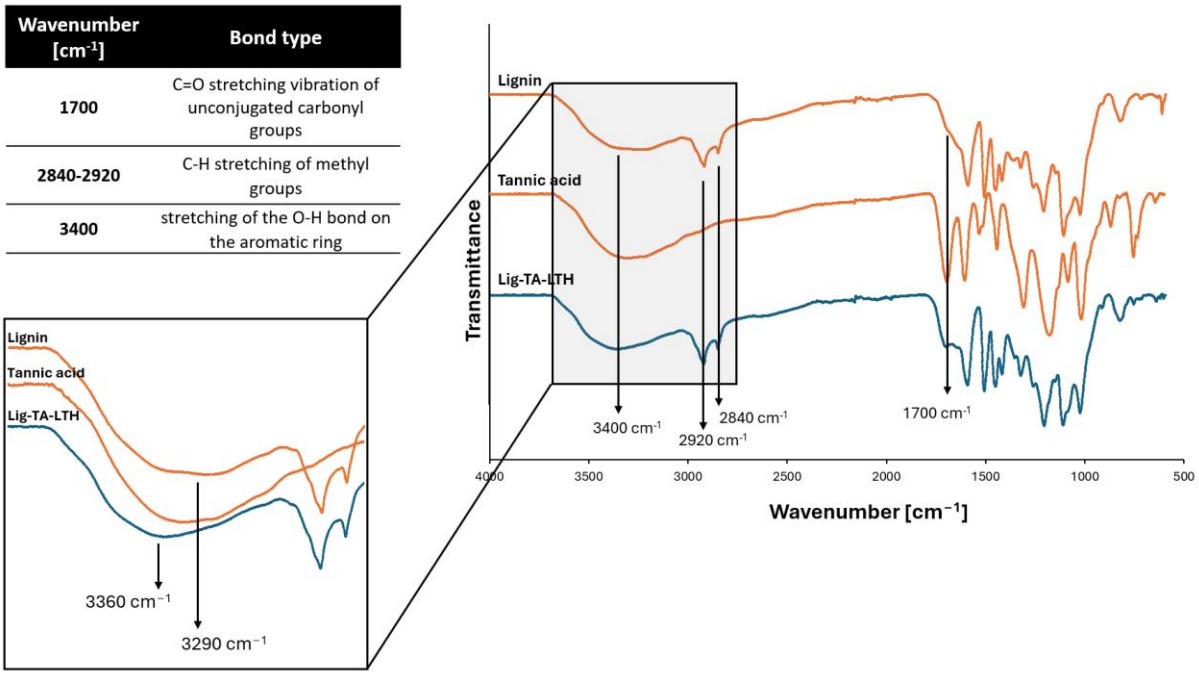


Figure 3.4. FT-IR spectra of Lig-TA-LTH compared to Lig and tannic acid.

3.3.2. Synthesis and characterization of CoLig NPs

The conjugated Lig was utilized as a reducing agent for the synthesis of CoLig NPs. This process induced a noticeable change in the solution color, transitioning from light to dark brown. The presence of cobalt in the NPs was confirmed via ICP-MS, with a measured quantity of 41.6 ± 0.2 µg per mg of CoLig NPs. Furthermore, a reduction in phenolic content from 150 ± 7 to 110 ± 5 µg GAE per mg of material ($p = 0.001$) confirmed cobalt's reduction.

Table 3.1 summarize the size and morphological characterizations of CoLig NPs. NPs of small size, below 200 nm, were obtained. The size of CoLig NPs appeared monodisperse, as indicated by the monomodal size distribution (shown in Figure 3.5.A) and by the polydispersity index (PDI) of 0.22 ± 0.01. Moreover, particles displayed a negative surface charge (ζ potential) of -23.1 ± 0.8 mV, indicating colloidal stability.

SEM images unveiled an irregular round shape of the CoLig NPs, likely resulting from the formation of compact clusters after the interaction between Co and Lig-TA-LTH (Figure 3.5.B). This observed morphology closely resembles that of tellurium–Lig NPs [49] and silver–Lig NPs [43] synthesized using a similar methodology in previous studies. Notably, the size of the dried NPs evaluated from SEM images was smaller (93 nm) as compared to DLS analysis, which measures the hydrodynamic diameter.

Table 3.1. Characteristic parameters (size, PDI and zeta potential) of CoLig NP obtained by DLS.

Size (nm)	PDI	ζ Potential (mV)	Co loading efficiency (µg/mg NPs)
192 ± 1	0.22 ± 0.01	−23.1 ± 0.8	41.6 ± 0.2

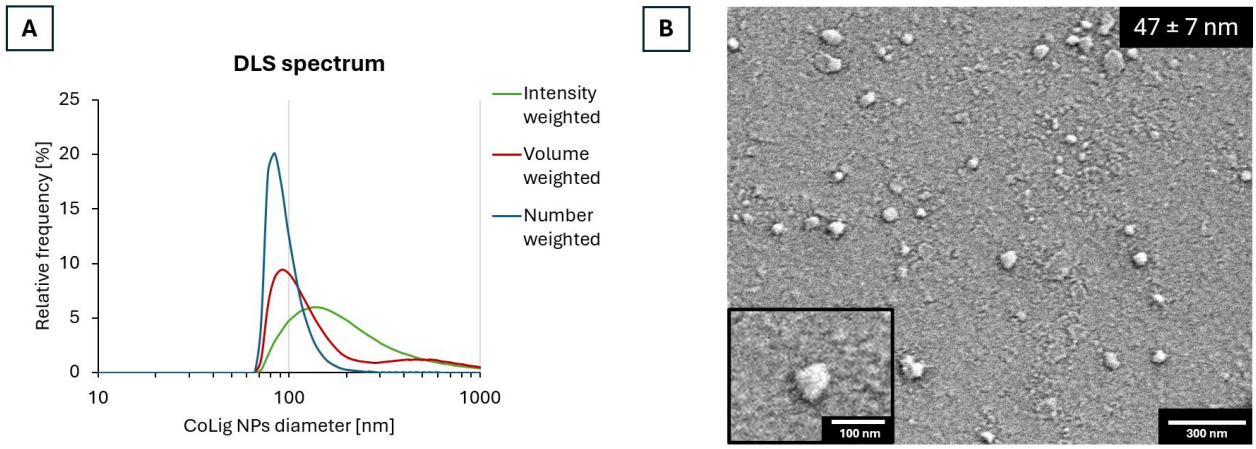


Figure 3.5. CoLig NPs characterization. (A) Size distribution of CoLig NPs measured by DLS analysis. (B) SEM micrographs of the CoLig NPs at 80 kx magnification. The inset shows a zoomed detail.

3.3.2.1. Antioxidant and anti-inflammatory activity of CoLig NPs

The CoLig NPs were evaluated for their ability to inhibit MPO and MMPs. Remarkably, high inhibitory efficacy (>80%) was observed in both cases, with statistically significant differences compared to pristine Lig ($p < 0.001$) (Figure 3.6). In detail, for both MPO and MMPs tests, pristine Lig presented almost no inhibitory activity, while inhibition of enzymatic activity with Lig-TA-LTH reached 50% and 60%, for MPPs and MPO, respectively. The inhibitory activity significantly improved (above 85%) for both empty and Co-containing NPs, with the empty Lig NPs presenting a slightly higher inhibitory activity.

As already discussed, MMPs and MPO are upregulated in CWs and impede the wound-healing process during the inflammatory phase. In particular, MPO catalyzes substrate oxidation, generating oxidizing and halogenating agents that induce the degradation of the healthy tissue [72]. Natural compounds containing phenols can function as radical scavengers by donating hydrogen atoms from their hydroxyl groups [73], thereby alleviating inflammation [66]. MMPs are Zn-containing peptidases implicated in ECM degradation [61], [74]. Compounds containing hydroxamic groups, such as LTH and TA, have the potential to inhibit MMPs by strongly interacting with Zn(II) in their active site [61][66].

As shown in Figure 3.6, CoLig NPs displayed both, MPO and MMPs inhibitory activity, where MPO inhibition could be attributed to the increased phenolic content of Lig [53], while the inhibition of MMPs could be ascribed to the synergistic action of LTH and TA. Interestingly, the inhibitory efficacy of the NPs, with or without Co, surpassed that of Lig-TA-LTH alone. This enhancement may be attributed to the nanoscopic size of the particles and to their higher surface/volume ratio as compared to the macroscopic material, which enhanced the interactions between the material and the surrounding environment facilitating binding to the target enzyme and its degradation/inactivation [75]. The presence of cobalt reduced MMPs and MPO inhibition by NPs of around 5-10% in comparison to empty Lig NPs (Lig NPs), likely due to the interactions between Co and the phenolic groups in Lig, which resulted in reduced availability of phenol groups, diminishing their interactions with the target enzymes (Figure 3.6).

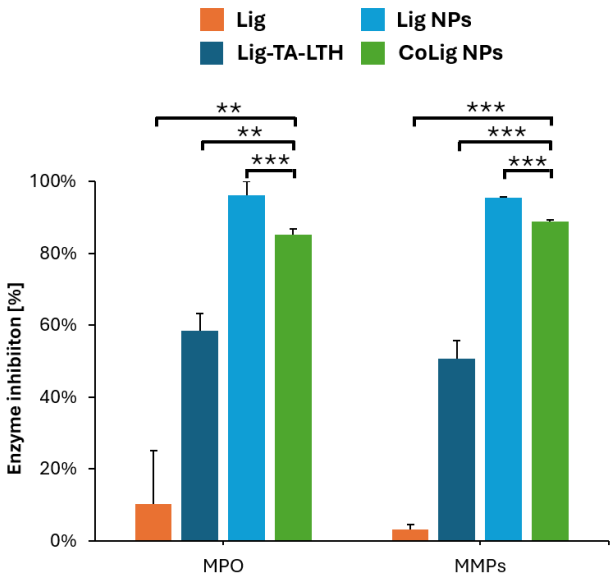


Figure 3.6. MPO and MMPs inhibitory activity of CoLig NPs compared to lignin, Lig-TA-LTH and Lig NPs.

The MMPs inhibitory activity of CoLig NPs was also confirmed using wound exudates obtained from patients (Figure 3.7). Colig NPs presented an 88% inhibitory capacity, significantly higher than the inhibitory capacity of the starting materials, lignin and Lig-TA-LTH, which inhibited nearly 40% of MMPs.

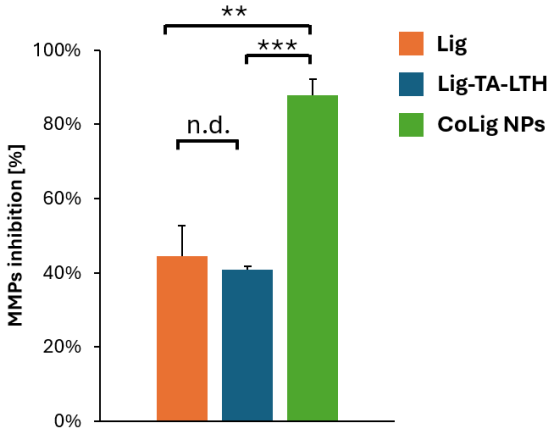


Figure 3.7. Ex vivo MMPs inhibitory activity of CoLig NPs compared to Lig and Lig-TA-LTH.

Additionally, CoLig NPs displayed a concentration-dependent antioxidant capacity, as indicated by their ROS scavenging activity (Figure 3.8), albeit lower in comparison to pristine Lig and Lig-TA-LTH. This decreased antioxidant activity of CoLig NPs in comparison to the pristine materials could again be attributed to the diminished presence of phenolic groups caused by cobalt reduction.

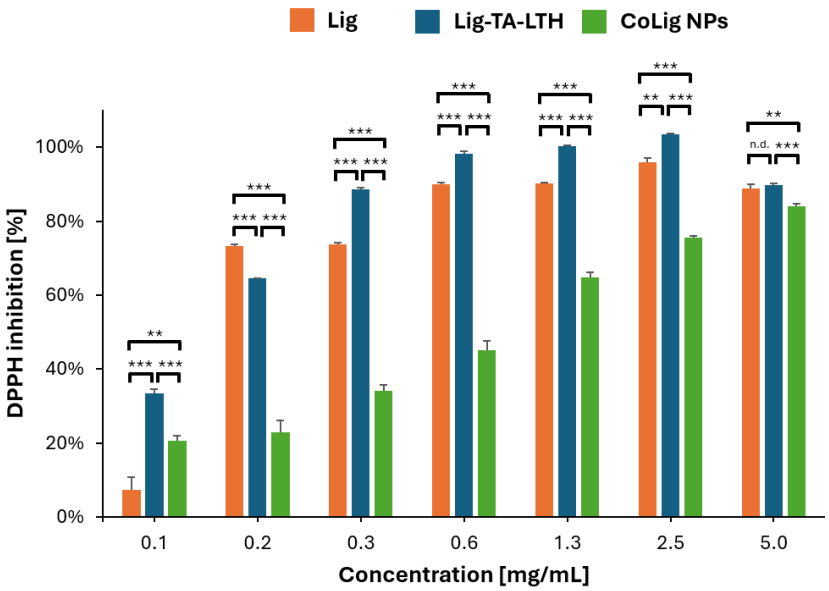


Figure 3.8. Antioxidant inhibition of CoLig NPs, Lig, and Lig-TA-LTH.

3.3.2.2. Cytocompatibility of CoLig NPs

Cell viability data (Figure 3.9) indicated that concentrations of CoLig NPs up to 0.6 mg/mL were well tolerated by both, fibroblasts (BJ-5ta) and keratinocytes (HaCaT). Indeed, cell viability exceeded 70% for both cell lines. A significant ($p < 0.001$) decrease in viability was observed for both cell lines when the treatment concentration was increased to 1.2 mg/mL (Figure 3.9). The IC_{50} values were 0.9 mg/mL and 1.1 mg/mL for HaCaT and BJ-5ta, respectively. The observed cytotoxicity primarily stems from the presence of cobalt, as Lig NPs, derived from Lig-TA-LTH without cobalt, exhibited toxicity on fibroblasts only at concentrations surpassing 2 mg/mL (Figure 3.10). Previous studies noted toxicity of cobalt ions and cobalt oxide NPs at concentrations between 5 and 25 µg/mL [76], [77]. Here CoLig NPs at the cytocompatible concentration of 0.6 mg/mL, display a cobalt content of 25 µg/mL. Notably, these results suggest that cobalt's reduction within CoLig NPs may mitigate its cytotoxicity.

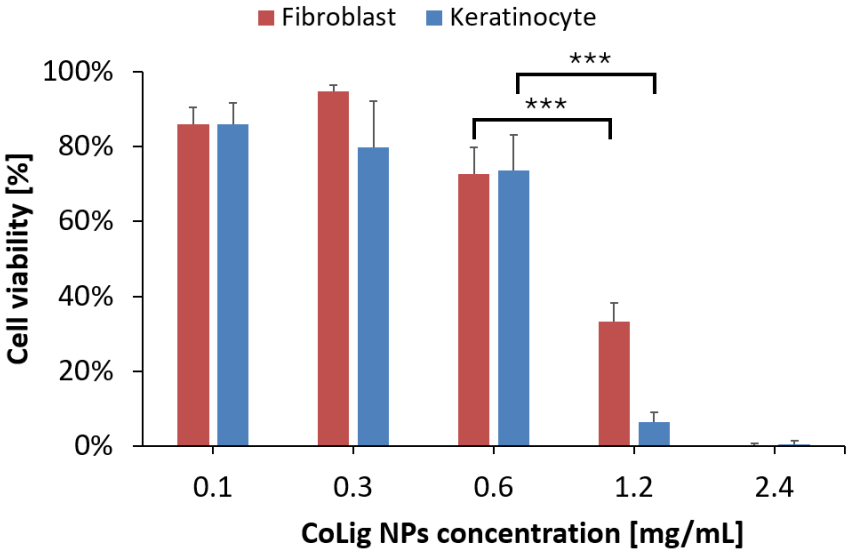


Figure 3.9. Cytocompatibility of CoLig NPs for fibroblast and keratinocytes human cell lines using AlamarBlue viability assays.

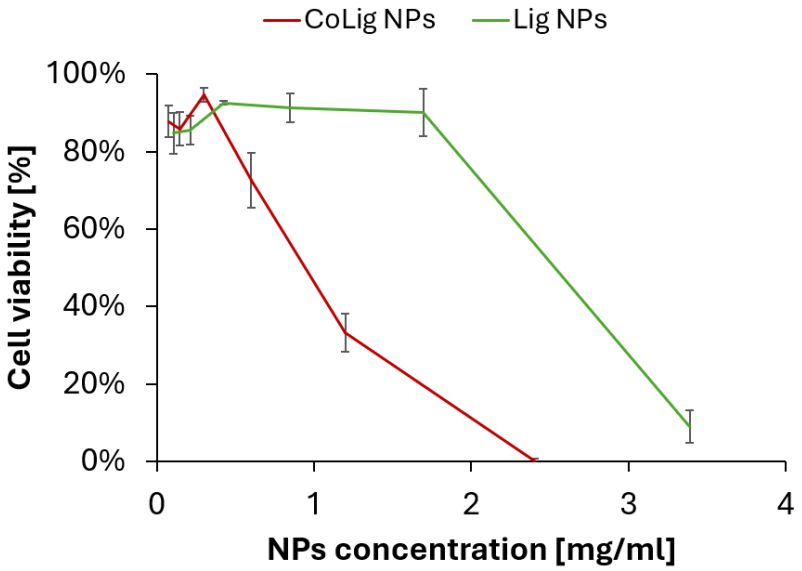


Figure 3.10. Comparing the cytocompatibility of CoLig NPs and Lig NPs for human fibroblast.

3.3.2.3. Antibacterial and antibiofilm activity of CoLig NPs

The antibacterial properties of CoLig NPs were evaluated against two prevalent pathogens in CWs: the Gram-negative *P. aeruginosa* and the Gram-positive *S. aureus* [78], [79]. MIC values were determined as 1.2 mg/mL for *S. aureus* and 2.4 mg/mL for *P. aeruginosa* (Table 3.2). Nevertheless, CoLig NPs showed inhibition of *S. aureus* above 80% also at 0.3 mg/mL and presented inhibition of *P. aeruginosa* above 60% at 1.2 mg/mL (Figure 3.11.A). In contrast, Lig NPs exhibited a MIC value of 3.3 mg/mL for both bacterial strains, suggesting that the superior antibacterial activity of CoLig NPs can be attributed to the presence of cobalt.

Table 3.2. MIC values (mg/mL) of CoLig NPs and Lig NPs for S. aureus and P. aeruginosa species.

	S. aureus	***P. aeruginosa***
CoLig NPs	1.2 mg/mL	2.4 mg/mL
Lig NPs	3.3 mg/mL	3.3 mg/mL

The difference in susceptibility between Gram-positive and Gram-negative species can be ascribed to variations in their cell wall components. CoLig NPs likely exerted their antibacterial effect by disrupting the cell membrane, a mode of action observed in prior studies analyzing the antibacterial mechanism of Lig and Lig NPs [57], [80]. SEM analysis of bacteria treated with CoLig NPs confirmed alterations in their morphology, with both *S. aureus* and *P. aeruginosa* cells displaying irregular and wrinkled surfaces, along with some depressed areas, compared to regular and smooth surfaces of untreated bacteria (Figure 3.11.B). These results support the proposed mechanism of action of CoLig NPs, based on interaction with the bacterial membrane.

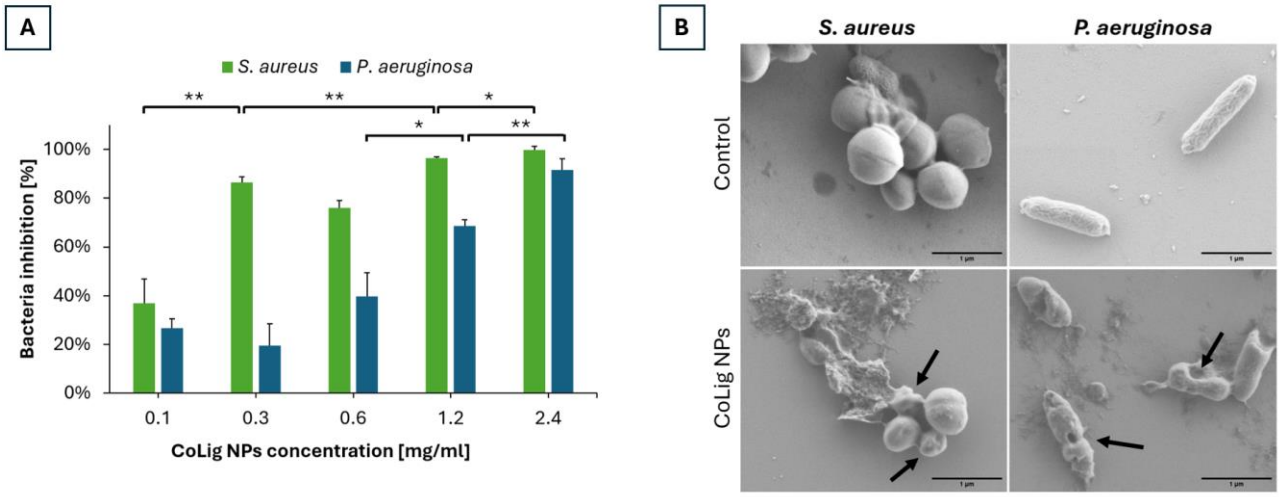


Figure 3.11. (A) Bacterial inhibition of CoLig NPs assessed using the broth dilution method and (B) SEM images of P. aeruginosa and S. aureus treated with CoLig NPs. Arrows indicate cells with damaged membranes.

Figure 3.12 compares the *S. aureus* inhibition with fibroblast viability of CoLig NPs at different concentrations. Interestingly, the CoLig NPs concentration of 0.6 mg/mL effectively inhibited S. aureus growth (with nearly 80% inhibition) while preserving fibroblast viability (above 75%). Therefore, we identified the CoLig NPs concentration of 0.6 mg/ml as the optimal concentration capable of effectively inhibiting *S. aureus* growth while maintaining cytocompatibility.

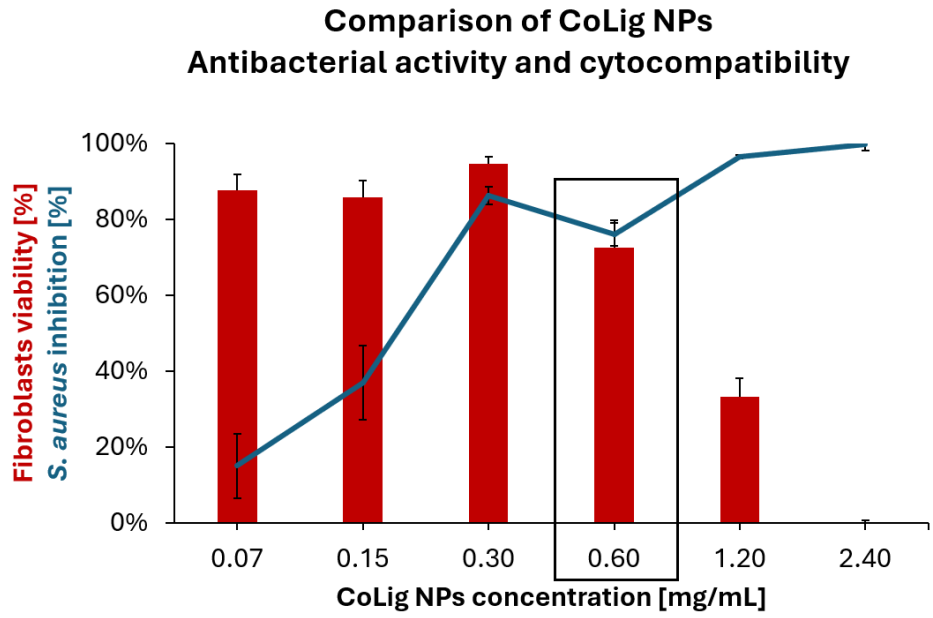


Figure 3.12. Comparison of CoLig NPs antibacterial activity for S. aureus and cytocompatibility for human fibroblast.

CoLig NPs were also tested for their ability to induce dispersion of preformed *S. aureus* and *P. aeruginosa* biofilms. However, at the concentrations tested an increase in biofilm biomass was observed compared to untreated biofilms, even though this difference was significant only for *S. aureus* when comparing the maximal concentration with the control (Figure 3.13). These results indicated that, albeit possessing good antibacterial properties, CoLig NPs do not possess the ability to act against bacteria in biofilms. On the contrary, they may stimulate biofilm deposition, possibly thanks to the presence of the natural origin lignin-based material. This could pose a problem for

the treatment of wounds in which a biofilm is already established since the antibacterial activity of CoLig NPs could prevent biofilm formation, but not eradicate preformed biofilms.

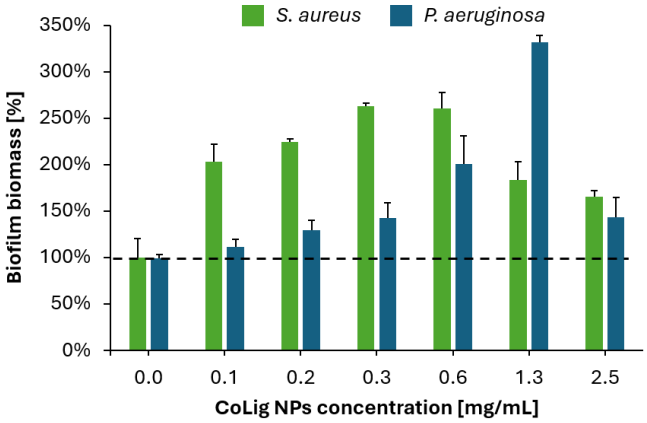


Figure 3.13. Antibiofilm activity of CoLig NPs against S. aureus (green) and P. aeruginosa (blue). The dotted line indicates 100% of biofilm biomass corresponding to the control.

3.3.3. SM-gel loaded with CoLig NPs

The CoLig NPs were incorporated at a concentration of 2.5 mg/mL into the SM-gel developed in Section 2 (3% w/v PEUs concentration, CHP407:SHF68 weight ratio of 80:20, and 10% w/v α-CDs). The integration of CoLig NPs yielded a uniformly distributed hydrogel with a brown color, attributed to the presence of the CoLig-NPs (Figure 3.14).

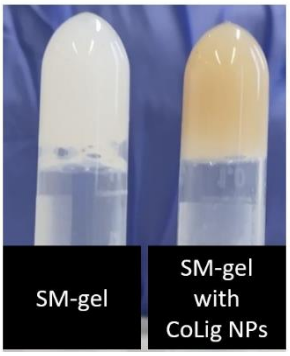


Figure 3.14. Appearance of an SM-gel as such and an SM-gel loaded with CoLig NPs

3.3.3.1. Rheological properties of SM-gel loaded with CoLig NPs

Strain sweep tests were employed to determine the linear viscoelastic region (LVE) and ascertain parameters such as the yield point (τ_y), the flow point (τ_f) and the flow transition index. The SM-gel containing NPs exhibited elevated G' and G'' values within the LVE, measuring 7152 Pa and 842 Pa, respectively, alongside increased τ_y and τ_f compared to the virgin SM-gel (Figure 3.15.A and Table 3.3). However, the flow transition index was reduced for the NPs loaded gel, indicating a tendency toward a more brittle network. Furthermore, a noticeable gel stiffening effect was observed in the presence of CoLig NPs, evidenced by the rise in G' values upon repeating the strain sweep test following a 15-minute recovery period (Figure 3.15.B and C). These findings suggest that the incorporation of NPs into the SM-gel led to system stiffening, potentially attributed to interactions between phenols on the NPs' shell and components of the SM-gel, such as α-CDs or exposed primary amines along SHF68 polymeric chains.

Table 3.3. Summary of the rheological characteristics of SM-gel with and without CoLig NPs extracted from the strain sweep test.

	τ_y (Pa)	τ_f (Pa)	Flow transition index	G'_{LVE} (Pa)	G''_{LVE} (Pa)	G'_{LVE} recovery (Pa)	G''_{LVE} recovery (Pa)	G' recovery (%)
CoLig NPs + SM-gel	17.16	161.92	9.44	7152	842	8804	1095	**123%**
SM-gel	10.67	151.25	14.18	4639	391	4008	454	**86%**

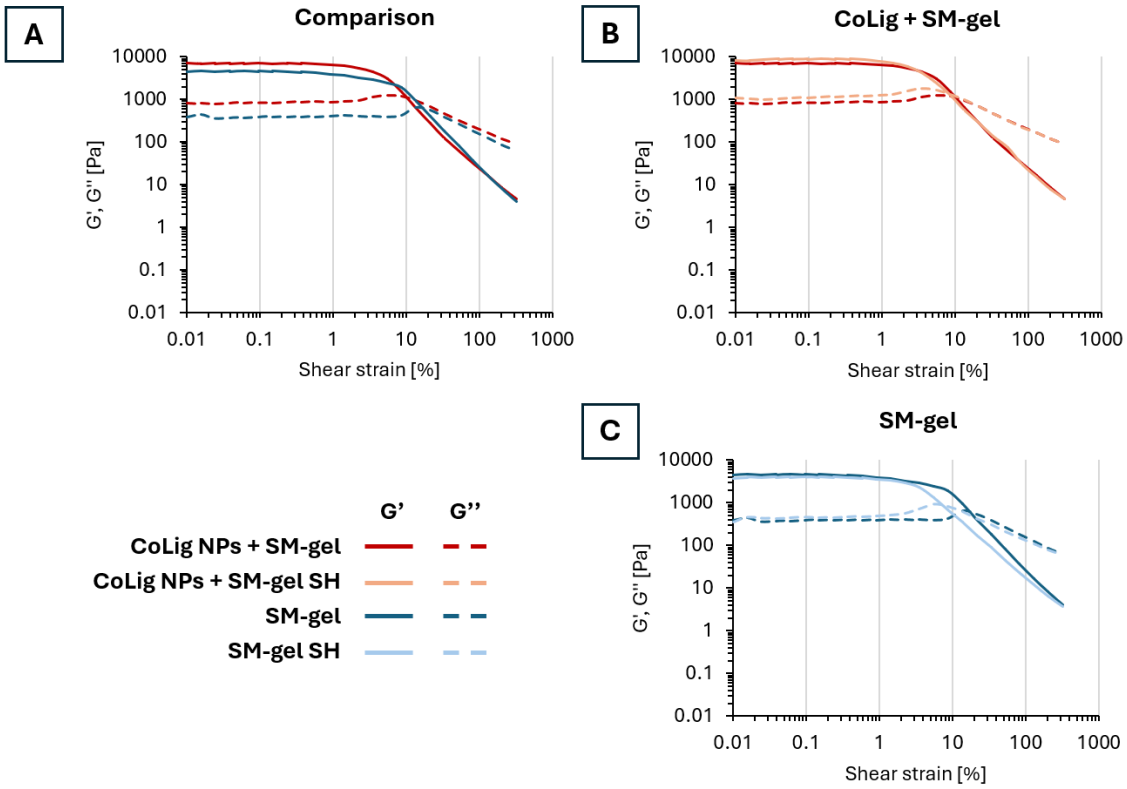


Figure 3.15. Rheological strain sweep test performed at 37 °C. (A) Trends of G' (continuous line) and G'' (dashed line) for SM-gel with (blue) and without (red) CoLig NPs (acronyms CoLig NPs + SM-gel and SM-gel, respectively). (B) Trends of G' (continuous line) and G'' (dashed line) for SM-gel with CoLig NPs before (red) and after 15 min recovery (SH) (light red) (acronyms CoLig NPs + SM-gel and CoLig NPs + SM-gel SH, respectively). (C) Trends of G' (continuous line) and G'' (dashed line) for SM-gel before (blue) and after 15 min recovery (SH) (light blue) (acronyms SM-gel and SM-gel SH, respectively).

Frequency sweep tests were conducted to assess the extent of SM-gel development. Both the SM-gel and CoLig NPs + SM-gel formulations exhibited the characteristics of a fully developed gel, with slight temperature dependency (Figure 3.16). Across all the tested frequencies, the storage modulus G' was greater than G'', and independent of angular frequency. The SM-gel incorporating CoLig NPs demonstrated enhanced mechanical properties, evidenced by a G' value of 5659 Pa at 1 rad/s, compared to 4308 Pa for the virgin SM-gel (Table 3.4), thereby corroborating previous findings from the strain sweep tests.

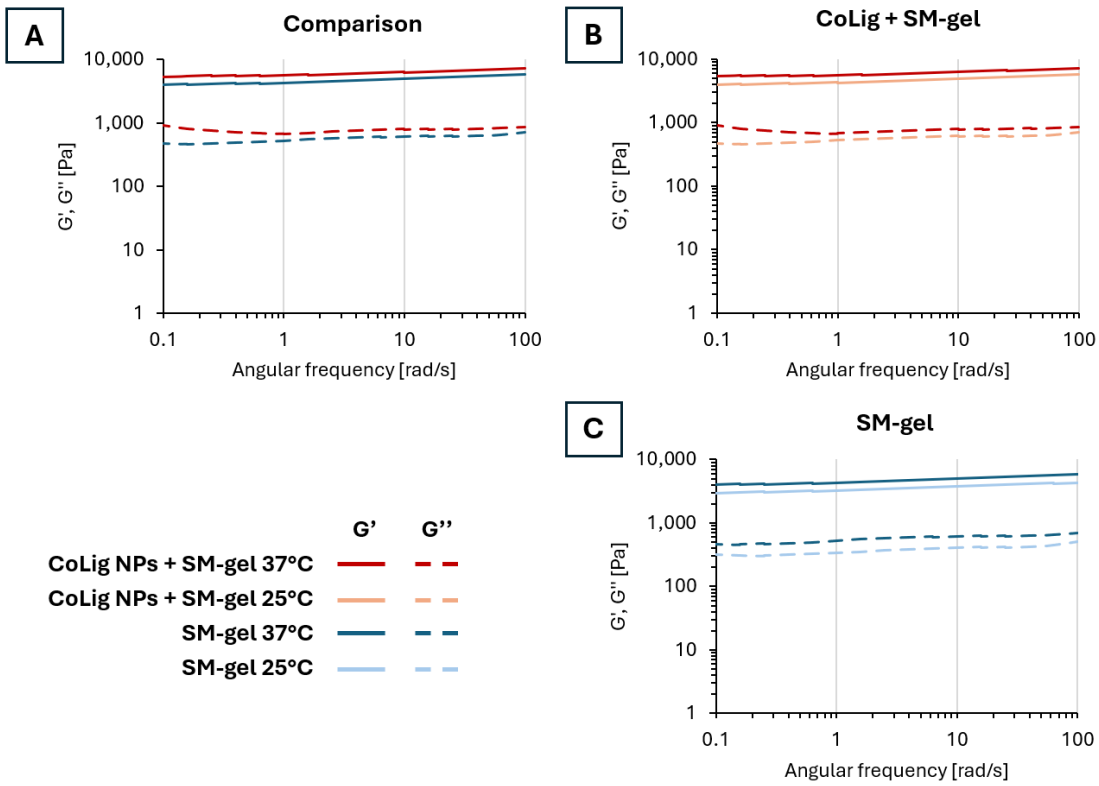


Figure 3.16. Rheological frequency sweep tests at 25 and 37 °C. (A) Trends of G' (continuous line) and G'' (dashed line) for SM-gel at 37 °C with (blue) and without (red) CoLig NPs (acronyms CoLig NPs + SM-gel 37°C and SM-gel 37°C, respectively). (B) Trends of G' (continuous line) and G'' (dashed line) for CoLig NPs + SM-gel at 37 °C (red) and 25 °C (light red). (C) Trends of G' (continuous line) and G'' (dashed line) for SM-gel at 37 °C (blue) and 25 °C (light blue).

Table 3.4. Summary of the rheological characteristics extracted from the frequency sweep test performed on SM-gel and CoLig NPs + SM-gel.

	G' at 1 rad/s 25°C (Pa)	G' at 1 rad/s 37°C (Pa)
CoLig NPs + SM-gel	4308	5659
SM-gel	3272	4308

Finally, shear tests were conducted to evaluate the self-healing capability of CoLig NPs + SM-gel during the application of rapid rupture cycles. Interestingly, the presence of CoLig NPs did not affect the self-healing capacity of the hydrogel, as already highlighted in strain sweep tests (Figure 3.17). Specifically, the percentages of G' recovery after three rupture cycles were 87% and 89% for SM-gel and CoLig NPs + SM-gel, respectively. Conversely, strain sweep tests evidenced a recovery of 86% and 123% for the virgin and the NPs loaded formulation, respectively. This disparity between the two tests may be attributed to the distinct conditions of rupture and recovery experienced by the samples. In the strain sweep test, the hydrogel had a longer recovery period (15 minutes), potentially allowing for a better network reorganization, which may not be feasible in the shorter recovery steps (2 minutes) of the shear test.

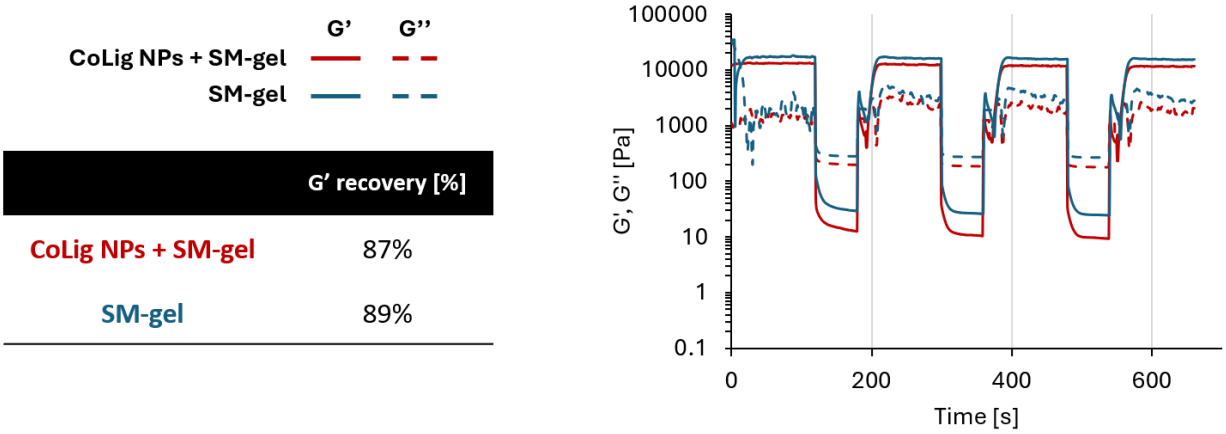


Figure 3.17. Rheological strain test performed at 37 °C. Trends of G' (continuous line) and G'' (dashed line) for CoLig NPs + SM-gel (red) and SM-gel (blue).

3.3.3.2. Stability of SM-gel loaded with CoLig NPs

The stability of the SM-gel loaded with CoLig NPs was assessed to investigate differences compared to the empty SM-gel. In agreement with the findings from Section 2, the CoLig NPs + SM-gel hydrogel exhibited minimal variation in wet weight in the first 24h of the test, while at 48 h it lost its integrity and only some residues were observed in the SM-gel loaded with CoLig NPs (Figure 3.18.A). Meanwhile, the dry weight progressively decreased in the first 24 h and at 48 h some residual material could be measured for the loaded SM-gel (Figure 3.18.B). This suggests that the formulation was undergoing material exchange with the surrounding medium, but it managed to maintain a stable network although a significant portion of polymeric and αCD content was released. The incorporation of CoLig NPs slightly improved the long-term stability of the formulation, which still presented some residues at 48 h. The enhanced properties observed in this test lend further support to the hypothesis proposed to explain the results of the rheological tests. Indeed, the simultaneous presence of various interactions between CoLig NPs and hydrogel components could fortify the gel network. Electrostatic interactions may occur between the highly reactive phenolic groups on the CoLig NPs and the primary amines exposed by SHF68 in the SM-gel. Additionally, α-CDs are known to form inclusion complexes with phenols [81], suggesting that free α-CDs within the SM-gel could aid in crosslinking with CoLig NPs. Lastly, interactions between aromatic groups on the CoLig NPs may also contribute to the formation of the gel network [82].

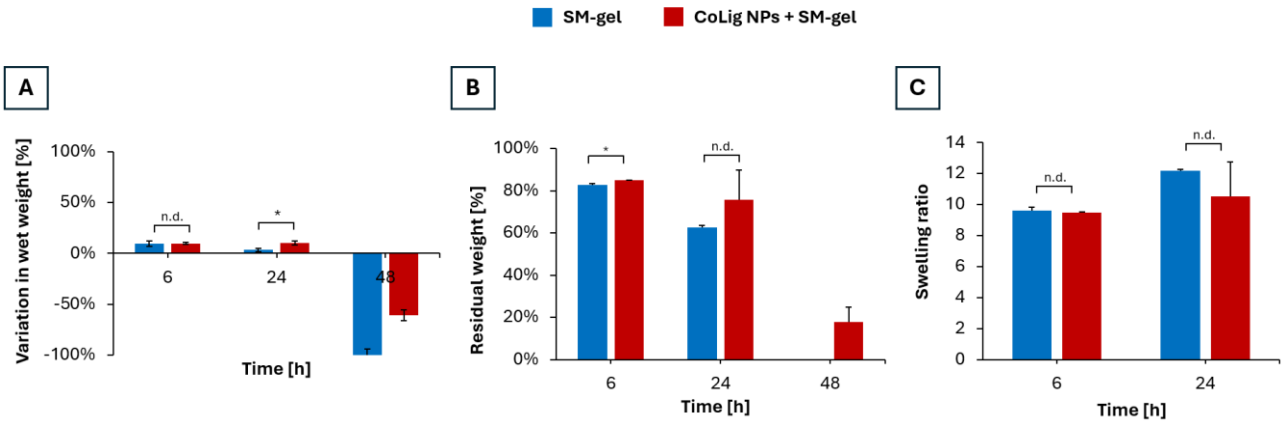


Figure 3.18. Stability of SM-Gel (blue) and CoLig NPs + SM-gel (red). (A) Dry weight loss, (B) PBS uptake and (C) swelling ratio at the different time point.

To investigate more in detail the nature of the interactions between CoLig NPs and the hydrogel components, cryoSEM and ATR-FTIR analyses were performed.

CryoSEM, a technique necessitating samples to be frozen at cryogenic temperatures and imaged under high vacuum, mitigates damage associated with drying and is commonly used to examine delicate samples like hydrogels [83], [84]. In the presence of CoLig NPs, a more branched structure was observed compared to the virgin SM-gel sample (Figure 3.19), corroborating the hypothesis of an enhanced crosslinking within the CoLig NPs + SM-gel network compared to the SM-gel as such. This increase of crosslinking was quantified by counting the number of branches which increased from 4579 in SM-gel to 5376 in SM-gel with CoLig NPs (Figure 3.19.B).

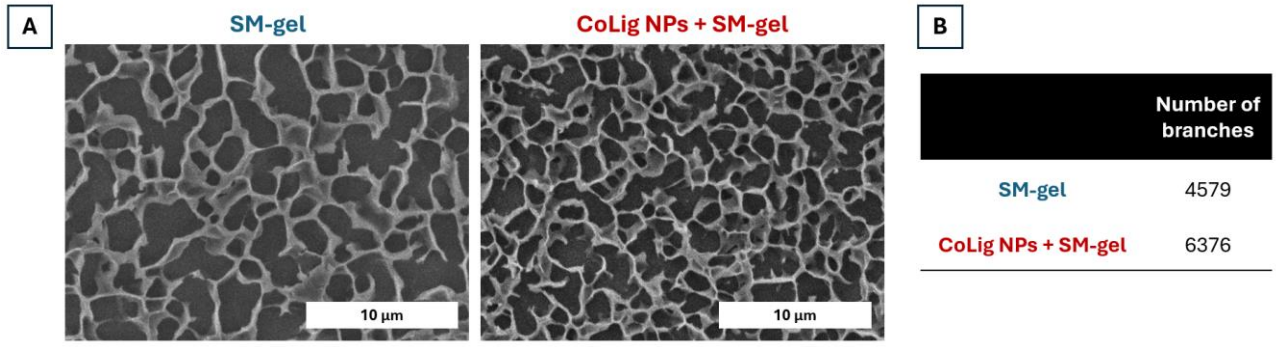


Figure 3.19. (A) CryoSEM images of SM-gel and CoLig NPs + SM-gel. (B) number of branches counted on CryoSEM images using the Skeleton tool of ImageJ.

As previously hypothesized, CoLig NPs + SM-gel higher crosslinking can be due to the occurrence of non-covalent interactions between CoLig NPs and hydrogel components. To investigate the nature of this crosslinking and assess the effective occurrence of the hypothesized interactions, CoLig NPs and SHF68 or CoLig NPs and αCDs were mixed and left to interact overnight at 37 °C. Subsequently, the samples (SHF68 + CoLig NPs and CDs + CoLig NPs) were analyzed using ATR-FTIR spectroscopy. SHF68, αCDs and CoLig NPs were also analyzed as references (Figure 3.20 and Figure 3.21). The interaction of CoLig NPs and CHP407 was not investigated since CHP407 does not present pending side chains and thus should not interact with the NPs.

The spectra of the SHF68 + CoLig NPs mixture revealed distinct features. A peak at 1590 cm^{-1}, associated to the stretching of the benzene ring of the phenolated NPs, and another at 1720 cm^{-1}, linked to the C=O stretching of the urethane bonds of SHF68, were observed. Interestingly, there was a notable shift in the broad peak around 3400 cm^{-1} from 3320 cm^{-1} to 3360 cm^{-1}. The shift in this band relative to the stretching of the -OH bond on the aromatic ring, suggests potential interactions between the phenolic groups on CoLig NPs and the polymer (Figure 3.20).

On the other hand, interactions between CoLig NPs and α-CDs were also confirmed. In the CDs + CoLig NPs mixture, a peak at 1640 cm^{-1} and a peak at 2920 cm^{-1} were observed. These peaks correspond to H-O-H deformation bands of water present in α-CDs and to the stretching of C-H bonds in α-CDs and Lig, respectively. The disappearance of the peak at 1590 cm^{-1} (Figure 3.21), associated to the stretching vibration of the benzene ring in NPs, suggests the formation of host-guest interactions with between CoLig NPs and α-CDs[85].

Taken together, these results suggest that CoLig NPs in the SM-gel interacted with both free α-CDs and SHF68.

Wavenumber [cm^{-1}]	Bond type
1590	stretching of the benzene ring
1720	C=O stretching of the polyurethane bond
3400	stretching of the O-H bond on the aromatic ring

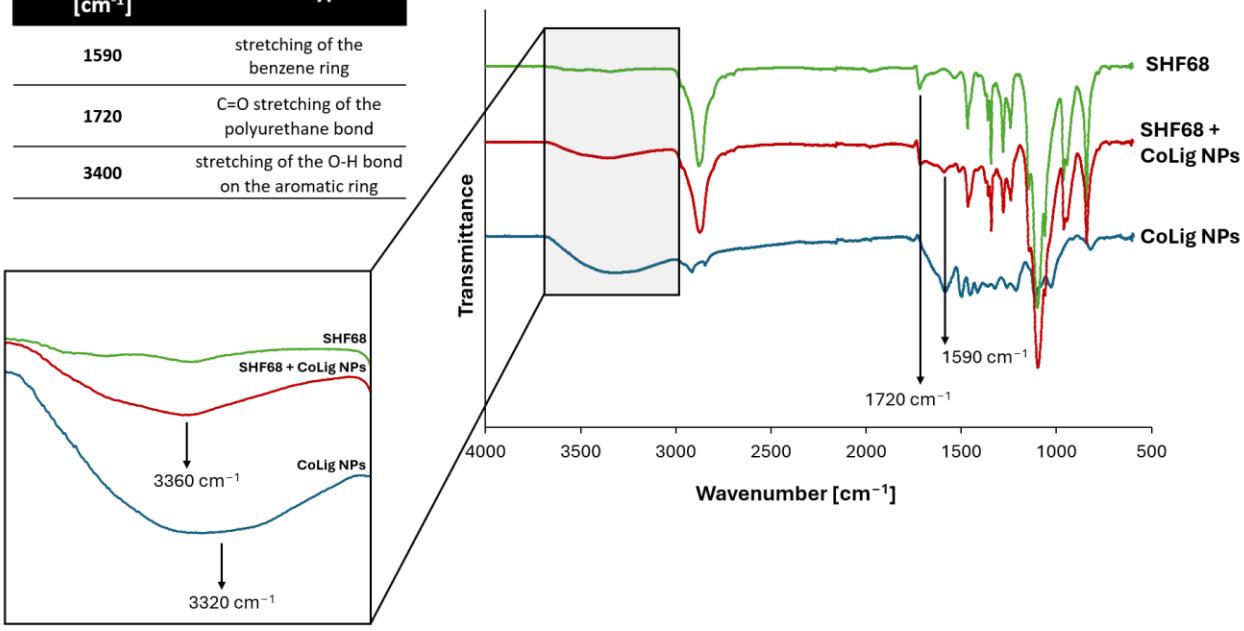


Figure 3.20. ATR-FTIR spectra of SHF68 (green), CoLig NPs (blue) and their mixture SHF68 + CoLig NPs (red).

Wavenumber [cm^{-1}]	Bond type
1590	stretching of the benzene ring
1640	H–O–H deformation bands of water
2840-2920	C-H stretching

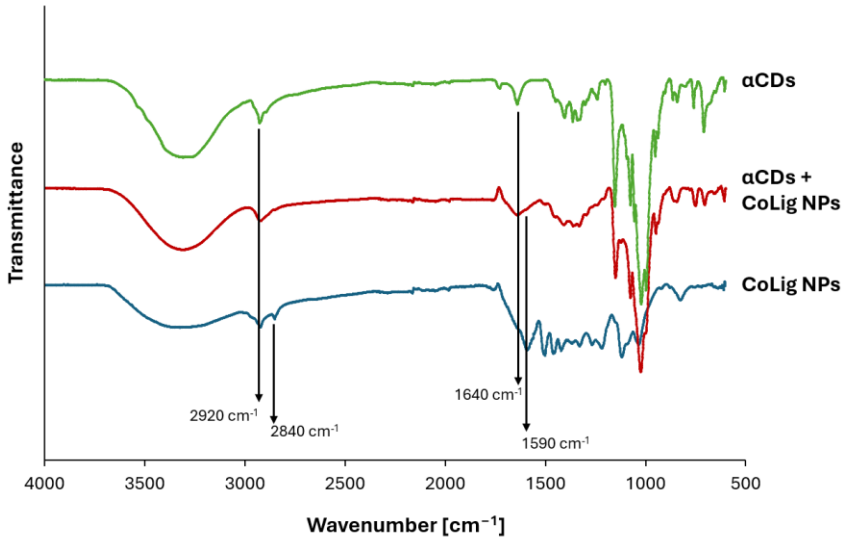


Figure 3.21. ATR-FTIR spectra of αCDs (green), CoLig NPs (blue) and their mixture αCDs + CoLig NPs (red).

3.3.3.3. Release of CoLig NPs from SM-gel

NPs release from the gel was assessed by determining both, Co release by ICP and Lig release by fluorescence spectroscopy. The two methods provided a similar release pattern for Co and Lig, indicating that CoLig NPs are released from the gel in a controlled fashion without losing their integrity (Figure 3.22). CoLig NPs displayed a linear release pattern up to 24 hours, with a release rate of *ca.* 7 µg CoLig NPs per hour, which then increased to 40 µg CoLig NPs per hour between 24 and 48 h (Figure 3.22). This release pattern mirrored the dissolution behavior of the SM-gel observed in stability tests (Figure 3.18), suggesting that cargo release from the gel is driven by the gel's gradual dissolution. The Korsmeyer–Peppas model, describing drug release from polymeric systems, confirmed these results. The release exponents (n), obtained after fitting the results of the first 24 h of the release test, were 0.6 for the Co release curve (green line in Figure 3.22) and

0.87 for the Lig release curve (orange line in figure Figure 3.22). These data indicate that the release occurred according to a non-Fickian mode of transport, combining diffusion and matrix erosion effects [67], [68]. The obtained n values indicate a zero-order release kinetic (n = 0.89), which represents a consistent release rate with a reduced burst effect. At 24 hours, approximately 17% of the payload was released, equivalent to 0.2 mg of CoLig NPs (8 µg of Co), a cytocompatible amount [76], [77]. Nevertheless, further tests are required to confirm the biocompatibility of the released materials.

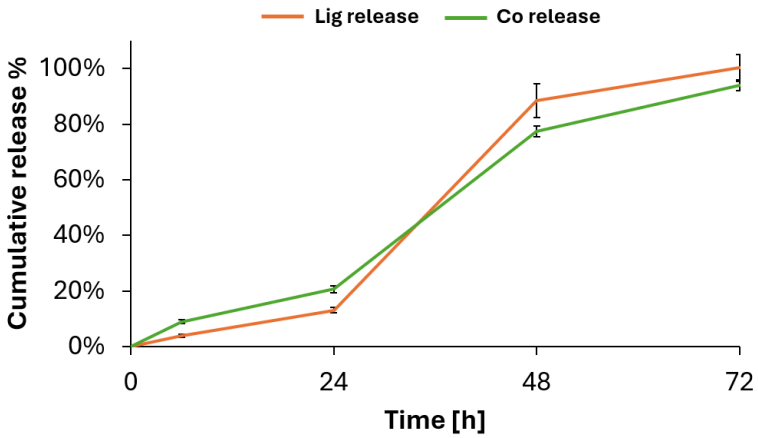


Figure 3.22. Cumulant release of Lig (orange line) and Co (green line) from CoLig NPs + SM-gels samples. Lig and Co were quantified through fluorescence spectroscopy and ICP, respectively.

3.3.3.4. Cytocompatibility of SM-gel loaded with CoLig NPs

The biocompatibility of the CoLig NPs + SM-gel formulation was assessed according to the ISO 10993:5 guidelines with fibroblasts (BJ-5ta) and keratinocytes (HaCaT). Cell viability exceeding 70% was observed on both cell lines treated with the eluates collected from SM-gel and CoLig NPs + SM-gel samples (Figure 3.23.A). This behavior was confirmed by the Live/Dead assay results (Figure 3.23.B), further corroborating the biocompatibility of the system.

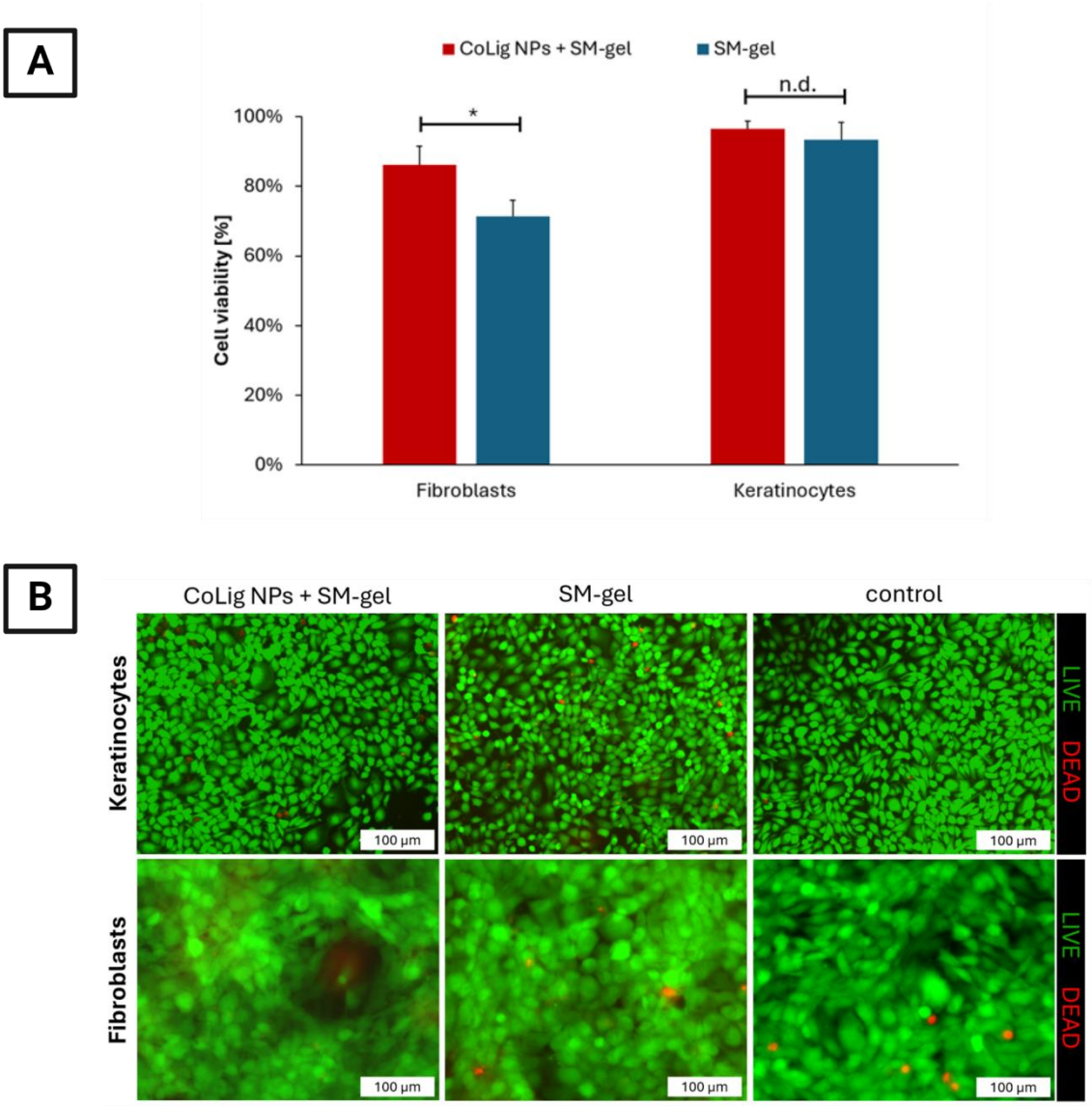


Figure 3.23. (A) Cytocompatibility of CoLig NPs + SM-gel (red) and SM-gel (blue). (B) Live/Dead staining of fibroblasts and keratinocytes treated with the eluates collected from CoLig NPs + SM-gel and the virgin SM-gel samples.

3.3.3.5. Antioxidant capacity of the CoLig NPs released from the SM-gel

As shown in Figure 3.24, the virgin SM-gel exhibited any ROS scavenging activity confirming the hydrogel material does not possess an intrinsic antioxidant capacity. On the other hand, the released NPs from the SM-gel loaded with CoLig NPs showed evident antioxidant properties, with ROS scavenging ability of nearly 40% in the first 24 h, which increased to 80% at 48 hours. This ROS scavenging activity correlated directly with the release of NPs from the SM-gel, which was low in the initial 24 hours and increased as the hydrogel gradually dissolved.

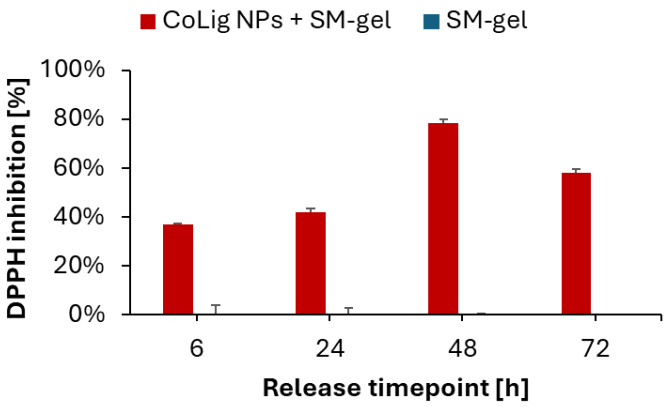


Figure 3.24. Antioxidant activity of the CoLig NPs released from the SM-gel.

3.3.3.6. Antibacterial activity of the CoLig NPs released from the SM-gel

The release solutions collected after 24 hours from CoLig NPs + SM-gel formulations were used to treat *S. aureus* and *P. aeruginosa*. In both cases, the released materials induced alterations in the bacterial surface (Figure 3.25), confirming the previously observed mechanism of action involving the interaction of Co with the bacterial membranes. Interestingly, the release medium collected from the empty SM-gel also induced partial surface modifications, likely due to the amphiphilic nature of the poly(urethane)s, as suggested in previous studies [86].

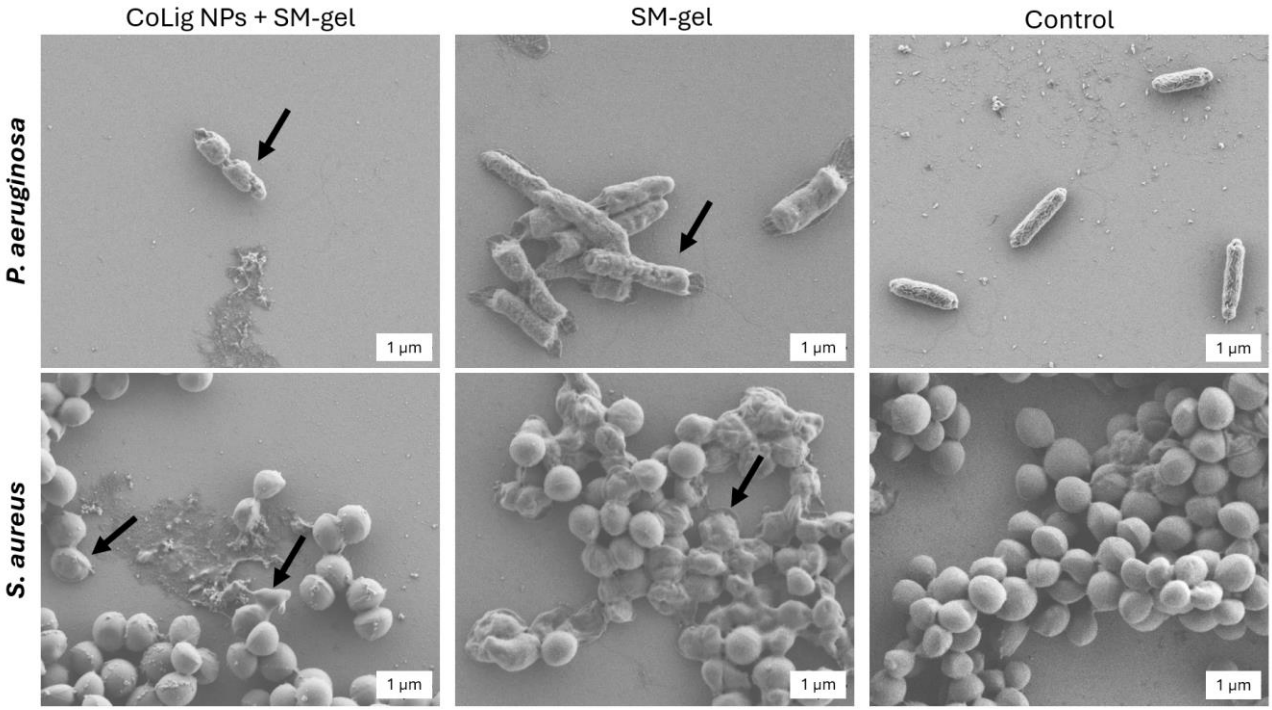


Figure 3.25. SEM images of bacteria treated with the release solutions collected from CoLig NPs + SM-gel and SM-gel samples after 24 h of incubation. Bacteria cultured under normal conditions were used as control. Black arrows indicate cells with damaged membranes.

3.4. Conclusions

CoLig NPs were successfully synthesized and integrated into the SM-gel developed in Section 2. CoLig NPs exhibited monodisperse characteristics, colloidal stability, and significant inhibitory efficacy against MPO and MMPs, as well as a remarkable ROS scavenging activity. CoLig NPs also demonstrated antibacterial activity against Gram-negative and Gram-positive bacteria commonly

found in CWs and cytocompatibility in *in vitro* tests on human skin cell lines at antibacterial concentrations. The integration of CoLig NPs into the SM-gel (CoLig NPs + SM-gel) resulted in a hybrid hydrogel with enhanced mechanical properties and stability, in comparison to the un-loaded gel. Controlled release of CoLig NPs from the hydrogel was achieved, with linear kinetics and sustained release without burst effect. The released NPs maintained their antioxidant and antibacterial activity, suggesting the therapeutic potential of the CoLig NP-loaded hydrogel for CWs treatment.

Nevertheless, the developed CoLig NPs did not exhibit the ability to disperse preformed biofilms, which represents an unsolved issue in CWs [87]. Thus, to respond to the need for therapies that induce biofilm dispersion and destruction, section 4 will explore potential modifications to the CoLig NPs to incorporate this capability.

Another aspect highlighted by the results presented in Section 2 and Section 3 is the lack of intrinsic therapeutic potential in the hydrogel component. Indeed, the outlined antibacterial and anti-inflammatory features are solely provided by the CoLig NPs. However, the gradual release of NPs from the SM-gel, results in limited antioxidant activity in the initial 24 hours, due to the low amount of CoLig NPs released. Therefore, an active hydrogel component with intrinsic antioxidant ability could improve the therapeutic performance of the system by offering ROS scavenging capacity from the early stages of gel implant.

Additionally, while NPs incorporation seemed to stabilize the hydrogel network and to improve the mechanical properties of the composite system, the SM-gel loaded with CoLig NPs remained intact only for the first day, losing its structural integrity at 48 h. This result matches the requirements of moderately to highly exudative wounds, such as infected CWs, where dressings are typically changed every 24-48 hours [88]. Nevertheless, extending the durability of the SM-gel beyond 48 h could reduce the frequency of dressing changes, making the system more appealing. Therefore, Section 5 will explore the possibility of enhancing the stability and durability of the SM-gel, while also providing it with intrinsic antioxidant properties.

3.5. References

[1] I. Khan, K. Saeed, and I. Khan, 'Nanoparticles: Properties, applications and toxicities', *Arabian Journal of Chemistry*, vol. 12, no. 7, pp. 908–931, Nov. 2019, doi: 10.1016/j.arabjc.2017.05.011.

[2] K. McNamara and S. A. M. Tofail, 'Nanoparticles in biomedical applications', *Advances in Physics: X*, vol. 2, no. 1, pp. 54–88, Jan. 2017, doi: 10.1080/23746149.2016.1254570.

[3] N. K. Rajendran, S. S. D. Kumar, N. N. Houreld, and H. Abrahamse, 'A review on nanoparticle based treatment for wound healing', *Journal of Drug Delivery Science and Technology*, vol. 44, pp. 421–430, Apr. 2018, doi: 10.1016/j.jddst.2018.01.009.

[4] H. S. Sofi, T. Akram, A. H. Tamboli, A. Majeed, N. Shabir, and F. A. Sheikh, 'Novel lavender oil and silver nanoparticles simultaneously loaded onto polyurethane nanofibers for wound-healing applications', *International Journal of Pharmaceutics*, vol. 569, p. 118590, Oct. 2019, doi: 10.1016/j.ijpharm.2019.118590.

[5] H. Nurhasni *et al.*, 'Nitric oxide-releasing poly(lactic-co-glycolic acid)-polyethylenimine nanoparticles for prolonged nitric oxide release, antibacterial efficacy, and in vivo wound healing activity', *Int J Nanomedicine*, vol. 10, pp. 3065–3080, Apr. 2015, doi: 10.2147/IJN.S82199.

[6] J. Xiao *et al.*, 'Copper Metal–Organic Framework Nanoparticles Stabilized with Folic Acid Improve Wound Healing in Diabetes', *ACS Nano*, vol. 12, no. 2, pp. 1023–1032, Feb. 2018, doi: 10.1021/acsnano.7b01850.

[7] G. Gainza *et al.*, 'A novel strategy for the treatment of chronic wounds based on the topical administration of rhEGF-loaded lipid nanoparticles: *In vitro* bioactivity and *in vivo* effectiveness in healing-impaired *db*/*db* mice', *Journal of Controlled Release*, vol. 185, pp. 51–61, Jul. 2014, doi: 10.1016/j.jconrel.2014.04.032.

[8] F. Saporito *et al.*, 'Essential oil-loaded lipid nanoparticles for wound healing', *International Journal of Nanomedicine*, vol. 13, pp. 175–186, Dec. 2018, doi: 10.2147/IJN.S152529.

[9] N. Li *et al.*, 'Tannic Acid Cross-linked Polysaccharide-Based Multifunctional Hemostatic Microparticles for the Regulation of Rapid Wound Healing', *Macromolecular Bioscience*, vol. 18, no. 11, p. 1800209, 2018, doi: 10.1002/mabi.201800209.

[10] K. Khezri, M. R. Farahpour, and S. Mounesi Rad, 'Accelerated infected wound healing by topical application of encapsulated Rosemary essential oil into nanostructured lipid carriers', *Artificial Cells, Nanomedicine, and Biotechnology*, vol. 47, no. 1, pp. 980–988, Dec. 2019, doi: 10.1080/21691401.2019.1582539.

[11] T. Bruna, F. Maldonado-Bravo, P. Jara, and N. Caro, 'Silver Nanoparticles and Their Antibacterial Applications', *International Journal of Molecular Sciences*, vol. 22, no. 13, Art. no. 13, Jan. 2021, doi: 10.3390/ijms22137202.

[12] S. Tang and J. Zheng, 'Antibacterial Activity of Silver Nanoparticles: Structural Effects', *Advanced Healthcare Materials*, vol. 7, no. 13, p. 1701503, 2018, doi: 10.1002/adhm.201701503.

[13] A. Gupta *et al.*, 'Synthesis of Silver Nanoparticles Using Curcumin-Cyclodextrins Loaded into Bacterial Cellulose-Based Hydrogels for Wound Dressing Applications', *Biomacromolecules*, vol. 21, no. 5, pp. 1802–1811, May 2020, doi: 10.1021/acs.biomac.9b01724.

[14] P. Orlowski *et al.*, 'Tannic acid-modified silver nanoparticles for wound healing: the importance of size', *International Journal of Nanomedicine*, vol. 13, pp. 991–1007, Feb. 2018, doi: 10.2147/IJN.S154797.

[15] J. Salvo and C. Sandoval, 'Role of copper nanoparticles in wound healing for chronic wounds: literature review', *Burns & Trauma*, vol. 10, p. tkab047, Jan. 2022, doi: 10.1093/burnst/tkab047.
[16] T. E. Paterson *et al.*, 'Multifunctional Copper-Containing Mesoporous Glass Nanoparticles as Antibacterial and Proangiogenic Agents for Chronic Wounds', *Front. Bioeng. Biotechnol.*, vol. 8, p. 246, Mar. 2020, doi: 10.3389/fbioe.2020.00246.
[17] C. T. Anuradha and P. Raji, 'Effect of annealing temperature on antibacterial, antifungal and structural properties of bio-synthesized Co3O4 nanoparticles using Hibiscus Rosa-sinensis', *Mater. Res. Express*, vol. 6, no. 9, p. 095063, Jul. 2019, doi: 10.1088/2053-1591/ab2f9e.
[18] W. Anupong *et al.*, 'Cobalt nanoparticles synthesizing potential of orange peel aqueous extract and their antimicrobial and antioxidant activity', *Environmental Research*, vol. 216, p. 114594, Jan. 2023, doi: 10.1016/j.envres.2022.114594.
[19] L. O. Simonsen, H. Harbak, and P. Bennekou, 'Cobalt metabolism and toxicology—A brief update', *Science of The Total Environment*, vol. 432, pp. 210–215, Aug. 2012, doi: 10.1016/j.scitotenv.2012.06.009.
[20] S. Iravani and R. S. Varma, 'Sustainable synthesis of cobalt and cobalt oxide nanoparticles and their catalytic and biomedical applications', *Green Chemistry*, vol. 22, no. 9, pp. 2643–2661, 2020, doi: 10.1039/D0GC00885K.
[21] E. Papis *et al.*, 'Engineered cobalt oxide nanoparticles readily enter cells', *Toxicology Letters*, vol. 189, no. 3, pp. 253–259, Sep. 2009, doi: 10.1016/j.toxlet.2009.06.851.
[22] A. Petit, F. Mwale, C. Tkaczyk, J. Antoniou, D. J. Zukor, and O. L. Huk, 'Induction of protein oxidation by cobalt and chromium ions in human U937 macrophages', *Biomaterials*, vol. 26, no. 21, pp. 4416–4422, Jul. 2005, doi: 10.1016/j.biomaterials.2004.11.019.
[23] E. Lester, G. Aksomaityte, J. Li, S. Gomez, J. Gonzalez-Gonzalez, and M. Poliakoff, 'Controlled continuous hydrothermal synthesis of cobalt oxide (Co3O4) nanoparticles', *Progress in Crystal Growth and Characterization of Materials*, vol. 58, no. 1, pp. 3–13, Mar. 2012, doi: 10.1016/j.pcrysgrow.2011.10.008.
[24] J. D. Blakemore, H. B. Gray, J. R. Winkler, and A. M. Müller, 'Co3O4 Nanoparticle Water-Oxidation Catalysts Made by Pulsed-Laser Ablation in Liquids', *ACS Catal.*, vol. 3, no. 11, pp. 2497–2500, Nov. 2013, doi: 10.1021/cs400639b.
[25] J. Deng *et al.*, 'Solution combustion synthesis of cobalt oxides (Co3O4 and Co3O4/CoO) nanoparticles as supercapacitor electrode materials', *Electrochimica Acta*, vol. 132, pp. 127–135, Jun. 2014, doi: 10.1016/j.electacta.2014.03.158.
[26] T. He, D. Chen, X. Jiao, Y. Xu, and Y. Gu, 'Surfactant-Assisted Solvothermal Synthesis of Co3O4 Hollow Spheres with Oriented-Aggregation Nanostructures and Tunable Particle Size', *Langmuir*, vol. 20, no. 19, pp. 8404–8408, Sep. 2004, doi: 10.1021/la0488710.
[27] A. T. Khalil, M. Ovais, I. Ullah, M. Ali, Z. K. Shinwari, and M. Maaza, 'Physical properties, biological applications and biocompatibility studies on biosynthesized single phase cobalt oxide (Co3O4) nanoparticles via *Sageretia thea* (Osbeck.)', *Arabian Journal of Chemistry*, vol. 13, no. 1, pp. 606–619, Jan. 2020, doi: 10.1016/j.arabjc.2017.07.004.
[28] G. J. Gil-Chávez, S. S. P. Padhi, C. V. Pereira, J. N. Guerreiro, A. A. Matias, and I. Smirnova, 'Cytotoxicity and biological capacity of sulfur-free lignins obtained in novel biorefining process', *International Journal of Biological Macromolecules*, vol. 136, pp. 697–703, Sep. 2019, doi: 10.1016/j.ijbiomac.2019.06.021.
[29] L. Zheng *et al.*, 'Understanding the relationship between the structural properties of lignin and their biological activities', *International Journal of Biological Macromolecules*, vol. 190, pp. 291–300, Nov. 2021, doi: 10.1016/j.ijbiomac.2021.08.168.

[30] A. Barapatre, A. S. Meena, S. Mekala, A. Das, and H. Jha, 'In vitro evaluation of antioxidant and cytotoxic activities of lignin fractions extracted from Acacia nilotica', *International Journal of Biological Macromolecules*, vol. 86, pp. 443–453, May 2016, doi: 10.1016/j.ijbiomac.2016.01.109.

[31] S. Sugiarto, Y. Leow, C. L. Tan, G. Wang, and D. Kai, 'How far is Lignin from being a biomedical material?', *Bioactive Materials*, vol. 8, pp. 71–94, Feb. 2022, doi: 10.1016/j.bioactmat.2021.06.023.

[32] M. P. Vinardell and M. Mitjans, 'Lignins and Their Derivatives with Beneficial Effects on Human Health', *International Journal of Molecular Sciences*, vol. 18, no. 6, Art. no. 6, Jun. 2017, doi: 10.3390/ijms18061219.

[33] Y. Zhang *et al.*, 'Novel lignin–chitosan–PVA composite hydrogel for wound dressing', *Materials Science and Engineering: C*, vol. 104, p. 110002, Nov. 2019, doi: 10.1016/j.msec.2019.110002.

[34] D. Mahata *et al.*, 'Lignin-graft-Polyoxazoline Conjugated Triazole a Novel Anti-Infective Ointment to Control Persistent Inflammation', *Sci Rep*, vol. 7, no. 1, p. 46412, Apr. 2017, doi: 10.1038/srep46412.

[35] K. Ravishankar *et al.*, 'Biocompatible hydrogels of chitosan-alkali lignin for potential wound healing applications', *Materials Science and Engineering: C*, vol. 102, pp. 447–457, Sep. 2019, doi: 10.1016/j.msec.2019.04.038.

[36] J. Xu *et al.*, 'Lignin-Incorporated Nanogel Serving As an Antioxidant Biomaterial for Wound Healing', *ACS Appl. Bio Mater.*, vol. 4, no. 1, pp. 3–13, Jan. 2021, doi: 10.1021/acsabm.0c00858.

[37] Y. Zhou, Y. Han, G. Li, S. Yang, and F. Chu, 'Lignin-Based Hollow Nanoparticles for Controlled Drug Delivery: Grafting Preparation Using β-Cyclodextrin/Enzymatic-Hydrolysis Lignin', *Nanomaterials*, vol. 9, no. 7, Art. no. 7, Jul. 2019, doi: 10.3390/nano9070997.

[38] L. Siddiqui, H. Mishra, P. K. Mishra, Z. Iqbal, and S. Talegaonkar, 'Novel 4-in-1 strategy to combat colon cancer, drug resistance and cancer relapse utilizing functionalized bioinspiring lignin nanoparticle', *Medical Hypotheses*, vol. 121, pp. 10–14, Dec. 2018, doi: 10.1016/j.mehy.2018.09.003.

[39] F. Coccia, L. Tonucci, D. Bosco, M. Bressan, and N. d'Alessandro, 'One-pot synthesis of lignin - stabilised platinum and palladium nanoparticles and their catalytic behaviour in oxidation and reduction reactions', *Green Chemistry*, vol. 14, no. 4, pp. 1073–1078, 2012, doi: 10.1039/C2GC16524D.

[40] S. Hu and Y.-L. Hsieh, 'Silver nanoparticle synthesis using lignin as reducing and capping agents: A kinetic and mechanistic study', *International Journal of Biological Macromolecules*, vol. 82, pp. 856–862, Jan. 2016, doi: 10.1016/j.ijbiomac.2015.09.066.

[41] A. G. Morena, I. Stefanov, K. Ivanova, S. Pérez-Rafael, M. Sánchez-Soto, and T. Tzanov, 'Antibacterial Polyurethane Foams with Incorporated Lignin-Capped Silver Nanoparticles for Chronic Wound Treatment', *Ind. Eng. Chem. Res.*, vol. 59, no. 10, pp. 4504–4514, Mar. 2020, doi: 10.1021/acs.iecr.9b06362.

[42] W. Yang *et al.*, 'Highly-toughened PVA/nanocellulose hydrogels with anti-oxidative and antibacterial properties triggered by lignin-Ag nanoparticles', *Materials Science and Engineering: C*, vol. 129, p. 112385, Oct. 2021, doi: 10.1016/j.msec.2021.112385.

[43] A. G. Morena, A. Bassegoda, J. Hoyo, and T. Tzanov, 'Hybrid Tellurium–Lignin Nanoparticles with Enhanced Antibacterial Properties', *ACS Appl. Mater. Interfaces*, vol. 13, no. 13, pp. 14885–14893, Apr. 2021, doi: 10.1021/acsami.0c22301.

[44] H. Jafari *et al.*, 'Tannic acid: a versatile polyphenol for design of biomedical hydrogels', *J. Mater. Chem. B*, vol. 10, no. 31, pp. 5873–5912, Aug. 2022, doi: 10.1039/D2TB01056A.

[45] V. Karuppagounder *et al.*, 'Tannic acid modulates NFκB signaling pathway and skin inflammation in NC/Nga mice through PPARγ expression', *Cytokine*, vol. 76, no. 2, pp. 206–213, Dec. 2015, doi: 10.1016/j.cyto.2015.05.016.

[46] J. Yeo, J. Lee, S. Yoon, and W. Jong Kim, 'Tannic acid-based nanogel as an efficient anti-inflammatory agent', *Biomaterials Science*, vol. 8, no. 4, pp. 1148–1159, 2020, doi: 10.1039/C9BM01384A.

[47] Z. Guo *et al.*, 'Tannic acid-based metal phenolic networks for bio-applications: a review', *J. Mater. Chem. B*, vol. 9, no. 20, pp. 4098–4110, May 2021, doi: 10.1039/D1TB00383F.

[48] H.-Y. Lee, C.-H. Hwang, H.-E. Kim, and S.-H. Jeong, 'Enhancement of bio-stability and mechanical properties of hyaluronic acid hydrogels by tannic acid treatment', *Carbohydrate Polymers*, vol. 186, pp. 290–298, Apr. 2018, doi: 10.1016/j.carbpol.2018.01.056.

[49] N. Ninan, A. Forget, V. P. Shastri, N. H. Voelcker, and A. Blencowe, 'Antibacterial and Anti-Inflammatory pH-Responsive Tannic Acid-Carboxylated Agarose Composite Hydrogels for Wound Healing', *ACS Appl. Mater. Interfaces*, vol. 8, no. 42, pp. 28511–28521, Oct. 2016, doi: 10.1021/acsami.6b10491.

[50] F. Xu, B. Weng, R. Gilkerson, L. A. Materon, and K. Lozano, 'Development of tannic acid/chitosan/pullulan composite nanofibers from aqueous solution for potential applications as wound dressing', *Carbohydrate Polymers*, vol. 115, pp. 16–24, Jan. 2015, doi: 10.1016/j.carbpol.2014.08.081.

[51] B. Lu *et al.*, 'Healing of skin wounds with a chitosan–gelatin sponge loaded with tannins and platelet-rich plasma', *International Journal of Biological Macromolecules*, vol. 82, pp. 884–891, Jan. 2016, doi: 10.1016/j.ijbiomac.2015.11.009.

[52] P. Taheri, R. Jahanmardi, M. Koosha, and S. Abdi, 'Physical, mechanical and wound healing properties of chitosan/gelatin blend films containing tannic acid and/or bacterial nanocellulose', *International Journal of Biological Macromolecules*, vol. 154, pp. 421–432, Jul. 2020, doi: 10.1016/j.ijbiomac.2020.03.114.

[53] I. Perelshtein, E. Ruderman, A. Francesko, M. M. Fernandes, T. Tzanov, and A. Gedanken, 'Tannic acid NPs – Synthesis and immobilization onto a solid surface in a one-step process and their antibacterial and anti-inflammatory properties', *Ultrasonics Sonochemistry*, vol. 21, no. 6, pp. 1916–1920, Nov. 2014, doi: 10.1016/j.ultsonch.2013.11.022.

[54] J. Chen, L. Qiu, Q. Li, J. Ai, H. Liu, and Q. Chen, 'Rapid hemostasis accompanied by antibacterial action of calcium crosslinking tannic acid-coated mesoporous silica/silver Janus nanoparticles', *Materials Science and Engineering: C*, vol. 123, p. 111958, Apr. 2021, doi: 10.1016/j.msec.2021.111958.

[55] X. He *et al.*, 'Tannic acid-reinforced methacrylated chitosan/methacrylated silk fibroin hydrogels with multifunctionality for accelerating wound healing', *Carbohydrate Polymers*, vol. 247, p. 116689, Nov. 2020, doi: 10.1016/j.carbpol.2020.116689.

[56] A. G. Morena, S. Pérez-Rafael, and T. Tzanov, 'Lignin-Based Nanoparticles as Both Structural and Active Elements in Self-Assembling and Self-Healing Multifunctional Hydrogels for Chronic Wound Management', *Pharmaceutics*, vol. 14, no. 12, Art. no. 12, Dec. 2022, doi: 10.3390/pharmaceutics14122658.

[57] A. G. Morena, A. Bassegoda, M. Natan, G. Jacobi, E. Banin, and T. Tzanov, 'Antibacterial Properties and Mechanisms of Action of Sonoenzymatically Synthesized Lignin-Based Nanoparticles', *ACS Appl. Mater. Interfaces*, vol. 14, no. 33, pp. 37270–37279, Aug. 2022, doi: 10.1021/acsami.2c05443.

[58] P. J. Strong and H. Claus, 'Laccase: A Review of Its Past and Its Future in Bioremediation', *Critical Reviews in Environmental Science and Technology*, vol. 41, no. 4, pp. 373–434, Jan. 2011, doi: 10.1080/10643380902945706.

[59] E. Muri, M. Nieto, R. Sindelar, and J. Williamson, 'Hydroxamic Acids as Pharmacological Agents', *CMC*, vol. 9, no. 17, pp. 1631–1653, Sep. 2002, doi: 10.2174/0929867023369402.
[60] J. Keth, T. Johann, and H. Frey, 'Hydroxamic Acid: An Underrated Moiety? Marrying Bioinorganic Chemistry and Polymer Science', *Biomacromolecules*, vol. 21, no. 7, pp. 2546–2556, Jul. 2020, doi: 10.1021/acs.biomac.0c00449.
[61] R. P. Verma, 'Hydroxamic Acids as Matrix Metalloproteinase Inhibitors', in *Matrix Metalloproteinase Inhibitors*, vol. 103, S. P. Gupta, Ed., in Experientia Supplementum, vol. 103. , Basel: Springer Basel, 2012, pp. 137–176. doi: 10.1007/978-3-0348-0364-9_5.
[62] W. L. Mock and H. Cheng, 'Principles of Hydroxamate Inhibition of Metalloproteases: Carboxypeptidase A', *Biochemistry*, vol. 39, no. 45, pp. 13945–13952, Nov. 2000, doi: 10.1021/bi001497s.
[63] X.-C. Cheng, R.-L. Wang, Z.-K. Dong, J. Li, Y.-Y. Li, and R.-R. Li, 'Design, synthesis and evaluation of novel metalloproteinase inhibitors based on l-tyrosine scaffold', *Bioorganic & Medicinal Chemistry*, vol. 20, no. 19, pp. 5738–5744, Oct. 2012, doi: 10.1016/j.bmc.2012.08.014.
[64] H. Liang, S. J. Russell, D. J. Wood, and G. Tronci, 'A hydroxamic acid–methacrylated collagen conjugate for the modulation of inflammation-related MMP upregulation', *Journal of Materials Chemistry B*, vol. 6, no. 22, pp. 3703–3715, 2018, doi: 10.1039/C7TB03035E.
[65] G. Crivello *et al.*, 'Lignin–Cobalt Nano-Enabled Poly(pseudo)rotaxane Supramolecular Hydrogel for Treating Chronic Wounds', *Pharmaceutics*, vol. 15, no. 6, Art. no. 6, Jun. 2023, doi: 10.3390/pharmaceutics15061717.
[66] M. Díaz-González, T. Vidal, and T. Tzanov, 'Phenolic compounds as enhancers in enzymatic and electrochemical oxidation of veratryl alcohol and lignins', *Appl Microbiol Biotechnol*, vol. 89, no. 6, pp. 1693–1700, Mar. 2011, doi: 10.1007/s00253-010-3007-3.
[67] R. W. Korsmeyer, R. Gurny, E. Doelker, P. Buri, and N. A. Peppas, 'Mechanisms of solute release from porous hydrophilic polymers', *International Journal of Pharmaceutics*, vol. 15, no. 1, pp. 25–35, May 1983, doi: 10.1016/0378-5173(83)90064-9.
[68] M. P. Paarakh, P. A. Jose, C. Setty, and G. V. Peter, 'Release Kinetics – Concepts and applications', vol. 8, 2018.
[69] B. Jiang, Y. Zhang, L. Gu, W. Wu, H. Zhao, and Y. Jin, 'Structural elucidation and antioxidant activity of lignin isolated from rice straw and alkali-oxygen black liquor', *International Journal of Biological Macromolecules*, vol. 116, pp. 513–519, Sep. 2018, doi: 10.1016/j.ijbiomac.2018.05.063.
[70] P. Jiang *et al.*, 'Preparation and characterization of thermo-sensitive gel with phenolated alkali lignin', *Sci Rep*, vol. 8, no. 1, Art. no. 1, Sep. 2018, doi: 10.1038/s41598-018-32672-z.
[71] B. Luo, Z. Jia, H. Jiang, S. Wang, and D. Min, 'Improving the Reactivity of Sugarcane Bagasse Kraft Lignin by a Combination of Fractionation and Phenolation for Phenol–Formaldehyde Adhesive Applications', *Polymers*, vol. 12, no. 8, Art. no. 8, Aug. 2020, doi: 10.3390/polym12081825.
[72] T. Momić, Z. Vujčić, and V. Vasić, 'Kinetics of inhibition of peroxidase activity of myeloperoxidase by quercetin', *Int. J. Chem. Kinet.*, vol. 40, no. 7, pp. 384–394, Jul. 2008, doi: 10.1002/kin.20319.
[73] F. A. R. Mota, S. A. P. Pereira, A. R. T. S. Araújo, B. Gullón, M. L. C. Passos, and M. L. M. F. S. Saraiva, 'Automatic Identification of Myeloperoxidase Natural Inhibitors in Plant Extracts', *Molecules*, vol. 27, no. 6, Art. no. 6, Jan. 2022, doi: 10.3390/molecules27061825.
[74] N. J. Trengove *et al.*, 'Analysis of the acute and chronic wound environments: the role of proteases and their inhibitors', *Wound Repair and Regeneration*, vol. 7, no. 6, pp. 442–452, 1999, doi: 10.1046/j.1524-475X.1999.00442.x.

[75] Z. Wu, B. Zhang, and B. Yan, 'Regulation of Enzyme Activity through Interactions with Nanoparticles', *International Journal of Molecular Sciences*, vol. 10, no. 10, Art. no. 10, Oct. 2009, doi: 10.3390/ijms10104198.
[76] C. Fleury *et al.*, 'Effect of cobalt and chromium ions on human MG-63 osteoblasts in vitro: Morphology, cytotoxicity, and oxidative stress', *Biomaterials*, vol. 27, no. 18, pp. 3351–3360, Jun. 2006, doi: 10.1016/j.biomaterials.2006.01.035.
[77] S. Alarifi, D. Ali, A. O. S. Y, M. Ahamed, M. A. Siddiqui, and A. A. Al-Khedhairy, 'Oxidative stress contributes to cobalt oxide nanoparticles-induced cytotoxicity and DNA damage in human hepatocarcinoma cells', *International Journal of Nanomedicine*, vol. 8, pp. 189–199, Dec. 2013, doi: 10.2147/IJN.S37924.
[78] C. Pouget, C. Dunyach-Remy, A. Pantel, S. Schuldiner, A. Sotto, and J.-P. Lavigne, 'Biofilms in Diabetic Foot Ulcers: Significance and Clinical Relevance', *Microorganisms*, vol. 8, no. 10, Oct. 2020, doi: 10.3390/microorganisms8101580.
[79] C. Mottola, J. J. Mendes, J. M. Cristino, P. Cavaco-Silva, L. Tavares, and M. Oliveira, 'Polymicrobial biofilms by diabetic foot clinical isolates', *Folia Microbiol*, vol. 61, no. 1, pp. 35–43, Jan. 2016, doi: 10.1007/s12223-015-0401-3.
[80] X. Dong, M. Dong, Y. Lu, A. Turley, T. Jin, and C. Wu, 'Antimicrobial and antioxidant activities of lignin from residue of corn stover to ethanol production', *Industrial Crops and Products*, vol. 34, no. 3, pp. 1629–1634, Nov. 2011, doi: 10.1016/j.indcrop.2011.06.002.
[81] R. Nakamura, Y. Matsushita, K. Umemoto, A. Usuki, and K. Fukushima, 'Enzymatic Polymerization of Coniferyl Alcohol in the Presence of Cyclodextrins', *Biomacromolecules*, vol. 7, no. 6, pp. 1929–1934, Jun. 2006, doi: 10.1021/bm060045d.
[82] C. A. Hunter, K. R. Lawson, J. Perkins, and C. J. Urch, 'Aromatic interactions', *Journal of the Chemical Society, Perkin Transactions 2*, vol. 0, no. 5, pp. 651–669, 2001, doi: 10.1039/B008495F.
[83] C. Marmorat, A. Arinstein, N. Koifman, Y. Talmon, E. Zussman, and M. Rafailovich, 'Cryo-Imaging of Hydrogels Supermolecular Structure', *Sci Rep*, vol. 6, no. 1, Art. no. 1, May 2016, doi: 10.1038/srep25495.
[84] Z. Kaberova, E. Karpushkin, M. Nevoralová, M. Vetrík, M. Šlouf, and M. Dušková-Smrčková, 'Microscopic Structure of Swollen Hydrogels by Scanning Electron and Light Microscopies: Artifacts and Reality', *Polymers*, vol. 12, no. 3, Art. no. 3, Mar. 2020, doi: 10.3390/polym12030578.
[85] H. Rachmawati, C. A. Edityaningrum, and R. Mauludin, 'Molecular Inclusion Complex of Curcumin–β-Cyclodextrin Nanoparticle to Enhance Curcumin Skin Permeability from Hydrophilic Matrix Gel', *AAPS PharmSciTech*, vol. 14, no. 4, pp. 1303–1312, Dec. 2013, doi: 10.1208/s12249-013-0023-5.
[86] R. Laurano *et al.*, 'Custom-design of intrinsically antimicrobial polyurethane hydrogels as multifunctional injectable delivery systems for mini-invasive wound treatment', *Engineered Regeneration*, vol. 2, pp. 263–278, Jan. 2021, doi: 10.1016/j.engreg.2021.12.001.
[87] G. Crivello, L. Fracchia, G. Ciardelli, M. Boffito, and C. Mattu, 'In Vitro Models of Bacterial Biofilms: Innovative Tools to Improve Understanding and Treatment of Infections', *Nanomaterials*, vol. 13, no. 5, Art. no. 5, Jan. 2023, doi: 10.3390/nano13050904.
[88] G. S. Schultz *et al.*, 'Wound bed preparation: a systematic approach to wound management', *Wound Repair Regeneration*, vol. 11, no. s1, Mar. 2003, doi: 10.1046/j.1524-475X.11.s2.1.x.

4. Strategies to impart antibiofilm features to NPs

4.1. Introduction

The objective of the work described in this section, is to design CoLig NPs with additional antibiofilm functionalities starting from the NPs developed in Section 3. To this aim, two strategies were explored: the first based on stimulating biofilm dispersion through local Nitric oxide (NO) release, and the second adopting physical methods to induce photothermal disruption of the biofilm. To achieve this, CoLig NPs were either coated with amino cellulose functionalized with S-nitroso glutathione (GSNO) which is a NO donor capable of inducing biofilm dispersion, or cobalt-phthalocyanine (CoPc) complexes were used instead of Co to obtain CoPc-Lig NPs with photothermal activity.

As discussed in the previous section, biofilm development represents an unsolved medical issue in CWs that are colonized by multiple bacteria species. Bacteria organize into complex communities embedded in a self-secreted matrix of extracellular polymeric substances, called biofilms (EPS) [1]. Such communities are more difficult to eliminate than free bacteria because of their firm adhesion to tissues, while the EPS matrix poses a physical barrier to the penetration of antibiotics and antimicrobials, as well as to the action of the host immune cells, such as neutrophils and macrophages [2], [3], [4].

The prevalence of biofilms in CWs is estimated to be above 60% [5], [6], making their eradication extremely relevant to achieve clinical success. Studies indicate that biofilms in CWs are heterogeneous, with the coexistence of 4 to nearly 20 different bacterial species per wound [7], [8]. The prevalent species found in CWs biofilms are the gram-positive *Staphylococcus aureus* and the gram-negative *Pseudomonas aeruginosa* [4], [5], [9], [10], which are particularly critical because of the increasing number of antibiotic-resistant strains [11] [12], [13], [14]. Antibiotic resistance is also driven by the peculiar phenotypic state of bacteria in biofilms, known as the sessile state. Sessile microorganisms display a slow growth rate, reducing the action of most antibiotics which are designed to mainly target rapidly dividing cells. This low exposure to antibiotics, coupled with the genetic diversity and mutual cooperation of bacteria in heterogeneous biofilms, results in the development of antibiotic-resistant bacteria populations [1], [15] [3]. Moreover, the release of virulence factors from bacteria in biofilms [9] results in the chronic recruitment of neutrophils and in the release of pro-inflammatory cytokines and proteases, which may further aggravate the inflammatory state and inhibit healing [16]. The perpetuation of the inflammation also increases capillary permeability, resulting in a higher nutrient supply to bacteria [3]. For example, the synergistic action of *Staphylococcus aureus* and *Pseudomonas aeruginosa* in biofilms results in persistent biofilms that delay wound healing and worsen the clinical outcomes [11], [17], [18].

Given the deleterious effect of biofilm on wound healing and the variety of species involved, developing new broad-spectrum antibacterial dressings capable of actively targeting biofilm dispersion and eradication is crucial for promoting regeneration in CWs. Indeed, treatments focusing on biofilm eradication showed promising results [19]. The gold standard to treat infected wounds is surgical debridement coupled with antibiotic therapy, since after debridement bacteria become more susceptible to antibacterial compounds [20]. However, biofilms are difficult to remove as they are tightly adherent to the wound bed. Moreover, debridement also removes newly-formed tissue interfering with proper regeneration [19]. Therefore, therapeutic agents capable of acting specifically on the biofilm without damaging the healthy tissue are needed.

Different compounds targeting biofilms have been identified. For instance, quorum-sensing inhibitors, such as furanone C30 and RNA-III inhibiting peptide (RIP) impair the chemical signaling within the biofilm, thus blocking the biofilm formation and the action of virulence factors. However, this strategy is not very effective on mature biofilms. Additionally, these compounds do not actively kill the bacterial cells and require the combination with antimicrobial agents [21]. Some antimicrobial peptides, such as the human cathelicidin LL-37, are capable of killing bacteria by acting on the bacterial membrane while preventing biofilm formation or inducing biofilm disruption [22]. However, peptides are expensive and prone to degradation in the CWs environment, rich in proteases. EPS degraders, such as dispersin B, deoxyribonuclease I (DNase I), and acylase, act specifically on EPS components, altering biofilm integrity. Their action unshields bacteria from EPS protection, making them more susceptible to antibacterial agents [23].

Nitric oxide (NO) is another interesting agent because of its known role in vasodilatation, cell proliferation, angiogenesis, biofilm dispersion and pathogen control [24]. NO delivery in CWs has the potential to reduce the infection burden, while concomitantly stimulating the regeneration process. However, the therapeutic action of NO is strongly related to its concentration, with low concentrations (nM) inducing cell proliferation and biofilm dispersion [25], [26], and high concentrations (μM) stimulating apoptosis [31],[32]. Moreover, NO's half-life is very short (seconds), which limits its field of action to ~100 μm from the delivery site [29]. For this reason, systems capable of controlling NO release and protecting the molecule until it reaches the site of interest are highly desirable. Glutathione (GSH), a known NO donor, that can be nitrosylated to form GSNO has been proposed for this purpose [30]. GSNO has been combined with various polymers and hydrogels to obtain local NO delivery in wounds [31], [32], [33], [34], [35], [36], [37], [38], [39]. For instance, Kim et al. [32] prepared GSNO-containing chitosan films that showed antimicrobial activity against *S. aureus* and *P. aeruginosa* and were able to improve wound closure *in vivo*. In another study, Lee et al. [36], [38] conjugated GSNO to PLGA and used the new material to obtain NPs capable of inhibiting methicillin-resistant *S. aureus* and of promoting wound regeneration in an *in vivo* infected wound model.

In recent years, treatments based on physical removal, without debridement, have also been explored for the elimination of biofilms. These methods exploit ultrasound, electric field, light irradiation, or magnetic field to stimulate biofilm detachment or disaggregation [40], [41]. For instance, Dong et al. [42] prepared magnetic NPs capable of biofilm disruption through mechanical friction of the NPs under an external magnetic field. These NPs were used to remotely remove biofilms within narrow tubes, such as catheters. Photothermal therapy (PTT) is another promising treatment against biofilms. In PTT, a photo-excitable molecule is stimulated with near-infrared (NIR) light resulting in increased local temperature and in the thermal ablation of target cells [43], [44]. This strategy has been used to remotely eradicate biofilms on titanium implants in *in vivo* models [45]. However, heat generation may damage healthy tissues. Therefore, a combination of mild PTT with the local release of antimicrobial compounds has the potential to enhance treatment efficacy while reducing the thermal damage to healthy tissue [46], [47]. For instance, Zhao et al. [46] proposed thermosensitive liposomes encapsulating the antibiotic drug tobramycin and a photosensitive cyanine dye. Upon NIR irradiation, the photosensitive dye increased the local temperature to 45°C, which stimulated tobramycin release and potentiated its anti-biofilm activity both *in vitro* and *in vivo*.

Based on the above considerations, this chapter focuses on providing antibiofilm properties to CoLig NPs, following the two strategies described in Figure 4.1. In the first approach (Figure 4.1.A), GSNO was first conjugated to amino cellulose. This new biomaterial was characterized to confirm

and quantify the successful conjugation of GSNO and used as a coating on the CoLig NPs developed in Section 3. The resulting NPs (NO-CoLig NPs) were characterized and the antibacterial and antibiofilm activity was measured against *P. aeruginosa* and *S. aureus* strains.

The second approach exploits phthalocyanines (Pc) for the photothermal ablation of biofilms. Pcs are photosensitive compounds presenting absorbance in the NIR spectrum used in clinical trials as photosensitizers for photodynamic treatment (PDT) or photoimmunotherapy [48]. In this work, CoPc, a commercially available complex of cobalt and Pc, was combined with the Lig-TA-LTH synthesized in Section 3 to obtain CoPc-Lig NPs with photothermal properties (Figure 4.1.B).

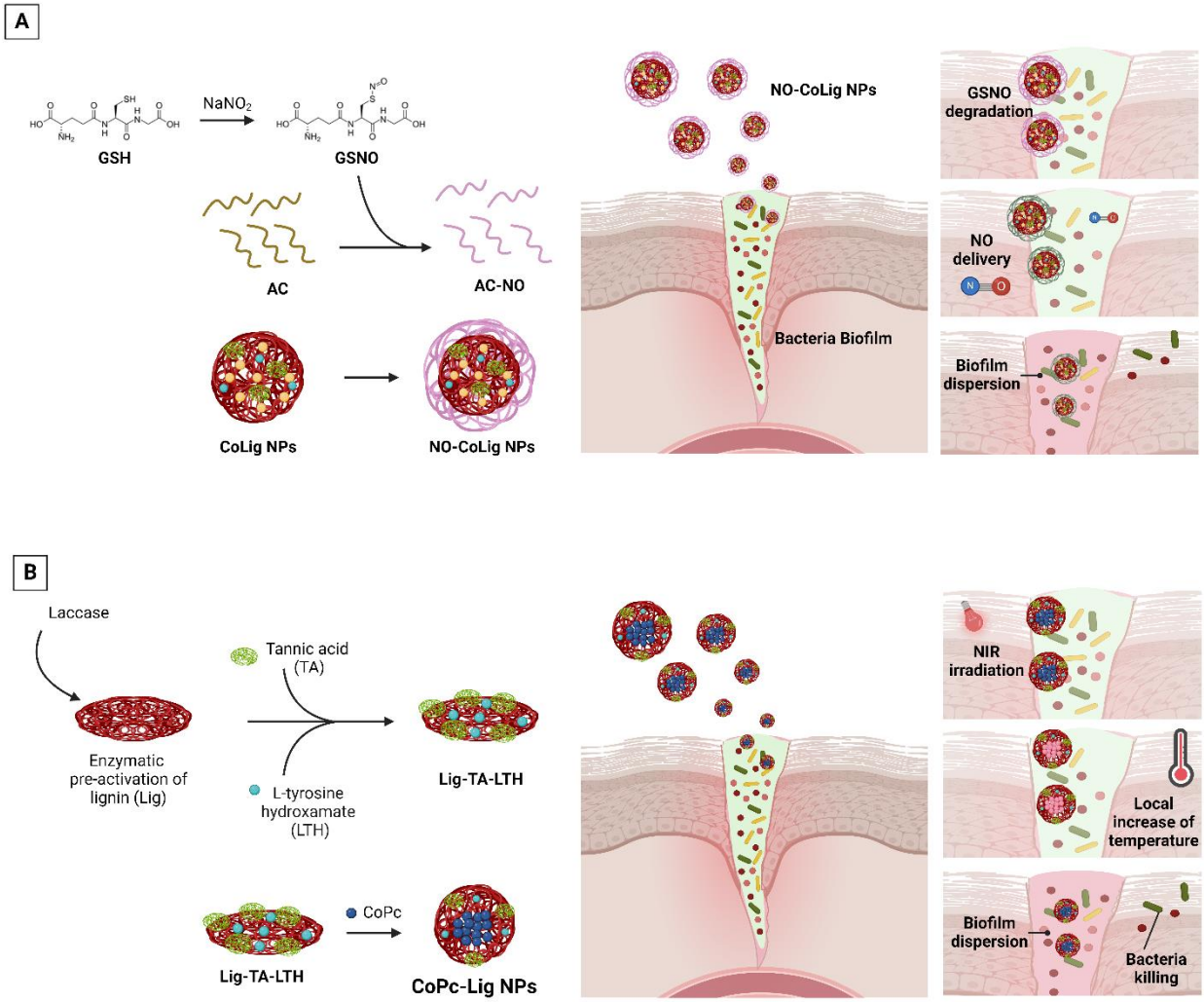


Figure 4.1. Strategies to include antibiofilm activity in Colig NPs. (A) Coating of CoLig NPs with NO-donor to achieve NO delivery. (B) Using CoPc to obtain NPs sensitive to NIR irradiation.

4.2. Materials and methods

4.2.1. Materials and reagents

Glutathione (GSH), sodium nitrite, acetone, cobalt-phthalocyanine (CoPc), 4',6-diamidino-2-phenylindole (DAPI), Alexa Fluor 594 phalloidin, hydrochloric acid (HCl), and centrifugal filter units (10000 MWCO cut-off) were obtained from ThermoFisher Scientific (Milan, Italy). Tryptic Soy Broth (TSB), 1-Ethyl-3-(3-dimethylaminopropyl)carbodiimide (EDC), N-hydroxysuccinimide (NHS), paraformaldehyde (PFA 4%), 5,5'-dithiobis-(2-nitrobenzoic acid) (DTNB), cysteine, and sodium

tripolyphosphate (TPP) were purchased from Sigma-Aldrich (Madrid, Spain and Milan, Italy). 6-Deoxy-6-(ω-aminoethyl) AC was purchased from the Centre of Excellence of Polysaccharide Research (Germany).

Human fibroblast cell line (ATCC-SCRC-1041, HFF-1) was purchased from the American Type Culture Collection (ATCC LGC Standards, Italy), and human keratinocytes (HaCaT) were purchased from "Istituto Zooprofilattico Sperimentale Della Lombardia E Dell'emilia Romagna Bruno Ubertini" (Italy). The other reagents were purchased as indicated in the previous Sections.

4.2.2. Preparation and characterization NPs delivering NO

4.2.2.1. GSH S-nitrosylation to GSNO

GSH and sodium nitrite were solubilized separately at 1.25 M in aqueous solutions of HCl (0.625M). Then, the solutions were mixed at a 1:1 volume ratio to have a final concentration of GSH and sodium nitrite of 0.625 M, and the mix was stirred for 40 min in the dark at 4 °C. The obtained solution was washed three times in acetone by centrifugation for 5 min at 4500 rpm and 4 °C followed by similar washing in petroleum ether. The pink pellet was left to dry overnight in the dark, and the obtained powder was stored at -20°C, protected from light.

The obtained GSNO was analyzed through ATR-FTIR to assess the reaction success. UV-Vis spectroscopy (Perkin Elmer Lambda 25 UV/Vis spectrometer, Waltham, MA, USA) was used to confirm the conversion of GSH to GSNO through the appearance of a peak at 335 nm. ATR-FTIR analysis was carried out utilizing a PerkinElmer Spectrum 100 FTIR spectrometer (PerkinElmer, Waltham, MA, USA). Spectra were generated by averaging 32 scans over the spectral range from 4000 to 600 cm−1 at a resolution of 1 cm−1. All analyses were carried out at room temperature. Spectra of GSH were also obtained for comparative purposes. To evaluate the complete conversion of free thiols, Ellman's assay was performed. Briefly, 125 µL of GSNO or GSH samples were added to 1.125 mL of reaction buffer (0.1 M sodium phosphate, pH 8, with 1 mM EDTA) and mixed with 25 µL of DTNB (4 mg/mL in reaction buffer). After 15 min of incubation, the absorbance at 415 nm was measured. To quantify the free thiols, cysteine was used for calibration.

Stability tests were also performed at different temperatures and pH conditions to verify the stability of GSNO in aqueous environments. Briefly, GSNO was solubilized in distilled water at 1 mg/mL and incubated at various temperatures (4 °C, 25°C and 37°C) and pH conditions (3, 5, 7, 8) with or without exposition to natural light. At selected time points (1, 3, 5 24, 48, 72 h), the absorbance at 335 nm was measured and compared to the initial absorbance.

4.2.2.2. Functionalization of amino cellulose with GSNO

The conjugation of GSNO to AC was performed using carbodiimide chemistry. AC at 10 mg/mL in deionized water was mixed with GSNO at a NH_2:GSNO molar ratio of 2:1. Then, EDC (NH_2:EDC mol ratio 1:4) and NHS (EDC:NHS mol ratio 1:1) were added. The pH was adjusted to 5.5 and the solution was stirred in the dark overnight at 4°C. After the incubation, the solution was filtered through centrifuge filters with a 10'000 MWCO cut-off. The collected compound (AC-GSNO) was freeze-dried and stored in the freezer.

AC-GSNO was characterized through ATR-FTIR, as previously described, and the GSNO conjugation was quantified both by measuring the absorbance peak at 335 nm, related to the S-NO bond and through free amine quantification through Kaiser test (Sigma-Aldrich Milan, Italy). For Kaiser test, the samples were solubilized in 60% ethanol. Then 600 µL of the solutions were mixed with 75 µL of phenol (80% in ethanol), 75 µL of ninhydrin solution (6% in ethanol) and 150 µL potassium cyanide solution (H2O/pyridine). The solutions were incubated at 120 °C for 15 min and the

absorbance at 570 nm was measured. To quantify the primary amine, glycine was used as a calibration and the results were reported as mg of glycine equivalent (GE)/ mg polymer. The test was performed in triplicates.

4.2.2.3. Coating of CoLig NPs with AC-GSNO

CoLig NPs produced in Section 3 were coated using the Layer-by-Layer method. CoLig NPs were diluted at 0.5 mg/mL in deionized water. Then, AC-GSNO was added to obtain a final concentration of 1 mg/mL. The solution was stirred at 300 rpm in an orbital shaker for 1 h. The excess of AC-GSNO was eliminated through centrifugation for 50 min at 18 000 g and 4°C. The NO-CoLig NPs were analyzed at the DLS to check the changes in particle size and ζ potential, as previously described.

4.2.2.4. Cytocompatibiltiy of NO-CoLig NPs

The cytocompatibility of NO-CoLig NPs was tested on fibroblasts (ATCC-CRL-4001, BJ-5ta) and keratinocytes (HaCaT). Cells were seeded in a 96-well tissue-culture-treated polystyrene plate at a density of 60,000 cells per well in 100 µL of DMEM supplemented with 200 mM of L-glutamine, 1% penicillin, and 10% (v/v) fetal bovine serum. After 24 hours of incubation (37 °C, 5% CO_2), NO-CoLig NPs dispersed in medium were added at various concentrations. Following an additional 24-hour incubation period, cell viability was assessed using the AlamarBlue assay. The medium was replaced with 100 µL of fresh medium containing AlamarBlue reagent (dilution 1:10), and fluorescence at $\lambda_{ex/em}$ = 560/590 nm was measured after 4 hours of incubation. Cells cultured without NPs served as a control (representing 100% cell viability).

4.2.2.5. Antibacterial and anti-biofilm activity of NO-CoLig NPs

The antibacterial activity of NO-CoLig NPs was tested on *S. aureus* and *P. aeruginosa* through MIC tests Briefly, different dilutions of NO-CoLig NPs were incubated with bacterial suspensions (5 × 105 CFU/mL) in Nutrient broth at 37 °C. After 24 hours, the optical density at 600 nm was measured using the Ultramark Microplate Imaging System (Bio-Rad Laboratories S.r.l., Segrate, Italy). CoLig NPs, without NO coating, were tested for comparison.

The anti-biofilm capacity of NO-CoLig NPs and GSNO was assessed by evaluating the ability of the NPs to disperse a preformed biofilm. Briefly, *S. aureus* and *P. aeruginosa* were grown overnight at 37°C in the appropriate medium (Tryptic Soy Broth (TSB) for *S. aureus* and Brain Heart Infusion (BHI) medium for *P. aeruginosa,* both additionated with 1% glucose). Then, 50 µL of medium and 50 µL bacteria inoculum (OD_{600}=0.01, ~10^5-10^6 CFU/mL) were mixed and incubated at 37 °C. After 24 h, the non-adherent bacteria were eliminated by two washes with PBS and the NPs resuspended in TBS were added to the formed biofilms. After incubation for 24 h, non-adherent bacteria were eliminated by washing, and the biofilms were analyzed to assess dispersion. Biofilm dispersion was measured with crystal violet assay to assess the matrix quantity. Briefly, the samples were dried at 60 °C for 2 h. Then, the residual matrices were stained for 10 min with 0.1% crystal violet solution, washed twice with MilliQ water and dried at 60°C. To dissolve the crystal violet, acetic acid at 30% v/v was added and incubated for 15 min at room temperature. Finally, the absorbance at 595 nm was measured.

4.2.3. Preparation and characterization of CoPc-Lig NPs

4.2.3.1. Preparation of CoPc-Lig NPs

CoPc-Lig NPs were obtained by adapting the protocol used for CoLig NPs. This adaptation was necessary since the reaction between CoPc and Lig-TA-LTH does not involve metal reduction, but the lignin-based material acts as a dispersant of CoPc [49]. Therefore, the protocol used for CoLig

NPs was used as a reference for obtaining Lig-TA-LTH solubilization in water. Briefly, CoPc at 7.85 mg/mL was suspended in DMSO through sonication for 2 minutes, while Lig-TA-LTH was dissolved at 5 mg/mL in deionized water at pH 8.5. The two solutions were mixed at 60 °C to obtain different mass ratios between Lig-TA-LTH and CoPc and stirred at 500 rpm for 2 h at 60 °C. To purify the samples from unreacted components, centrifugation at 17000 rpm for 20 minutes was performed. Then, the pellet was resuspended in MilliQ water and sonicated for 30 seconds. A second centrifugation step was performed at 1200 rpm for 5 minutes to remove large aggregates. The analysis was performed in triplicate. The yield of the NPs production process was calculated on the freeze-dried products of synthesis by using Equation (1):

$$\text{Yield of production} = \frac{M_{NPs}}{M_{tot}}\ 100 \qquad (1)$$

Where M_{NPs} is the measured mass of the CoPc-Lig NPs after freeze-drying and M_{tot} is the total weight of product obtained before purification.

The presence of cobalt in the selected CoPc-Lig NP was also quantified using ICP-MS. Briefly, samples were digested with 20% (v/v) HNO3 at 100 ◦C for 3 h, then diluted to a final concentration of HNO3 of 2% v/v and filtered through a 0.2 µm filter. Quantification of cobalt content within the CoLig NPs was carried out via ICP-MS (ICP-MS 7800, Agilent Technologies, Santa Clara, CA, USA). Calibration was performed using an internal standard with 45Rh and a standard curve of 59Co.

The obtained CoPc-Lig NPs were characterized through DLS to evaluate the particle size, PDI and ζ potential; ATR-FTIR to assess the interactions among the NPs components; and UV-Vis spectroscopy to quantify the presence of CoPc.

CoPc-Lig NPs morphology was assessed by transmission electron microscopy (TEM) (TALOS F200X, Thermo Scientific). To confirm the presence of Cobalt, Energy Dispersive X-ray Spectrometry (EDX) analysis was coupled with TEM imaging.

4.2.3.2. Cytocompatibility and cell internalization of CoPc-Lig NPs

The cytocompatibility of CoPc-Lig NPs was assessed on fibroblasts (HFF-1) and keratinocytes (HaCaT) as described above.

The internalization of CoPc-Lig NPs into fibroblasts and keratinocytes was assessed through fluorescence microscopy using a spinning disk confocal microscope. Briefly, cells were seeded at 70’000 cells per well in a 48-well plate on glass sides and incubated at 37 °C. After 24 h, CoPc-Lig NPs were added at 0.5 mg/mL and incubated for an additional 24 h. Then, the cells were fixed for 20 minutes with PFA at 4%, permeabilized with TritonX 0.5% for 10 minutes and stained with DAPI, to mark cell nuclei, and Alexa Fluor 594-phalloidin, to mark the cytoskeleton. Images in brightfield and fluorescence were obtained.

4.2.3.3. Antioxidant activity of CoPc-Lig NPs

The ROS scavenging capacity of CoPc-Lig NPs was assessed through the DPPH assay. Briefly, 25 µL of sample suspension (0.1-5 mg/mL in MilliQ water) and 75 µLof DPPH solution (0.1 mM in pure ethanol) were mixed and incubated for 30 min at room temperature. After incubation, the samples were centrifuged at 10000 rpm for 5 min to eliminate the suspended materials and the absorbance at 517 nm was measured. Samples mixed with ethanol were used as background, while DPPH mixed with MilliQ water represented the 100% DPPH signal.

4.2.3.4. MMPs inhibitory assay

The MMP inhibition capacity of CoPc-Lig NPs was determined using the EnzCheck Gelatinase/Collagenase Assay Kit, with some modifications. Initially, CoPc-Lig NPs at different concentrations (0.1, 0.2, 0.4 and 0.8 mg/mL) were dispersed in 500 µL of reaction buffer (0.05 M Tris HCl, 0.15 M NaCl, 5 mM $CaCl_2$, 0.2 mM sodium azide, pH 7.6). Subsequently, 5 µL of 500 U/mL collagenase type IV from Clostridium histolyticum were added to achieve a final concentration of 5 U/mL. The solution was then incubated at 37°C for 24 hours. After incubation, 100 µL of the sample were mixed with 80 µL of reaction buffer and 20 µL of fluorescein-conjugated gelatine (100 µg/mL in Milli-Q water). The plate was incubated for 20 minutes in darkness at room temperature, and fluorescence was measured at $\lambda_{ex/em}$ = 493/528 nm. Collagenase activity was determined as a percentage of enzyme inhibition compared to the control (a reaction mixture with enzyme and substrate but without NPs).

4.2.3.5. Antibacterial activity of CoPc-Lig NPs

The antibacterial and antibiofilm activity of CoPc-Lig NPs was tested on *S. aureus* and *P. aeruginosa* as previously indicated for NO-CoLig NPs. Additionally, the colony forming unit (CFU) test was performed. Briefly, the bacteria were incubated with CoPc-Lig NPs following the protocol of MIC test. After 24h incubation, the different conditions were serially diluted in PBS and plated onto agar plates to count the forming colonies. The test was performed in triplicate and controls with untreated bacteria were considered as reference. The reduction of bacterial growth was calculated as indicated in equation (2):

$$\text{Log reduction of bacterial growth} = \log(C_t) - \log(C_c) \quad (2)$$

Where C_t and C_c are the concentrations of CFU for the treated and untreated bacteria, respectively. The concentration of CFU is calculated as:

$$C_t = \frac{n_t * 10\hat{}d}{v} \quad (3)$$

Where n_t is the number of colonies counted, d is the dilution at which n_t was calculated and v is the volume of solution used.

4.2.3.6. Internalization of CoPc-Lig NPs into S. aureus and P. aeruginosa biofilms

The internalization of CoPc-Lig_NPs into *S. aureus* biofilms was assessed through UV-Vis spectroscopy. Briefly, *S. aureus* biofilms were formed as described above and incubated with CoPc-Lig NPs at different concentrations. After 24 h the biofilm was lysed with DMSO/0.1 M glycine buffer (pH 10.2) solution (7:1) and the absorbance at 620 nm was measured.

SEM imaging was also performed to verify the internalization of CoPc-Lig NPs in biofilms. Briefly, *S. aureus* and *P. aeruginosa* biofilms were formed on silicon wafers. *S. aureus* and *P. aeruginosa* suspensions were prepared as previously described and seeded at 10^7 CFU/mL. After 24h incubation, the formed biofilms were treated with CoPc-Lig NPs at 0.5 mg/mL. After further incubation for 24 hours at 37°C, the liquid was removed, and the remaining bacteria on the wafers were fixed for 1h in a 4% paraformaldehyde solution. Subsequently, the bacteria were dehydrated by successive incubation steps with increasing concentrations of ethanol for 1 hour each (25%, 50%, 75%, and 100%). This process was repeated for untreated bacteria biofilms as a control. The samples were subjected to SEM analysis and Energy Dispersive X-Ray Analysis (EDX).

4.2.3.7. Photothermal activity of CoPc-Lig NPs

For testing the photothermal activity of CoPc-Lig NPs within *S. aureus* biofilm, the bacteria biofilms were grown on 0.5 thick custom-made polydimethylsiloxane (PDMS; Sylgard 184, Dow Chemical,

Midland, USA) slides. To form the PDMS slides, a PDMS solution was prepared by mixing the polymeric base with a curing agent in a 10:1 weight ratio. The solution was poured into 6-well plate molds and incubated for 48 h to allow the complete cross-linking of PDMS. *S. aureus* suspension was prepared as previously described and seeded at 10^7 CFU/mL on the PDMS slides. After 24 h of incubation, the slides were washed with PBS to remove non-adherent bacteria and moved to a new well plate, where the CoPc-Lig NPs were added at a concentration of 0.5 mg/mL. After 24h of incubation, the biofilms were washed again with PBS and fixed for 1h with PFA 4% before imaging.
Near Infrared Thermal Imaging was performed by illuminating the Biofilm samples through continuous wavelength (CW) laser illumination at 660 nm under controlled conditions: room temperature and humidity, laser beam light and power distribution. The Biofilm samples were illuminated by the laser for 120 seconds, recording the thermal gradient by the near-infrared camera FLIR T560. The datasets were collected in post-processing by using the FRS Software (FLIR), and then fitted by the curve fitting tool in Matlab.

To test anti-biofilm activity after NIR irradiation, *S. aureus* and *P. aeruginosa* biofilms were treated for 24 h with CoPc-Lig NPs at 4 mg/mL. Then, the biofilms were irradiated for 15 min at 660 nm and the bacteria viability was assessed through CellTiter 96® assay (Promega, Milan, Italy) immediately and after 24 h. Briefly, 100 µL of bacteria medium was mixed with 20 µL of the reagent solution, added to the biofilm and incubated for 30 min at 37°C. Then, the medium was collected and the absorbance at 490 nm was measured. For verifying the biofilm integrity, SEM imaging was performed by preparing biofilm samples as described above. Additionally, the biofilms' structure was observed also at the confocal microscope. For this purpose, biofilms were grown on glass slides and incubated for 24 h with the CoPc-Lig NPs at 4 mg/mL to allow internalization. After treatment with NIR light, the liquid was removed, and the biofilms were fixed for 1 h in a 4% paraformaldehyde solution and then the cells nuclei were stained with DAPI as described in *4.2.3.2.* After washing with PBS, the samples were analyzed using a spinning disk confocal microscope.

4.2.3.8. Photoacoustic activity of CoPc-Lig NPs

Photoacoustic (PA) activity of CoPc-Lig NPs was measured with a commercial PAI system (VevoLAZR, VisualSonics Inc.), which produces PA images co-registered with B-mode images of the surrounding structures. The samples were stimulated within a wavelength range of 680-970 nm and with a wavelength switching time of <0.4 s. The laser illumination was transmitted to the sample at 26 mJ by a PA probe (LZ250, VisualSonics Inc.) equipped with two glass windows placed on both sides of the echographic linear array transducer. The PA probe was operated between 13 and 24 MHz, with a field of view around 23 mm × 30 mm at an angle of 30° with the imaging plane. The axial resolution was 75 µm, while the lateral resolution was 165 µm. The acquisition time for the absorption spectrum was ∼60 s for 146 wavelengths.
PA characterization of CoPc-Lig NPs was performed by placing the NPs in a custom-made phantom [50], comprising a plastic box with a series of coplanar micro-medical polyethylene (PE) tubes with internal diameter (ID) of 860 µm and external diameter (ED) of 1320 µm that were non-radiopaque, non-reactive, and did not contain plasticizers. The CoPc-Lig NPs at 0.2 mg/mL were loaded into PE tubes (~40 µL each tube). A tube loaded with water was used as background. The loaded PE tubes were inserted into a plastic box filled with water as a probe coupling medium and analyzed with the PA probe. The PA values were measured in regions of interest (ROIs), which were selected around the section of each tube.

The PA activity of CoPc-Lig NPs was also measured in *ex vivo* phantoms, composed of bovine muscular tissues. These phantoms were injected with the NPs at 0.2 mg/mL and analyzed with the PA probe. The PA values were measured in two ROIs of the same dimensions, the first around the NPs injection zone and the second in an area not interested in the injection.
The PA activity of CoPc-Lig NPs within S. aureus biofilm was also measured. The bacteria biofilms were grown on 0.5 thick custom-made polydimethylsiloxane (PDMS; Sylgard 184, Dow Chemical, Midland, USA) slides, as described in 4.2.3.7. After incubation with CoPc-Lig NPs at 0.5 mg/mL for 24h, the biofilms were washed with PBS and fixed for 1h with PFA 4%. To facilitate imaging with the ultrasound probe, an additional PDMS layer was poured on the fixed biofilms and the samples were incubated for 48h at room temperature to allow complete formation of the PDMS before analysis.
For each ROI, the photostability (PHSt) and PA spectral trend were analyzed. The PA spectrum was evaluated within 680 to 970 nm. The PHSt was evaluated under pulsed irradiation at 710 nm for over 1 min.

4.2.4. Statistical Analysis

Results are reported as mean ± standard deviation. Statistical analysis was performed through Microsoft Excel for Windows 10. To compare results, one-way ANOVA analyses were performed, followed by Bonferroni's multiple comparison test. Statistical significance was assessed as follows: n.d.—non-significant difference, * $p < 0.05$, ** $p < 0.01$, and *** $p < 0.001$.

4.3. Results and discussion

4.3.1. Preparation and characterization of Nitric oxide delivering NPs

4.3.1.1. GSH S-nitrosylation to GSNO

GSNO was successfully synthesized from GSH. The UV-Vis spectra of the obtained GSNO revealed the presence of a new peak at 335 nm, related to S-nitrosothiols (Figure 4.2.A) [30]. Furthermore, thiols quantification using Ellman's assay indicated their complete absence in GSNO, suggesting the successful nitrosylation of these groups. ATR-FTIR spectra further confirmed the success of the nitrosylation process (Figure 4.2.B). Specifically, the peak at 2520 cm^{-1} associated with S-H stretching was present in GSH but disappeared in GSNO, indicating that thiol groups were involved in the nitrosylation reaction. Further confirmation is given by the presence of a new peak at 1477 cm^{-1} in GSNO, corresponding to N=O stretching, which was not present in GSH [51], [52]. Additionally, preliminary tests performed on GSNO stability showed that this compound was stable in water at different pH values for more than 24 h, if kept at 4°C protected from light. Therefore, undesired GSNO degradation is not expected during the functionalization of AC with GSNO, which takes place at pH 5.5 in water.

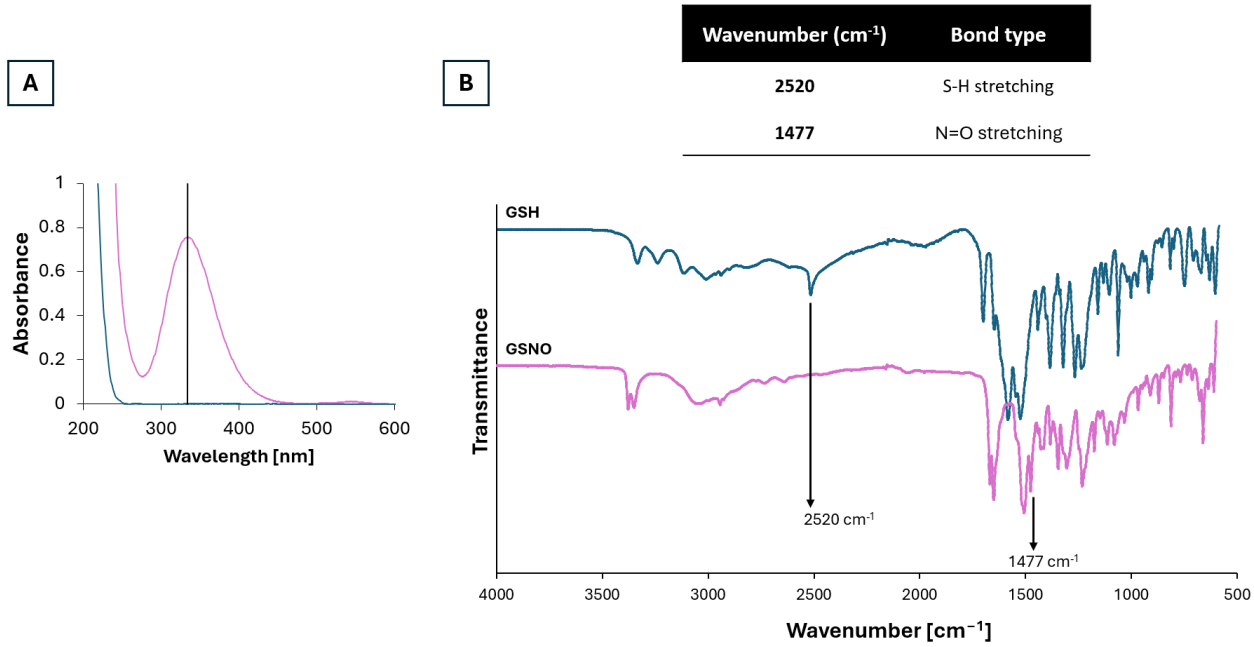


Figure 4.2. GSNO sythesis. (A) UV-vis spectra of GSH (blue) and GSNO (pink) show the appearance of a peak at 335 nm typical of S-NO bond formation. (B) ATR-FTIR of GSH (blue) and GSNO (pink) shows the absence of the peak related to thiols and the presence of a peak corresponding to nitric oxide.

4.3.1.2. Functionalization of amino cellulose with GSNO

GSNO was conjugated to AC, using the carbodiimide chemistry. The ATR-FTIR spectroscopy confirmed the presence of GSNO by the appearance of a peak at 1530 cm^{-1} corresponding to -SNO bonds [53] (Figure 4.3). The GSNO conjugated to AC was quantified directly by measuring the absorbance peak at 335 nm and indirectly by evaluating the amino groups present on AC after the process. The reaction resulted in the conjugation of 0.66 ± 0.02 mg of GSNO per milligram of material, corresponding to 45% of the NH_2 groups on AC being occupied by GSNO. The amine content of AC measured by Kaiser test, showed a decrease from 135.8 ± 7.7 µg GE/ mg of material to 87.5 ± 5.7 µg GE/mg material after conjugation, which corresponds to 36% of the amines being occupied by GSNO. The slightly higher value obtained with the direct quantification was attributed to the specific test conditions. Indeed, AC exhibited a background signal at 335 nm, which may interfere with the accurate quantification of GSNO, leading to an overestimation of the conjugated GSNO. Conversely, direct quantification of primary amines quantifies the groups present in both AC and GSNO. Therefore, the signal obtained in AC-GSNO is a sum of these two contributions. Thus, this test likely underestimates the percentage of reacted amines.

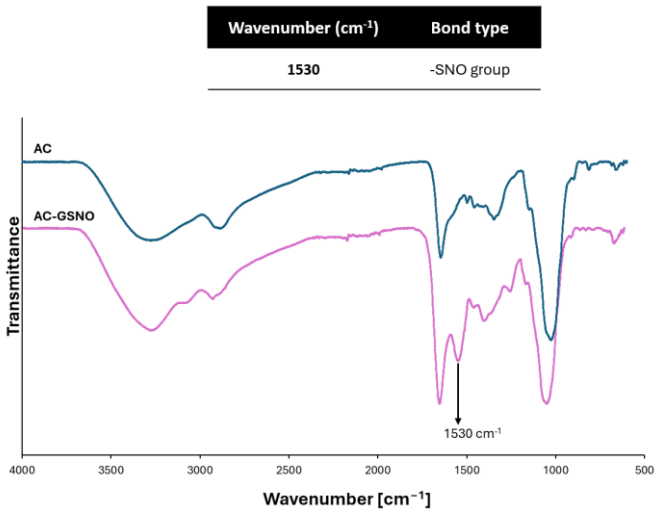


Figure 4.3. ATR-FTIR of GSH (green) and GSNO (pink) showing the appearance of the peak corresponding to nitric oxide.

4.3.1.3. Coating of CoLig NPs with AC-GSNO

CoLig NPs were coated with AC-GSNO and analyzed through DLS. The NO-CoLig NPs presented a larger diameter ($p < 0.001$) of 210 nm and a positive ζ potential of 36 mV, while the size of CoLig NPs was 192 nm with a negative surface charge of -23 mV (Table 4.1). These results confirmed the success of the coating process.

Table 4.1. Summary of NO-CoLig NPs characteristics from DLS analysis.

	Size(nm)	PDI	ζ Potential (mV)
CoLig NPs	192±1	0.22±0.01	-23±0.2
NO-CoLig NPs	210±1	0.26±0.01	36±0.2

4.3.1.4. Cytocompatibility of NO-CoLig NPs

The cytocompatibility of NO-CoLig NPs was assessed on both keratinocytes and fibroblasts (Figure 4.4). NO-CoLig NPs presented reduced cytotoxicity compared to uncoated CoLig NPs. This was expected, since the surface coating shields the cobalt core, reducing its direct interaction with cells and increasing its cytocompatibility. Cobalt inhibits crucial enzymes for mitochondrial respiration, causes calcium signaling dysfunction, and promotes oxidative stress [54]. All these Co-related toxicity mechanisms require direct interaction between the cells and cobalt, which is limited by the AC-GSNO coating, indicating that coating may improve the tolerability of this metal and reduce its toxic effects.

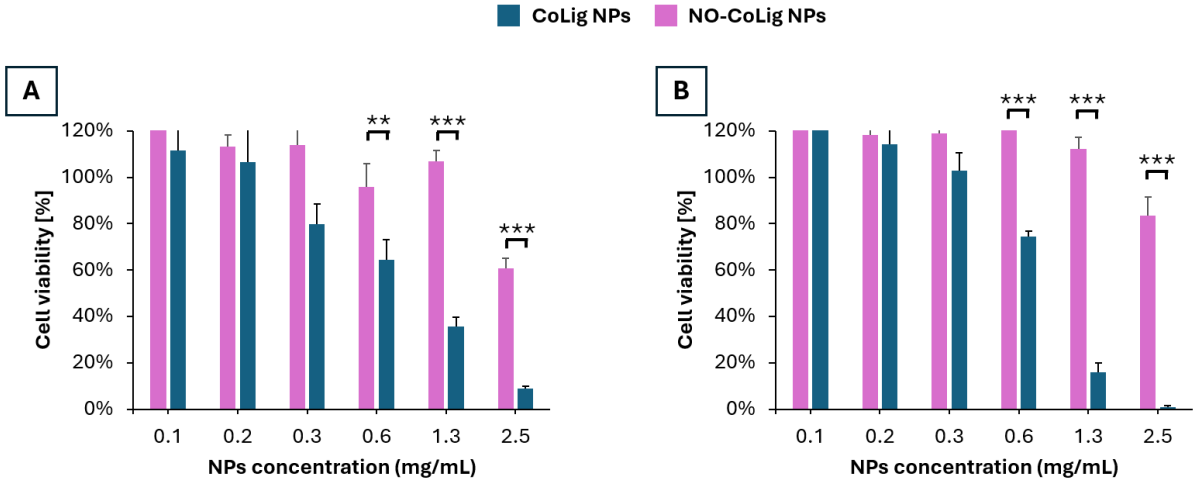


Figure 4.4. The cytocompatibility of NO-CoLig NPs against (A) fibroblasts and (B) keratinocytes.

4.3.1.5. Antibacterial and antibiofilm activity of NO-CoLig NPs

NO-CoLig NPs were tested for their antibacterial and antibiofilm activity against *S. aureus* and *P. aeruginosa*. The NPs presented reduced inhibitory capacity against both bacterial species compared with CoLig NPs (Figure 4.5). Indeed, at 0.6 mg/mL, the concentration selected in Section 3 as promising for combining antibacterial effects with good cytocompatibility, NO-CoLig NPs did not present inhibitory activity on either, *S. aureus* or *P. aeruginosa*. Some antibacterial effects could be observed at 2.5 mg/mL (60% for *S. aureus* and 50% for *P. aeruginosa*). As observed in Section 3, cobalt exerts its antimicrobial activity by interacting with cellular membranes. This reduction in the antibacterial activity can therefore be attributed to the coating, which shields cobalt and reduces its interaction with the bacterial membrane. Additionally, NO-delivery is expected to have an antibacterial activity at concentrations in the µM range [31],[32]. In NO-CoLig NPs the GSNO content could not be measured directly. However, it could be estimated since the coating of CoLig NPs represented no more than 20% of the total NPs mass. Therefore, considering the quantity of GSNO conjugated to AC (estimated to be 0.66 mg GSNO/ mag material), the concentration of NO that could be delivered for NPs at 2.5 mg/mL was in the nM range, which is insufficient to exert antibacterial activity. This, combined with the shielding of the cobalt related to the presence of the coating, explains the reduction in antibacterial activity of NO-CoLig NPs.

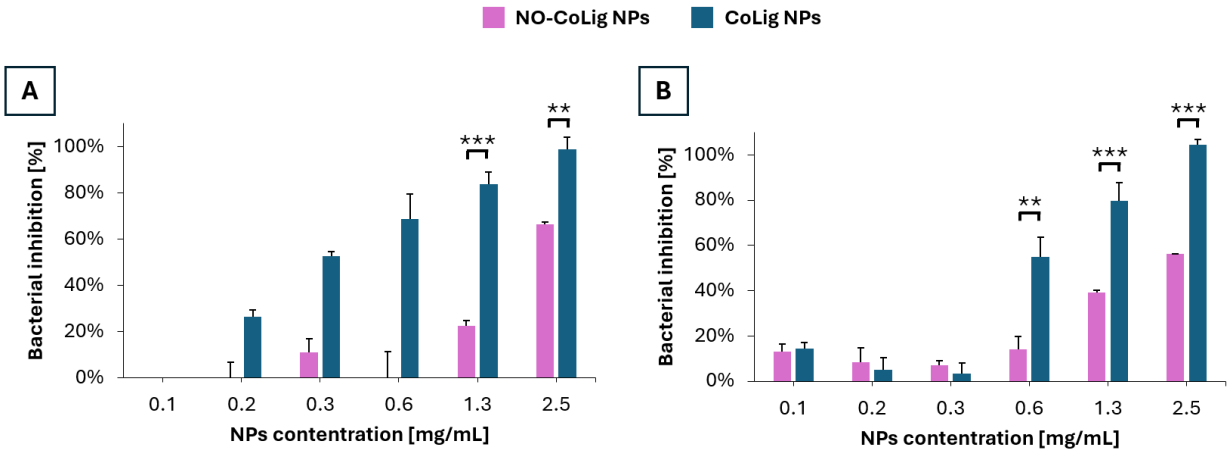


Figure 4.5. Antibacterial activity of NO-CoLig NPs for (A) S. aureus and (B) P. aeruginosa.

NO-CoLig NPs were also analyzed for their antibiofilm action by measuring the change in the mass of the biofilm matrix (Figure 4.6). In the literature, NO delivery in the nM range is known to induce biofilm dispersion [25], [26]. In the previous paragraph, the NO content within NO-CoLig NPs was estimated to be in the nM range at 2.5 mg/mL, thus a value that should exert antibiofilm action. However, for both bacterial species, no reduction of biofilm mass could be observed in the biofilms treated with NO-CoLig NPs compared to untreated biofilm. On the contrary, an increase in the bacteria biomass was observed following a trend similar to the one of uncoated CoLig NPs. Therefore, it may be that the NO release from the NPs does not match the estimated NO content, thus being insufficient to induce antibiofilm effects. Additionally, the increase in biofilm biomass could be related to the lignin-based material as discussed in 3.3.2.3.

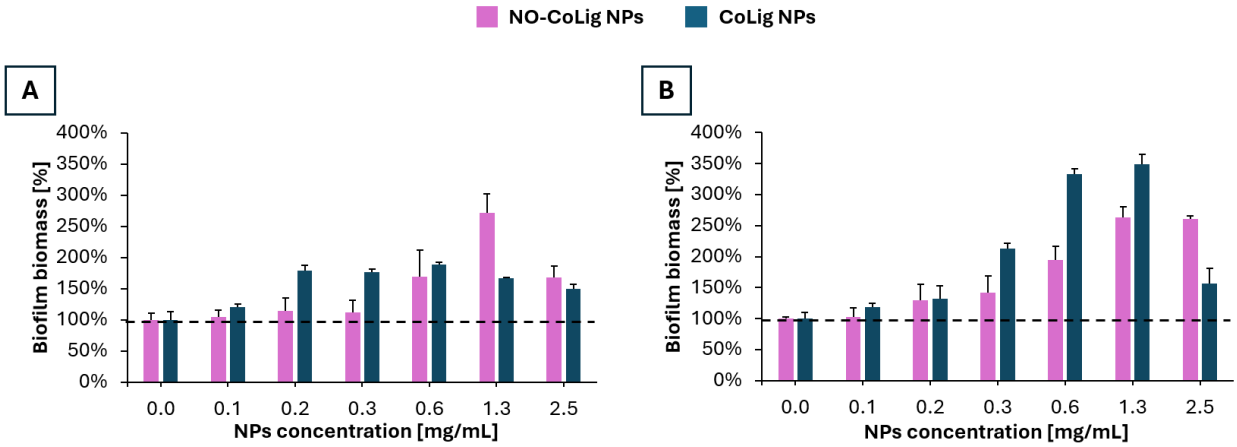


Figure 4.6. Antibiofilm activity of NO-CoLig NPs (pink) compared to uncoated CoLig NPs (blue) against (A) S. aureus and (B) P. aeruginosa. The dotted line indicates 100% of biofilm biomass corresponding to the control.

To better understand the GSNO capacity to induce biofilm dispersion, free GSNO at different concentrations were put in contact with preformed biofilms, showing that only for GSNO concentrations above 5 mg/mL, corresponding to 15 µM of NO, a reduction of biofilm biomass was observed (Annex Figure S4.1). This result is in contrast with the literature in which nM concentrations of NO are capable of inducing biofilm dispersion [25], [26]. In this case, the dissociation of GNSO to produce NO may be low, thus requiring a high amount of GSNO to achieve the NO content necessary to disperse the biofilm. However, such high quantities may not be easily incorporated on the surface of NPs. Indeed, AC-GSNO contains 0.66 mg GSNO per mg of material. Therefore, higher concentrations of NPs may be required to reach sufficient GSNO concentrations, which may not be compatible with the cytocompatibility requirements.

A way to bypass this problem is to exploit alternative mechanisms to induce the decomposition of GSNO to free NO. Indeed, the SNO bond in S-nitrosothiols can be subjected to different decomposition mechanisms, including hydrolysis, homolysis, photolysis, metal-ion mediated decomposition, and enzymatic release [30], [54]. Additionally, some authors showed that integration of GSNO into nanoformulations or hydrogels prevents NO dissociation through these alternative pathways [56], [57], [58]. Therefore, the attachment of GSNO to AC on NPs may prevent NO dissociation, resulting in its suboptimal concentration and in the lack of antibiofilm activity. To accelerate NO release, GSNO degradation may be forced through the application of external stimuli. For instance, preliminary tests to evaluate GSNO stability showed decomposition within 48 h when GSNO was exposed to light. This property could be used to induce NO release *in situ*. Indeed, after UV irradiation, Pelegrino et al. [39] were able to accelerate NO release from chitosan NPs containing GSNO, in *ex vivo* human skin models. Wang et al. [52] exploited temperature

increase to induce NP release from GSNO-loaded dopamine NPs, resulting in enhanced antibacterial activity.

4.3.1.6. Consideration on NO-CoLig NPs

NO-CoLig NPs were successfully obtained and presented adequate dimension and ζ potential. NPs coating enhanced the cytocompatibility, with significant improvements in comparison to CoLig NPs. However, the coating also reduced the antibacterial activity without providing antibiofilm capacity. The quantity of NO released from the system is probably insufficient to induce the antimicrobial and antibiofilm effects observed in other studies [36], [38]. Future tests should consider triggering NO release on-site through light irradiation to induce GSNO degradation.

4.3.2. Synthesis and characterization of CoPc-Lig NPs

4.3.2.1. Optimization of the Lig-TA-LTH content in CoPc-Lig NPs

CoPc-Lig NPs were synthesized by combining CoPc and the lignin-based material obtained in Section 3 (Lig-TA-LTH) at various weight ratios. Lignin is expected to interact with the Pc surface through hydrophobic and π–π stacking interactions, facilitated by the aromatic groups on both compounds. [49]. Furthermore, the presence of Pc in the CoPc complex is expected to provide photoacoustic and photothermal ability to the NPs, while maintaining the antibacterial activity of Co. The synthesis process was optimized in two steps. Firstly, NPs were obtained at a fixed CoPc amount by enhancing the content of Lig-TA-LTH. Then, under the optimal Lig-TA-LTH condition, the amount of CoPc was also varied.

In detail, four different amounts of Lig-TA-LTH were tested, namely 10 mg, 12.5 mg, 15 mg, and 17.5 mg. The samples were named after the amount of Lig-TA-LTH as, CoPc-Lig_10, CoPc-Lig_12.5, CoPc-Lig_15 and CoPc-Lig_17.5. As shown in Table 4.2, the production yield increased with increasing Lig-TA-LTH content, from 4.5% to 6.5% for the sample containing the highest amount of lig-TA-LTH.

Table 4.2. Production yield of CoPc-Lig NPs.

Sample name	Production yield (%)
CoPc-Lig_10	4.5%
CoPc-Lig_12.5	5.9%
CoPc-Lig_15	3.6%
CoPc-Lig_17.5	6.5%

UV-vis was performed on the collected CoPc-Lig NPs as well as on the waste products obtained after washing. The waste products were collected separately after the two washing steps and were analyzed separately with the sample names NPs waste I and NPs waste II. This analysis was performed for all tested Lig-TA-LTH amounts and reported as Annex Figure S4.2. As no differences were observed in the UV profiles of the different samples, hereafter representative graphs indicative of the CoPc-Lig_17.5 sample are commented. The collected CoPc-Lig NPs present a similar UV spectrum, with two adsorption peaks at 630 nm and 710 nm, as the bare CoPc, confirming that the compound was present in the NPs. A similar spectrum profile was detected for NPs waste II, which was collected during the second washing step at low centrifugation speed (Figure 4.7). On the other hand, in the sample NPs-waste I, no peaks indicative of CoPc were found and the spectrum was more similar to that of Lig-TA-LTH. These results indicated that the first

centrifugation step mainly eliminated the unreacted Lig-TA-LTH, while unreacted CoPc and CoPc-Lig NPs aggregates were removed during the second centrifugation step.

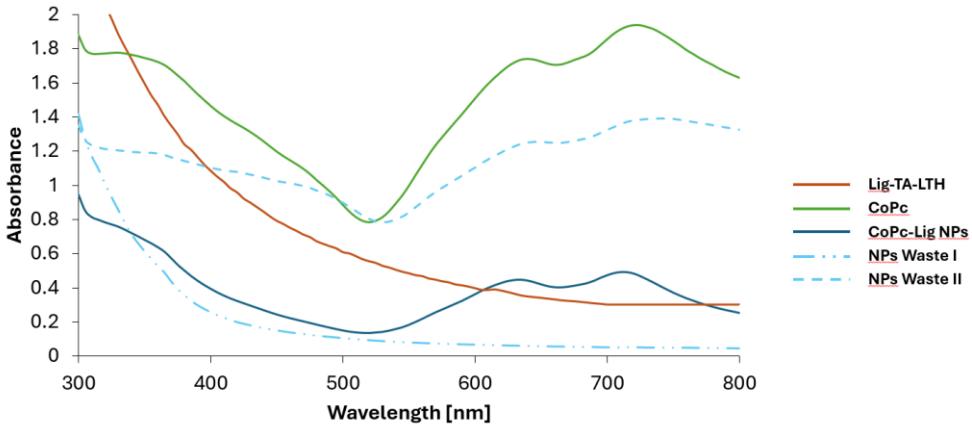


Figure 4.7. UV-vis spectra of the collected CoPc-Lig NPs and spectra of the residual products collected after the two centrifugation steps (the analysis is relative to the representative sample CoPc-Lig_17.5). Spectra of the starting materials are reported for reference.

ATR-FTIR spectroscopy was also conducted on the same samples, with representative results for the CoPc-Lig_17.5 sample, reported in Figure.4.8-Figure 4.13. The spectra of all other samples are reported in Annex Figures S4.3-S4.5 The Lig-TA-LTH material is characterized by peaks at [59], [60]:

- 3400 cm^{-1}, corresponding to the stretching of the O-H bond on the aromatic ring;
- 2840 and 2920 cm^{-1}, related to the C-H stretching of methyl groups;
- 1700 cm^{-1}, attributed to C=O stretching of non-conjugated carbonyl;
- 1590 cm^{-1}, related to the aromatic ring vibration;
- 1210 cm^{-1}, corresponding to the aromatic C–O stretching;
- 1030 cm^{-1}, attributed to the OH stretching of primary alcohols.

While CoPc characteristic peaks that can be identified at [61]:

- 1520 cm^{-1}, related to the C=N stretching;
- 1090 cm^{-1}, attributed to the deformation of in-plane C-H bonds;
- 780 cm^{-1}, related to the C=N vibration;
- 755 cm^{-1}, corresponding to the Co-N vibration;
- 730 cm^{-1}, attributed to the deformation of out-of-plane C-H bonds.

As shown in Figure.4.8-Figure 4.9, CoPc-Lig NPs presented characteristic peaks of both, Lig-TA-LTH and CoPc. Interestingly, the peak at 3400 cm^{-1}, corresponding to the stretching of the O-H bond on the aromatic ring of Lig-TA-LTH, appeared slightly shifted in CoPc-Lig NPs, suggesting an interaction of the CoPc compound with the phenolic groups of Lig-TA-LTH. The waste collected after the first centrifugation presented only the characteristic peaks of lignin (Figure 4.10-Figure 4.11) while the waste collected after the second centrifugation, only exhibited the characteristic peaks of CoPc (Figure 4.12-Figure 4.13). These results confirm the observations after UV-Vis analysis.

Wavenumber (cm^{-1})	Lignin related bonds
1030	OH stretching of primary alcohol
1210	Aromatic C–O stretching
1590	Aromatic ring vibration
1700	C=O stretching non-conjugated carbonyl
2840-2920	C-H stretching of methyl groups
3400	stretching of the O-H bond on the aromatic ring

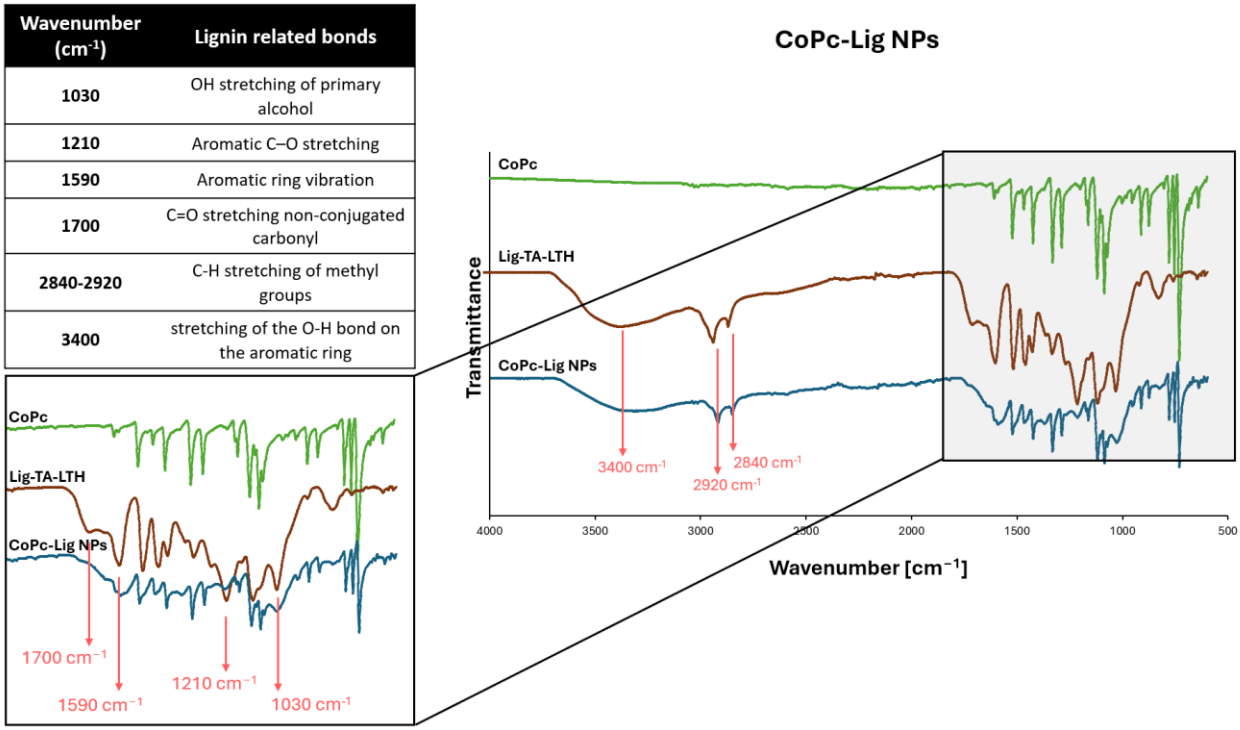


Figure.4.8. ATR-FTIR spectra of the CoPc-Lig NPs (representative sample CoPc-Lig_17.5) in comparison to the spectrum of bare Lig-TA-LTH

Wavenumber (cm^{-1})	CoPc related bonds
730	C-H out of plane deformation
755	Co-N bond vibration
780	C=N in plane stretching vibration
1090	C-H in plane deformation
1520	C=N stretching

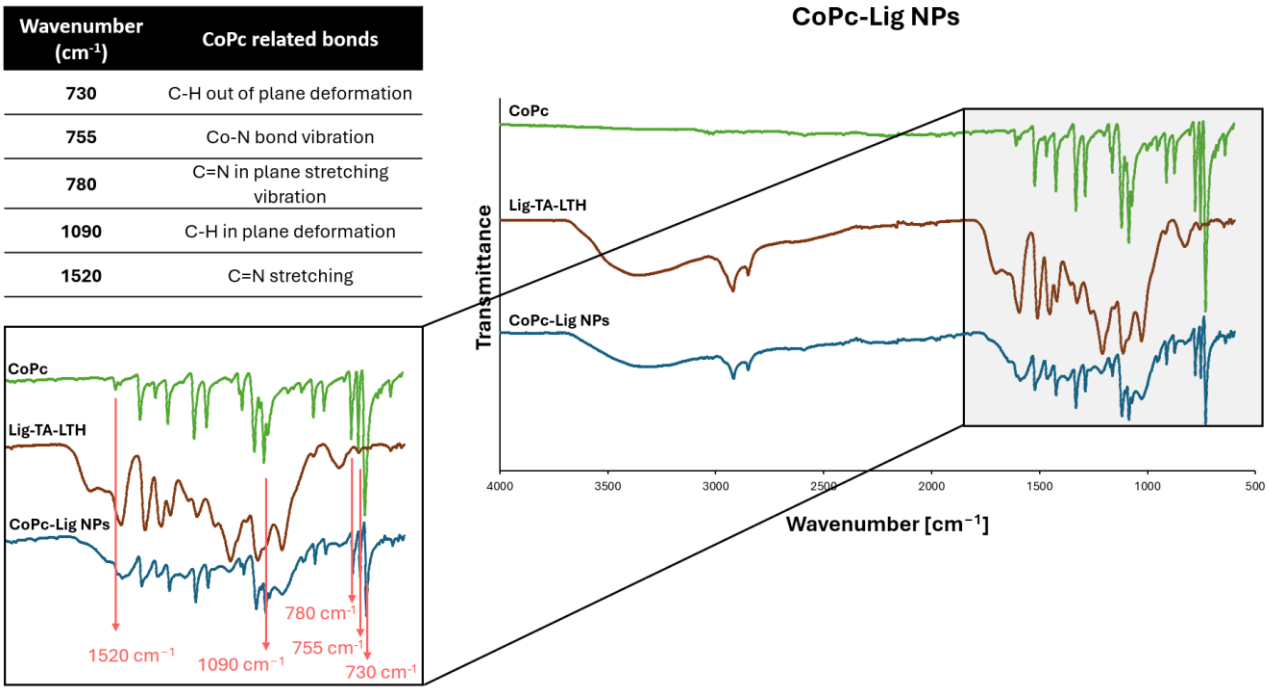


Figure 4.9. ATR-FTIR spectra of the CoPc-Lig NPs (representative sample CoPc-Lig_17.5) in comparison to the spectrum of bare CoPc.

Wavenumber (cm^{-1})	Lignin related bonds
1030	OH stretching of primary alcohol
1210	Aromatic C–O stretching
1590	Aromatic ring vibration
1700	C=O stretching non-conjugated carbonyl
2840-2920	C-H stretching of methyl groups

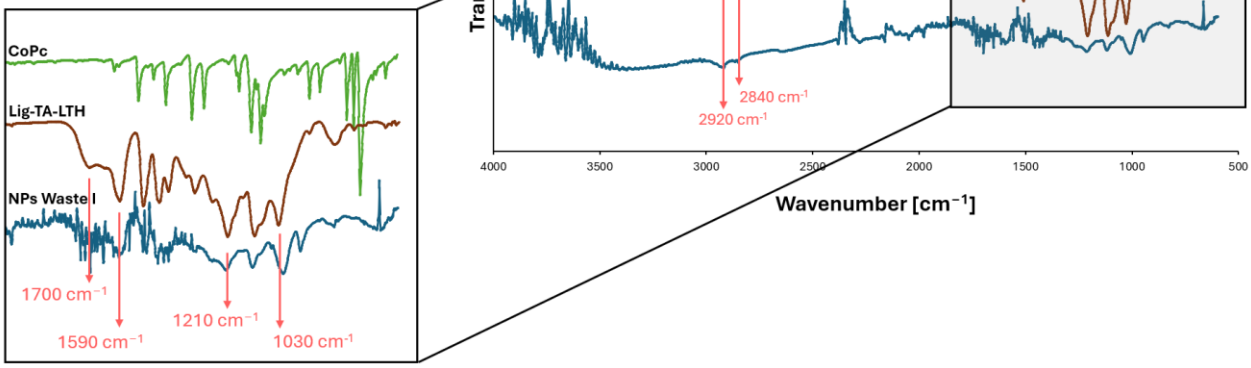


Figure 4.10. ATR-FTIR spectra of the collected residues after the first centrifugation step (representative sample CoPc-Lig_17.5) in comparison to the spectrum of bare Lig-TA-LTH.

Wavenumber (cm^{-1})	CoPc related bonds
730	C-H out of plane deformation
755	Co-N bond vibration
780	C=N in plane stretching vibration
1090	C-H in plane deformation
1520	C=N stretching

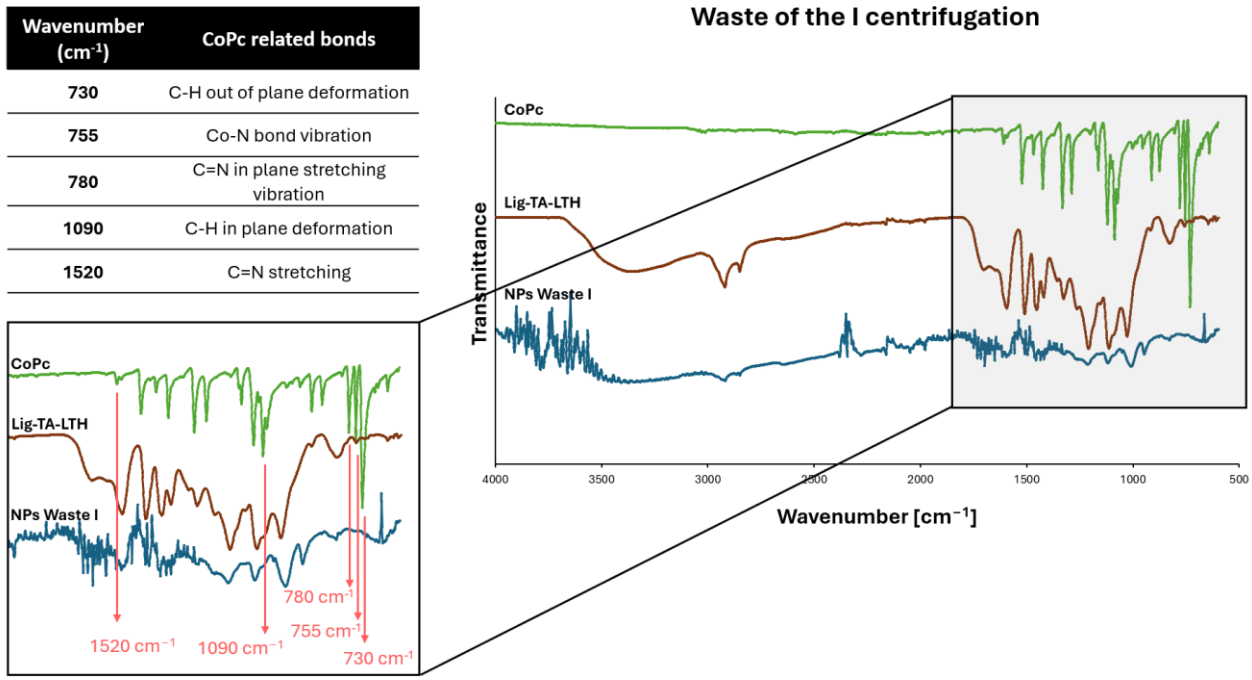


Figure 4.11. ATR-FTIR spectra of the collected residues after the first centrifugation step (representative sample CoPc-Lig_17.5) in comparison to the spectrum of bare CoPc.

Wavenumber (cm^{-1})	Lignin related bonds
1030	OH stretching of primary alcohol
1210	Aromatic C–O stretching
1590	Aromatic ring vibration
1700	C=O stretching non-conjugated carbonyl
2840-2920	C-H stretching of methyl groups

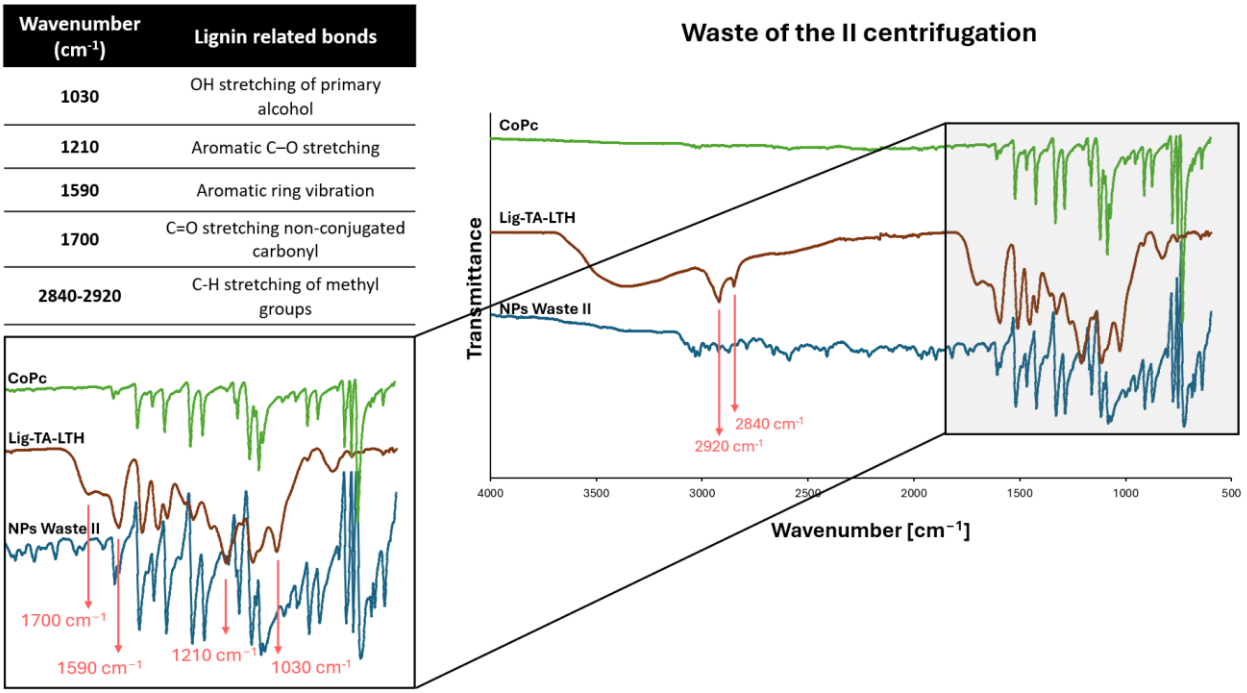


Figure 4.12. ATR-FTIR spectra of the collected residues after the second centrifugation step (representative sample CoPc-Lig_17.5) in comparison to the spectrum of bare Lig-TA-LTH.

Wavenumber (cm^{-1})	CoPc related bonds
730	C-H out of plane deformation
755	Co-N bond vibration
780	C=N in plane stretching vibration
1090	C-H in plane deformation
1520	C=N stretching

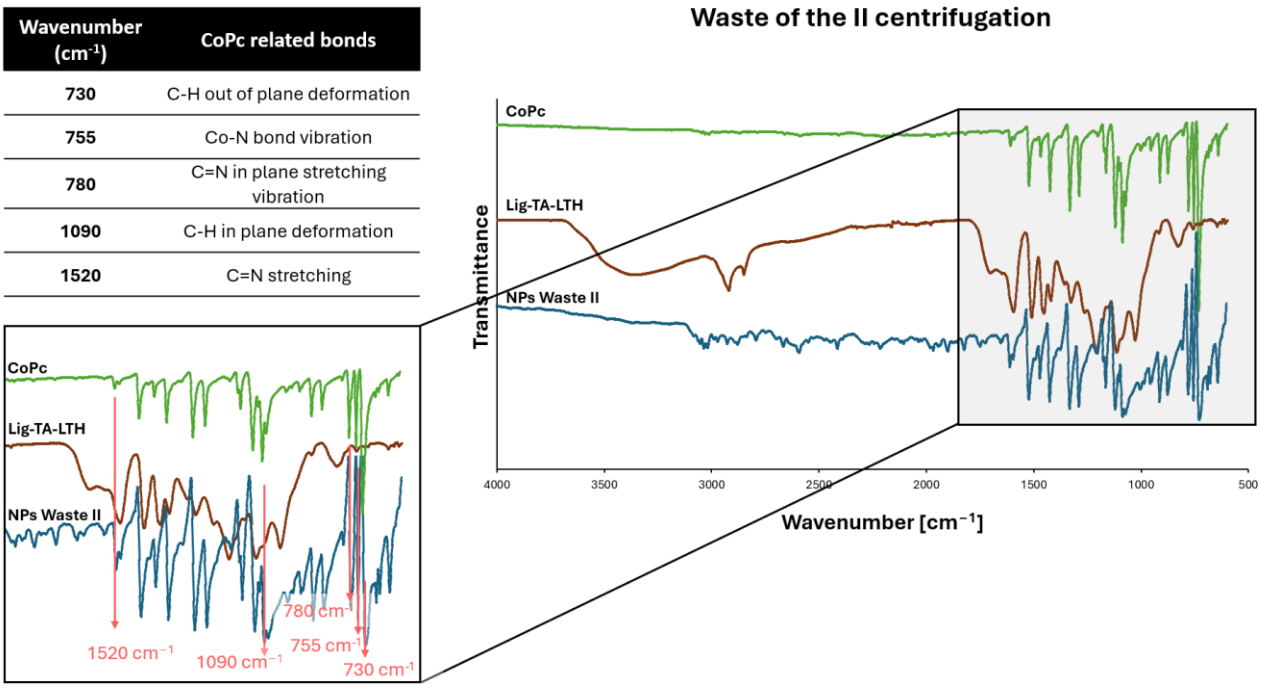


Figure 4.13. ATR-FTIR spectra of the collected residues after the second centrifugation step (representative sample CoPc-Lig_17.5) in comparison to the spectrum of bare CoPc.

DLS analysis of CoPc-Lig NPs is reported in Table 4.3. Regardless of the amount of Lig-TA-LTH, all NPs displayed a small size of around 200-230 nm and a low PDI (< 0.2), indicating monodispersed NPs. However, a deeper examination of the size distributions highlighted some differences among the tested conditions (Figure 4.14.A-D). In particular, DLS profiles of samples CoPc-Lig_10, CoPc-Lig_12.5 and CoPc-Lig_15 showed a polydisperse distribution with two peaks in the volume-

weighted and in the number-weighted distributions. In detail, a second peak corresponding to a population of NPs with smaller diameters was observed. The NPs obtained with an amount of Lig-Ta-LTH of 17.5 mg (sample CoPc-Lig_17.5) showed a monodispersed distribution for all conditions (number-, intensity, and volume-weighted) with overlapping profiles. This confirms the monodispersity of the sample, as also indicated by its lowest PDI (0.14). These results suggest an optimal interaction between CoPc and Lig-TA-LTH under this condition.

All the NPs presented negative ζ potential values, ranging from -29 to -32 mV, which were intermediate between the ζ potential values of CoPc (-28±0.3 mV) and Lig-TA-LTH (-40±0.8 mV), suggesting interactions between the two components. The condition with the lowest superficial charge was the CoPc-Lig_17.5, which, in accordance with the results from size and PDI, suggests an optimal interaction between Lig-TA-LTH and CoPc. This sample also presented the highest production yield (Table 4.3). For these reasons, an amount of Lig-TA-LTH of 17.5 mg was selected for further optimization.

Table 4.3. Summary of CoPc-Lig NPs characteristics from DLS analysis.

	Size (nm)	PDI	ζ Potential (mV)
CoPc-Lig_10	238±13	0.18±0.03	-29±0.3
CoPc-Lig_12.5	194±3	0.16±0.04	-30±0.2
CoPc-Lig_15	190±4	0.17±2	-31±0.5
CoPc-Lig_17.5	247±1	0.14±0.03	-32±0.5

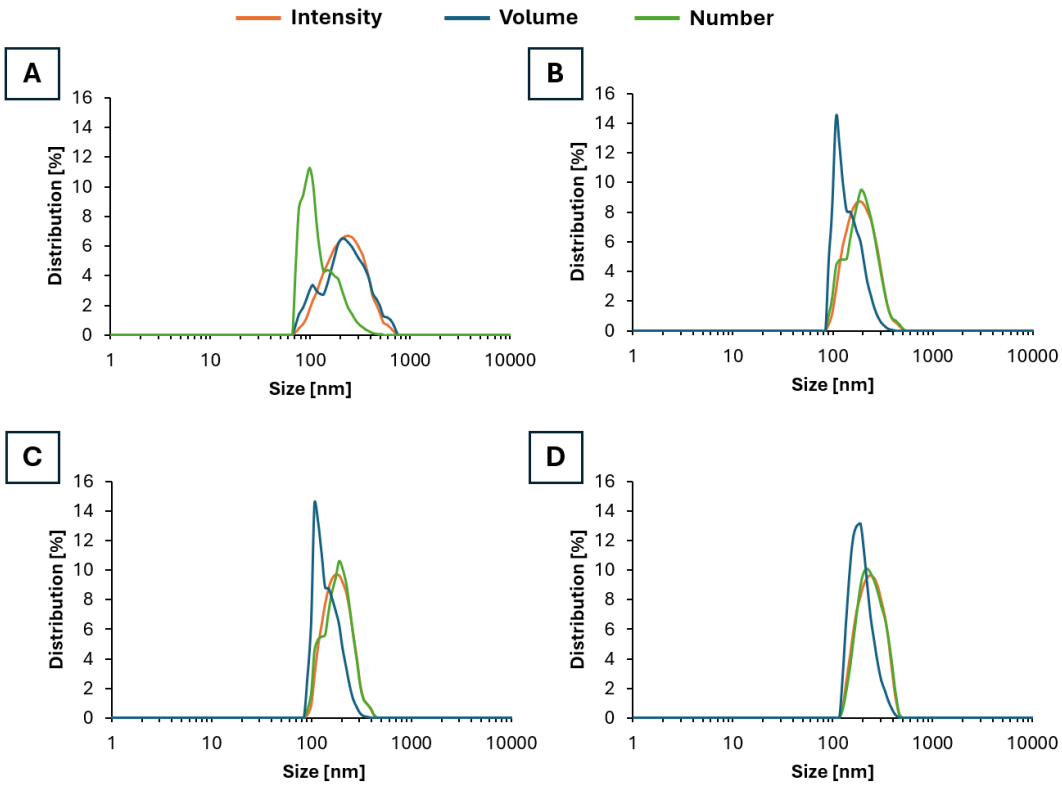


Figure 4.14. Intensity (orange), volume (blue), and number (green) - weighted size distribution functions for the CoPc-Lig NPs for samples (A) CoPc-Lig_10, (B) CoPc-Lig_12.5 (C) CoPc-Lig_15 (D) CoPc-Lig_17.5.

4.3.2.2. Optimization of the CoPc content in CoPc-Lig NPs

After fixing the amount of Lig-Ta-LTH to 17.5 mg, NPs were further optimized by varying the CoPc content. Starting from the initial 12 mg of CoPc (12_CoPc-Lig_17.5), the content was reduced to 8 mg and 4 mg, obtaining 8_CoPc-Lig_17.5 and 4_ CoPc-Lig_17.5, respectively.

For these new batches of NPs, the production yield was similar, ranging from 4.6% to 6.5% (Table 4.4). Additionally, UV-vis and ATR-FTIR spectroscopy were performed on the NPs and the corresponding waste from the two centrifugation steps. Both UV-vis and ATR-FTIR spectra confirmed the previous observations (Annex Figure S4.2 and Figures S4.6-S4.8), indicating that the CoPc-Lig NPs presented signals of both, Lig-TA-LTH and CoPc and that the first centrifugation step eliminated the unreacted Lig-TA-LTH, while the second centrifugation removed the unreacted CoPC and NPs agglomerates.

Table 4.4. Production yield of CoPc-Lig NPs.

Sample name	Production yield (%)
12_CoPc-Lig_17.5	6.5%
8_CoPc-Lig_17.5	4.6%
4_CoPc-Lig_17.5	6%

DLS analysis (Table 4.5) showed a similar size for all NPs, ranging from 230 nm for the lowest CoPc content to 247 nm for the particles containing 12 mg of CoPc. PDI values slightly increased with decreasing CoPc content from 0,14 for 12_CoPc-Lig_17.5 to 0,21 for 4_CoPc-Lig_17.5. DLS profiles (Figure 4.15) indicate monodispersed distribution, with the appearance of small additional peaks related to larger subpopulation in the volume-weighted and number-weighted size distributions of 4_CoPc-Lig_17.5. Particles obtained with the highest CoPc content displayed the lowest ζ Potential value.

These results suggest that the interaction between Lig-TA-LTH and CoPC is more stable for the NPs with higher CoPc content.

Table 4.5. Summary of CoPc-Lig NPs characteristics obtained from DLS analysis.

	Size (nm)	PDI	ζ Potential (mV)
12_CoPc-Lig_17.5	247±1	0.14±0.03	-31.7±0.5
8_CoPc-Lig_17.5	232±1	0.19±0.03	-28.9±0.2
4_CoPc-Lig_17.5	231±6	0.21±0.03	-30.2±0.2

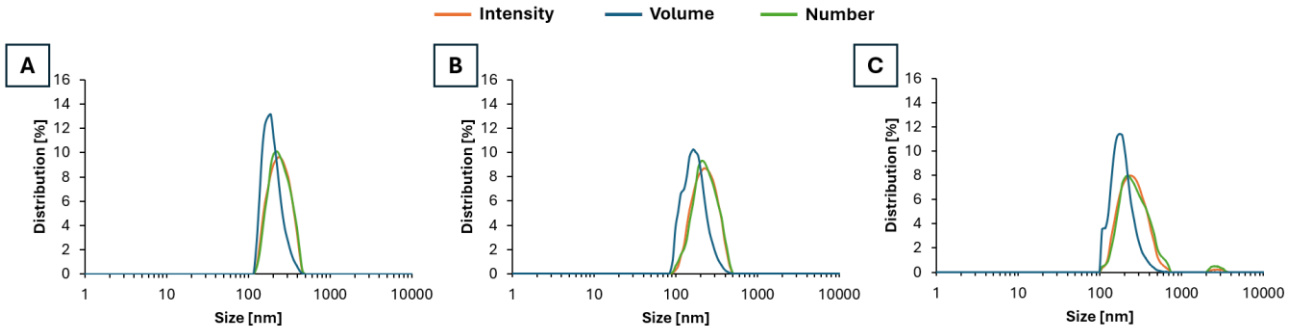


Figure 4.15. Intensity (orange), volume (blue), and number (green) - weighted size distribution functions for the CoPc-Lig NPs for samples (A) 12_CoPc-Lig_17.5, (B) 8_CoPc-Lig_17.5 (C) 4_CoPc-Lig_17.5.

To assess the antioxidant capacity of the NPs, DPPH assay was performed. Table 4.6 shows that all conditions tested presented ROS scavenging activity at the concentration of 0.2 mg/mL. These antioxidant properties of the NPs were mainly attributed to the presence of lignin since no evidence in the literature was found suggesting a direct antioxidant action of CoPc. This confirms the presence of lignin in all formulations. The CoLig NPs developed in Section 3 presented minimal total ROS scavenging concentration at 2.5 mg/mL (Section 3.3.2.1.). Therefore, the CoPc-Lig NPs presented antioxidant properties at a more than 12-fold lower concentration as compared to Co-Lig NPs. This could be related to the higher availability of the phenolic groups in Lig-Ta-LTH, which are less involved in cobalt reduction in this formulation.

Table 4.6. Minimal NPs concentration to observe the antioxidant activity.

	Min. concentration to have DPPH inhibition (mg/mL)
12_CoPc-Lig_17.5	0.2
8_CoPc-Lig_17.5	0.2
4_CoPc-Lig_17.5	0.2

Given the DLS results and the similar trend in antioxidant activity among the three formulations, the 12_CoPc-Lig_17.5 NPs were selected for further characterization and referred to hereafter as CoPc-Lig NPs.

4.3.2.3. Morphological characterization of CoPc-Lig NPs through TEM

TEM imaging of CoPc-Lig NPs (Figure 4.16.A) shows that NPs presented an irregular round shape. EDX analysis confirmed the presence of cobalt homogeneously distributed within the NPs (Figure 4.16.B).

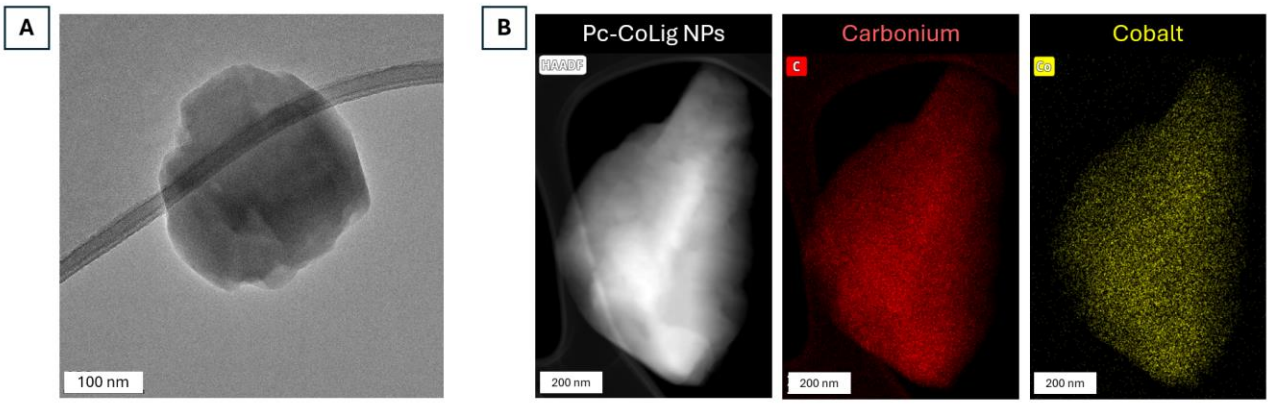


Figure 4.16. CoPc-Lig NPs morphology analyzed by TEM microscopy. (A) TEM image of CoPc-Lig NPs. (B) EDX analysis coupled to TEM imaging for CoPc-Lig NPs, showing the distribution of Carbonium (red) and Cobalt (yellow) in the NPs matrix.

4.3.2.4. MMPs inhibitory activity of CoPc-Lig NPs

CoPc-Lig NPs exhibited a 50% inhibition of MMPs activity at 0.4 mg/mL and over 80% inhibition at 0.8 mg/mL (Figure 4.17). The CoLig NPs developed in Section 3 presented MMPs inhibition above 80% at a concentration of 2 mg/mL. Therefore, the MMPs inhibitory activity of CoPc-Lig NPs is achieved at 2-fold lower concentration in comparison to CoLig NPs. This further confirms that Lig-TA-LTH in this formulation may have a higher amount of free phenolic groups and therefore maintains a better antioxidant and anti-inflammatory potential in comparison to CoLig NPs.

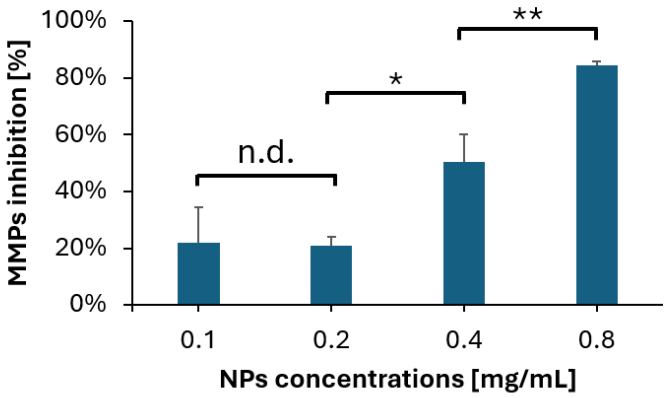


Figure 4.17. MMPs inhibition of CoPc-Lig NPs

4.3.2.5. Cytocompatibility of CoPc-Lig NPs

CoPc-Lig NPs showed cytocompatibility for all tested concentrations on both, fibroblasts and keratinocytes (Figure 4.18.A). The content of Co in the CoPc-Lig NPs, measured through ICP-MS analysis, was 15.7 ± 3.9 µg Co/mg NPs and corresponded to 60 µg Co/mL for the maximal concentration tested in the cytocompatibility assay. Interestingly, the CoLig NPs obtained in Section 3 presented toxicity at an equivalent Co concentration. This suggests that Co cytotoxic activity is reduced in CoPc-Lig NPs, probably due to its coordination in the CoPc complex and to the presence of the Lig-TA-LTH matrix.

Confocal microscope observations show that CoPc-Lig NPs were internalized by both cell types (Figure 4.18.B) and dispose around cell nuclei in both cell types. This further confirms the cytocompatibility of CoPc-Lig NPs.

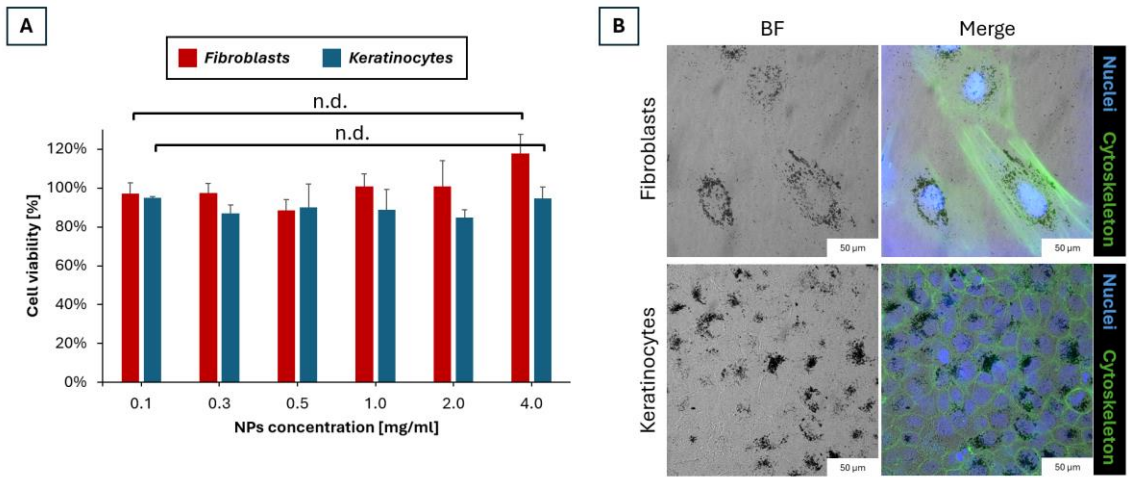


Figure 4.18. Cytocompatibility of CoPc-Lig NPs. (A) Cell viability of fibroblast and keratinocytes exposed to different concentrations of CoPc-Lig NPs. (B) The internalization of CoPc-Lig NPs at 0.5 mg/mL within cells. Dark spots are NPs, blue indicates cell nuclei and green stains the cytoskeleton. BF: brightfield.

4.3.2.6. Antibacterial activity

The CoPc-Lig NPs were tested for their antibacterial activity against *S. aureus* and *P. aeruginosa.* The CFU assay showed that the NPs at 4 mg/mL could inhibit *S. aureus* growth with a 4.8 log reduction (Figure 4.19.A). No inhibition for *P. aeruginosa* was observed at the tested concentrations. This could be correlated to the Co content within the NPs. Indeed, at 4 mg/mL the Co concentration was 60 µg/mL. In the CoLig NPs obtained in the previous Section, the Co contents required for *S. aureus* and *P. aeruginosa* inhibition were 50 µg/mL and 100 µg/mL, respectively. Therefore, the results obtained for CoPc-Lig NPs for *S. aureus* are in accordance with what was observed for CoLig NPs. Additional tests at higher concentrations are required to confirm the antibacterial activity against *P. aeruginosa.* Antibiofilm tests at the same concentrations did not show antibiofilm activity. However, this was expected since CoPc itself is not known for antibiofilm properties. Indeed, the antibiofilm capacity of the NPs should stem from their photothermal activity, for which internalization in the biofilm is fundamental. CoPc-Lig NPs presented a negative surface charge, which is not considered favorable for biofilm interactions [62]. Nevertheless, CoPc-Lig NPs internalized into both bacteria biofilms, visible in the blue coloration related to CoPc. This phenomenon was particularly evident in *S. aureus* biofilm, for which an internalization of around 30% of the NPs dose was measured (see Figure 4.19.B). SEM imaging was used to confirm the internalization capacity of CoPc-Lig NPs in biofilms. Both *P. aeruginosa* and *S. aureus* biofilms treated with CoPc-Lig NPs presented agglomerated material, absent in untreated biofilm (Figure 4.20.A). EDX test confirmed the presence of Co in the biofilms treated with CoPc-Lig NPs, supporting the hypothesis that the observed agglomerations were CoPc-Lig NPs (Figure 4.20.B-C).

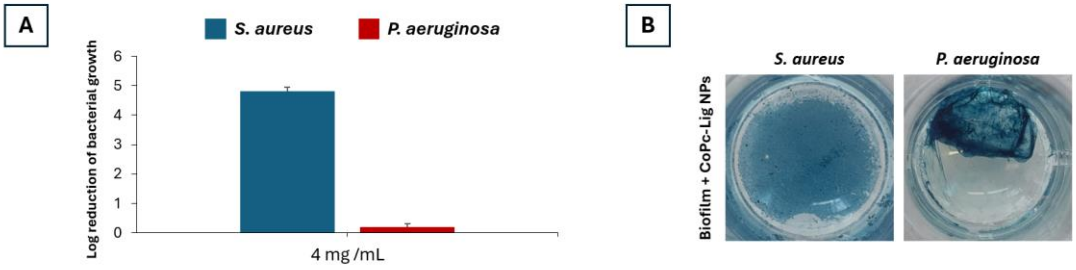


Figure 4.19. Antibacterial activity of CoPc-Lig NPs. (A) CFU test for S. aureus and P. aeruginosa treated with CoPc-Lig NPs at 4 mg/mL. (B) The internalization of CoPc-Lig NPs into S. aureus and P. aeruginosa biofilms.

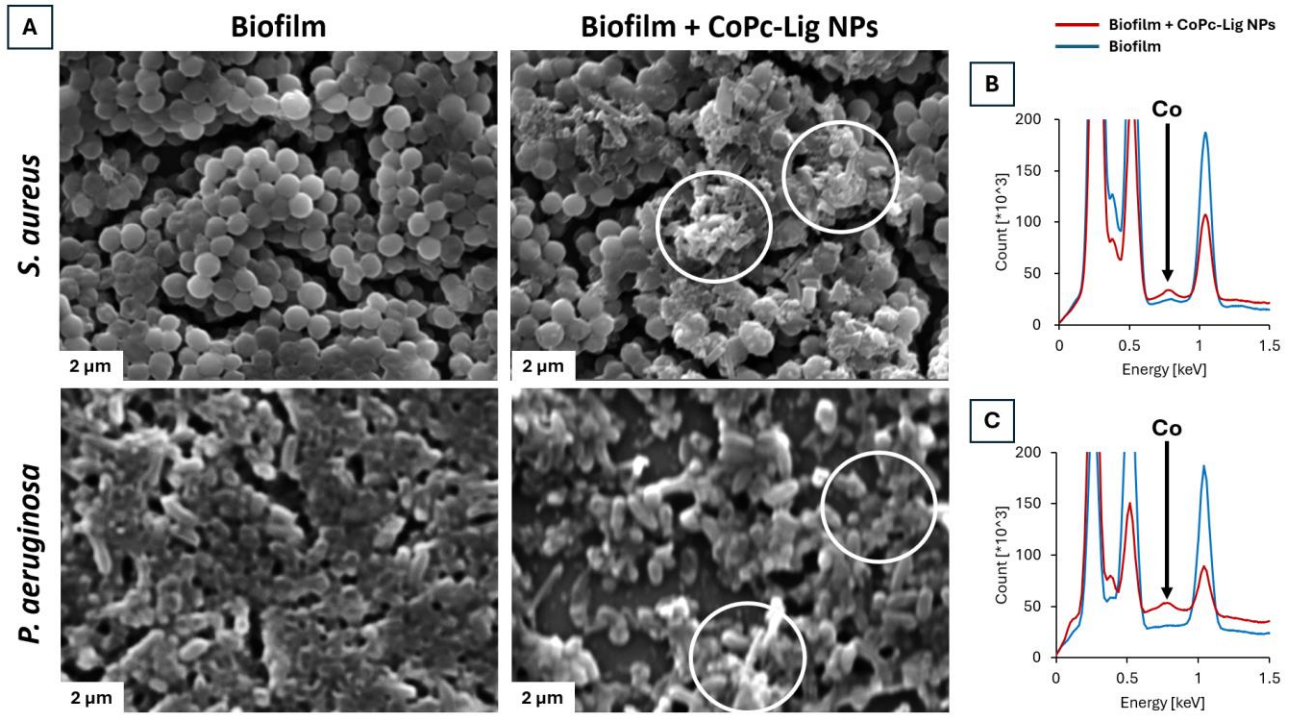


Figure 4.20. Internalization of CoPc-Lig NPs into S. aureus and P. aeruginosa biofilms. (A) SEM images of CoPc-Lig NPs at 0.5 mg/mL. White circles indicate NPs agglomerates. (B-C) EDX spectrum showing the appearance of the peak typical of Co in biofilm treated with CoPc-Lig NPs (red) compared to untreated biofilms (blue) for (B) S. aureus and (C) P. aeruginosa.

4.3.2.7. Photothermal activity

The photothermal effect of CoPc-Lig NPs within the biofilm matrix was studied under NIR irradiation. The NPs were internalized inside the biofilm and the increase of temperature of the matrix was measured. The biofilm treated with CoPc-Lig NPs showed a 7 °C increase in temperature after 2 min of irradiation at 660 nm (Figure 4.21), while the untreated biofilm did not register significant temperature variations under the same treatment conditions (Annex Figure S4.9). Literature reports an antibacterial effect for temperatures above 50 °C [63]. However, these temperatures can also damage the surrounding tissue, since they result in permanent protein denaturation and cytotoxicity [64]. Therefore, they are not optimal for treating conditions in which normal cells and bacteria are heavily intertwined, as in CWs. Interestingly, mild heat treatments at around 45 °C showed to burst the potency of conventional antimicrobials and overcome the resistance mechanisms in bacteria [46], [65]. Additionally, mild heat treatment at 40-42 °C can stimulate tissue regeneration in CWs, inducing endothelial cell maturation and promoting vascularization [66], [67]. Therefore, photothermal treatments for CWs should focus on achieving temperatures between 42 and 45 °C. The thermal gradient observed in the CoPc-Lig NPs falls within this range, making these NPs promising for CWs treatment, as they have the potential to potentiate the antimicrobial properties of cobalt, while simultaneously inducing tissue regeneration.

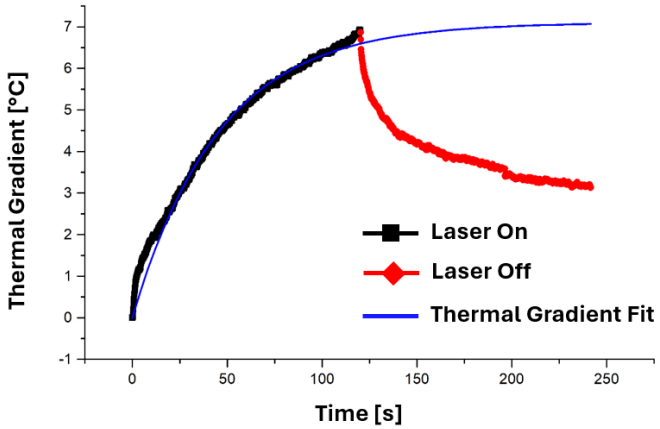


Figure 4.21. Photothermal activity of CoPc-Lig NPs for treated biofilm. The graph presents the increase of temperature following NIR light excitation (black line) of the CoPc-Lig NPs internalized into S. Aureus biofilms. After two minutes of irradiation, a temperature increase of 7 °C was observed. The temperature rapidly decreased when the NIR stimulation was removed (red line). Using these data, it was possible to obtain a Thermal gradient fit indicating the expected increase in temperature if the laser is maintained active for a longer time (Blue line).

To evaluate the effect of the thermal increment on bacteria biofilms, S. aureus and P. aeruginosa biofilms with CoPc-Lig NPs were treated with NIR irradiation, and the bacteria viability was evaluated (Figure 4.22). Immediately after NIR irradiation, the bacteria viability decreased by 40% and 25% for S. aureus and P. aeruginosa, respectively (Figure 4.22.A). This result is promising since it proves that the photothermal treatment with the CoPc-Lig NPs affected the bacteria within the biofilm. Nevertheless, the NIR treatment is not sufficient to kill the bacteria and eliminate the biofilm and after 24 h the viability is restored (Figure 4.22.B).

Additionally, the integrity of S. aureus biofilm was observed through fluorescence and SEM microscopy. P. aeruginosa biofilms could not be analyzed due to technical issues in the biofilm handling. Figure 4.23 shows the CoPc-Lig NPs distribution (brightfield images), the bacteria distribution (fluorescence images) and the colocalization of CoPc-Lig NPs within the biofilm (merged images). The treatment with NIR actively reduced the biofilm integrity, promoting its disruption. This increased fragility could also be perceived during sample preparation.

These results suggest that the NIR treatment is not sufficient to kill the bacteria but has an impact on bacteria viability and biofilm integrity. To completely eradicate the infection, repeated treatments may be necessary combined with stronger antibacterial agents, such as broad-spectrum antibiotics or the CoLig NPs developed in Section 3. Indeed, photothermal treatments have been shown to improve the potency of antibacterial compounds [46], [47]. Additionally, the increased fragility of the biofilm after NIR treatment could facilitate its mechanical removal through debridement. The combination of CoPc-Lig NPs-mediated mild photothermal treatment with antibacterial agents and debridement will be investigated more deeply in future experiments.

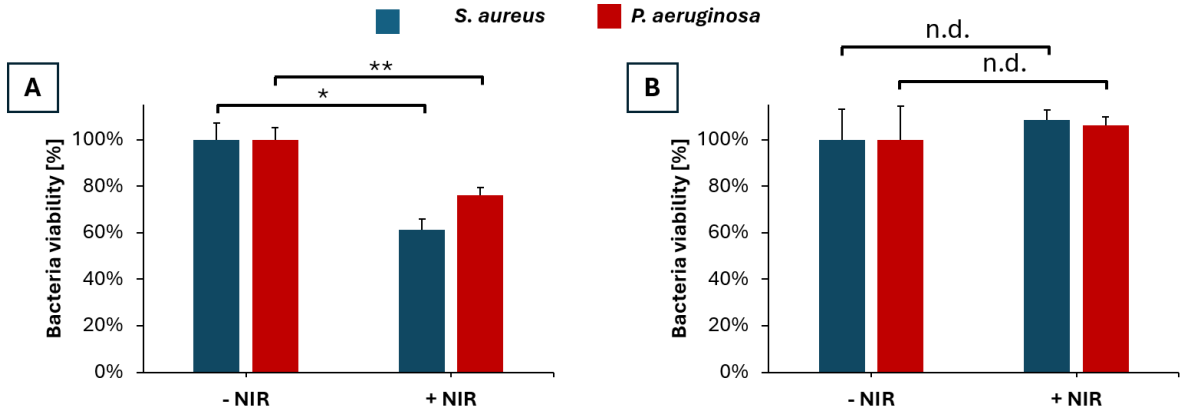


Figure 4.22. S. aureus (blue) and P. aeruginosa (red) viability within biofilm treated with CoPc-Lig NPs before (- NIR) and after (+ NIR) treatment with NIR irradiation. The viability was assessed (A) immediately after treatment and (B) after 24 h.

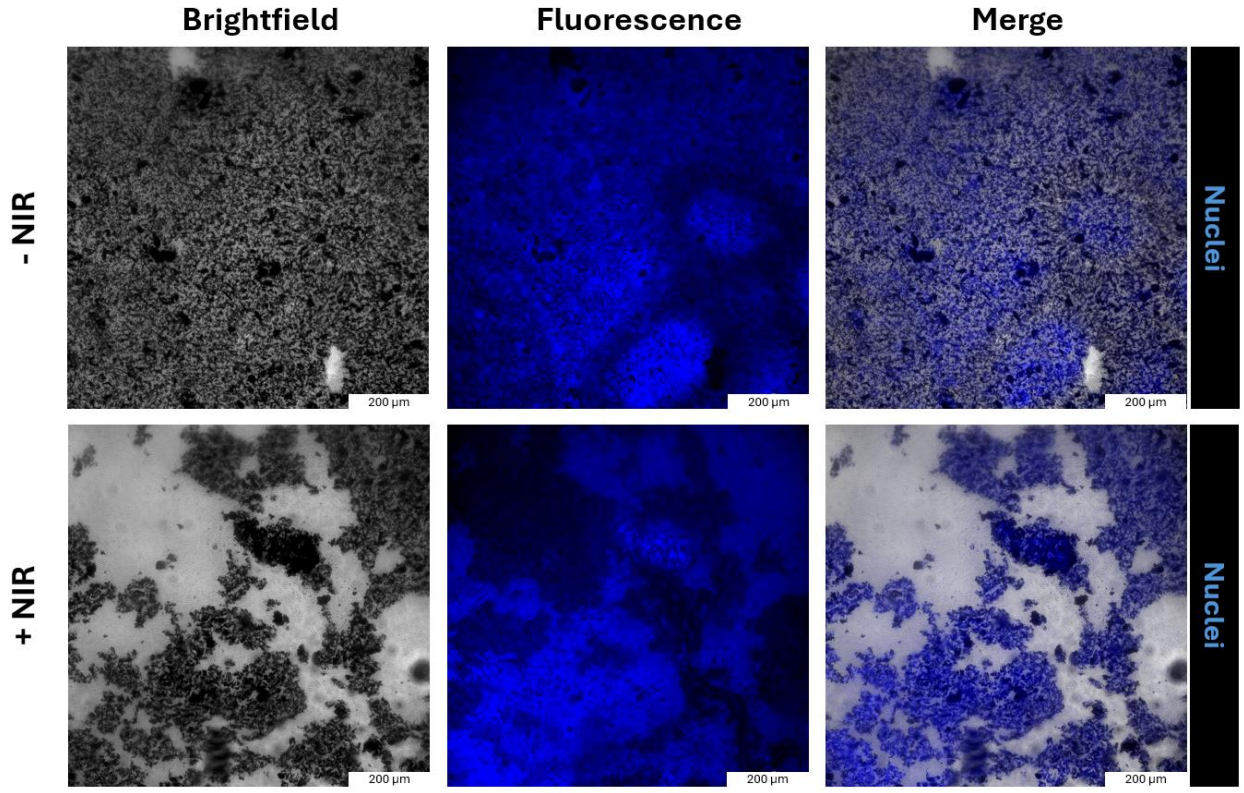


Figure 4.23. Morphology of the S. aureus biofilm before (- NIR) and after (+ NIR) treatment with NIR irradiation. Brightfield images show CoPc-Lig NPs, fluorescence images show the bacteria nuclei and the merged images show the colocalization of NPs and bacteria cells.

4.3.2.8. Photoacoustic activity

Given the CoPc-Lig NPs excitability in the NIR spectrum, the PA activity of these NPs was also tested. This property was studied under three conditions: NPs suspended in an aqueous medium (Figure 4.24.A), NPs injected into animal muscular tissue *ex vivo* (Figure 4.24.B) and NPs internalized within *S. aureus* biofilm (Figure 4.24.C). For all three conditions, CoPc-Lig NPs presented an evident PA effect with a maximum PA effect for excitation wavelengths in the range of 700-715 nm. For the NPs suspended in aqueous media, signal bleaching was observed under continuous light irradiation at 710 nm (Figure 4.25.A), that was not present once the NIR

irradiation was shielded by a tissue or a biological matrix (Figure 4.25.B-C). These properties are promising for expanding the applicability of CoPc-Lig NPs to PA imaging in CWs. Figure 4.26 confirms that the localization of CoLig-NPs within muscle tissue phantom can be followed by PA imaging over time.

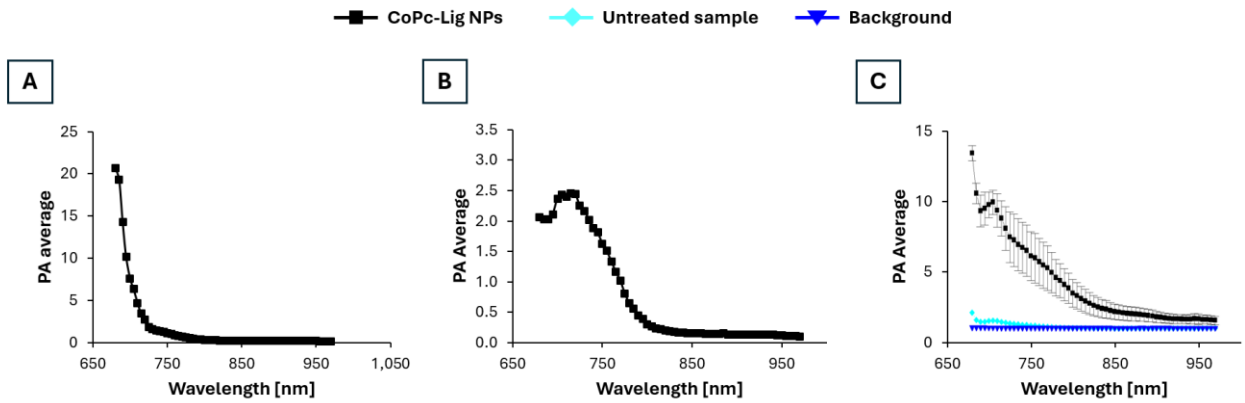


Figure 4.24. PA spectra of excitation of CoPc-Lig NPs at different wavelengths for (A) in vitro test, (B) Ex vivo test, and (C) CoPc-Lig NPs internalized into S. aureus biofilm.

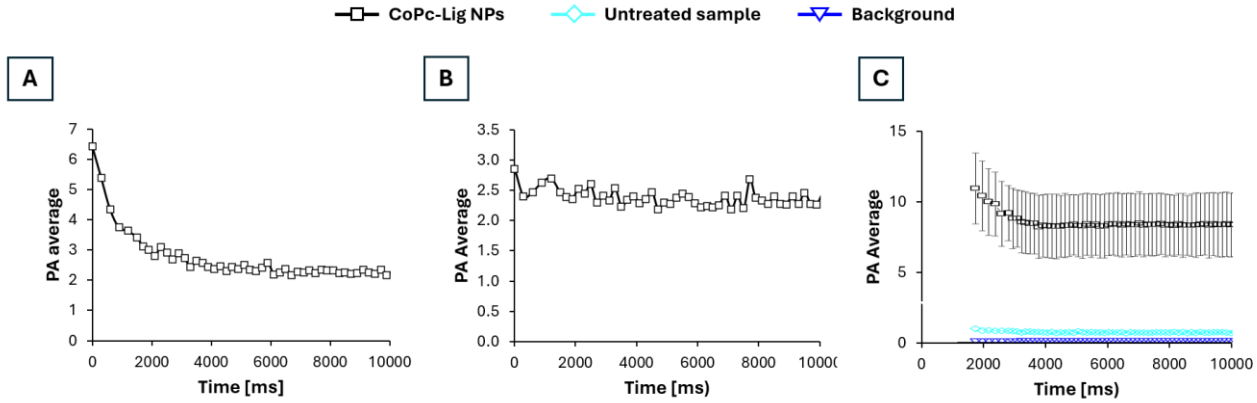


Figure 4.25 PA stability of CoPc-Lig NPs under continuous irradiation at 710 nm for (A) in vitro test, (B) Ex vivo test, and (C) CoPc-Lig NPs internalized into S. aureus biofilm.

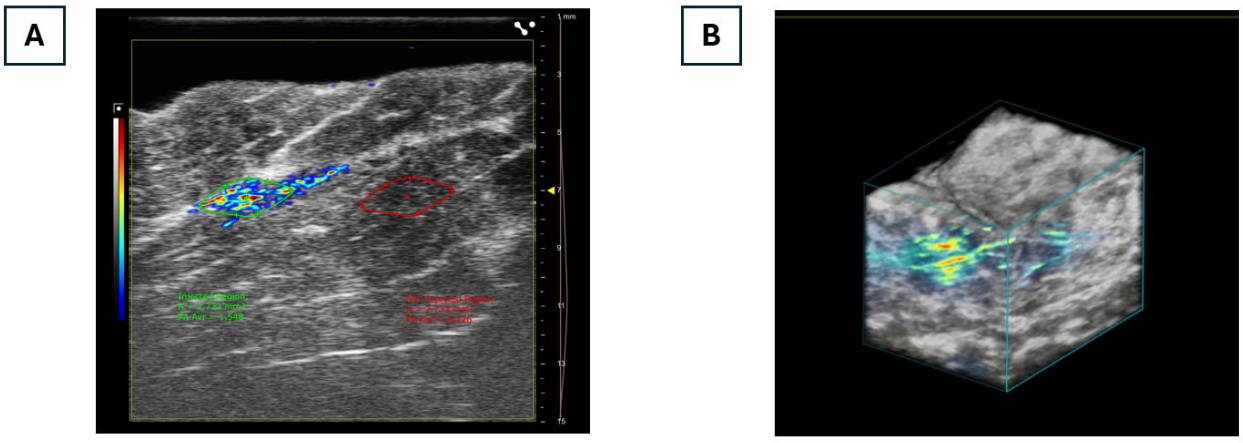


Figure 4.26. Localization of CoPc-Lig NPs ex vivo. (A) PA image of the tissue section presenting CoPc-Lig NPs. (D) 3D PA reconstruction of the tissue presenting CoPc-Lig NPs.

4.3.2.9. Considerations on CoPc-Lig NPs

CoPc-Lig NPs were successfully obtained and presented adequate dimensions and ζ potential. These particles also presented higher antioxidant activity and MMPs inhibition ability, as well as better cytocompatibility in comparison to CoLig NPs. However, the antibacterial activity was lower than for CoPc NPs, probably due to cobalt being complexed with Pc and, therefore, less available for interaction with bacterial membranes and to its lower concentration in the NPs. Indeed, an antibacterial effect was observed only for *S. aureus*. On the other hand, the presence of Pc in the CoPc complex was able to generate an evident thermal increment after NIR light excitation, which reduced bacteria viability and induced partial biofilm disruption. Moreover, CoPc-Lig NPs could be easily internalized into bacterial biofilms, a fundamental aspect to maximize the interaction with bacterial cells during photothermal treatments. Additionally, CoPc-Lig NPs presented a marked PA activity and could be easily localized within a tissue phantom as well as in the biofilm. This property opens the possibility of using these NPs for imaging purposes.

Overall, these results prove CoPc-Lig NPs to be a promising system for mild photothermal treatment of CWs, deserving further investigation.

4.4. Conclusions

In this Section, two approaches to introduce antibiofilm properties to CoLig NPs were investigated. The first method involved coating CoLig NPs with a nitric oxide (NO) donor, capable of modulating nitroxidative stress [30]. NO delivery is known to have beneficial effects on controlling infections and stimulating wound regeneration [38], [53], [56], [57]. However, NO half-life in the biological environment is limited to a few seconds, limiting its action to ~100 µm from its source [29]. Free GSNO delivery in wound beds has been proposed and beneficial effects were observed at high concentrations. GSNO is known to release NO in biological fluids [55] and has successfully delivered NO in *in vivo* models when it was freely incorporated into hydrogels [56], [57], [58]. Unfortunately, direct GSNO delivery does not allow controlled NO release [33], [56], [57]. [36], [38], [52]. In this thesis, NO-CoLig NPs with small size, monodispersed distribution, and improved cytocompatibility compared to CoLig NPs were obtained. However, the coating reduced the antibacterial activity of NPs without providing antibiofilm capacity. This could be caused either by a too-fast or a too-slow decomposition of GSNO, resulting in an inefficient delivery of NO. The -SNO bond in S-nitrosothiols undergoes several mechanisms of decomposition through various mechanisms, including hydrolysis, homolysis, photolysis, metal-ion mediated decomposition, and enzymatic release [30], [55]. Moreover, the inclusion of GSNO in the nanoformulations may have protected GSNO resulting in low NO release, which could explain the lack of antibiofilm effect in NO-CoLig NPs. External stimuli could be used to trigger GSNO decomposition [39] [53]. Future tests may focus on triggering NO with light irradiation, as suggested by our preliminary tests on GSNO stability.

The second method focused on adding photo-excitable compounds to lignin-based NPs. With this aim, CoPc was combined with the lignin-based material to obtain CoPc-Lig NPs with promising properties. These NPs exhibited appropriate size, round-shaped morphology, antioxidant properties, and cytocompatibility at high concentrations. Some antibacterial activity could also be observed against *S. aureus*, but no intrinsic antibiofilm capacity was detected, as CoPc does not have antibiofilm activity *per se* but may exert such property through photothermal excitation [46]. The NPs were easily internalized into bacterial biofilms, a fundamental aspect for maximizing the interaction with bacterial cells during photothermal treatments. Additionally, they showed evident thermal increment when excited with NIR light, though below 50°C [63]. This mild temperature

increase may be beneficial in CWs, where reaching higher temperatures may damage the newly formed tissue and induce cytotoxicity in cells [64]. Additionally, these temperatures are known to favor tissue regeneration and improve the antibacterial potency of other compounds [46], [47]. Therefore, the antibacterial activity of the cobalt present in the NPs could be potentiated by the photothermal treatment. Indeed, a reduction in bacteria viability and a loss in biofilm integrity was observed after treatment with NIR irradiation. Future tests will focus on optimizing the photothermal treatment conditions to potentiate the antibiofilm action. With the same aim, the combination of photothermal treatment with debridement and other antibacterial agents will be investigated. Another advantage of CoPc-Lig NPs, in their PA behavior, which could be used for PA imaging, an emerging technique that uses the capacity of electromagnetic energy to generate acoustic waves [68], [69]. This technique allows to localize chromophores *in vivo* with high spatial/temporal resolution, without using ionizing radiations [70]. Indeed, the CoPc-Lig NPs could be localized in *ex vivo* phantoms and within *S. aureus* biofilm. This opens the road for future applications of these NPs in the theragnostic field.

4.5. Annex figures

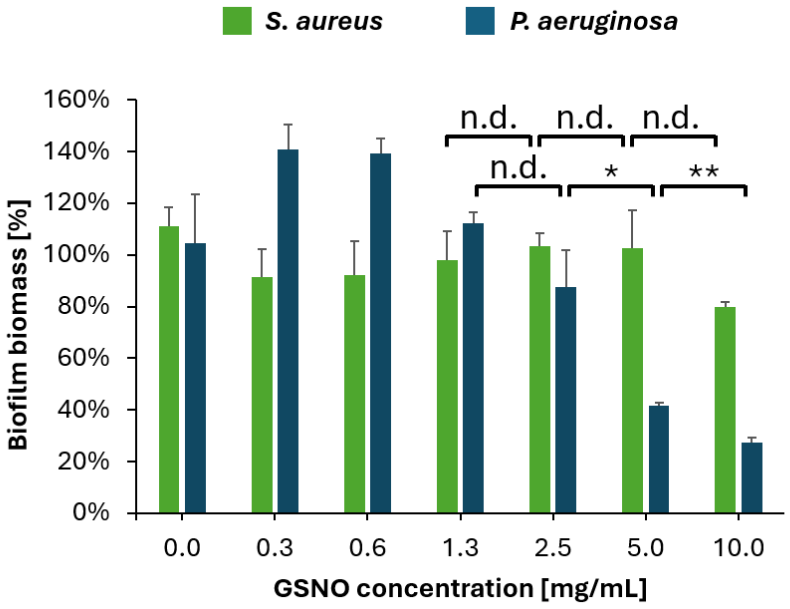


Figure S4.1 Antibiofilm activity of GSNO for S. aureus (green) and P. aeruginosa (blue).

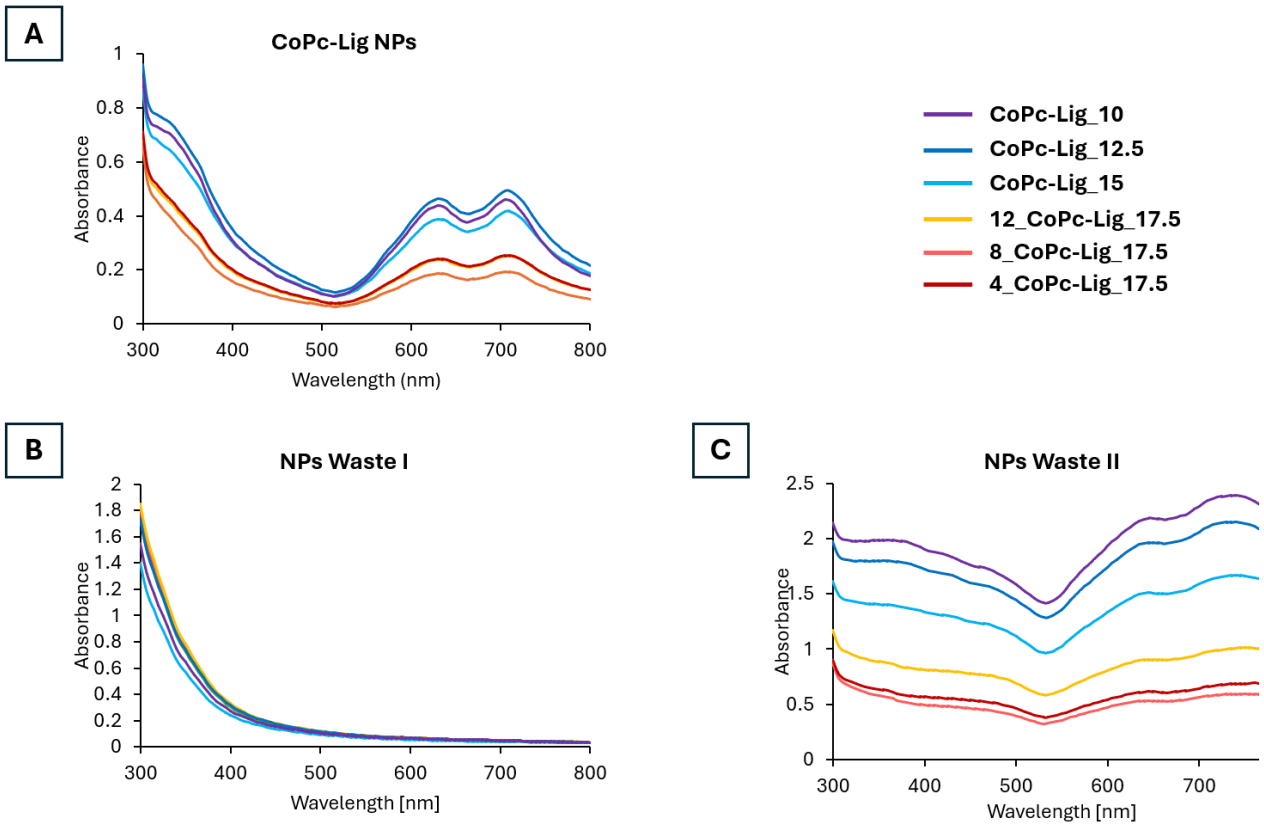


Figure S4.2. UV-Vis spectra of (A) all the CoPc-Lig NP conditions and (B-C) their wastes extracted during the centrifugation steps.

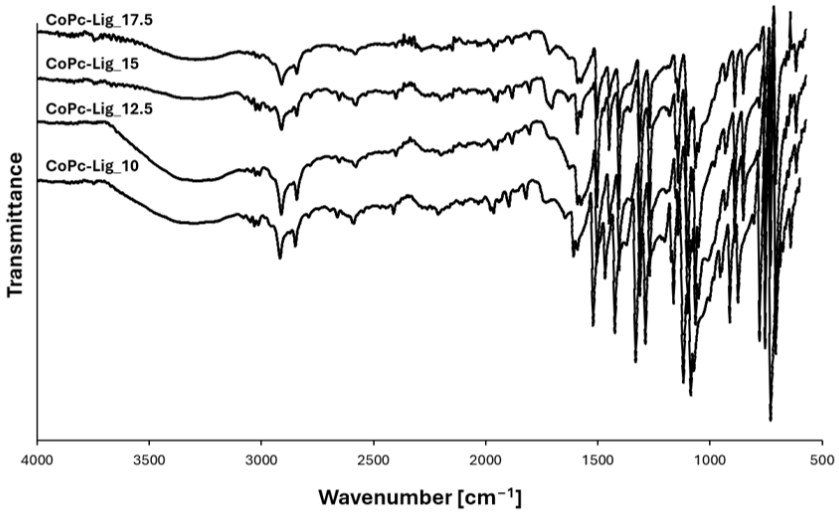


Figure S4.3. ATR-FTIR spectra of the CoPc-Lig NPs for CoPc-Lig_10, CoPc-Lig_12.5, CoPc-Lig_15 and CoPc-Lig_17.5.

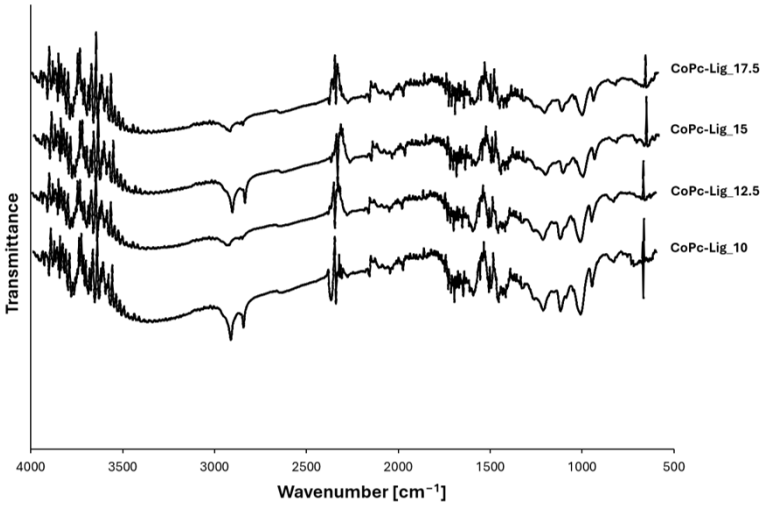


Figure S4.4. ATR-FTIR spectra of the NPs Waste I for CoPc-Lig_10, CoPc-Lig_12.5, CoPc-Lig_15 and CoPc-Lig_17.5.

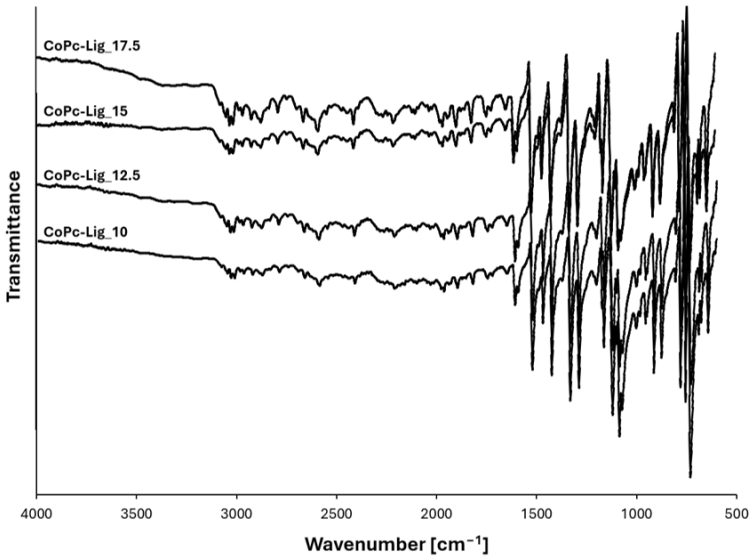


Figure S4.5. ATR-FTIR spectra of the NPs Waste II for CoPc-Lig_10, CoPc-Lig_12.5, CoPc-Lig_15 and CoPc-Lig_17.5.

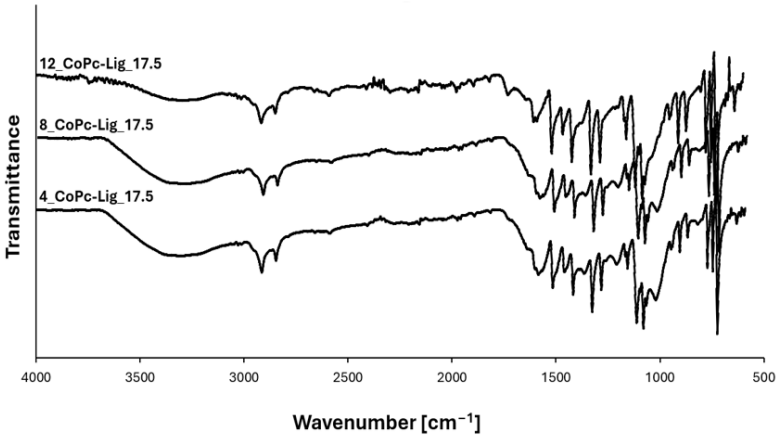


Figure S4.6. ATR-FTIR spectra of the CoPc-Lig NPs for 12_CoPc-Lig _17.5, 8_CoPc-Lig_17.5 and 4_CoPc-Lig_17.5.

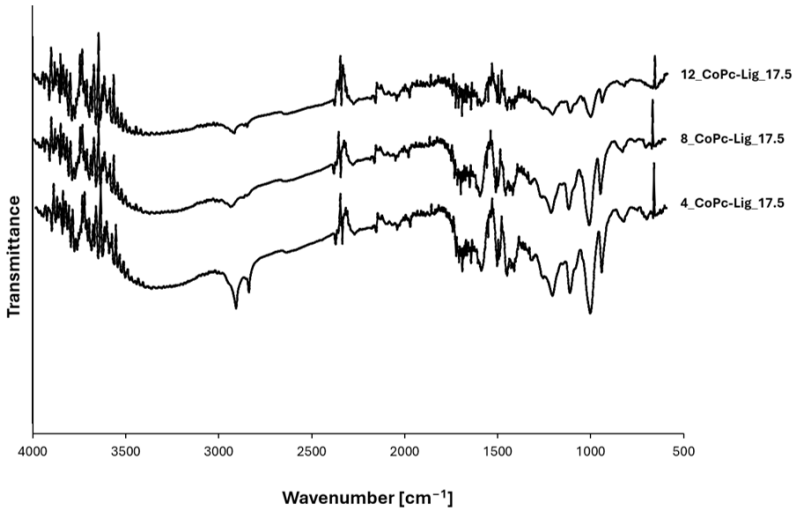


Figure S4.7. ATR-FTIR spectra of the NPs Waste I for 12_CoPc-Lig _17.5, 8_CoPc-Lig_17.5 and 4_CoPc-Lig_17.5.

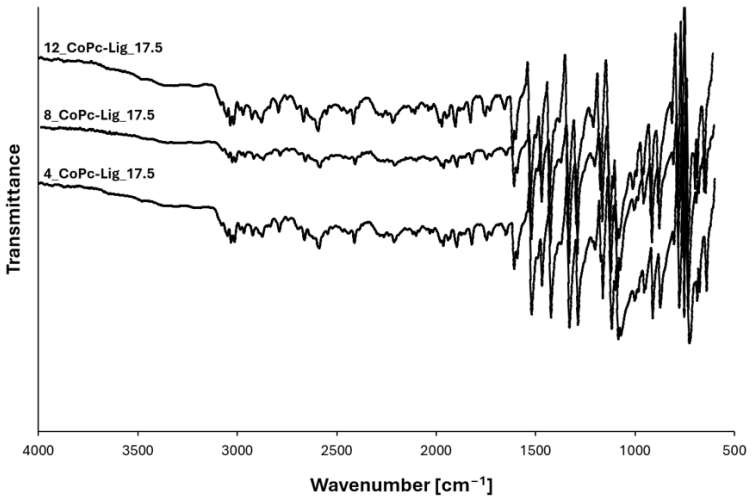


Figure S4.8. ATR-FTIR spectra of the NPs Waste II for 12_CoPc-Lig _17.5, 8_CoPc-Lig_17.5 and 4_CoPc-Lig_17.5.

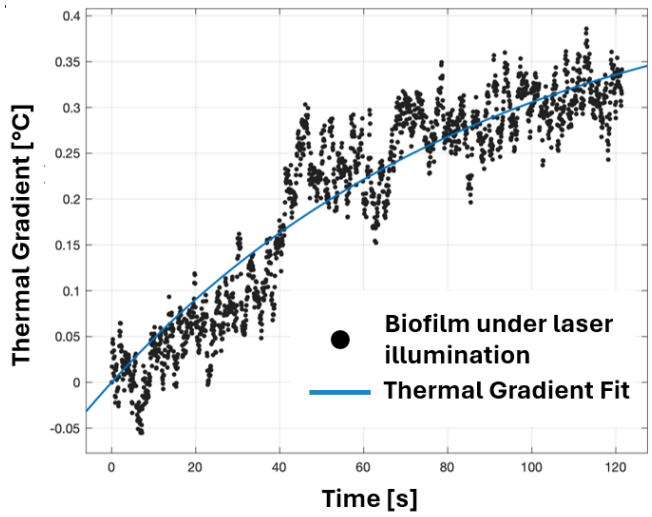


Figure S4.9. Photothermal activity of untreated S. aureus biofilm.

4.6. References

[1] G. Crivello, L. Fracchia, G. Ciardelli, M. Boffito, and C. Mattu, 'In Vitro Models of Bacterial Biofilms: Innovative Tools to Improve Understanding and Treatment of Infections', *Nanomaterials*, vol. 13, no. 5, Art. no. 5, Jan. 2023, doi: 10.3390/nano13050904.

[2] C. Attinger and R. Wolcott, 'Clinically Addressing Biofilm in Chronic Wounds', *Advances in Wound Care*, vol. 1, no. 3, pp. 127–132, Jun. 2012, doi: 10.1089/wound.2011.0333.

[3] R. D. Wolcott *et al.*, 'Chronic wounds and the medical biofilm paradigm', *Journal of Wound Care*, vol. 19, no. 2, pp. 45–53, Feb. 2010, doi: 10.12968/jowc.2010.19.2.46966.

[4] K. Ganesh, M. Sinha, S. S. Mathew-Steiner, A. Das, S. Roy, and C. K. Sen, 'Chronic Wound Biofilm Model', *Adv Wound Care (New Rochelle)*, vol. 4, no. 7, pp. 382–388, Jul. 2015, doi: 10.1089/wound.2014.0587.

[5] K. R. Kirker and G. A. James, 'In vitro studies evaluating the effects of biofilms on wound-healing cells: a review', *APMIS*, vol. 125, no. 4, pp. 344–352, 2017, doi: https://doi.org/10.1111/apm.12678.

[6] M. Malone *et al.*, 'The prevalence of biofilms in chronic wounds: a systematic review and meta-analysis of published data', *J Wound Care*, vol. 26, no. 1, pp. 20–25, Jan. 2017, doi: 10.12968/jowc.2017.26.1.20.

[7] T. R. Thomsen *et al.*, 'The bacteriology of chronic venous leg ulcer examined by culture-independent molecular methods', *Wound Repair and Regeneration*, vol. 18, no. 1, pp. 38–49, 2010, doi: 10.1111/j.1524-475X.2009.00561.x.

[8] I. C. Thaarup and T. Bjarnsholt, 'Current In Vitro Biofilm-Infected Chronic Wound Models for Developing New Treatment Possibilities', *Advances in Wound Care*, vol. 10, no. 2, pp. 91–102, Feb. 2021, doi: 10.1089/wound.2020.1176.

[9] A. K. Seth, M. R. Geringer, S. J. Hong, K. P. Leung, T. A. Mustoe, and R. D. Galiano, 'In vivo modeling of biofilm-infected wounds: A review', *Journal of Surgical Research*, vol. 178, no. 1, pp. 330–338, Nov. 2012, doi: 10.1016/j.jss.2012.06.048.

[10] G. Brackman and T. Coenye, 'In Vitro and In Vivo Biofilm Wound Models and Their Application', in *Advances in Microbiology, Infectious Diseases and Public Health*, vol. 897, G. Donelli, Ed., in Advances in Experimental Medicine and Biology, vol. 897. , Cham: Springer International Publishing, 2015, pp. 15–32. doi: 10.1007/5584_2015_5002.

[11] T. F. Bahamondez-Canas, L. A. Heersema, and H. D. C. Smyth, 'Current Status of In Vitro Models and Assays for Susceptibility Testing for Wound Biofilm Infections', *Biomedicines*, vol. 7, no. 2, Art. no. 2, Jun. 2019, doi: 10.3390/biomedicines7020034.

[12] I. Pastar *et al.*, 'Interactions of Methicillin Resistant Staphylococcus aureus USA300 and Pseudomonas aeruginosa in Polymicrobial Wound Infection', *PLOS ONE*, vol. 8, no. 2, p. e56846, Feb. 2013, doi: 10.1371/journal.pone.0056846.

[13] S. DeLeon, A. Clinton, H. Fowler, J. Everett, A. R. Horswill, and K. P. Rumbaugh, 'Synergistic Interactions of Pseudomonas aeruginosa and Staphylococcus aureus in an In Vitro Wound Model', *Infection and Immunity*, vol. 82, no. 11, pp. 4718–4728, Oct. 2014, doi: 10.1128/iai.02198-14.

[14] A. Hotterbeekx, S. Kumar-Singh, H. Goossens, and S. Malhotra-Kumar, 'In vivo and In vitro Interactions between Pseudomonas aeruginosa and Staphylococcus spp.', *Front. Cell. Infect. Microbiol.*, vol. 7, Apr. 2017, doi: 10.3389/fcimb.2017.00106.

[15] J. L. Del Pozo and R. Patel, 'The Challenge of Treating Biofilm-associated Bacterial Infections', *Clin Pharmacol Ther*, vol. 82, no. 2, pp. 204–209, Aug. 2007, doi: 10.1038/sj.clpt.6100247.

[16] R. D. Wolcott, D. D. Rhoads, and S. E. Dowd, 'Biofilms and chronic wound inflammation', *J Wound Care*, vol. 17, no. 8, pp. 333–341, Aug. 2008, doi: 10.12968/jowc.2008.17.8.30796.

[17] C. Pouget, C. Dunyach-Remy, A. Pantel, S. Schuldiner, A. Sotto, and J.-P. Lavigne, 'Biofilms in Diabetic Foot Ulcers: Significance and Clinical Relevance', *Microorganisms*, vol. 8, no. 10, Oct. 2020, doi: 10.3390/microorganisms8101580.

[18] R. Serra *et al.*, 'Chronic wound infections: the role of *Pseudomonas aeruginosa* and *Staphylococcus aureus*', *Expert Review of Anti-infective Therapy*, vol. 13, no. 5, pp. 605–613, May 2015, doi: 10.1586/14787210.2015.1023291.

[19] R. D. Wolcott and D. D. Rhoads, 'A study of biofilm-based wound management in subjects with critical limb ischaemia', *J Wound Care*, vol. 17, no. 4, pp. 145–155, Apr. 2008, doi: 10.12968/jowc.2008.17.4.28835.

[20] R. D. Wolcott *et al.*, 'Biofilm maturity studies indicate sharp debridement opens a time-dependent therapeutic window', *J Wound Care*, vol. 19, no. 8, pp. 320–328, Aug. 2010, doi: 10.12968/jowc.2010.19.8.77709.

[21] X.-H. Li and J.-H. Lee, 'Antibiofilm agents: A new perspective for antimicrobial strategy', *J Microbiol.*, vol. 55, no. 10, pp. 753–766, Oct. 2017, doi: 10.1007/s12275-017-7274-x.

[22] K. E. Ridyard and J. Overhage, 'The Potential of Human Peptide LL-37 as an Antimicrobial and Anti-Biofilm Agent', *Antibiotics*, vol. 10, no. 6, Art. no. 6, Jun. 2021, doi: 10.3390/antibiotics10060650.

[23] K. P. Rumbaugh and K. Sauer, 'Biofilm dispersion', *Nature Reviews Microbiology*, vol. 18, no. 10, Art. no. 10, Oct. 2020, doi: 10.1038/s41579-020-0385-0.

[24] M. T. Pelegrino, L. C. Silva, C. M. Watashi, P. S. Haddad, T. Rodrigues, and A. B. Seabra, 'Nitric oxide-releasing nanoparticles: synthesis, characterization, and cytotoxicity to tumorigenic cells', *J Nanopart Res*, vol. 19, no. 2, p. 57, Feb. 2017, doi: 10.1007/s11051-017-3747-4.

[25] D. McDougald, S. A. Rice, N. Barraud, P. D. Steinberg, and S. Kjelleberg, 'Should we stay or should we go: mechanisms and ecological consequences for biofilm dispersal', *Nature Reviews Microbiology*, vol. 10, no. 1, Art. no. 1, Jan. 2012, doi: 10.1038/nrmicro2695.

[26] N. Barraud, D. J. Hassett, S.-H. Hwang, S. A. Rice, S. Kjelleberg, and J. S. Webb, 'Involvement of Nitric Oxide in Biofilm Dispersal of Pseudomonas aeruginosa', *JB*, vol. 188, no. 21, pp. 7344–7353, Nov. 2006, doi: 10.1128/JB.00779-06.

[27] T. Yang, A. N. Zelikin, and R. Chandrawati, 'Progress and Promise of Nitric Oxide-Releasing Platforms', *Advanced Science*, vol. 5, no. 6, p. 1701043, 2018, doi: https://doi.org/10.1002/advs.201701043.

[28] D. P. Arora, S. Hossain, Y. Xu, and E. M. Boon, 'Nitric Oxide Regulation of Bacterial Biofilms', *Biochemistry*, vol. 54, no. 24, pp. 3717–3728, Jun. 2015, doi: 10.1021/bi501476n.

[29] A. W. Carpenter and M. H. Schoenfisch, 'Nitric oxide release: Part II. Therapeutic applications', *Chem. Soc. Rev.*, vol. 41, no. 10, pp. 3742–3752, Apr. 2012, doi: 10.1039/C2CS15273H.

[30] K. A. Broniowska, A. R. Diers, and N. Hogg, 'S-Nitrosoglutathione', *Biochimica et Biophysica Acta (BBA) - General Subjects*, vol. 1830, no. 5, pp. 3173–3181, May 2013, doi: 10.1016/j.bbagen.2013.02.004.

[31] M. J. Malone-Povolny, S. E. Maloney, and M. H. Schoenfisch, 'Nitric Oxide Therapy for Diabetic Wound Healing', *Advanced Healthcare Materials*, vol. 8, no. 12, p. 1801210, 2019, doi: https://doi.org/10.1002/adhm.201801210.

[32] J. O. Kim *et al.*, 'Nitric oxide-releasing chitosan film for enhanced antibacterial and in vivo wound-healing efficacy', *International Journal of Biological Macromolecules*, vol. 79, pp. 217–225, Aug. 2015, doi: 10.1016/j.ijbiomac.2015.04.073.

[33] A. B. Seabra *et al.*, 'S-nitrosoglutathione-containing hydrogel increases dermal blood flow in streptozotocin-induced diabetic rats', *Br J Dermatol*, vol. 156, no. 5, pp. 814–818, May 2007, doi: 10.1111/j.1365-2133.2006.07718.x.

[34] Y. Li and P. I. Lee, 'Controlled Nitric Oxide Delivery Platform Based on S-Nitrosothiol Conjugated Interpolymer Complexes for Diabetic Wound Healing', *Mol. Pharmaceutics*, vol. 7, no. 1, pp. 254–266, Feb. 2010, doi: 10.1021/mp900237f.

[35] S. M. Shishido, A. B. Seabra, W. Loh, and M. Ganzarolli de Oliveira, 'Thermal and photochemical nitric oxide release from S-nitrosothiols incorporated in Pluronic F127 gel: potential uses for local and controlled nitric oxide release', *Biomaterials*, vol. 24, no. 20, pp. 3543–3553, Sep. 2003, doi: 10.1016/S0142-9612(03)00153-4.

[36] S. P. Hlaing *et al.*, 'S-Nitrosoglutathione loaded poly(lactic-co-glycolic acid) microparticles for prolonged nitric oxide release and enhanced healing of methicillin-resistant Staphylococcus aureus-infected wounds', *European Journal of Pharmaceutics and Biopharmaceutics*, vol. 132, pp. 94–102, Nov. 2018, doi: 10.1016/j.ejpb.2018.09.009.

[37] M. T. Pelegrino, D. R. de Araújo, and A. B. Seabra, 'S-nitrosoglutathione-containing chitosan nanoparticles dispersed in Pluronic F-127 hydrogel: Potential uses in topical applications', *Journal of Drug Delivery Science and Technology*, vol. 43, pp. 211–220, Feb. 2018, doi: 10.1016/j.jddst.2017.10.016.

[38] J. Lee *et al.*, 'Nitric Oxide-Releasing S-Nitrosoglutathione-Conjugated Poly(Lactic-Co-Glycolic Acid) Nanoparticles for the Treatment of MRSA-Infected Cutaneous Wounds', *Pharmaceutics*, vol. 12, no. 7, Art. no. 7, Jul. 2020, doi: 10.3390/pharmaceutics12070618.

[39] M. T. Pelegrino, R. B. Weller, A. Paganotti, and A. B. Seabra, 'Delivering nitric oxide into human skin from encapsulated S-nitrosoglutathione under UV light: An in vitro and ex vivo study', *Nitric Oxide*, vol. 94, pp. 108–113, Jan. 2020, doi: 10.1016/j.niox.2019.11.003.

[40] D. Liu, Q. Huang, W. Gu, and X.-A. Zeng, 'A review of bacterial biofilm control by physical strategies', *Critical Reviews in Food Science and Nutrition*, vol. 62, no. 13, pp. 3453–3470, May 2022, doi: 10.1080/10408398.2020.1865872.

[41] G. Hughes and M. A. Webber, 'Novel approaches to the treatment of bacterial biofilm infections', *British Journal of Pharmacology*, vol. 174, no. 14, pp. 2237–2246, 2017, doi: 10.1111/bph.13706.

[42] Y. Dong *et al.*, 'Magnetic Microswarm Composed of Porous Nanocatalysts for Targeted Elimination of Biofilm Occlusion', *ACS Nano*, vol. 15, no. 3, pp. 5056–5067, Mar. 2021, doi: 10.1021/acsnano.0c10010.

[43] J. Fang and Y.-C. Chen, 'Nanomaterials for Photohyperthermia: A Review', *CPD*, vol. 19, no. 37, pp. 6622–6634, Sep. 2013, doi: 10.2174/1381612811319370006.

[44] R. S. Norman, J. W. Stone, A. Gole, C. J. Murphy, and T. L. Sabo-Attwood, 'Targeted Photothermal Lysis of the Pathogenic Bacteria, Pseudomonas aeruginosa, with Gold Nanorods', *Nano Lett.*, vol. 8, no. 1, pp. 302–306, Jan. 2008, doi: 10.1021/nl0727056.

[45] Z. Yuan *et al.*, 'Remote eradication of biofilm on titanium implant via near-infrared light triggered photothermal/photodynamic therapy strategy', *Biomaterials*, vol. 223, p. 119479, Dec. 2019, doi: 10.1016/j.biomaterials.2019.119479.

[46] Y. Zhao *et al.*, 'Near-Infrared Light-Activated Thermosensitive Liposomes as Efficient Agents for Photothermal and Antibiotic Synergistic Therapy of Bacterial Biofilm', *ACS Appl. Mater. Interfaces*, vol. 10, no. 17, pp. 14426–14437, May 2018, doi: 10.1021/acsami.8b01327.

[47] W.-C. Huang, P.-J. Tsai, and Y.-C. Chen, 'Functional gold nanoparticles as photothermal agents for selective-killing of pathogenic bacteria', *Nanomedicine*, vol. 2, no. 6, pp. 777–787, Dec. 2007, doi: 10.2217/17435889.2.6.777.

[48] B.-D. Zheng, Q.-X. He, X. Li, J. Yoon, and J.-D. Huang, 'Phthalocyanines as contrast agents for photothermal therapy', *Coordination Chemistry Reviews*, vol. 426, p. 213548, Jan. 2021, doi: 10.1016/j.ccr.2020.213548.

[49] J. Yang, X. Wang, and H. Liu, 'Lignins and Lignin Derivatives as Dispersants for Copper Phthalocyanine Pigment Nanoparticles', *ACS Sustainable Chem. Eng.*, vol. 11, no. 22, pp. 8199–8207, Jun. 2023, doi: 10.1021/acssuschemeng.2c04657.

[50] P. Armanetti *et al.*, 'Spectroscopic and photoacoustic characterization of encapsulated iron oxide super-paramagnetic nanoparticles as a new multiplatform contrast agent', *Spectrochimica Acta Part A: Molecular and Biomolecular Spectroscopy*, vol. 199, pp. 248–253, Jun. 2018, doi: 10.1016/j.saa.2018.03.025.

[51] S. U. Shah, M. Socha, C. Sejil, and S. Gibaud, 'Spray-dried microparticles of glutathione and S-nitrosoglutathione based on Eudragit® FS 30D polymer', *Annales Pharmaceutiques Françaises*, vol. 75, no. 2, pp. 95–104, Mar. 2017, doi: 10.1016/j.pharma.2016.09.001.

[52] A. C. Melvin, W. M. Jones, A. Lutzke, C. L. Allison, and M. M. Reynolds, '*S*-Nitrosoglutathione exhibits greater stability than *S*-nitroso-*N*-acetylpenicillamine under common laboratory conditions: A comparative stability study', *Nitric Oxide*, vol. 92, pp. 18–25, Nov. 2019, doi: 10.1016/j.niox.2019.08.002.

[53] W. Wang *et al.*, 'S-nitrosoglutathione functionalized polydopamine nanoparticles incorporated into chitosan/gelatin hydrogel films with NIR-controlled photothermal/NO-releasing therapy for enhanced wound healing', *International Journal of Biological Macromolecules*, vol. 200, pp. 77–86, Mar. 2022, doi: 10.1016/j.ijbiomac.2021.12.125.

[54] L. O. Simonsen, H. Harbak, and P. Bennekou, 'Cobalt metabolism and toxicology—A brief update', *Science of The Total Environment*, vol. 432, pp. 210–215, Aug. 2012, doi: 10.1016/j.scitotenv.2012.06.009.

[55] N. Naghavi, A. de Mel, O. S. Alavijeh, B. G. Cousins, and A. M. Seifalian, 'Nitric Oxide Donors for Cardiovascular Implant Applications', *Small*, vol. 9, no. 1, pp. 22–35, 2013, doi: 10.1002/smll.201200458.

[56] J. L. Georgii, T. P. Amadeu, A. B. Seabra, M. G. de Oliveira, and A. Monte-Alto-Costa, 'Topical S-nitrosoglutathione-releasing hydrogel improves healing of rat ischaemic wounds', *Journal of Tissue Engineering and Regenerative Medicine*, vol. 5, no. 8, pp. 612–619, 2011, doi: https://doi.org/10.1002/term.353.

[57] T. P. Amadeu, A. B. Seabra, M. D. Oliveira, and A. M. A. Costa, 'S-nitrosoglutathione-containing hydrogel accelerates rat cutaneous wound repair', *Journal of the European Academy of Dermatology and Venereology*, vol. 21, no. 5, pp. 629–637, 2007, doi: https://doi.org/10.1111/j.1468-3083.2006.02032.x.

[58] T. P. Amadeu, Amedea. B. Seabra, M. G. de Oliveira, and A. Monte-Alto-Costa, 'Nitric Oxide Donor Improves Healing if Applied on Inflammatory and Proliferative Phase', *Journal of Surgical Research*, vol. 149, no. 1, pp. 84–93, Sep. 2008, doi: 10.1016/j.jss.2007.10.015.

[59] Z. Shi *et al.*, 'Structural characterization of lignin from D. sinicus by FTIR and NMR techniques', *Green Chemistry Letters and Reviews*, vol. 12, no. 3, pp. 235–243, Jul. 2019, doi: 10.1080/17518253.2019.1627428.

[60] I. A. Gilca, R. E. Ghitescu, A. C. Puitel, and V. I. Popa, 'Preparation of lignin nanoparticles by chemical modification', *Iran Polym J*, vol. 23, no. 5, pp. 355–363, May 2014, doi: 10.1007/s13726-014-0232-0.

[61] X. Ji *et al.*, 'Cobalt phthalocyanine nanowires: Growth, crystal structure, and optical properties', *Crystal Research and Technology*, vol. 51, no. 2, pp. 154–159, 2016, doi: 10.1002/crat.201500244.

[62] S. Fulaz, S. Vitale, L. Quinn, and E. Casey, 'Nanoparticle–Biofilm Interactions: The Role of the EPS Matrix', *Trends in Microbiology*, vol. 27, no. 11, pp. 915–926, Nov. 2019, doi: 10.1016/j.tim.2019.07.004.

[63] N. Xu *et al.*, 'Biomedical applications and prospects of temperature-orchestrated photothermal therapy', *MedComm – Biomaterials and Applications*, vol. 1, no. 2, p. e25, 2022, doi: 10.1002/mba2.25.
[64] C. L. West, A. C. V. Doughty, K. Liu, and W. R. Chen, 'Monitoring tissue temperature during photothermal therapy for cancer', *J BioX Res*, vol. 2, no. 4, pp. 159–168, Dec. 2019, doi: 10.1097/jbr.0000000000000050.
[65] L. Tan *et al.*, 'Overcoming Multidrug-Resistant MRSA Using Conventional Aminoglycoside Antibiotics', *Advanced Science*, vol. 7, no. 9, p. 1902070, 2020, doi: 10.1002/advs.201902070.
[66] L. Sheng *et al.*, 'A novel "hot spring"-mimetic hydrogel with excellent angiogenic properties for chronic wound healing', *Biomaterials*, vol. 264, p. 120414, Jan. 2021, doi: 10.1016/j.biomaterials.2020.120414.
[67] X. Zhang, B. Tan, Y. Wu, M. Zhang, X. Xie, and J. Liao, 'An injectable, self-healing carboxymethylated chitosan hydrogel with mild photothermal stimulation for wound healing', *Carbohydrate Polymers*, vol. 293, p. 119722, Oct. 2022, doi: 10.1016/j.carbpol.2022.119722.
[68] M. Xu and L. V. Wang, 'Photoacoustic imaging in biomedicine', *Review of Scientific Instruments*, vol. 77, no. 4, p. 041101, Apr. 2006, doi: 10.1063/1.2195024.
[69] P. Beard, 'Biomedical photoacoustic imaging', *Interface Focus.*, vol. 1, no. 4, pp. 602–631, Aug. 2011, doi: 10.1098/rsfs.2011.0028.
[70] I. Steinberg, D. M. Huland, O. Vermesh, H. E. Frostig, W. S. Tummers, and S. S. Gambhir, 'Photoacoustic clinical imaging', *Photoacoustics*, vol. 14, pp. 77–98, Jun. 2019, doi: 10.1016/j.pacs.2019.05.001.

5. Design of new SM-gels with antioxidant and anti-inflammatory properties and enhanced stability

5.1. Introduction

The hydrogel developed and thoroughly studied in Sections 2 and 3 is a promising candidate to be used in the treatment of chronic wounds. However, its main function is to control the delivery of loaded compounds and it cannot act directly in reducing oxidative stress. Additionally, its durability in environments simulating heavy exudative wounds is limited to 48 h. This time is sufficient considering the frequency of dressing changes in these conditions, which is every 24-48 h. Nevertheless, a system capable of lasting longer could be clinically relevant to reduce the need for frequent changes of bandages which increase the treatment cost and could be detrimental for wound healing. In this Section, these two challenges were addressed to obtain an SM-gel with improved properties and applicability to the treatment of chronic wounds.

Hydrogels with intrinsic antioxidant properties usually comprise polymers of various origins modified with antioxidant compounds presenting high ROS scavenging capacity such as citric acid and polyphenols [1]. For instance, Yang et al. [2] copolymerized citric acid, poly(ethylene glycol) (PEG), and poly-N-isopropylacrylamide (PNIPAAm), obtaining an antioxidant material capable of undergoing sol-to-gel transition at body temperature. The hydrogel obtained was also loaded with copper NPs by Xiao et al. [3] demonstrating the controlled release of the metal ion. The synergic action of antioxidant and copper release promoted wound closure and improved angiogenesis, collagen deposition, and re-epithelialization in a murine diabetic wound model. In another study, Liang et al. [4] grafted dopamine to gelatin and obtained an antioxidant hydrogel by combining this material with chitosan. Furthermore, the loading of the antibiotic doxycycline provided additional antibacterial properties. The multifunctional system improved wound healing by promoting blood vessels, epidermis and hair follicle formation in an infected murine wound model.

Starting from this premises, in this Section, with the aim to provide the hydrogel with additional antioxidant and anti-inflammatory activity, a polyphenolic lignin-based material (Lig-TA) was enzymatically conjugated using laccase to the SHF68 PEU by exploiting the primary amines exposed on the PEU backbone (Figure 5.1.A). The obtained polymer (Lig-SHF68) was thoroughly characterized, and the SM-gel obtained by its combination with α-CDs was investigated.

On the other hand, SM-gel stability is strictly related to the physical nature of its network. The SM-gel is formed through the synergic combination of two mechanisms: the micellization of the amphiphilic PEUs and the formation of inclusion complexes between α-CDs and the PEO chains present in Poloxamers®. These mechanisms contribute to the formation of a network based on physical interactions which provide sustained delivery, injectability and self-healing properties but do not result in a fully stable matrix. Indeed, physical hydrogels present relevant mass exchange with aqueous environments which leads to their complete dissolution within a few days, as described in the previous Sections. This limitation can be overcome by introducing chemical crosslinks within the network. Chemical hydrogels present, in fact, a higher stability but their crosslinking processes can damage the therapeutic compounds encapsulated in the gel and often require chemical additives that could have toxic effects. Therefore, a system combining physical and chemical interactions could merge the benefits of both strategies. Taking advantage of the supramolecular nature of the hydrogel developed in this PhD work, physical interactions could be initially established, followed by *in situ* stabilization through chemical crosslinking. For example, this approach was exploited to improve the properties of physical hydrogels used as bioinks in

additive manufacturing techniques [5]. Particularly interesting are the approaches combining photocurable polymers with PPRs-based supramolecular structures [6], [7], [8]. For instance, Zhao et al. [9], [10] obtained a photocurable polymer by grafting acrylate groups to Pluronic® F68. Then, they exploited either the PEO or the PPO blocks of F68 to form inclusion complexes with α-CDs or β-CDs, respectively. After complete self-assembly into PPRs, the additional UV-induced crosslinking greatly improved the mechanical properties of the hydrogel.

These studies suggest a promising approach that could be easily integrated into the system developed in this PhD work. To do so, a commercially available poly(ethylene glycol) was modified to present terminal acrylate groups (PEG-DA), which allowed for both the formation of PPRs through the interaction with α-CDs and the photo-crosslinking mediated by light irradiation in the presence of a catalytic amount of a photo-initiator. Therefore, this polymer could be combined with the phenolated SHF68 (Lig-SHF68) to obtain an enhanced hydrogel with antioxidant activity and improved stability (Figure 5.1.B). The new system was characterized and used to encapsulate different compounds, suggesting an enhancement of the SM-gel properties that could benefit the treatment of chronic wounds.

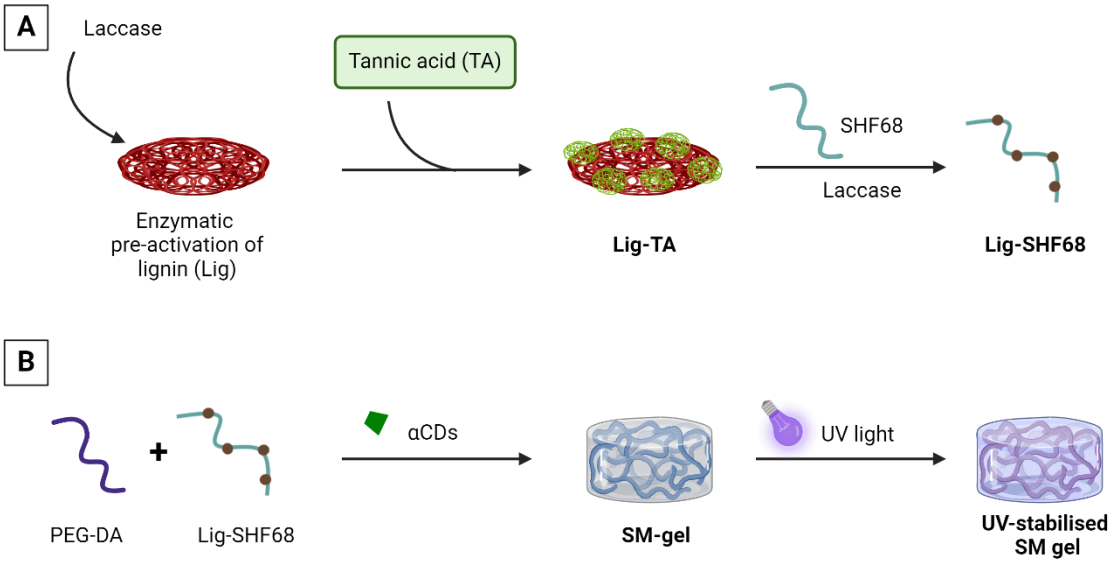


Figure 5.1. Scheme summarizing the approaches adopted to improve SM-gel features. (A) Functionalization of SHF68 with a lignin-based material to obtain Lig-SHF68. (B) Combination of Lig-SHF68 and PEG-DA with αCDs to develop a new SM-gel with additional stabilization potential through photo-crosslinking.

5.2. Materials and methods

5.2.1. Materials and reagents

Gallic acid, tannic acid, 3',5'-dimethoxy-4'hydroxyacetophenone (97%) (acetosyringone), guaiacol, hydrogen peroxide (H_2O_2), 2,2'-azino-bis(3-ethylbenzothiazoline-6-sulfonic acid) diammonium salt (ABTS), phosphate-buffered saline (PBS), Folin–Ciocalteu phenol reagent, sodium carbonate, fluorescamine, Lignosulfonic acid sodium salt, dimethyl sulfoxide (DMSO), and Dulbecco's modified Eagle's medium (DMEM) were obtained from Sigma-Aldrich (Madrid, Spain and Milan, Italy). α-cyclodextrins (αCDs) and lithium phenyl-2,4,6-trimethylbenzoylphosphinate (LAP, a photo-initiator) were purchased from TCI Chemicals Europe (Zwijndrecht, Belgium). AlamarBlue cell viability reagent, myeloperoxidase, and EnzChek™ Gelatinase/Collagenase Assay Kit were supplied by Invitrogen, Life Technologies Corporation (Madrid, Spain). Novozym 51003 laccase from

Miceliophtora termophila was provided by Novozymes (Bagsvaerd, Denmark). The laccase exhibited an enzymatic activity of 179 U/mL, defined as the quantity of enzyme needed to convert 1 µmol of ABTS to its cation radical (ε_{436} = 29,300 M^{-1} cm^{-1}) in 5 mM Britton Robinson buffer (pH 5) at 40 °C. Human fibroblast cell line (ATCC-SCRC-1041, HFF-1) was purchased from the American Type Culture Collection (ATCC LGC Standards, Italy) and human keratinocytes (HaCaT) were purchased from "Istituto Zooprofilattico Sperimentale Della Lombardia E Dell'emilia Romagna Bruno Ubertini" (Italy). The water utilized throughout the experiments was purified via a Milli-Q plus system (Millipore) with a resistivity of 18.2 MΩ cm.

5.2.2. Development of Lig-SHF68-based SM-gel

5.2.2.1. Enzymatic functionalization of lignin with TA and characterization (Lig-TA)

Sulfonate lignin was used for conjugation with TA adapting the protocol described in Section 3. Briefly, lignosulfonic acid sodium salt (10 mg/mL) was dissolved in sodium acetate buffer (50 mM, pH 5) added with acetosyringone at 1.5 mg/mL concentration. Laccase was incubated with the lignin solution at a concentration of 1% v/v for 1h at 50 °C under stirring to initiate the oxidative reaction. Then, TA in sodium acetate buffer was added to the solution for a final concentration of 10 mg/mL and the reaction mixture was kept under stirring for 2 h at 50 °C. To eliminate the unreacted TA, the solution was dialyzed against demineralized water for 24 h using a dialysis membrane with a cut-off of 10-12 kDa (regenerated cellulose, Sigma Aldrich, Italy) and then freeze-dried (Martin Christ ALPHA 2-4 LSC, Germany).

The obtained material was characterized through ATR-FTIR spectroscopy, quantification of phenolic content through the Folin-Ciocalteu assay, MPO and MMPs inhibition assays and DPPH ROS scavenging assay.

ATR-FTIR spectroscopy was carried out utilizing a PerkinElmer Spectrum 100 FTIR spectrometer (PerkinElmer, Waltham, MA, USA). Spectra were generated by averaging 32 scans over the spectral range from 4000 to 600 cm^{-1} at a resolution of 1 cm^{-1}. All analyses were carried out at room temperature. Spectra of Lig and TA were also obtained for comparative purposes.

The phenolic content of Lig-TA was determined spectrophotometrically using the Folin–Ciocalteu reagent. Briefly, 20 µL of a water solution containing Lig-TA (1 mg/mL) was combined with 100 µL of 20% w/v sodium carbonate (Na_2CO_3) and 80 µL of 0.2 N Folin–Ciocalteu phenol reagent. The resulting mixture was incubated for 10 minutes in the dark. Then, the absorbance at 765 nm was measured using an Infinite M200 spectrophotometer (TECAN). Gallic acid (GA) was used to obtain a calibration curve (0.1–1 mg/mL) and the results were expressed in GA equivalents (GAE) per g of material.

The MPO inhibition capacity of Lig-TA was evaluated using guaiacol as a substrate. Samples were solubilized at 1 mg/mL in 0.1 M sodium phosphate buffer with pH adjusted to 7.5 by adding 0.1 M sodium phosphate monobasic. Subsequently, 152 µL of each sample were combined with 32 µL of MPO (4.5 U/mL) and 96 µL of guaiacol solution (16 mM in the prepared buffer). The mixtures were then incubated at 37 °C for 90 minutes. Following incubation, 190 µL of the mixture was transferred to a 96-well plate, and 10 µL of a 10 mM H_2O_2 solution were added to initiate the reaction. The absorbance at 476 nm was recorded over time, and the slopes of the curves within the first 150 seconds were compared. The percentage of MPO inhibition was calculated assuming that control values (MPO without Lig-TA) represented 100% activity.

The MMP inhibition capacity of Lig-TA was determined using the EnzCheck Gelatinase/Collagenase Assay Kit, with some modifications. Initially, 1 mg of the sample was solubilized in 500 µL of buffer

(80% of 1 M Tris HCl buffer at pH 7.1 and 20% 1 M $CaCl_2$). Subsequently, 5 µL of 500 U/mL collagenase type IV from Clostridium histolyticum were added to achieve a final concentration of 5 U/mL. The solution was then incubated at 37 °C for 24 h. After incubation, 100 µL of the sample were mixed with 80 µL of buffer and 20 µL of fluorescein-conjugated gelatin (100 µg/mL in Milli-Q water). The plate was incubated for 20 minutes in darkness at room temperature, and fluorescence was measured at $\lambda_{ex/em}$ = 493/528 nm. Collagenase activity was determined as a percentage of enzyme inhibition compared to the control (a reaction mixture with enzyme and substrate but without Lig-TA).

The antioxidant activity of Lig-TA was assessed through the DPPH radical scavenging assay. Briefly, 25 µL of sample solution (0.1-5 mg/mL in MilliQ water) and 75 µL of DPPH solution (0.1 mM in pure ethanol) were mixed and incubated for 30 min at room temperature. After incubation, the samples were centrifuged at 10000 rpm for 5 min and then absorbance at 517 nm was measured. Samples mixed with ethanol were used as background, while DPPH mixed with MilliQ water represented the 100% DPPH signal. Each sample was analyzed in triplicate.

5.2.2.2. Enzymatic functionalization of SHF68 (Lig-SHF68)

The custom-made poly(urethane) exposing amino groups (SHF68), described in Section 2, was used for conjugation with Lig-TA, through the action of laccase. SHF68 (10 mg/mL) was dissolved in 50 mL of sodium acetate buffer (50 mM, pH 5) added with acetosyringone at 1.5 mg/mL concentration. Lig-TA was solubilized in sodium acetate buffer and added to the SHF68 solution to achieve a final concentration of 1 mg/mL, and the solution was then equilibrated at 50 °C. Laccase was added to the mixture at 0.1% v/v concentration and the reaction proceeded for 3 h at 50 °C under stirring. The obtained solution was dialyzed against demineralized water for 48h using a dialysis membrane with a cut-off of 14kDa (regenerated cellulose, Sigma Aldrich, Italy).

The obtained material was characterized through ATR-FTIR spectroscopy, quantification of phenolic content through the Folin-Ciocalteu assay and MPO and MMPs inhibition assays (at 10 mg/mL), as previously described. Additionally, Lig-SHF68 cytocompatibility was compared to pristine SHF68. Briefly, HFF-1 cells were cultured for 24 h. Then, Lig-SHF68 or SHF68 solubilized in cell medium at different concentrations (0.8-50 mg/mL) were added to each well and incubated for an additional 24 h. Cell viability was assessed using the CellTiterBlue assay. Briefly, the medium was discarded, and 100 µL of new medium added with 20 µL of CellTiterBlue reagent were added. After 3 h of incubation, the fluorescence at $\lambda_{ex/em}$ = 560/590 nm was measured. Cells incubated without PEUs were used as a growth control (100% cell viability).

5.2.2.3. Preparation and characterization of Lig-SHF68-based SM-gel

The Lig-SHF68-based SM-gel was prepared by combining α-CDs with Lig-SHF68, similar to the process described in Section 2. First, Lig-SHF68 was solubilized in phosphate buffer saline (PBS) at 4 °C; then, αCDs at 14% w/v concentration in PBS were added to the polymeric solutions to obtain a final formulation with 10% w/v αCDs concentration and different PEUs concentrations (3%, 5% w/v). The solutions were vortexed for 20 s and incubated at room temperature to allow gelation and obtain SM-gels.

The properties of the obtained SM-gels were characterized through rheological and stability tests as described in Section 2.

The rheological properties of SM-gels with varying PEU concentrations (3%, 5% w/v) were examined using a stress-controlled rheometer (MCR302, Anton Paar GmbH, Graz, Austria) with a 25 mm parallel plate setup. Before gelation, the hydrogels were prepared and loaded into a syringe

for an easier placement onto the rheological plate. Each experiment utilized approximately 0.4 mL of SM-gel, with a set sample thickness of 0.6 mm and no applied normal force. Strain sweep tests were conducted at 37 °C, employing an angular frequency of 1 rad s^{-1} and a strain range of 0.01–500%. After a 15-minute interval, tests were repeated to evaluate the hydrogels mechanical property recovery. Frequency sweep tests were carried out within the linear viscoelastic region (0.1% strain) at temperatures of 25 and 37 °C, by varying angular frequency between 100 and 0.1 rad s^{-1}. To assess the self-healing ability of SM-gels, self-healing strain tests were performed at a frequency of 1 Hz, subjecting the gels to cyclic deformations. Each cycle consisted of a recovery phase at low deformation (0.1%, 120 s) followed by a rupture phase at high deformation (100%, 60 s). After three cycles, the initial recovery phase was reinstated to evaluate residual mechanical properties.

For stability tests, the SM-gels at 3% and 5% w/v Lig-SHF68 content were prepared following the previously established procedure. Subsequently, 500 µL of the solution was dispensed into vials before gelation and incubated for 48 h at room temperature to ensure complete development of the SM-gel network. Following gelation, the vials were weighed ($W_{gel,i}$), after which 500 µL of phosphate buffer saline (PBS) was added, and the vials were further incubated at 37 °C. At specified time intervals (6, 24, 48, and 72 h), samples were collected, weighed after the removal of residual PBS ($W_{gel,f}$), subjected to lyophilization, and weighed again (W_{dry}). PBS refresh occurred for all samples at each time point to mimic exudate renewal. Hydrogel dissolution (residual weight %) was calculated using Equation (1), employing a sample lyophilized before incubation with PBS as a reference ($W_{dry,cntr}$). The variation in wet weight (wet weight %) was calculated as per Equation (2), while the swelling ratio was measured as in Equation (3):

$$\text{Residual weight \%} = \left(1 - \frac{W_{dry} - W_{dry,cntr}}{W_{dry,cntr}}\right) 100 \quad (1)$$

$$\text{Wet weight \%} = \frac{W_{gel,i} - W_{gel,f}}{W_{gel,i}} 100 \quad (2)$$

$$\text{Swelling ratio} = \frac{W_{gel,f} - W_{dry}}{W_{dry}} \quad (3)$$

The antioxidant activity of the components released from the SM-gel was assessed through the DPPH assay as described previously. The release solutions from SM-gels were collected and mixed with DPPH using the same proportion as previously indicated (5.2.2.1.). Similarly, the MMPs inhibitory capacity of the components released from the hydrogels were assessed. Briefly, 150 µl of release were mixed with 1.5 µL of 500 U/mL collagenase type IV from Clostridium histolyticum (final concentration 5 U/mL). The solution was then incubated at 37 °C for 24 h and the samples were analyzed as explained in 5.2.2.1.

Cytocompatibility was also evaluated as described in Section 3 using a fibroblast HFF-1 cell line and following ISO 10993:5 recommendations. Vials containing 100 mg of SM-gel, composed of a 3% w/v or 5% w/v Lig-SHF68 concentration, were prepared. Subsequently, 1 mL of cell culture medium was introduced into each vial. After a 24-h incubation period at 37 °C, hydrogel extracts were obtained and filtered through a 0.22 µm syringe filter (PES, LLG labware). Concurrently, HFF-1 cells were cultured for 24 h. Then, 100 µL of the filtered samples was added to each well containing cultured cells and incubated for additional 24 h. Cell viability was assessed using the CellTiterBlue assay. Briefly, the medium was discarded, and 100 µL of new medium added with 20 µL of CellTiterBlue reagent were added. After 3 h of incubation, the fluorescence at $\lambda_{ex/em}$ = 560/590 nm

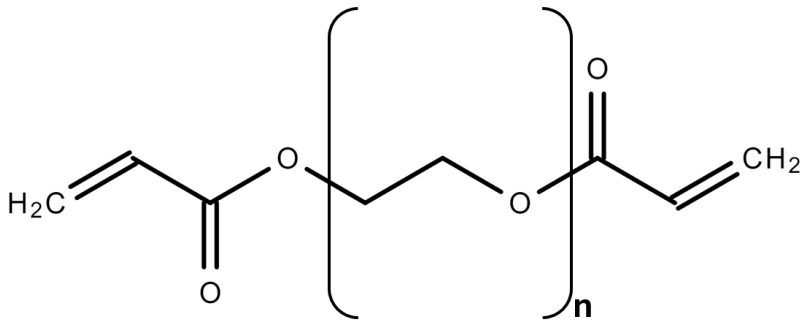
was measured. Cells incubated without hydrogel extracts were used as a growth control (100% cell viability).

5.2.3. Development of photo-crosslinked SM-gel (UV-SM-gel)

5.2.3.1. PEG-DA synthesis and characterization

The PEG-DA (Figure 5.2) used in this work was synthesized by our group in the framework of another project by reacting PEG with acryloyl chloride. Briefly, PEG (6000 Da, Sigma-Aldrich, Italy) was functionalized with acrylate groups by reacting its hydroxyl end groups with acryloyl chloride (AC, Sigma-Aldrich, Italy). PEG at 30% w/v in dichloromethane (DCM, Carlo Erba, Italy) was mixed with triethylamine (TEA, Sigma-Aldrich, Italy) and AC at a molar ratio of 2:1 and 4:1 with respect to PEG, respectively. The reaction was conducted for 24 h under nitrogen flux protected from the light. Then, a potassium carbonate (Sigma-Aldrich, Italy) solution (1.5 M in deionized water) was added with a 1:4 volume ratio with respect to the DCM total volume, to neutralize the hydrochloric acid formed during the reaction. After 20 h of decantation, two different phases were formed: an upper aqueous phase containing potassium carbonate, TEA and not functionalized PEG and a bottom phase containing PEGDA dissolved in DCM. The PEGDA solution was collected and dried magnesium sulfate (Sigma-Aldrich, Italy) was added to absorb residual water. The solution was purified by centrifugation (6000 rpm at 0°C for 20 minutes) and the collected solution was then concentrated through rotary evaporation and precipitated in diethyl ether (DEE, Carlo Erba, Italy) (5:1 volume ratio with respect to DCM). Precipitated PEGDA was dried overnight and stored under vacuum at 4 °C until use.

PEG-DA was characterized in our group through ATR-FTIR spectroscopy, ^{1}H-NMR spectroscopy and SEC showing a degree of acrylation of 77%, an average of 1.54 acrylate groups per polymeric chain, and weight average molecular weight and polydispersity index of 6000 Da and 1.05, respectively. This PEG-DA was then used in blend with Lig-SHF68 to obtain SM-gels that could be additionally photo-crosslinked through UV irradiation.



PEG-DA

Figure 5.2. Chemical structure of PEG-DA.

5.2.3.2. Preparation and optimization of an SM-gel combining PEG-DA and Lig-SHF68

The new SM-gels based on a blend of Lig-SHF68 and PEG-DA were prepared by mixing these polymers with αCDs, similar to the process described in Section 2. Briefly, Lig-SHF68 and PEG-DA were first solubilized in PBS with 0.05% w/v LAP at 4 °C; then, α-CDs at 14% w/v in PBS containing LAP at 0.05% w/v were added to the polymeric solutions to obtain a final formulation with 10% w/v α-CDs and different PEUs concentrations (i.e., 1%, 3% and 5% w/v). The samples were vortexed for 20 s, mixed at different Lig-SHF68:PEG-DA weight ratios (i.e., 80:20 and 50:50), and

then incubated for 24 h in the dark to allow gelation. The formed gels were then exposed to UV light (for 1 min at 365 nm and 10 mW/cm^2) on both sides to guarantee homogenous crosslinking.

Cytocompatibility, gelation and preliminary stability tests were conducted to perform a screening among the developed formulations before proceeding with further characterizations. Briefly, the physical gelation of the developed formulations before photo-curing was assessed by tube inverting test. The hydrogels were prepared as previously described (500 µL in vials with a 17 mm diameter and 7 mL volume) and monitored by gentle rotation to assess the time required to obtain a stable network. On the other hand, the stability of the UV-SM-gels in aqueous environments was tested by putting the hydrogels in contact with PBS at 37 °C and refreshing the medium at specific time points (6 h, 24 h, 48 h, 72 h, 96 h, 120 h and 168 h). The time point at which the UV-SM-gel completely dissolved was recorded. Lastly, cytocompatibility was tested as described above using a fibroblast HFF-1 cell line. Upon this preliminary screening, the properties of the selected UV-SM-gels were assessed through stability, ROS scavenging activity (DPPH assay) and MMPs inhibition properties as described in 5.2.2.3. Rheological and photo-rheological tests were also conducted. Photorheology was conducted to assess formulation responsiveness to light irradiation. Conversely, rheological properties were tested on the developed formulations after photo-curing and according to the protocols reported above.

5.2.3.3. Photorheology of the UV-SM-gel

Photo-rheological characterization was performed on physically cross-linked formulations to evaluate differences in mechanical properties induced by light irradiation. In detail, the hydrogel was prepared as previously described and loaded into a syringe to facilitate the sample loading on the rheometer lower plate. After 48 h of incubation at room temperature to allow complete gelation, 0.4 mL of sample were loaded on the photorheometer plate (MCR302, Anton Paar GmbH, Graz, Austria. Equipped with a photorheology modulus). G' and G'' were evaluated over time in oscillation (1 Hz, 0.1% strain, 0 N normal force) for 90 seconds. Then, the sample was exposed to UV light for 120 seconds at 365 nm and 10 mW/cm^2 and G' and G'' were registered for an additional 12 minutes (15 min of test in total) to assess the time required for crosslinking stabilization and the stability of the photo-crosslinked network.

5.2.3.4. Incorporation and release of CoPc-Lig NPs and curcumin

Curcumin and CoPc-Lig NPs were incorporated into the UV-SM-gels at a concentration of 0.5 mg/mL and 3 mg/mL for curcumin and CoPc-Lig NPs, respectively. The UV-SM-gels were produced as described previously with curcumin and CoPc-Lig NPs dispersed in the CDs solution prior to mixing with the polymers solutions. Then, the compounds released from the UV-SM-gels were studied as described in Section 3. Briefly, 500 µL of PBS were added to each vial containing the payload-containing UV-SM-gels (500 µL), and the samples were further incubated at 37 °C. At specified time intervals (6, 24, 48, 72, 96, 120 and 144 h), the supernatant was collected, its volume measured, and fresh PBS was added to the vials. The collected release solutions were then analyzed to quantify curcumin and CoPc-Lig NPs by measuring fluorescence at $\lambda_{ex/em}$ = 467/550 nm and absorbance at 710 nm, respectively. The release rate was calculated using Equation (4):

$$\text{Release rate} = \frac{Mi}{\Delta t} \quad (4)$$

Where M_i represents the quantity of released compounds in mg at a defined time step i, and Δt denotes the duration of the time step in hours.

To elucidate the release kinetics, the Korsmeyer–Peppas model (Power law) was applied to the release data collected within the first 96 h. Specifically, Equation (5) was employed to determine the release exponent, n:

$$\frac{Mt}{M\infty} = Kt^n ; Log(\frac{Mt}{M\infty}) = nLog(t) + Log(K) \quad (3)$$

Where M_t identifies the mass of released CoPc-Lig NPs or curcumin at a defined time step t, M_∞ denotes the total encapsulated payload, and K represents the dissolution rate constant. For cylindrical samples, n values of 0.45 and 0.89 correspond to release mechanisms based on diffusion or swelling, respectively. Values falling between 0.45 and 0.89 suggest anomalous transport, a combination of diffusion and swelling phenomena. n values exceeding 0.89 indicate a mode of transport characterized by tension within the hydrogel network generated via solvent uptake and significant mass exchange with the external environment [11], [12].

5.2.4. Statistical analysis

Results are reported as mean ± standard deviation. Statistical analysis was performed through Microsoft Excel for Windows 10. To compare results, one-way ANOVA analyses were performed, followed by Bonferroni's multiple comparison test. Statistical significance was assessed as follows: n.d.—non-significant difference, * $p < 0.05$, ** $p < 0.01$, and *** $p < 0.001$.

5.3. Results and discussion

In this section, the SM-gel developed in Section 2 was modified to add antioxidant and anti-inflammatory functionalities and to increase its stability in aqueous environments. The work initially focused on functionalizing a custom-made PEU with lignin-based antioxidant and anti-inflammatory moieties and on characterizing the resulting SM-gels. This new polymer was then used in a blend with PEG-DA to obtain a photo-curable hydrogel with improved stability.

5.3.1. Enzymatic functionalization of lignin with TA and characterization

5.3.1.1. Lig-TA chemical characterization and phenolic content quantification

A novel lignin-based material was developed by conjugating tannic acid (TA) to sulfonated lignin using laccase, adapting the methodology outlined in Section 3. In this case, sulfonated lignin was chosen due to its enhanced solubility in aqueous solutions [13], which facilitates the subsequent conjugation with SHF68. The Lig-TA material exhibited an increase in phenolic content from 99 ± 6 µg GAE per mg of pristine lignin to 180 ± 7 µg GAE per mg of Lig-TA conjugate ($p = 0.0002$), indicating successful TA conjugation. Moreover, ATR-FTIR analysis (Figure 5.3) confirmed the presence of TA, as evidenced by the intensification in Lig-TA spectrum of the peak at 1700 cm^{-1} attributed to the C=O stretching vibration of unconjugated carbonyl groups [14], which is observed as a slight shoulder in pristine lignin. Additionally, a shift in the band around 3400 cm^{-1} (from 3270 cm^{-1} to 3400 cm^{-1}), related to the stretching of the -OH bond on the aromatic ring [15], [16], suggested the occurrence of cross-linking between lignin and tannic acid during laccase-assisted phenolation [17]. The peaks at 2920 cm^{-1} and 2840 cm^{-1} corresponded to the C-H stretching of methyl groups and were characteristic of lignin presence.

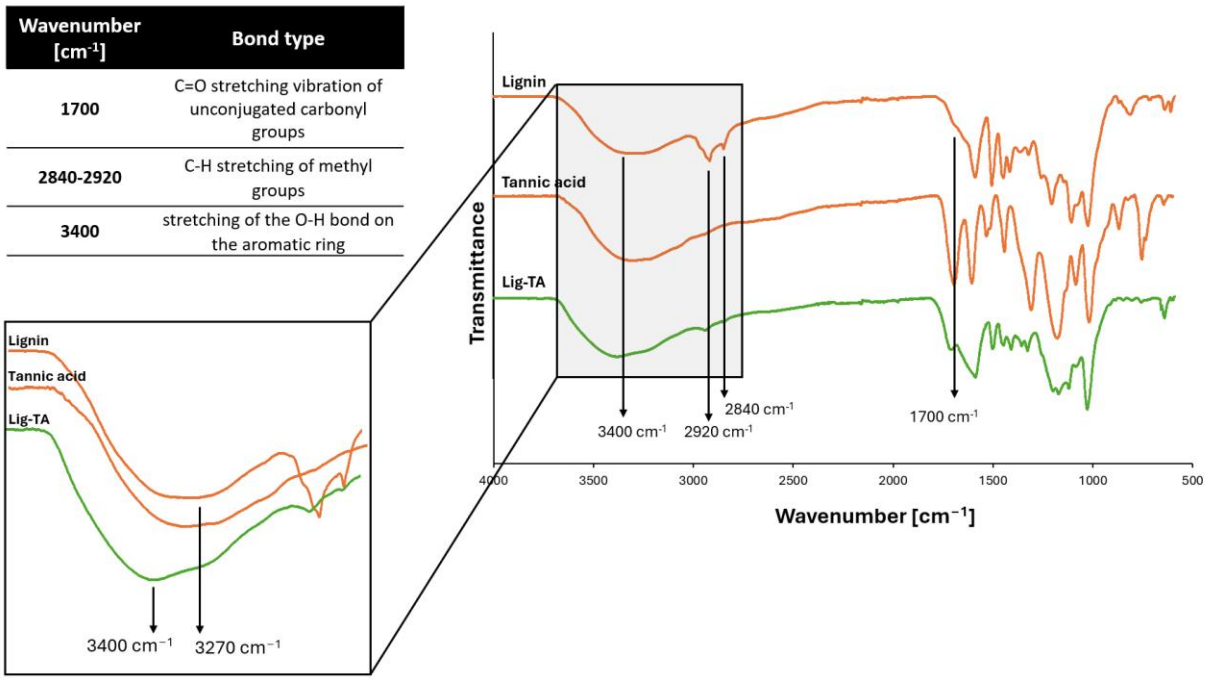


Figure 5.3. ATR-FTIR spectroscopy of the Lig-TA material obtained by reacting sulfonate lignin and TA. Lig-TA spectrum is reported in green, lignin and tannic acid spectra were also recorded as controls (in orange).

5.3.1.2. Lig-TA antioxidant and anti-inflammatory activity

The Lig-TA material was evaluated for its ability to inhibit both MPO and MMPs, which are typically upregulated in CWs, hindering the wound-healing process during the inflammatory phase. Remarkably, the material demonstrated a high inhibitory efficacy (>90%) in both cases, showing statistically significant differences compared to lignin ($p < 0.001$) (Figure 5.4.A). Moreover, tests on Lig-TA antioxidant capacity showed remarkable ROS scavenging activity compared to pristine lignin (Figure 5.4.B). Phenolic compounds found in natural substances can act as radical scavengers by donating hydrogen atoms via their hydroxyl groups [18]. Additionally, they can compete with MPO substrates and inhibit HOCl production [19]. MMPs, on the other hand, are a group of Zn-containing peptidases implicated in ECM degradation, and previous research has indicated the zinc-chelating activity of TA [13]. These results suggest that in Lig-TA the antioxidant activity and the MPO and MMPs inhibitory capability are related to the increased phenolic content compared to virgin lignin [20].

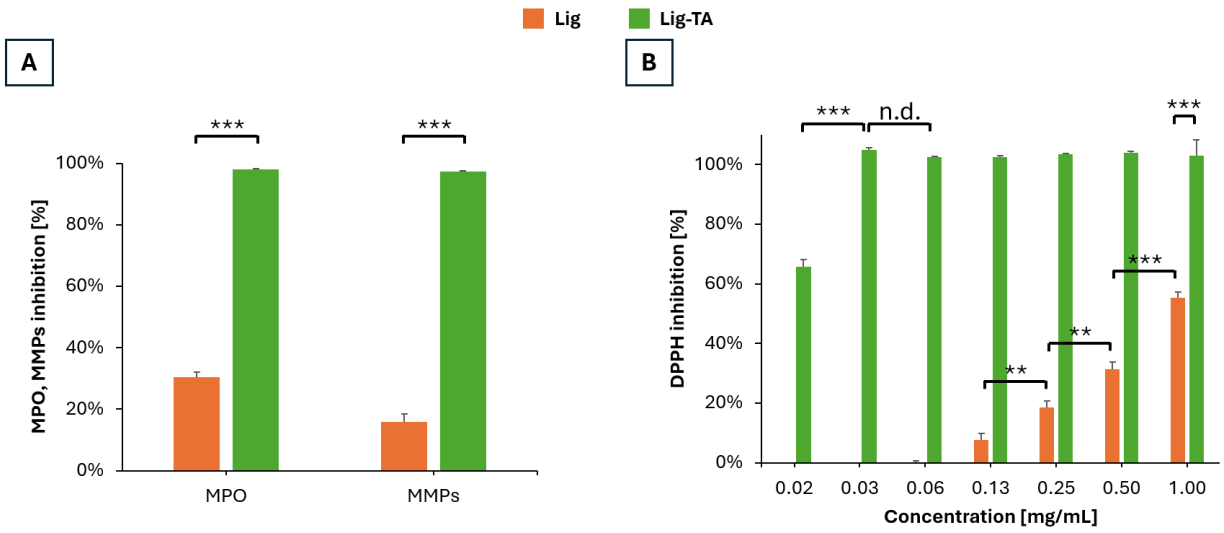


Figure 5.4. Antioxidant and anti-inflammatory activity of Lig-TA. (A) Inhibition of MPO and MMPs, and (B) ROS scavenging activity evaluated through the DPPH assay.

5.3.2. Preparation and characterization of Lig-SHF68-based SM-gel

5.3.2.1. Lig-SHF68 chemical characterization and quantification of phenolic groups

The Lig-TA material was conjugated to SHF68 through the action of laccase. This enzyme oxidates the phenols in the lignin-based material producing radicals that can further interact with other groups, such as the primary amines exposed along the SHF68 backbone. The obtained polymer presented the brown color characteristic of lignin and the phenolic groups conjugated to the polymer were measured to be 10.6 ± 1.6 µg GAE per mg of material. Additionally, in the ATR-FTIR spectrum of Lig-SHF68 a peak at 1590 cm^{-1} was observed, corresponding to the stretching of the benzene ring in phenolated materials (Figure 5.5). The peak at 1700 cm^{-1} is related to the C=O stretching of both urethane bonds and carbonyl groups on lignin.

Wavenumber [cm^{-1}]	Bond type
1590	stretching of the benzene ring
1720	C=O stretching of free carbonyl groups

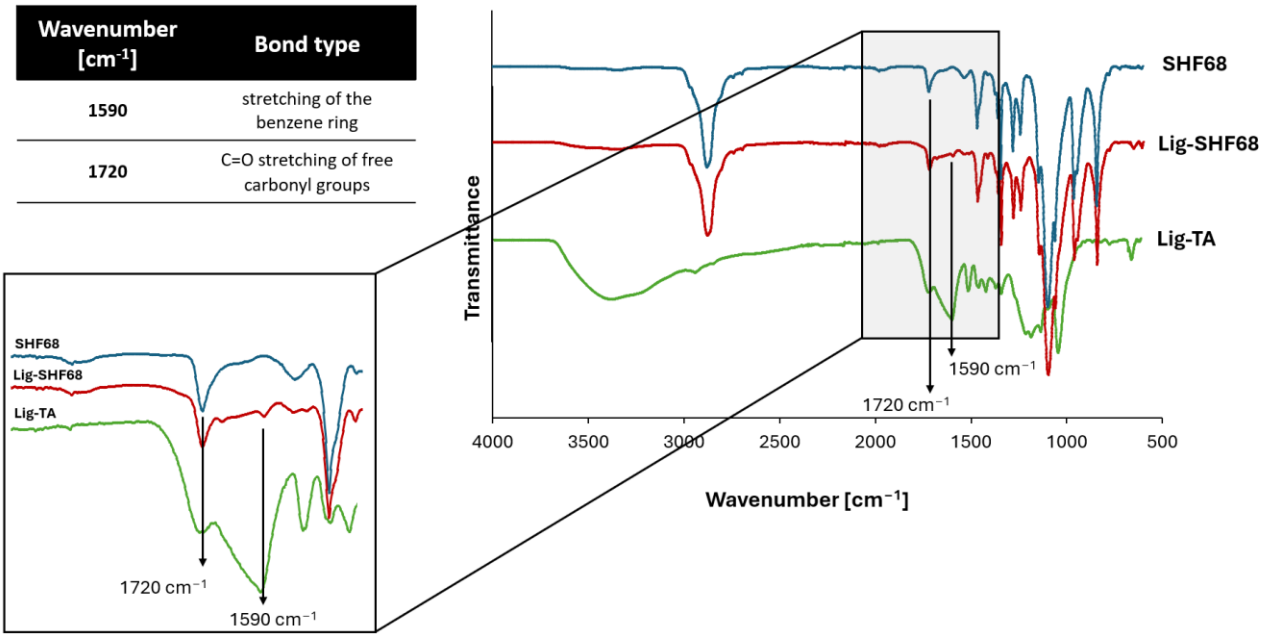


Figure 5.5. ATR-FTIR spectroscopy of Lig-SHF68 material obtained by reacting SHF68 and Lig-TA. Lig-SHF68 spectrum is reported in red. SHF68 and Lig-TA were also analyzed as control conditions (in blue and green, respectively).

5.3.2.2. Lig-SHF68 antioxidant and anti-inflammatory activity

The newly designed poly(urethane) was tested to investigate its antioxidant activity and MMPs and MPO inhibitory capacity. A ROS-scavenging ability could be observed that progressively increased with Lig-SHF68 concentration with 60% inhibition at 6.3 mg/mL and reaching around 90% (Figure 5.6.A) for concentrations higher than 25 mg/mL. Given this result, MMPs and MPO inhibitory capacity of Lig-SHF68 was tested at 10 mg/mL (Figure 5.6.B) showing around 50% inhibition for both enzymes. These results could be strictly correlated to the presence of Lig-TA grafted to the poly(urethane) backbone since for pristine SHF68 enzymes inhibition and ROS scavenging activities were negligible.

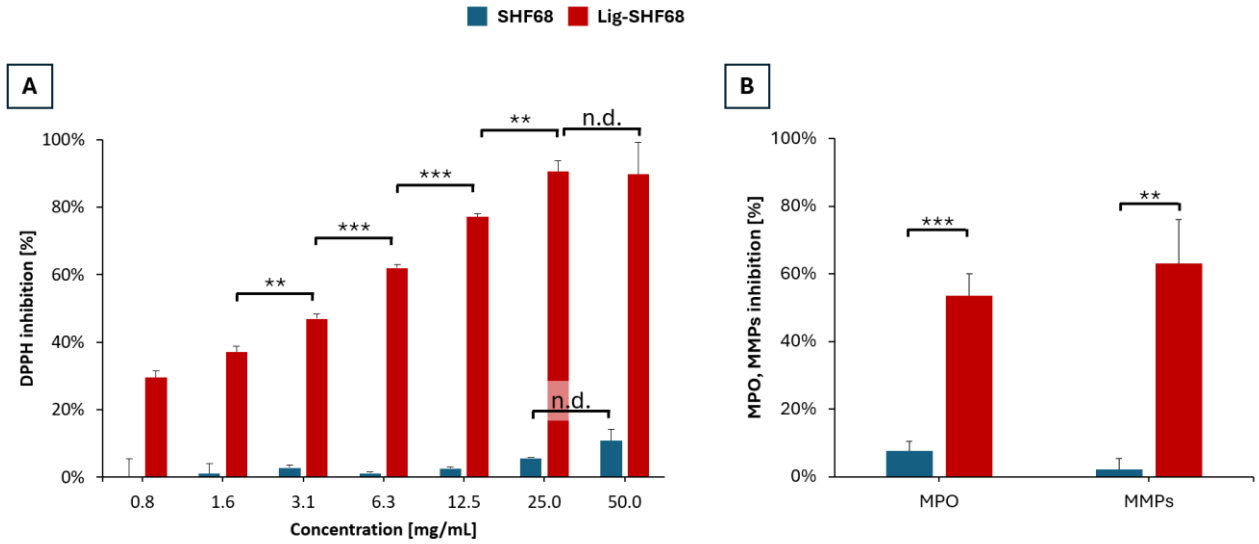


Figure 5.6. Antioxidant and anti-inflammatory activity of Lig-SHF68. (A) ROS scavenging activity evaluated with the DPPH assay, and (B) inhibition of MPO and MMPs at 10 mg/mL Lig-SHF68.

5.3.2.3. Cytocompatibility of Lig-SHF68

The cytocompatibility of Lig-SHF68 compared to pristine SHF68 was tested at different concentrations against HFF-1 human cell line, showing a slight increase in toxicity at concentrations higher than 6.3 mg/mL (Figure 5.7). This could be related to the presence of phenols that at high concentrations are known to have prooxidant effects [21]. Nevertheless, Lig-SHF68 can be used at low concentrations in the SM-gel thanks to its interaction with αCDs. Additionally, the release of the hydrogels components is controlled over time. Therefore, despite these concerns on materials cytocompatibility, Lig-SHF68 presented promising properties for the development of SM gels. The cytocompatibility of the final systems will also be tested in the following paragraphs to ensure safety.

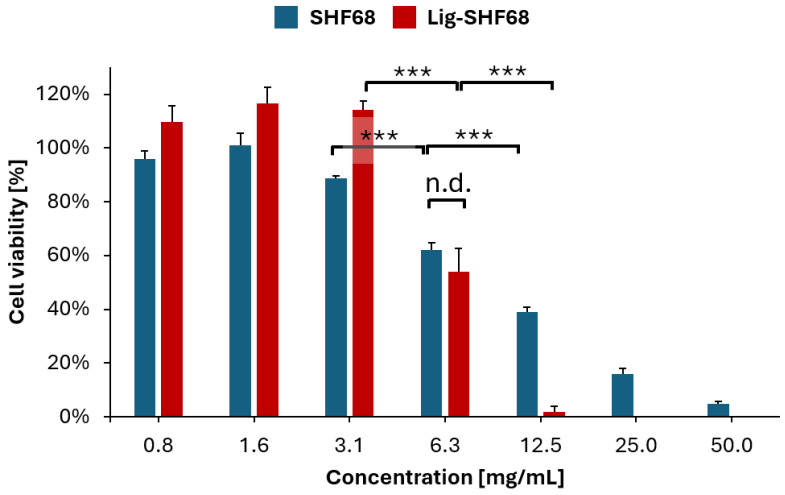


Figure 5.7. Cytocompatibility of Lig-SHF68 compared to pristine SHF68. Cytocompatibility was tested using HFF-1 *cells cultured with cell culture medium containing the polymers at predefined concentrations for 24 h.*

5.3.2.4. Rheological properties of Lig-SHF68-based SM-gels (Lig-SHF68-SM-gels)

Lig-SHF68-SM-gels were obtained by combining α-CDs at 10% w/v and Lig-SHF68 at 1%, 3% or 5% w/v PEU concentration and the hydrogels rheological properties were characterized as explained in Section 2. At 1% w/v concentration, Lig-SHF68 was not able to undergo gelation upon mixing with αCDs at 10% w/v concentration. Therefore, this condition was not investigated. Conversely, Lig-SHF68-SM-gels at 3% and 5% w/v Lif-SHF68 concentration underwent complete gelation through overnight incubation.

Strain sweep tests were conducted to assess the hydrogels capacity to withstand loads and undergo self-healing upon network breakage. Figure 5.8 reports the trends of G' and G'' registered for Lig-SHF68-SM-gels and SHF68 gels during strain sweep tests. For all the tested formulations, it was possible to identify a LVE region in which the gels behaved as viscoelastic solids, with G' and G'' independent over applied deformation. Then, the hydrogels started to mechanically fail until G' and G'' reached a crossover point and the networks behaved as viscoelastic liquids. These curve profiles indicate system injectability and were in accordance with the rheological results in Sections 2 and 3. Additionally, it was possible to observe a direct correlation between PEU content and G' values in the LVE region with G' values increasing from 433 Pa at 3%w/v Lig-SHF68 concentration to 780 Pa at 5%w/v polymer concentration (Table 5.1). This was expected since at higher polymeric content more interactions occur among the chains which result in better network development. Interestingly, Lig-SHF68-based gels presented reduced mechanical properties, with lower G' and G'' values within the LVE region compared to SHF68-based gels with the same polymer concentration (433 Pa compared to 2355 Pa at 3%w/v concentration, and 780 Pa compared to 2433 Pa at 5%w/v concentration). This could indicate a reduced capability of Lig-SHF68 to interact with α-CDs in the PPRs formation. Indeed, the presence of Lig-TA conjugated to the primary amines exposed along SHF68 chains could interfere with the PPRs assembly. This was also visible in the higher flow transition indexes observed (4.25 and 8.31 for 3%w/v and 5%w/v concentrated Lig-SHF68 SM-gels, respectively, compared to 2.09 and 5.14 for SHF68 based SM-gel at 3%w/v and 5%w/v concentration, respectively), which suggested also a creamier network able to bear higher applied strains.

Strain sweep tests were also performed to assess the self-healing capacities of the developed systems by repeating the test on the same sample after 15 minutes of recovery in quiescence at 37

°C. Figure 5.9. Rheological strain sweep test for SHF68- and Lig-SHF68-based SM gels. Trends of G' (continuous line) and G'' (dashed line) as a function of applied strain. (A) SHF68 SM-gels at 3% w/v concentration before (blue) and after 15 min recovery (SH) (light blue), (B) SHF68 SM-gels at 5% w/v concentration before (blue) and after 15 min recovery (SH) (light blue), (C) Lig-SHF68 SM-gels at 3% w/v concentration before (red) and after 15 min recovery (SH) (light red), and (D) Lig-SHF68 SM-gels at 5% w/v concentration before (red) and after 15 min recovery (SH) (light red). displays the trends of G' and G'' for each formulation as registered during strain sweep tests on the as-prepared samples and the healed samples after 15 minutes of recovery. A reduction of G' values in the LVE region was observed (e.g., for Lig-SHF68 SM-gels at 3% w/v concentration the G' value was reduced from 433 Pa to 356 Pa) but the overall G' recovery was above 70%. In accordance with Sections 2 and 3, the higher the PEU content, the lower the percentage of G' recovery, indicating a network in which the contribution of PPRs in the gelation is shadowed by the mechanism of micelles formation. Interestingly, the functionalization of SHF68 with Lig-TA did not affect the self-healing capacity of the resulting SM gels.

Table 5.1. Summary of the rheological characteristics of SHF68- and Lig-SHF68-based gels extracted from the strain sweep test.

PEU content [% w/v]		τ_y (Pa)	τ_f (Pa)	Flow transition index	G'_{LVE} (Pa)	G''_{LVE} (Pa)	G'_{LVE} recovery (Pa)	G''_{LVE} recovery (Pa)	G' recovery (%)
SHF68	3%	6.18	12.90	**2.09**	2355	234	1892	166	**80%**
	5%	16.20	83.30	**5.14**	2433	230	1788	153	**73%**
Lig-SHF68	3%	4.75	20.20	**4.25**	433	38	356	30	**82%**
	5%	5.39	44.80	**8.31**	780	75	578	51	**74%**

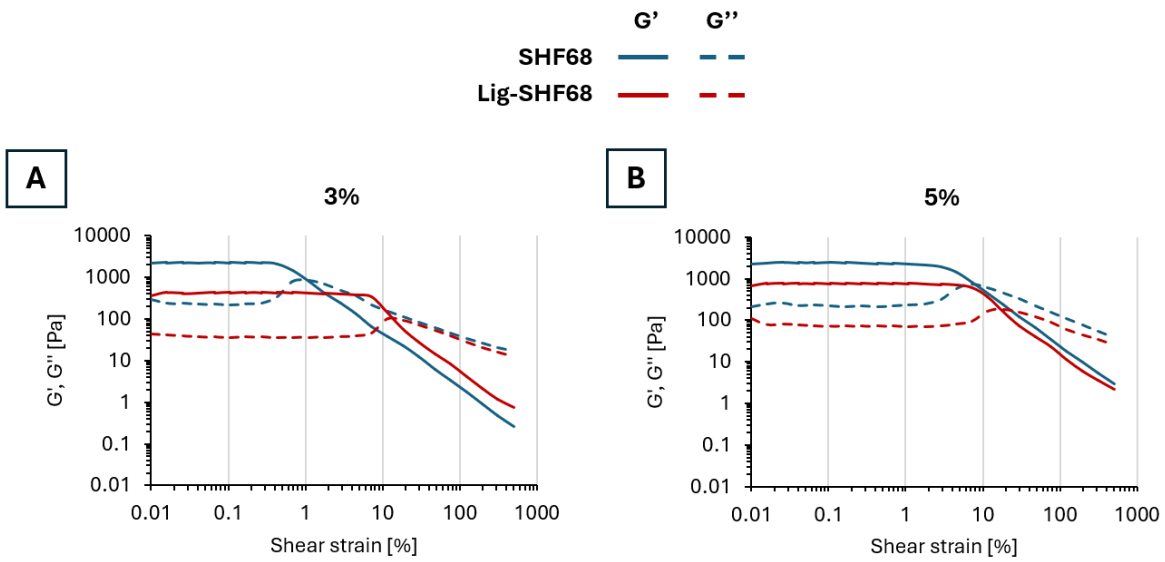


Figure 5.8. Rheological strain sweep test. Trends of G' (continuous line) and G'' (dashed line) as a function of applied strain for SHF68- (blue) and Lig-SHF68- (red) based gels at (A) 3%, and (B) 5% w/v polymer concentration.

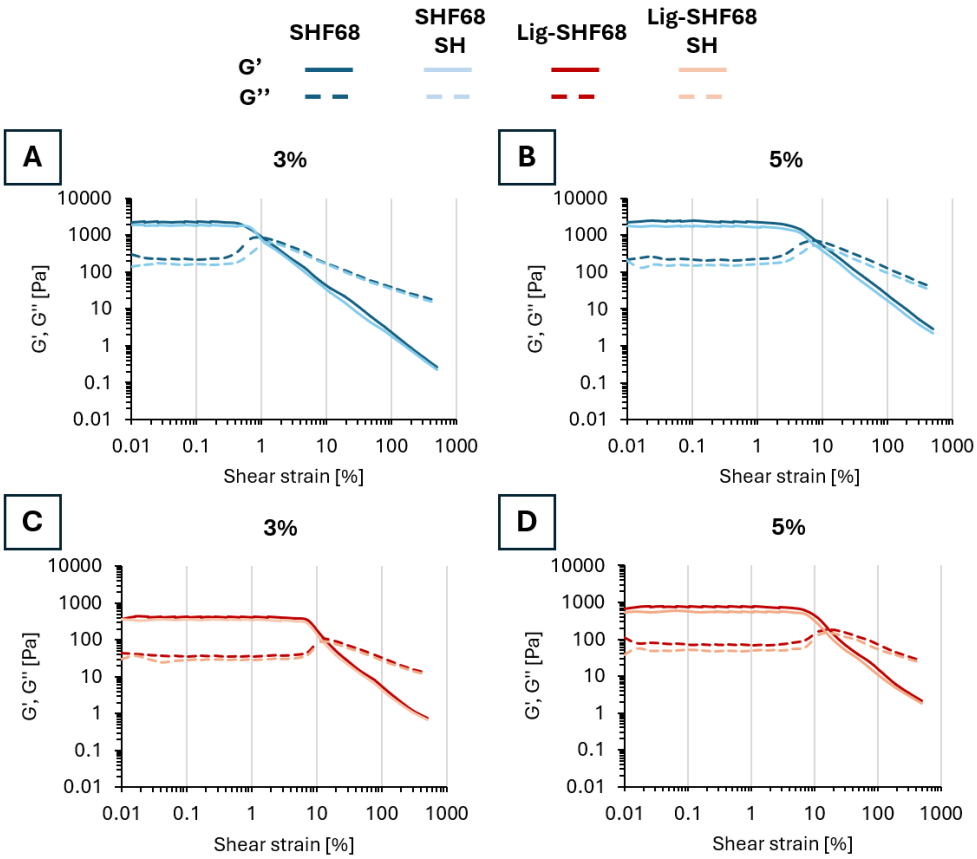


Figure 5.9. Rheological strain sweep test for SHF68- and Lig-SHF68-based SM gels. Trends of G' (continuous line) and G'' (dashed line) as a function of applied strain. (A) SHF68 SM-gels at 3% w/v concentration before (blue) and after 15 min recovery (SH) (light blue), (B) SHF68 SM-gels at 5% w/v concentration before (blue) and after 15 min recovery (SH) (light blue), (C) Lig-SHF68 SM-gels at 3% w/v concentration before (red) and after 15 min recovery (SH) (light red), and (D) Lig-SHF68 SM-gels at 5% w/v concentration before (red) and after 15 min recovery (SH) (light red).

Frequency sweep tests were performed to assess the attainment of fully developed hydrogels. Lig-SHF68-SM-gels were tested at different frequencies under a constant strain within the LVE region. The test was repeated at three different temperatures (25 °C, 30 °C and 37 °C) to assess the responsivity of the Lig-SHF68-SM-gels to thermal changes. As shown in Figure 5.10 and summarized in Table 5.2, for all angular frequencies, G' was higher than G'' and the curves were parallel and independent over angular frequency, implying that the hydrogels were fully developed and characterized by a marked gel state. Additionally, the values of G' increased with the increase of PEU content, in accordance with the strain sweep test (from 284 Pa at 3% w/v Lig-SHF68 concentration to 1050 Pa at 5% w/v polymer concentration). As observed in Section 2, no major differences were observed when comparing G' and G'' values at different temperatures (Figure 5.11), indicating that the developed SM gels do not significantly change their behavior as a function of temperature.

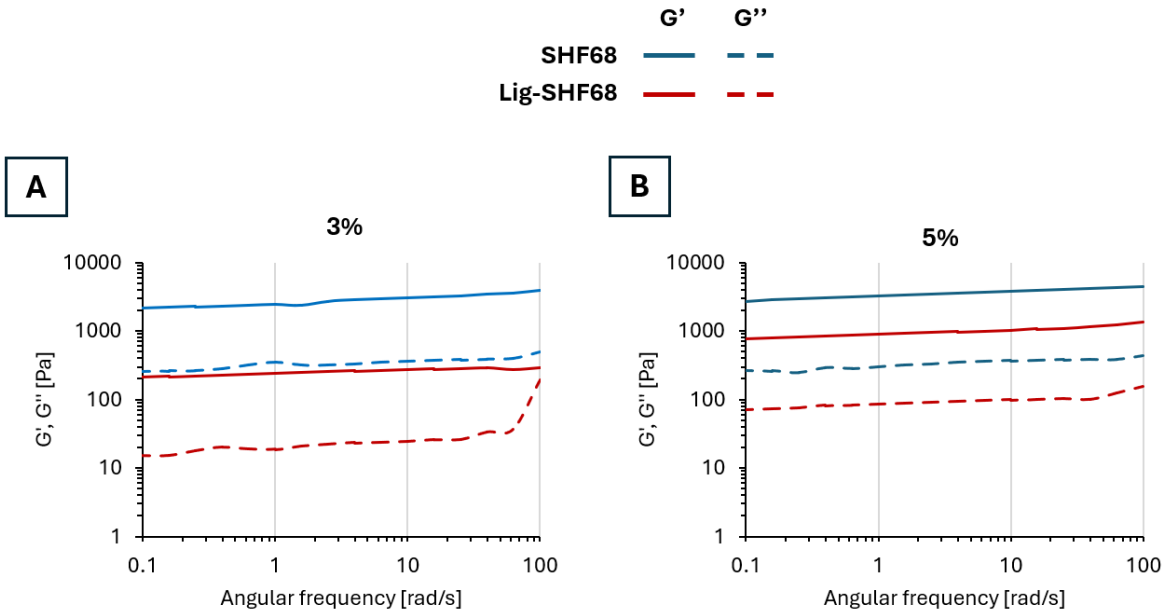


Figure 5.10. Rheological frequency sweep test performed at 37 °C. Trends of G' (continuous line) and G'' (dashed line) for SHF68- (blue) and Lig-SHF68- (red) based gels at (A) 3%, and (B) 5% w/v polymer concentration.

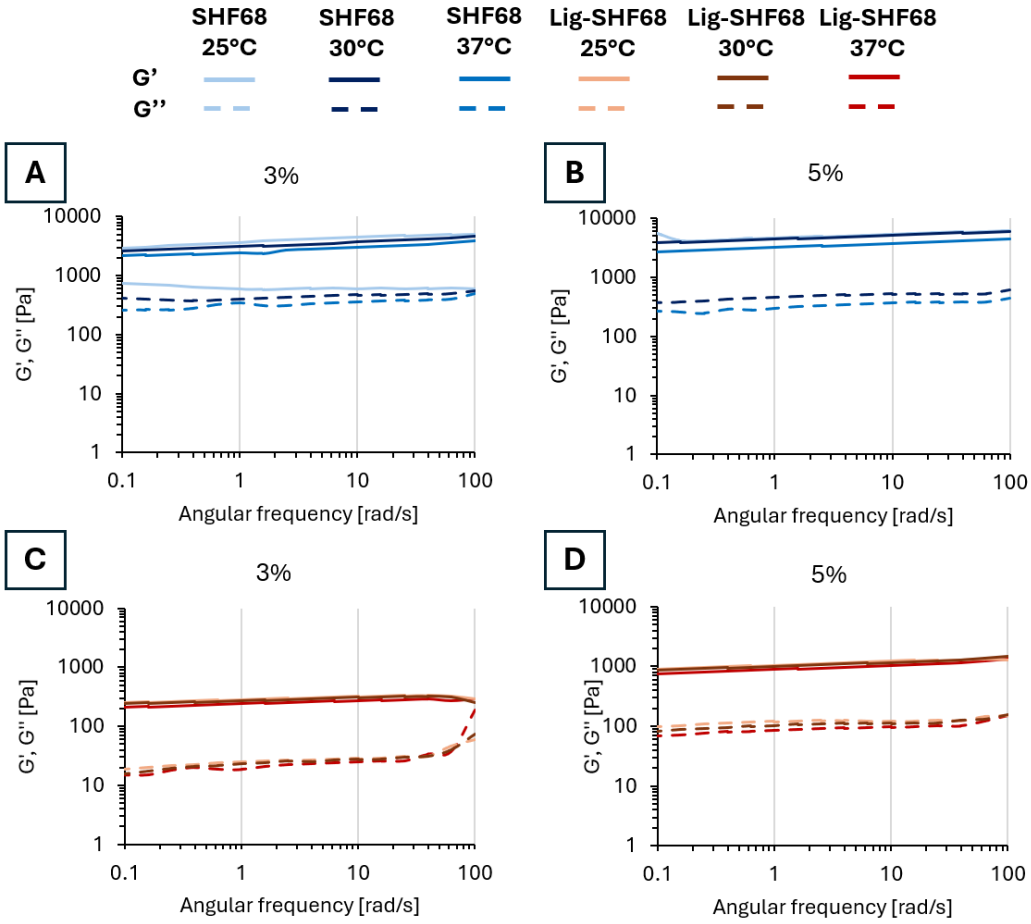


Figure 5.11. Rheological frequency sweep test. Trends of G' (continuous line) and G'' (dashed line) as a function of angular frequency for (A-B) SHF68-based gel at 3% w/v and 5% w/v concentration, respectively, tested at 25 °C (light blue), 30 °C (dark blue) and 37 °C (blue). (C-D) Lig-SHF68-based gel at 3% w/v and 5% w/v concentration, respectively, tested at 25 °C (light red), 30 °C (dark red) and 37 °C (red).

Table 5.2. Summary of the rheological characteristics of Lig-SHF68- and SHF68-based SM gels extracted from the frequency sweep test.

PEU content [% w/v]		G' at 1 rad/s 25 °C (Pa)	G' at 1 rad/s 30 °C (Pa)	G' at 1 rad/s 37 °C (Pa)
SHF68	3%	3680	3080	2410
	5%	4670	4450	3220
Lig-SHF68	3%	284	271	242
	5%	1050	1010	890

Finally, shear tests were performed at 37 °C to assess the self-healing capacity of the Lig-SHF68-SM-gels under repeated cycles of rupture. Values of G' and G'' were recorded while the samples underwent three cycles of rupture followed by a recovery period (Figure 5.12). The initial and final values of G' measured during the resting period were compared and the percentage of G' recovery was reported in Table 5.3. Interestingly, Lig-SHF68-SM-gels showed reduced self-healing properties compared to SHF68-based SM gels with the same polymer concentration (68% at 3% w/v and 46% at 5% w/v for Lig-SHF68 based SM-gels compared to 81% at 3% w/v and 72% at 5% w/v for SHF68 based SM-gels). This is in contrast with what was observed in the strain sweep test (Table 5.1). From these results it can be inferred that the grafting of Lig-TA to the SHF68 backbone probably interferes with the re-establishment of PPRs-based interactions upon rupture, thus reducing the capacity of the system to withstand rapid cycles of rupture. However, when left to recover for a longer period, the percentage of G' recovery for Lig-SHF68-SM-gels becomes comparable to SHF68-based SM gels with the same composition, indicating that the Lig-SHF68-SM-gels can regain their structural stability, probably with a slower kinetics compared to SHF68-based ones.

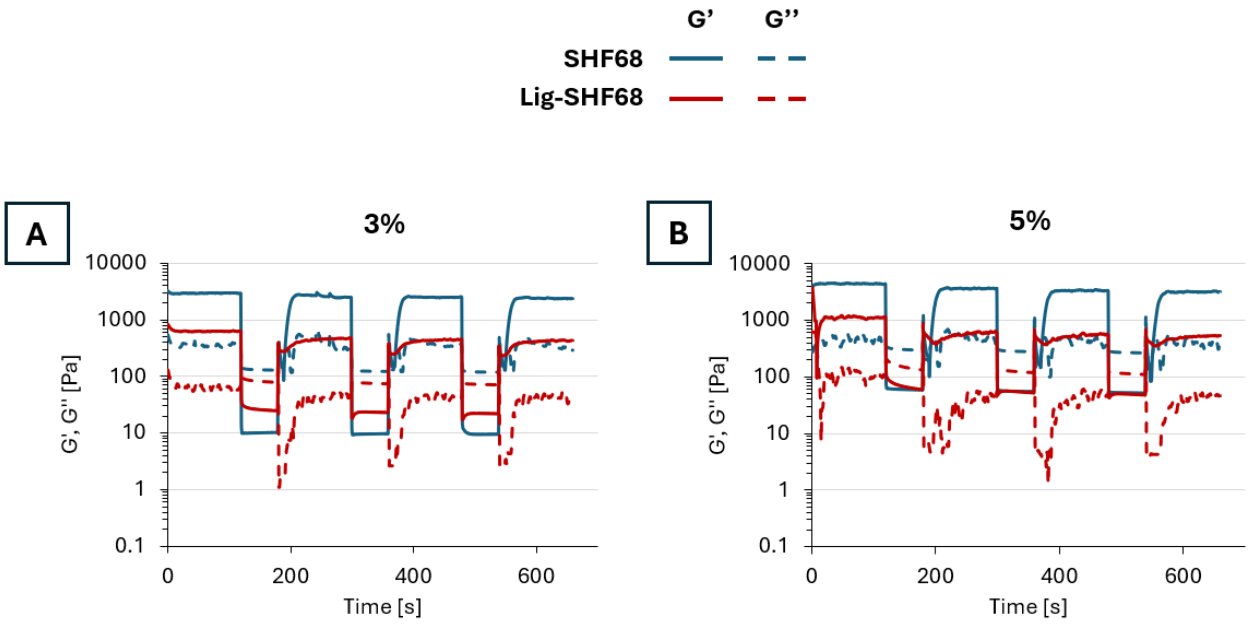


Figure 5.12. Rheological self-healing test. Trends of G' (continuous line) and G'' (dashed line) for SHF68- (blue) and Lig-SHF68- (red) based SM gels at (A) 3% and (B) 5% w/v polymer concentration.

Table 5.3. Summary of G' recovery values (%) for SHF68- and Lig-SHF68-based SM gels as evaluated through strain test at 37 °C.

PEU content [% w/v]	SHF68	Lig-SHF68
3%	81%	68%
5%	72%	46%

5.3.2.5. Stability of Lig-SHF68-SM-gels

In Section 2, SHF68 was characterized as a poly(urethane) with high responsiveness in aqueous environments. This characteristic significantly influenced the stability of SHF68-based SM gels, necessitating its blending with CHP407. Remarkably, the grafting of Lig-TA to SHF68 backbone substantially enhanced the durability of the resulting Lig-SHF68-SM-gels compared to similar formulations based on SHF68 as such (Figure 5.13.A and B). At 6h, all samples presented similar residual dry weight (around 80%) and variation in wet weight close to 0%, which resulted in a similar swelling ratio around 10 (Figure 5.13.C). However, SHF68-based gels dissolved within 24 h of incubation, while Lig-SHF68-SM-gels were still stable gels at that time point, showing a residual dry weight ranging between 40 and 60% depending on their polymer concentration. At this time point, a difference in the wet weight could be observed between the Lig-SHF68-based gels at 3% and 5% w/v concentration with wet weight of the SM-gels at 3% w/v starting to decrease. This is an clear indication that dissolution starts to prevail over fluid absorption for the SM-gel prepared at 3% w/v concentration. Indeed, after 48h of incubation with PBS, Lig-SHF68-SM-gels at 3% polymer concentration achieved complete destabilization and dissolution, while the formulations at 5% w/v concentration showed a residual dry weight of *ca.* 20% and a negative wet weight variation (around -40%). The improved stability of Lig-SHF68-SM-gels compared to similar formulations based on virgin SHF68 can be attributed to the presence of polyphenolic Lig-TA, which actively engages with other hydrogel components, augmenting the physical crosslinking within the network. These findings align with the observations from Section 3, where the interactions of the gel constituent polymers and α-CDs with CoLig NPs were investigated. However, the durability of the Lig-SHF68-SM-gels here described was comparable to the SM-gel selected in Section 2 and resulting from a blend between SHF68 and CHP407 at 3% w/v polymer concentration and CHP407:SHF68 weight ratio of 80:20. In that case, the hydrogel was also capable of maintaining its shape in the first 24 h of incubation, with a remaining dry weight of 60% and low variation in wet weight (lower than 10%), while underwent complete dissolution at 48 h. Therefore, additional chemical crosslinking is required to further improve formulation stability in watery environments.

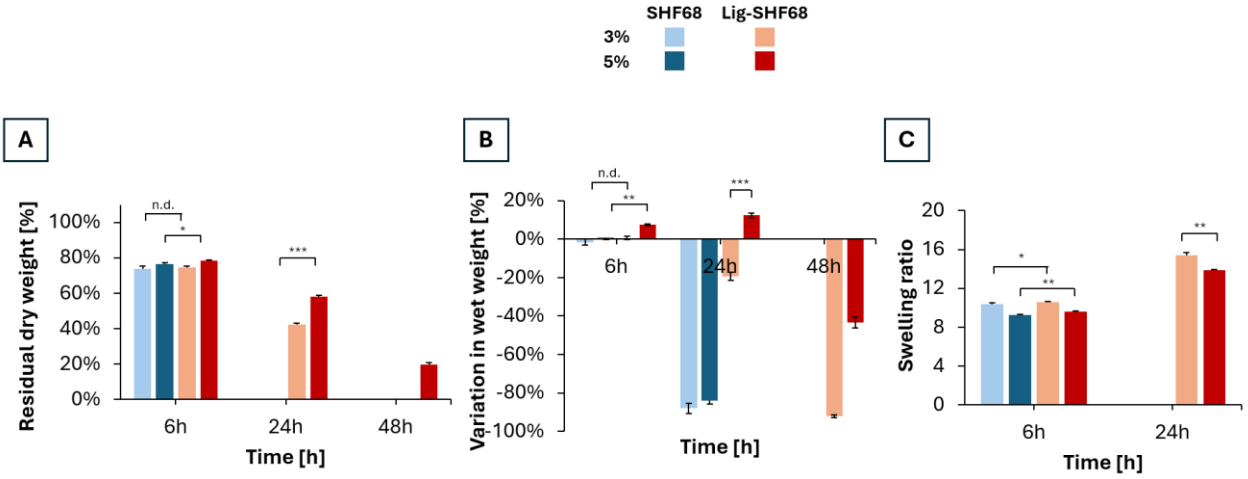


Figure 5.13. Stability of Lig-SHF68 (salmon and red at 3% and 5% w/v concentration, respectively) based SM-gels compared to SHF68 (light blue and blue at 3% and 5% w/v concentration, respectively) SM-gels. (A) Percentage of residual dry weight, (B) Variation of wet weight (%), and (C) swelling ratio measured at different time points during incubation in aqueous environment at 37 °C.

5.3.2.6. The cytocompatibility of Lig-SHF68-based SM-gels

The cytocompatibility of Lig-SHF68-based gels prepared at 3% and 5% w/v concentration was assessed against HFF-1 cell line following the ISO 10993:5 guidelines, as outlined previously. Cell viability approached 100% for both the tested formulations, underscoring the cytocompatibility of the hydrogels (Figure 5.14). Notably, Lig-SHF68-based gels presented higher cytocompatibility than the SHF68-based gels prepared at the same concentrations, contrary to the trends of the dose-response curves reported in Figure 5.7 ($p < 0.001$). This variance may be attributed to the enhanced stability of the Lig-SHF68-based hydrogels, resulting in a slower release of their components. Given the high cytocompatibility of the Lig-SHF68-based SM-gels at high PEUs contents, the formulation at 5% w/v PEU content was selected for further characterizations to maximize the antioxidant properties.

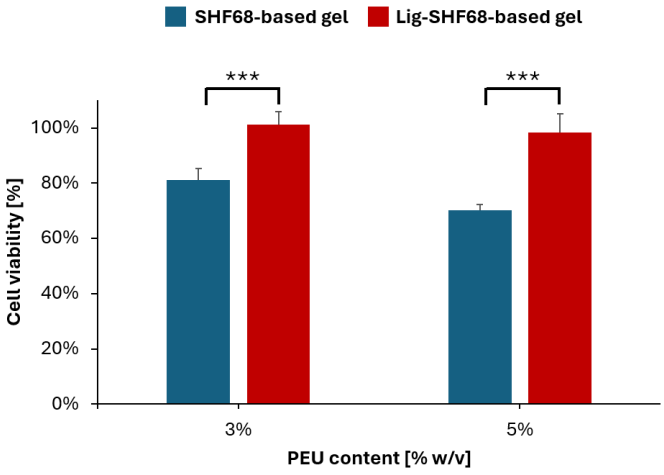


Figure 5.14. Cytocompatibility of Lig-SHF68- (blu) and SHF68- (red) based SM-gels prepared at 3% and 5% w/v polymer concentration.

5.3.2.7. Anti-inflammatory activity of the components released from the Lig-SHF68-based SM-gels

The Lig-SHF68-based SM gel with 5% w/v PEU content was exposed to aqueous media, and the antioxidant activity of the released components was assessed at specific time points. Interestingly,

the highest antioxidant capacity was observed within the initial 6 h, followed by a decline in subsequent time intervals (Figure 5.15). This trend was also confirmed when testing the MMPs inhibitory activity (Figure 5.16), where the inhibition was above 60% in the first 6 h and then decreased progressively. These trends could be attributed to the mode of dissolution of the hydrogel. Indeed, during the initial stages of interaction with external fluids, the Lig-SHF68-SM-gel releases components that are not directly incorporated into the network, such as free α-CDs, lignin-based constituents, or short PEU chains not participating in PPRs formation. This enables the Lig-SHF68-SM-gel to exhibit ROS-scavenging activity right from the onset of its application, potentially compensating for the limited effects that loaded actives have in the early stages (see 3.3.3.3. and 3.3.3.5. in Section 3). Indeed, in Section 3 the CoLig NPs were slowly released from the SM-gel and in the first 24 h presented an antioxidant activity of around 40% which increased to 80% at 48 h. This trend could pose a therapeutic problem in the first phases of treatment, which could be compensated by combining these NPs with a hydrogel presenting intrinsic antioxidant properties.

The MPO inhibitory activity will be tested in future experiments; nevertheless, Lig-SHF68- based SM-gel is also expected to present inhibition of this enzyme since the Lig-SHF68 material presented inhibitory activity itself (Figure 5.4).

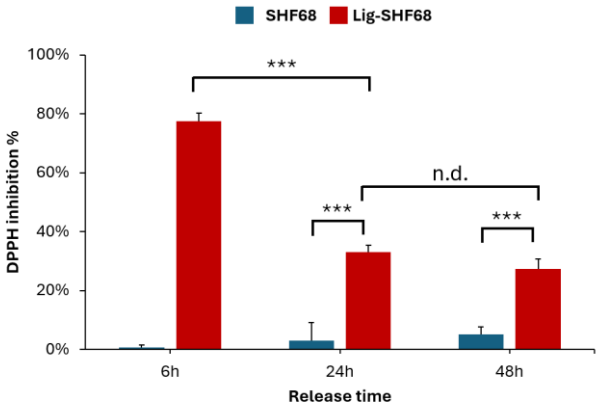


Figure 5.15. Antioxidant activity of the release media collected at 6h, 24h and 48h of incubation from Lig-SHF68- (red) and SHF68- (blu) based SM-gels prepared at 5% w/V PEU concentration.

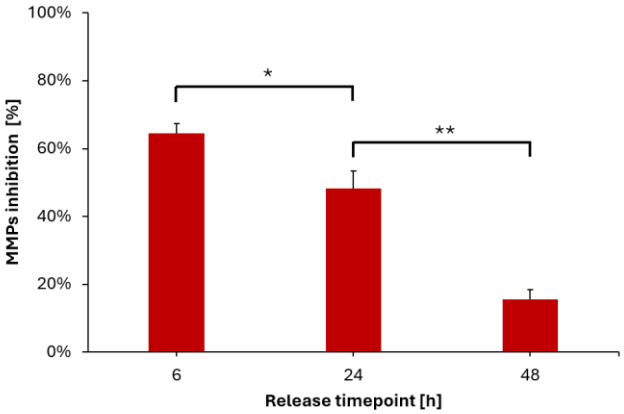


Figure 5.16. MMPs inhibitory activity of the release media collected at 6h, 24h and 48h of incubation from Lig-SHF68- based SM-gels prepared at 5% w/V PEU concentration.

5.3.3. Development of photo-crosslinked SM-gels

Given the poor mechanical properties and reduced stability of Lig-SHF68-based SM-gels, a photo-sensitive polymer (PEG-DA) was used in a blend with Lig-SHF68 to obtain an SM-gel with additional chemical crosslinking potential.

5.3.3.1. Optimization of UV-stabilized Lig-SHF68-based SM-gels

Cytocompatibility, gelation potential, and stability in the watery environment were assessed on a plethora of newly developed UV-stabilized SM-gels based on Lig-SHF68 and PEG-DA to perform a preliminary screening and identify the most promising ones before further characterization. In detail, two Lig-SHF68 to PEG-DA weight ratios (50:50 and 80:20) and three overall PEU concentrations (1%, 3%, and 5% w/v) were evaluated.

Results from the gelation tests revealed that the inclusion of PEG-DA significantly decreased gelation time from several hours for purely Lig-SFH68-based SM gels to a few minutes at 3% and 5% w/v concentration (Table 5.4) and to overnight gelation for the concentration at 1% w/v for which gelation was not observed in the Lig-SHF68 SM-gel. This phenomenon is attributed to the greater availability of PEG domains for PPR formation with the addition of PEG-DA, a small, linear polymer that readily interacts with αCDs. In the case of a Lig-SHF68 to PEG-DA 50:50 weight ratio, gelation occurred so rapidly that formulation handling became challenging. Conversely, at an 80:20 Lig-SHF68:PEG-DA weight ratio, the samples remain manipulable for a sufficient time interval to prepare them for subsequent experiments.

After incubation for a 24-h period to allow complete physical gelation, the samples underwent UV irradiation to promote photo-crosslinking. Preliminary stability studies indicated increased hydrogel durability across all tested formulations compared to hydrogels based solely on Lig-SHF68 (Table 5.5). Particularly interesting was the substantial improvement in hydrogel stability observed from 2 days for Lig-SHF68-based physical SM gels to 5-7 days in the photo-crosslinked gels. In particular, the formulation at 5% w/v PEU content and Lig-SHF68:PEG-DA 80:20 weight ratio presented the highest stability among the tested gels (7 days). In this condition, optimal synergy among PPRs, light-assisted crosslinking, micelle formation, and other non-covalent interactions involving the lignin counterpart most likely contributes to network stabilization. Remarkably, this condition also presents the highest content of the antioxidant Lig-SHF68, which make it a promising candidate for future characterization.

To ensure the applicability of the system to the biological environment, cytocompatibility was also tested using HFF-1 fibroblasts and according to the ISO 10993:5 guidelines. All tested formulations exhibited cytocompatibility, with cell viability exceeding 98% (Figure 5.17). Notably, lower PEU concentrations resulted in higher cell viability compared to the control. This effect may be attributed to the presence of free αCDs, which interact with cellular proteins and lipids, exerting beneficial effects [22]. Indeed, at lower PEU concentrations, PEG-DA chains with threaded αCDs are expected to better crosslink during light irradiation due to the presence of lower obstacles to their interactions. In such conditions, the αCDs threaded on crosslinked PEG-DA chains will not be immediately released in the surrounding medium during incubation, resulting in the release of αCDs at a proper concentration to promote cell proliferation.

Taking all these results together, the formulation at 5% w/v PEU content and 80:20 Lig-SHF68:PEG-DA weight ratio was selected for further characterization, since it presented gelation within a time interval that allowed easy manipulation, long-term durability and cytocompatibility.

Table 5.4. Gelation time of the developed hydrogel formulations. (O.N. = overnight)

Lig-SHF68:PEG-DA ratio / PEU content [% w/v]	0:100	50:50	80:20	100:0
1%	2 min	O.N.	O.N.	No gelation
3%	1 min	2 min	15 min	O.N.
5%	1 min	2 min	10 min	O.N.

Table 5.5. Assessment of hydrogel residence time for the developed hydrogel formulations. Lig-SHF68:PEG-DA weight ratio was set at 80:20 and 50:50. Purely PEG-DA- and Lig-SHF68-based formulations were also prepared for comparison (identified as 0:100 and 100:0, respectively). Lig-SHF68-based gel at 1% w/v concentration was not analyzed since it did not undergo gelation.

Lig-SHF68:PEG-DA ratio / PEU content [% w/v]	0:100	50:50	80:20	100:0
1%	7 days	5 days	5 days	-*
3%	>7 days	5 days	5 days	2 days
5%	>7 days	6 days	>7 days	2 days

** this condition was not tested since no gelation occurred*

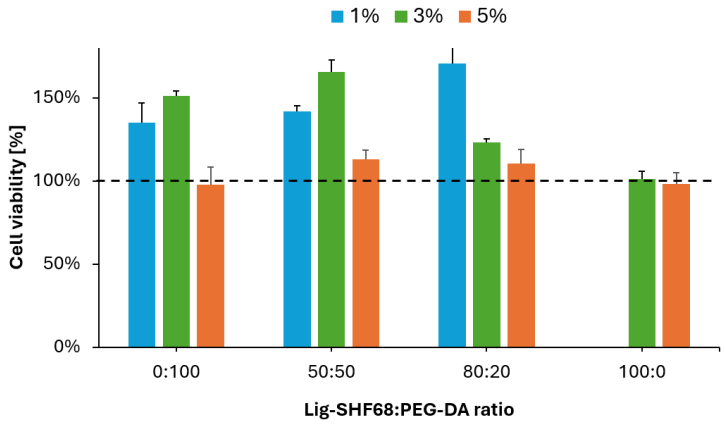


Figure 5.17. The cytocompatibility of the SM-gels based on Lig-SHF68 and PEG-DA at 1% w/v (blue), 3% w/v (green) and 5% w/v (orange) polymeric content. Lig-SHF68:PEG-DA weight ratio was set at 80:20 and 50:50. Purely PEG-DA- and Lig-SHF68-based formulations were also prepared for comparison (identified as 0:100 and 100:0, respectively). Lig-SHF68-based gel at 1% w/v concentration was not analyzed since it did not undergo gelation.

5.3.3.2. Stability test of the selected UV-SM-gel

Stability tests were performed for the photo-crosslinked formulation with 5% w/v PEU content and 80:20 Lig-SHF68:PEG-DA weight ratio, referred to as UV-SM-gel hereafter, and compared to the properties of the hydrogel selected in Section 2, which was prepared as a blend between CHP407 and SHF68 at 3% w/v polymer concentration and 80:20 CHP407:SHF68 weight ratio, and referred to as SM-gel.

As expected from the results of the preliminary stability tests described above (Table 5.5), the duration of the UV-SM-gel remarkably increased (Figure 5.18) to over 7 days, while the SM-gel developed in Section 2 already dissolved at 48 h. Interestingly, in the first 48 h of incubation, the UV-SM-gel lost over 60% of its dry content (Figure 5.18.A) while substantially maintaining its network and wet content (i.e., wet weight variation of *ca. 20%*) (Figure 5.18.B). Then, it lost part of its integrity, as highlighted by the measured negative wet weight change, but it was still capable of maintaining part of the network as evidenced by the residual dry weight percentage that was measured to be around 20% starting from 72 h of incubation up to 7 days. This progressive network dissolution is also reflected in the progressive increase in the gel swelling ratio (Figure 5.18.C).

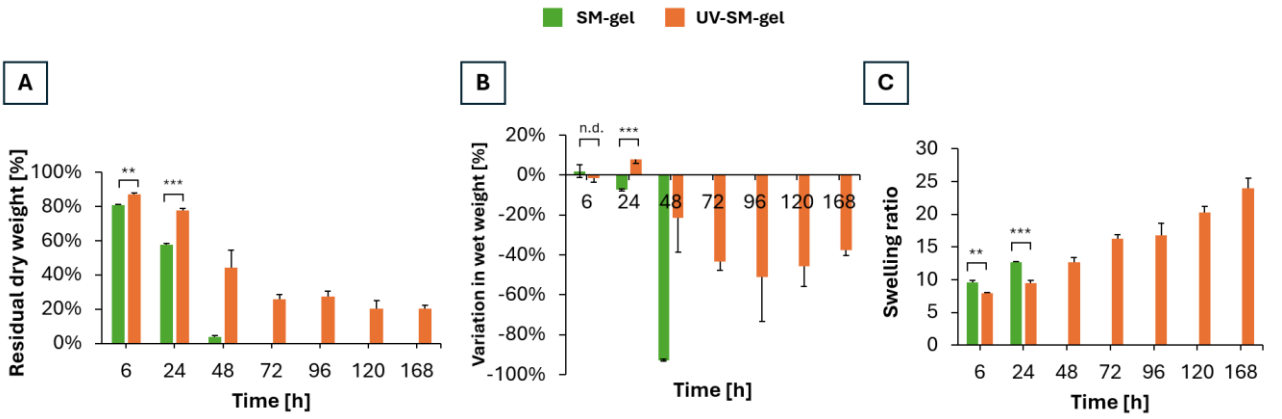


Figure 5.18. Stability of the UV-SM-gel (orange) (5% w/v PEU content and 80:20 Lig-SHF68:PEG-DA weight ratio) compared with the SM-gel (green) (3% w/v PEU content and 80:20 CHP407:SHF68 weight ratio). (A) Residual dry weight (%), (B) percentage of wet weight change, and (C) swelling ratio at different time points during incubation with PBS at 37 °C.

5.3.3.3. Photorheology of the UV-SM-gel

A photorheological test was performed on the formulation based on Lig-SHF68 and PEG-DA to study the photo-curing process. The hydrogel underwent continuous shearing at a defined frequency, while G' and G'' values were monitored over time. After 90 s of recording, the sample was exposed to 2 min of irradiation with UV light (365 nm, 10 mW/cm^2), and the change in G' and G'' were observed for 12 min. As illustrated in Figure 5.19, G' and G'' values exhibited a gradual increase following irradiation from G' values below 10000 Pa until reaching a plateau at around 12000 Pa after 10 minutes (13 min from the start of the test). This increase of G' and G'' indicated that the photo-crosslinking was taking place as expected. Interestingly, this augmentation did not immediately start with the activation of the light source, but it took approximately 30 to 60 seconds to observe the alteration in mechanical properties. Moreover, the increase persisted even after switching off the UV light, continuing until the plateau was reached. These phenomena are closely associated with the mechanism of action of the photoinitiator (LAP) utilized to induce UV-mediated crosslinking. LAP initiates a radical reaction that propagates in a cascade. Therefore, it takes some time before perceiving a variation of the rheological properties that progressively

increase with the increase of crosslinking. Additionally, the radical reaction is capable of persisting even after cessation of the light stimulus until the reactive acrylate groups are exhausted (Figure 5.20) [23], [24].

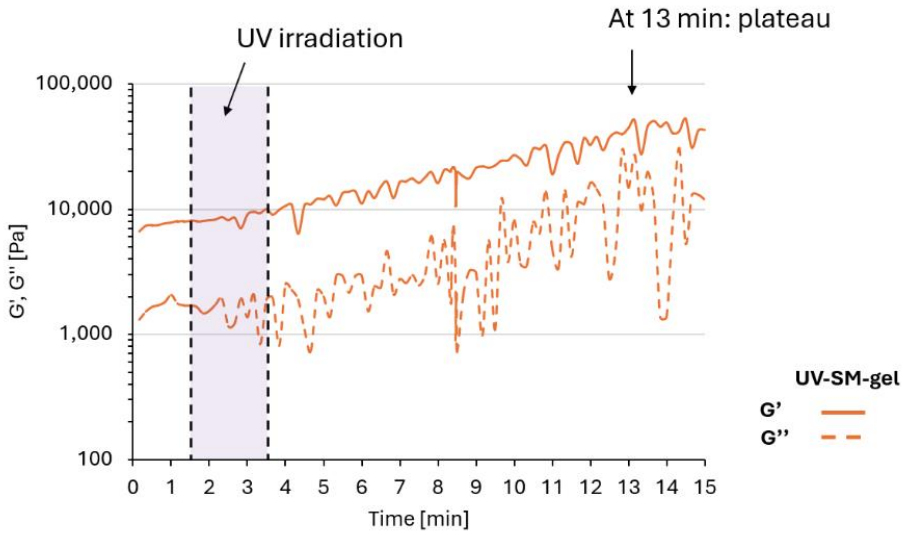


Figure 5.19. Photorheological time sweep test performed on the physically crosslinked formulation based on Lig-SHF68 and PEG-DA during light irradiation (365 nm, 10 mW/cm²). G' and G'' values were recorded for 90 s before starting a 2 min irradiation with UV light. The values of G' and G'' were recorded for a total of 15 min.

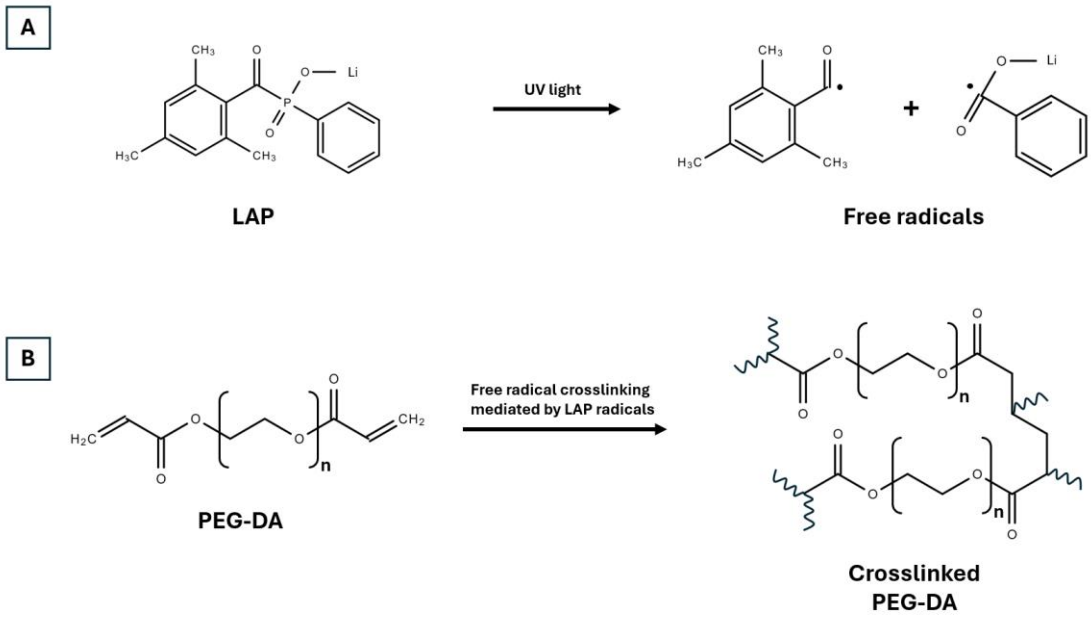


Figure 5.20. Scheme of the reaction leading to PEG-DA photo-crosslinking. (A) LAP decomposition into radicals mediated by UV light. (B) PEG-DA crosslinking mediated by UV-activated LAP.

5.3.3.4. Rheological tests of the UV-SM-gel

The rheological properties of the UV-SM-gel compared to the SM-gel designed in Section 2 were characterized as previously explained. The UV-SM-gel was photo-crosslinked prior to rheological tests and then placed on the rheometer plate using a syringe. Indeed, despite the photo-crosslinking reaction, the formulation still maintained the typical injectability of supramolecular formulations, that is a relevant property in view of hydrogel application in the wound cavity.

Strain sweep tests evaluate the ability of hydrogels to withstand loads and self-heal.

Figure 5.21 reports the trends of G' and G'' as a function of applied strain as registered during strain sweep tests of UV-SM-gel and SM-gel. For both formulations, an LVE region was identified, where the samples exhibited a viscoelastic solid behavior. Subsequently, the hydrogels underwent rupture until G' and G'' reached a crossover point, transitioning to a viscoelastic liquid behavior (Figure 5.21). These curve profiles clearly indicate the system injectability and align with the rheological findings in Sections 2 and 2. The G' values in the LVE region for the two gels were comparable (Table 5.6) with values of 10100 Pa for the SM-gel and 9350 Pa for the UV-SM-gel, indicating that PEG-DA, through both its interactions with αCDs and its UV-mediated crosslinking, greatly improves the poor stiffness of the hydrogels-based solely on Lig-SHF68 (Table 5.1). Furthermore, the values for τ_y, τ_t and the flow transition index were substantially higher in the UV-SM-gel than in the SM-gel, with values of 15.9 Pa, 120.5 Pa and 7.58, respectively, for UV-SM-gel compared to 6.51 Pa, 11.90 Pa and 1.83 in SM-gel. This difference suggests a creamier behavior of the UV-SM-gel that could be primarily attributed to the presence of Lig-SHF68, as observed in Lig-SHF68-based gels (Table 5.1).

Strain sweep tests were also conducted to evaluate the self-healing capabilities of these systems by repeating the test on the same sample after 15 minutes of recovery in quiescence at 37 °C.

Figure 5.21.B-C illustrates the trends of G' and G'' before and after the initial rupture, demonstrating complete recovery of G' for both formulations. Interestingly, the light-mediated crosslinking did not affect the self-healing capacity of the UV-SM-gel in this test. This suggests that the primary mechanism supporting the hydrogel network relies on the formation of inclusion complexes with αCDs, while the presence of photo-crosslinking aids in enhancing network strength.

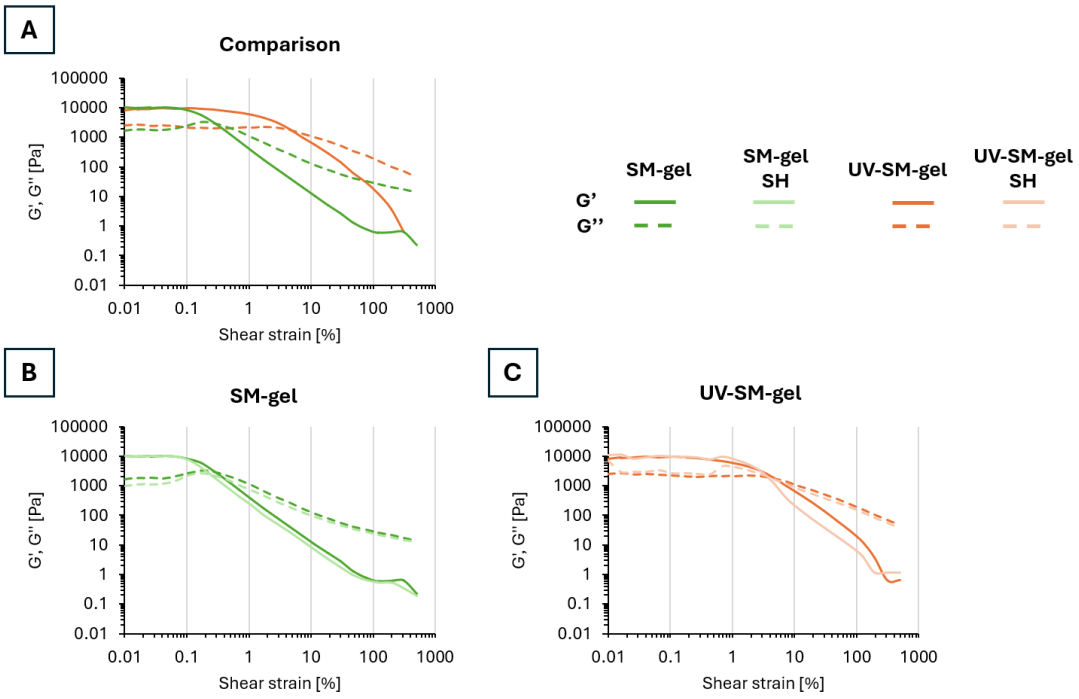


Figure 5.21. Rheological strain sweep test for the UV-SM-gel (5% w/v PEU content and 80:20 Lig-SHF68:PEG-DA weight ratio) and SM-gels (3% w/v PEU content and 80:20 CHP407:SHF68 weight ratio) formulations. Trends of G' (continuous line) and G'' (dashed line) for (A) UV-SM-gel (orange) and SM-gel (green) formulation; (B) the SM-gel formulation before (green) and after 15 min recovery (SH) (light green), and (C) the UV-SM-gel formulation before (orange) and after 15 min recovery (SH) (light red).

Table 5.6. Summary of the rheological characteristics of UV-SM-gel (5% w/v PEU content and 80:20 Lig-SHF68:PEG-DA weight ratio) and SM-gels (3% w/v PEU content and 80:20 CHP407:SHF68 weight ratio) extracted from the strain sweep test.

	τ_y (Pa)	τ_f (Pa)	Flow transition index	G'_{LVE} (Pa)	G''_{LVE} (Pa)	G'_{LVE} recovery (Pa)	G''_{LVE} recovery (Pa)	G' recovery (%)
SM-gel	6.51	11.90	**1.83**	10100	1840	10233	1137	**101%**
UV-SM-gel	15.90	120.50	**7.58**	9350	2397	9780	2990	**105%**

Frequency sweep tests were performed to assess the attainment of fully developed hydrogels. The UV-SM-gel was subjected to various frequencies while maintaining a constant shear strain within the LVE region. Testing was exclusively carried out at 37 °C, as previous experiments indicated minimal temperature dependency once the supramolecular network was formed. As showed in Figure 5.22, G' exceeded G'' within the whole range of analyzed frequencies and both parameters were almost completely independent over frequency, thus indicating a distinct gel state for the UV-SM-gel. The values of G' for the UV-SM-gel were lower than for the SM-gel, i.e., at 1 rad/s, G' was measured to be 5430 Pa and 12700 Pa for UV-SM-gel and SM-gel, respectively. This difference further suggests a creamier and softer consistency for the UV-SM-gel compared to SM-gel.

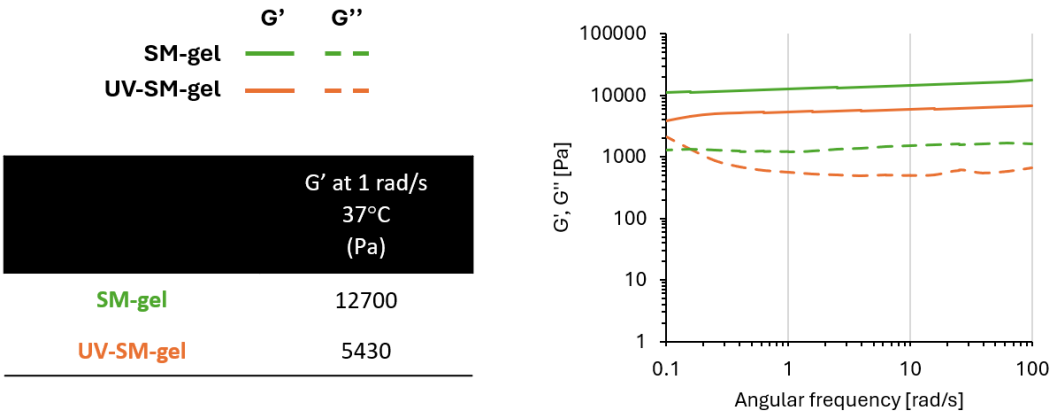
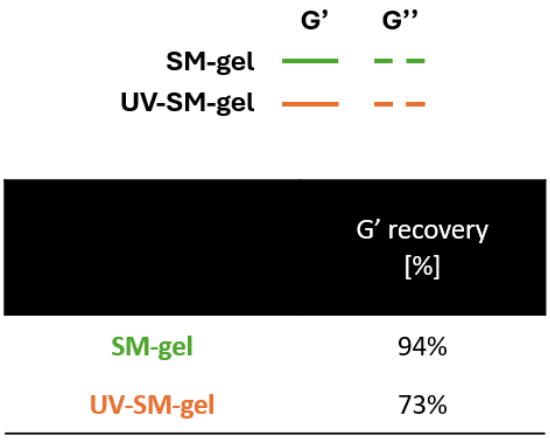


Figure 5.22. Rheological frequency sweep test at 37 °C performed on UV-SM-gel (5% w/v PEU content and 80:20 Lig-SHF68:PEG-DA weight ratio) compared with the SM-gel developed in Section 2 (3% w/v PEU content and 80:20 CHP407:SHF68 weight ratio). The table compares the G' values at 1 rad/s.

Finally, shear tests were conducted to assess the self-healing capacity of the formulations under repeated cycles of rupture. G' and G'' values were measured as the samples underwent three cycles of rupture followed by a recovery period (Figure 5.23). The initial and final values of G' during the resting period were compared, and the percentage of G' recovery was estimated. Interestingly, the UV-SM-gel exhibited reduced self-healing properties with a percentage of G' recovery of 73% compared to 94% for the SM-gel, and with G' values gradually increasing during the recovery period. This result contrasts the observations from the strain sweep test (Figure 5.21 and Table 5.6). This discrepancy is likely attributed to the presence of UV-mediated crosslinking and Lig-SHF68, which may interfere with the re-establishment of interactions based on PPRs, thereby reducing the system ability to withstand rapid cycles of rupture. However, when left to recover for longer periods, the G' recovery is complete, indicating that the UV-SM-gel can

ultimately regain its structural stability. This trend was similar to what was observed when analyzing the rheological properties of Lig-SHF68-based SM-gel.



	G' recovery [%]
SM-gel	94%
UV-SM-gel	73%

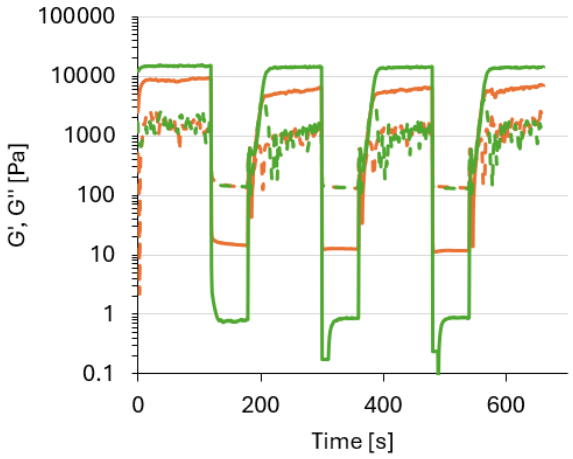


Figure 5.23. Rheological strain test for the UV-SM- gel (5% w/v PEU content and 80:20 Lig-SHF68:PEG-DA weight ratio) compared with the SM-gel developed in Section 2 (3% w/v PEU content and 80:20 CHP407:SHF68 weight ratio). The table compares the G' recovery (%) values.

5.3.3.5. Anti-inflammatory activity of the components released from the UV-SM-gel

The UV-SM-gel was immersed in aqueous media, and the antioxidant activity of the released components was evaluated at specific time intervals. Remarkably, the hydrogel displayed consistent antioxidant activity throughout its lifespan (Figure 5.24.A), with a higher activity (around 20%) in the first 72 h, that gradually decreased to 10% at day 7. This characteristic is particularly advantageous in systems intended for the treatment of inflammatory conditions, where sustained ROS scavenging over the dressing lifetime is essential. Furthermore, the intrinsic antioxidant activity exhibited by the UV-SM-gel can promote ROS scavenging from the outset of application and could act synergically with other antioxidant actives loaded within the system.

The MMPs inhibitory activity of the UV-SM-gel was also tested (Figure 5.24.B), showing a 20% of activity in the first 24 h that then decreased to close to zero for the following time points. The MPO inhibitory activity will be tested in future experiments; nevertheless, the UV-SM-gel is expected to present a trend of MPO inhibition similar to the one observed for MMPs since for the Lig-SHF68 material these two enzymes presented similar inhibitory activities (Figure 5.4).

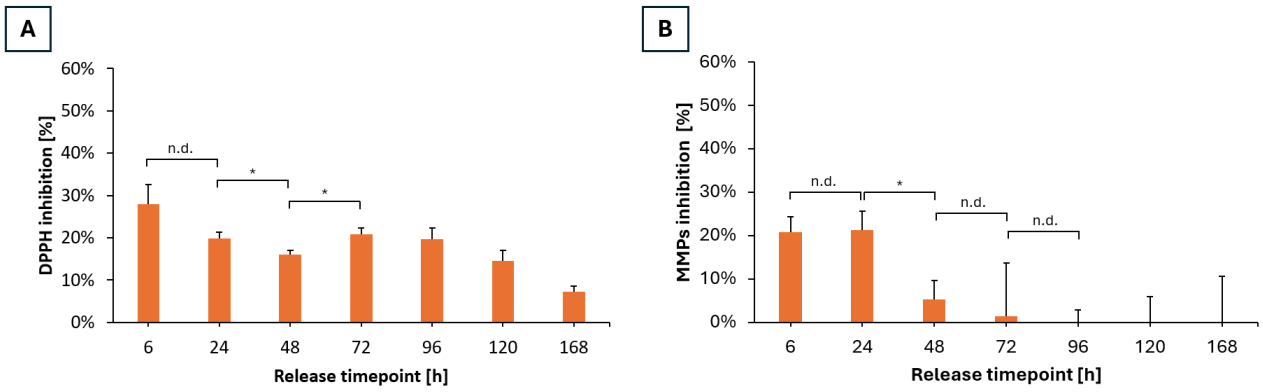


Figure 5.24. Anti-inflammatory activity of the release medium collected from the UV-SM-gel. (A) ROS scavenging activity and (B) MMPs inhibitory action.

5.3.3.6. Release of NPs and compounds from the new gel formulation

To investigate the efficacy of the new hydrogel in controlling the release of actives, compounds of varying natures were selected to be loaded into the UV-SM-gel. Curcumin is a well-known small antioxidant compound with poor solubility in aqueous media, thus requiring the use of vehicles that can transport it to the site of interest. CDs have demonstrated an ability to interact with curcumin, significantly enhancing its solubility [25], [26]. Additionally, the amphiphilic SHF68 can form micelles, further aiding in curcumin encapsulation. For this reason, this compound has served as a model molecule in prior research [27]. In contrast, the CoPc-Lig NPs developed in Section 3 are larger and form stable suspensions in water. Due to their distinct properties, these two compounds were chosen for release tests, exhibiting markedly different release kinetics (see Figure 5.25). After an initial burst release within the first 6 h of incubation, the release kinetics of curcumin displayed a linear trend, with a release rate of 1.5 µg/h, until reaching a plateau after 96 h (95% released). This release pattern aligns with a diffusion-based mechanism, as corroborated by the Korsmeyer–Peppas model, which describes drug release from polymeric systems. In this model, a release exponent (n) of 0.45 or lower indicates Fickian diffusion, while n values of 0.89 indicate 0-order kinetics. Between 0.45 and 0.89, the release is driven by a combination of diffusion and matrix erosion, while for values higher than 0.89 the release driving force is the network disentanglement [11], [12]. For curcumin release, the n exponent derived from fitting the data for the initial 96 h, was found to be 0.45, thus confirming the diffusion-driven release of this compound. On the other hand, CoPc-Lig NPs exhibited a sigmoidal release trend, with a burst release occurring after 48 h. This release pattern mirrored the dissolution behavior of the UV-SM-gel observed in the stability test (Figure 5.18), suggesting that the cargo release from the gel is driven by the network's gradual dissolution. Indeed, the n exponent in this case exceeded 0.89, indicating hydrogel disentanglement and erosion. These results suggest that the release kinetics of actives from UV-SM-gel highly depends on the dimension and nature of the compounds encapsulated. Therefore, selecting the appropriate compounds is fundamental to achieve therapeutic benefits.

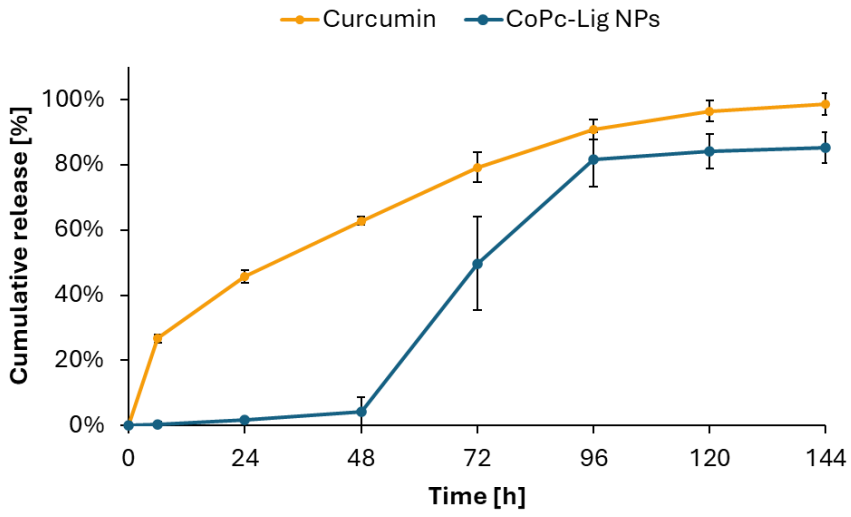


Figure 5.25. Release profiles of different compounds encapsulated into the UV-SM-gel: curcumin (yellow) and CoPc-Lig NPs (blue).

5.4. Conclusions

In this section, the SM-gel developed in Section 2 underwent modifications to incorporate antioxidant and anti-inflammatory functionalities and enhance its durability. Initially, SHF68 was enzymatically functionalized with lignin-based antioxidant and anti-inflammatory moieties. The resulting material (Lig-SHF68) presented antioxidant properties and inhibited MMPs and MPO activity, thanks to the presence of the lignin-based functionalities. The rheological properties of Lig-SHF68-based SM-gels were investigated, revealing a fully formed viscoelastic network, unaffected by temperature variations. However, these hydrogels exhibited reduced mechanical properties and self-healing capability under rapid rupture cycles compared to gels based on not-functionalized SHF68. This observation suggests that Lig-TA may interfere with the PPRs formation and network re-establishment upon rupture. Interestingly, stability tests demonstrated prolonged durability of Lig-SHF68-based hydrogels compared to control gels based on SHF68, indicating that interactions between Lig-TA and hydrogel components contribute to network stability, albeit not sufficiently to enhance hydrogel stiffness. Additionally, antioxidant activity and MMPs inhibitory assays showed sustained ROS scavenging throughout the hydrogel lifespan, potentially compensating for delayed release of therapeutic compounds encapsulated within the system.

The combination of Lig-SHF68 with PEG-DA allowed for the formation of a photo-crosslinked SM-gel. Notably, the selected formulation (5% w/v PEU content and 80:20 Lig-SHF68:PEG-DA weight ratio) exhibited rheological properties comparable to the one of the SM-gel developed in Section 2 (3% w/v PEU content and 80:20 CHP407:SHF68 weight ratio) while providing enhanced stability and consistent antioxidant activity throughout the hydrogel lifespan. Release studies of encapsulated curcumin and CoPc-Lig NPs revealed distinct release kinetics, with curcumin exhibiting diffusion-based release and CoPc-Lig NPs displaying dissolution-driven release. The results of these characterizations demonstrate the new system's potential for applications related to wound healing.

Future research will focus on completing the characterization of the system through MPO assays for the components released from the hydrogel over time. Additionally, *ex-vivo* wound extracts could be used to further validate the anti-inflammatory and antioxidant capacity of the system. Additionally, *in vitro* models of wounds could be used to assess the effectiveness of the hydrogel system before moving to *in vivo* testing, which is a fundamental requirement to finally validate the therapeutic efficacy and safety of a system.

5.5. References

[1] Z. Xu, S. Han, Z. Gu, and J. Wu, 'Advances and Impact of Antioxidant Hydrogel in Chronic Wound Healing', *Adv Healthcare Materials*, vol. 9, no. 5, p. 1901502, Mar. 2020, doi: 10.1002/adhm.201901502.

[2] J. Yang, R. van Lith, K. Baler, R. A. Hoshi, and G. A. Ameer, 'A Thermoresponsive Biodegradable Polymer with Intrinsic Antioxidant Properties', *Biomacromolecules*, vol. 15, no. 11, pp. 3942–3952, Nov. 2014, doi: 10.1021/bm5010004.

[3] J. Xiao, S. Chen, J. Yi, H. F. Zhang, and G. A. Ameer, 'A Cooperative Copper Metal–Organic Framework-Hydrogel System Improves Wound Healing in Diabetes', *Adv Funct Materials*, vol. 27, no. 1, p. 1604872, Jan. 2017, doi: 10.1002/adfm.201604872.

[4] Y. Liang, X. Zhao, T. Hu, Y. Han, and B. Guo, 'Mussel-inspired, antibacterial, conductive, antioxidant, injectable composite hydrogel wound dressing to promote the regeneration of infected skin', *Journal of Colloid and Interface Science*, vol. 556, pp. 514–528, Nov. 2019, doi: 10.1016/j.jcis.2019.08.083.

[5] D. Chimene, R. Kaunas, and A. K. Gaharwar, 'Hydrogel Bioink Reinforcement for Additive Manufacturing: A Focused Review of Emerging Strategies', *Advanced Materials*, vol. 32, no. 1, p. 1902026, Jan. 2020, doi: 10.1002/adma.201902026.

[6] H. Wei, J. He, L. Sun, K. Zhu, and Z. Feng, 'Gel formation and photopolymerization during supramolecular self-assemblies of α-CDs with LA–PEG–LA copolymer end-capped with methacryloyl groups', *European Polymer Journal*, vol. 41, no. 5, pp. 948–957, May 2005, doi: 10.1016/j.eurpolymj.2004.11.041.

[7] H. Wei *et al.*, 'Supramolecular structured hydrogel preparation based on self-assemblies of photocurable star-shaped macromers with α-cyclodextrins', *J. Polym. Sci. A Polym. Chem.*, vol. 43, no. 13, pp. 2941–2949, Jul. 2005, doi: 10.1002/pola.20773.

[8] H. Wei, H. Yu, A. Zhang, L. Sun, D. Hou, and Z. Feng, 'Synthesis and Characterization of Thermosensitive and Supramolecular Structured Hydrogels', *Macromolecules*, vol. 38, no. 21, pp. 8833–8839, Oct. 2005, doi: 10.1021/ma050887p.

[9] S.-P. Zhao and W.-L. Xu, 'Thermo-sensitive hydrogels formed from the photocrosslinkable polypseudorotaxanes consisting of β-cyclodextrin and Pluronic F68/PCL macromer', *J Polym Res*, vol. 17, no. 4, pp. 503–510, Jul. 2010, doi: 10.1007/s10965-009-9337-0.

[10] S.-P. Zhao, L.-M. Zhang, D. Ma, C. Yang, and L. Yan, 'Fabrication of Novel Supramolecular Hydrogels with High Mechanical Strength and Adjustable Thermosensitivity', *J. Phys. Chem. B*, vol. 110, no. 33, pp. 16503–16507, Aug. 2006, doi: 10.1021/jp063005c.

[11] R. W. Korsmeyer, R. Gurny, E. Doelker, P. Buri, and N. A. Peppas, 'Mechanisms of solute release from porous hydrophilic polymers', *International Journal of Pharmaceutics*, vol. 15, no. 1, pp. 25–35, May 1983, doi: 10.1016/0378-5173(83)90064-9.

[12] M. P. Paarakh, P. A. Jose, C. Setty, and G. V. Peter, 'Release Kinetics – Concepts and applications', vol. 8, 2018.

[13] W. Gao, J. P. W. Inwood, and P. Fatehi, 'Sulfonation of Phenolated Kraft Lignin to Produce Water Soluble Products', *Journal of Wood Chemistry and Technology*, vol. 39, no. 4, pp. 225–241, Jul. 2019, doi: 10.1080/02773813.2019.1565866.

[14] B. Jiang, Y. Zhang, L. Gu, W. Wu, H. Zhao, and Y. Jin, 'Structural elucidation and antioxidant activity of lignin isolated from rice straw and alkali-oxygen black liquor', *International Journal of Biological Macromolecules*, vol. 116, pp. 513–519, Sep. 2018, doi: 10.1016/j.ijbiomac.2018.05.063.

[15] P. Jiang *et al.*, 'Preparation and characterization of thermo-sensitive gel with phenolated alkali lignin', *Sci Rep*, vol. 8, no. 1, Art. no. 1, Sep. 2018, doi: 10.1038/s41598-018-32672-z.

[16] B. Luo, Z. Jia, H. Jiang, S. Wang, and D. Min, 'Improving the Reactivity of Sugarcane Bagasse Kraft Lignin by a Combination of Fractionation and Phenolation for Phenol–Formaldehyde Adhesive Applications', *Polymers*, vol. 12, no. 8, Art. no. 8, Aug. 2020, doi: 10.3390/polym12081825.

[17] A. G. Morena, A. Bassegoda, M. Natan, G. Jacobi, E. Banin, and T. Tzanov, 'Antibacterial Properties and Mechanisms of Action of Sonoenzymatically Synthesized Lignin-Based Nanoparticles', *ACS Appl. Mater. Interfaces*, vol. 14, no. 33, pp. 37270–37279, Aug. 2022, doi: 10.1021/acsami.2c05443.

[18] F. A. R. Mota, S. A. P. Pereira, A. R. T. S. Araújo, B. Gullón, M. L. C. Passos, and M. L. M. F. S. Saraiva, 'Automatic Identification of Myeloperoxidase Natural Inhibitors in Plant Extracts', *Molecules*, vol. 27, no. 6, Art. no. 6, Jan. 2022, doi: 10.3390/molecules27061825.

[19] M. Díaz-GonzáLez, G. Rocasalbas, A. Francesko, S. Touriño, J. L. Torres, and T. Tzanov, 'Inhibition of deleterious chronic wound enzymes with plant polyphenols', *Biocatalysis and Biotransformation*, vol. 30, no. 1, pp. 102–110, Feb. 2012, doi: 10.3109/10242422.2012.646676.

[20] I. Perelshtein, E. Ruderman, A. Francesko, M. M. Fernandes, T. Tzanov, and A. Gedanken, 'Tannic acid NPs – Synthesis and immobilization onto a solid surface in a one-step process and their antibacterial and anti-inflammatory properties', *Ultrasonics Sonochemistry*, vol. 21, no. 6, pp. 1916–1920, Nov. 2014, doi: 10.1016/j.ultsonch.2013.11.022.

[21] E. Sergedien≐, K. Jönsson, H. Szymusiak, B. Tyrakowska, I. M. C. M. Rietjens, and N. Č≐nas, 'Prooxidant toxicity of polyphenolic antioxidants to HL-60 cells: description of quantitative structure-activity relationships', *FEBS Letters*, vol. 462, no. 3, pp. 392–396, 1999, doi: 10.1016/S0014-5793(99)01561-6.

[22] T. Kovacs, P. Nagy, G. Panyi, L. Szente, Z. Varga, and F. Zakany, 'Cyclodextrins: Only Pharmaceutical Excipients or Full-Fledged Drug Candidates?', *Pharmaceutics*, vol. 14, no. 12, p. 2559, 2022, doi: 10.3390/pharmaceutics14122559.

[23] S. Wang, W. Liang, Z. Dong, V. G. B. Lee, and W. J. Li, 'Fabrication of Micrometer- and Nanometer-Scale Polymer Structures by Visible Light Induced Dielectrophoresis (DEP) Force', *Micromachines*, vol. 2, no. 4, pp. 431–442, Dec. 2011, doi: 10.3390/mi2040431.

[24] M. Hakim Khalili, R. Zhang, S. Wilson, S. Goel, S. A. Impey, and A. I. Aria, 'Additive Manufacturing and Physicomechanical Characteristics of PEGDA Hydrogels: Recent Advances and Perspective for Tissue Engineering', *Polymers*, vol. 15, no. 10, p. 2341, May 2023, doi: 10.3390/polym15102341.

[25] A. Gupta *et al.*, 'Synthesis of Silver Nanoparticles Using Curcumin-Cyclodextrins Loaded into Bacterial Cellulose-Based Hydrogels for Wound Dressing Applications', *Biomacromolecules*, vol. 21, no. 5, pp. 1802–1811, May 2020, doi: 10.1021/acs.biomac.9b01724.

[26] H. Rachmawati, C. A. Edityaningrum, and R. Mauludin, 'Molecular Inclusion Complex of Curcumin–β-Cyclodextrin Nanoparticle to Enhance Curcumin Skin Permeability from Hydrophilic Matrix Gel', *AAPS PharmSciTech*, vol. 14, no. 4, pp. 1303–1312, Dec. 2013, doi: 10.1208/s12249-013-0023-5.

[27] A. Torchio *et al.*, 'Injectable supramolecular hydrogels based on custom-made poly(ether urethane)s and α-cyclodextrins as efficient delivery vehicles of curcumin', *Materials Science and Engineering: C*, vol. 127, p. 112194, Aug. 2021, doi: 10.1016/j.msec.2021.112194.

6. General discussion

Chronic wounds (CWs) are particularly challenging diseases that necessitate long-term nurse-administered treatments, extended hospital stays, readmissions, and specialized medical or surgical interventions [1], [2]. CWs are caused by the concurrence of different exogenous and endogenous factors that disrupt the healing process and prevent progression beyond the inflammatory phase, resulting in hampered tissue regeneration, low matrix deposition, and incomplete wound closure [3]. In particular, CWs exhibit elevated levels of pro-inflammatory cytokines, reactive oxygen species (ROS), and proteases, such as matrix metalloproteases (MMPs) [4], [5]. Additionally, the excessive activity of neutrophils results in overexpression of myeloperoxidase (MPO), which further contributes to the degradation of biological molecules, such as MMPs' inhibitors [6], [7]. Since CWs remain open for an extended period, they are susceptible to infections from both the Gram-positive *S. aureus* and the Gram-negative *P. aeruginosa* [8]. These bacteria can aggravate the inflammatory state in the wound by secreting virulence factors that upregulate pro-inflammatory cytokines, MMPs, and ROS [9]. Additionally, they usually aggregate within a self-produced extracellular matrix (ECM) to form biofilms [10], which impart resilience against the host immune system and to conventional antibiotics, leading to the rise of antibiotic-resistant bacteria populations [11].

To address such a complex and multifactorial pathology, multifunctional therapeutic approaches are required. Therefore, new wound dressing solutions should display multiple therapeutic functions, such as maintaining the moisture balance, absorbing excessive exudate, exerting antioxidant and regenerative actions, and containing infections, while being easy to handle and to administer [12]. Additionally, innovative dressings should include stimuli-responsive moieties capable of exerting a therapeutic action in response to endogenous or exogenous triggers [13].

The rapidly expanding research in the field of wound healing proposed several approaches to obtain dressings combining multiple therapeutic actions [12], [14]. However, only a few of them were successfully translated into a commercial product, mainly due to the difficult scalability, high cost, and complicated dressing design [15], [16]. Therefore, treatment and proper management of CWs remain an unsolved medical issue. To address these needs, this PhD project aimed at developing an innovative hydrogel loaded with multifunctional nanoparticles (NPs) capable of reducing the inflammatory state in CWs while also controlling bacterial proliferation.

The hydrogel was obtained through physical supramolecular interactions between α-cyclodextrins (αCDs) and two custom-made poly(ether urethanes) (PEUs) developed in the group [17], CHP407, based on Poloxamer 407, 1,6-hexamethylene diisocyanate (HDI) and 1,4-cyclohexanedimethanol (CDM), and SHF68, an amino-groups bearing PEU derived from the Boc-deprotection of a PEU based on Pluronic F68, HDI and N-BOC-serinol. The use of custom-made synthetic polymers favors reproducibility and allows better control of the physico-chemical properties of the resulting hydrogels (as described in Section 2). Indeed, the goal was to obtain a reproducible delivery system that could be injected in the wound site, adapt to the patient's wound bed, present self-healing properties to comply with the patient's movements, and recover its initial mechanical properties after injection [16]. Additionally, the hydrogel should remain stable in aqueous environments for a period of time compatible with the typical frequency of dressing change (24-48 h for high exudative wounds), and interact with the wound exudate to favor healing by reestablishing the appropriate moisture [18]. To fully characterize the system, the properties of hydrogels based on CHP407 or SHF68 at 1%, 3%, and 5% w/v concentration were first investigated, proving that both PEUs could form completely developed hydrogels with self-healing properties and injectability at

all the conditions tested. Additionally, rheological tests showed better performance for CHP407-based hydrogels, with maximum G' and G'' values of 6 kPa and 0.7 kPa respectively at 5% w/v, as compared to 2.5 kPa and 0.2 kPa for SHF68-based hydrogels at the same concentration. However, SHF68-based hydrogels presented higher cytocompatibility with cell viability above 80% for all concentrations tested, while CHP407-based hydrogels presented cell viability above 80% only for the formulation at 1% w/v. To find a compromise between mechanical properties and cytocompatibility, CHP407:SHF68 blends at different weight ratios (80:20 and 50:50) and PEUs content (1%, 3% and 5% w/v) were investigated. The rheological properties greatly depended on these parameters. Indeed, the hydrogel stiffness increased with CHP407 content, showing G' and G'' values of 4.5 kPa and 0.5 kPa for the CHP407:SHF68 blend at 50:50 weight ratio and 3% w/v concentration, and values of 10 kPa and 1.8 kPa in the 80:20 weight ratio at the same concentration. Conversely, the presence of SHF68 provided plasticity to the network, visible in the increase of the flow transition index with SHF68 content, from 1.8 in the hydrogel at 80:20 weight ratio and 3% w/v concentration, to 3.6 in the hydrogel at 50:50 weight ratio and same concentration. Additionally, the hydrogel's capacity to rehydrate and absorb proteins from external fluids was assessed to investigate its ability to interact with wound exudate. The tests highlighted the pivotal role played by the total PEU content in determining hydrogel performances in watery environments, with the highest absorption observed at the lowest concentrations. Indeed, at 80:20 weight ratio, the hydrogels at 5% w/v absorbed around 20% of proteins from external fluids, while the hydrogels at 1% w/v PEU concentration showed more than 40% absorption. These results can be explained by the multiple mechanisms of gelation taking place in this type of hydrogel, which is driven by two forces, the first related to the PPRs formation by the interaction between αCDs and the poly(ethylene oxide) (PEO) blocks in the PEUs chains and the second associated with the amphiphilic nature of the PEUs that is responsible for micelles formation and assembly. CHP407, not presenting pending groups in the backbone, can better interact with αCDs in the formation of poly(pseudo)rotaxanes (PPRs), resulting in a stiffer network with higher values of G' and G''. Similarly, hydrogels with low PEU content present a network mostly based on PPR interactions, since micelles formation is favored at high concentrations due to a decrease in the critical micelle temperature (i.e., the minimal temperature at which micellization is observed) [19]. As a result, the more stable network favors the exchange of materials with the external environment resulting in the highest uptake of proteins. However, lower PEU content also signifies that a lower amount of polymer chains is available for micelles formation and interaction with αCDs, resulting in weaker networks. On the other hand, SHF68, presenting higher hydrophilicity and bearing pendant primary amines, provided the hydrogel with higher cytocompatibility. Considering all these aspects, the formulation at 3% w/v PEU concentration and 80:20 CHP407:SHF68 weight ratio was selected as the optimal compromise between rheological properties, absorption capability of external compounds, and cytocompatibility. Stability tests also confirmed this formulation as the best one in terms of durability in aqueous environments, maintaining its shape for 24 h, followed by complete dissolution at 48 h under conditions of high medium turnover, which simulates highly exudative wounds. This result matches the requirements of moderately to highly exudative wounds, such as infected CWs, where dressings are typically changed every 24-48 h [20]. Additionally, this hydrogel could be formulated in two different products depending on the patient's exudative needs. For highly exudative wounds, the dried formulation, capable of rehydration in a few seconds upon contact with aqueous fluids, could be applied to absorb the excess exudate, while if little or no exudate is present, the wet hydrogel could restore moisture balance in the wound bed. These two options grant versatility to the system, further supporting its applicability in CWs treatments.

These results proved the optimized hydrogel formulation to be a promising candidate for CWs treatment and prompted further tests in combination with hybrid metal/organic NPs. Multifunctional NPs were added to the hydrogel system to impart antibacterial, antioxidant, and antibiofilm functionalities (as described in Section 3). For this reason, NPs were prepared using cobalt (Co) and a lignin-based material, combining lignin (Lig), tannic acid (TA) and L-tyrosine hydroxamate (LTH). Lignin is a cheap polyphenolic compound from the paper industry. Its antioxidant activity could be improved by conjugation with TA, another phenol-rich molecule derived from plants [21]. Additionally, LTH is an inhibitor of MMPs [22], [23], therefore its integration in the Lig/TA material could provide specific activity against these enzymes. Lig-TA-LTH was obtained through a green method exploiting the activity of the enzyme laccase, which oxidizes the phenolic groups of lignin, TA and LTH, producing radicals that can then interact with each other or with other functional groups. The obtained material was then used to reduce cobalt and obtain the hybrid metal/organic CoLig NPs. The organic component of CoLig NPs provided antioxidant and MPO and MMP-inhibitory activity, while the presence of cobalt conferred antibacterial properties. This combination offered a multifunctional approach to wound healing. CoLig NPs were thoroughly evaluated, presenting a size of around 190 nm, a PDI of 0.22 and a ζ potential of *ca.* -23 mV. Moreover, CoLig NPs presented high efficacy in reducing inflammation by promoting ROS scavenging (around 60% at 1.3 mg/mL) and inhibiting the activity of MMPs and MPO (above 85% at 1 mg/mL). CoLig NPs presented relevant growth inhibition of *S. aureus* and *P. aeruginosa*, two bacterial species commonly found in CWs, at 0.3 mg/mL and 0.6 mg/mL, respectively. This is a fundamental aspect to tackle in CWs, since multi-species infections are commonly present [8], [24]. Nevertheless, the antimicrobial effect of the NPs on antimicrobial-resistant strains and on other clinically relevant bacterial species (e.g. *S. epidermidis, Escherichia coli* and *Enterococcus faecalis*) and fungi (*e.g. Saccharomyces cerevisiae* and *Candida utilis*) remains to be assessed. Cytocompatibility test evidenced that high cell viability (80%) of fibroblasts and keratinocytes was maintained up to a concentration of 0.6 mg/mL. This concentration was therefore selected being the best compromise between bacteria inhibition and cytocompatibility. Fibroblast and keratinocyte cell lines were selected for the preliminary cytocompatibility test since they are important cell types involved in the regeneration process. The cytocompatibility of CoLig NPs for other cell types relevant to wound healing, such as macrophages and neutrophils, will be investigated in future tests.

Subsequently, the NPs were integrated into the CHP407-SHF68-based hydrogel and their interaction was studied (as described in Section 3). The combination of these two components enhanced the stability and the mechanical properties of the hydrogel, probably because of the high surface reactivity of the polyphenolic NPs. The rheological tests presented more than 50% increase in G’ and G’’ values and a 40% reduction of the flow transition index, indicating a stiffer network, while the durability of the hydrogel was extended, lasting for 48 h and completely dissolving at 72 h. Cryo-scanning electron microscopy (CryoSEM) and Attenuated Total Reflectance–Fourier Transform Infrared (ATR-FTIR) analysis demonstrated a 40% increase in network crosslinking related to the interaction of the phenolic groups on the NPs with αCDs and SHF68. Additionally, the hydrogel was able to sustain the release of CoLig NPs. A combined diffusion-based and matrix erosion-driven release kinetics was observed, resulting in nearly zero-order release kinetics, which is highly desirable in drug delivery systems as reducing burst effects. Taken together, these results grant further testing of the developed system in CWs, by virtue of its multi-therapeutic action, injectability, and capacity to absorb exudate and maintain moisture balance. Additionally, most of the system components (αCDs, lignin and TA) are easily accessible and of low cost, while the custom-made PEUs, which may be considered the most expensive

components, were used at low concentrations, further containing the costs of the final product. The incorporation of CoLig NPs imparted antioxidant activity and broad-spectrum antibacterial properties to the system, particularly desirable in conditions like CWs, where contamination from different pathogens is common.

Release tests of CoLig NPs from the hydrogel showed that the antioxidant activity of the released compounds began after 24h, potentially leaving the first hours after dressing administration uncovered by pharmacological treatments. Indeed, the hydrogel did not present intrinsic therapeutic activity and relied on the loaded cargo to perform this function. Thus, a hydrogel with active functionalities was also developed to achieve therapeutic effects from the early stages post-administration. In detail, SHF68 underwent modifications to incorporate antioxidant and anti-inflammatory moieties through enzymatic functionalization with a lignin/TA conjugate (Lig-TA), obtaining Lig-SHF68 (as described in Section 5). The laccase-mediated reaction was used for both obtaining Lig-TA and conjugating it to the amino groups of SHF68. Lig-SHF68 acquired nearly 80% ROS scavenging ability at 12.5 mg/mL and MPO and MMPs inhibitory activity above 50% at 10 mg/mL. The antioxidant properties were maintained once Lig-SHF68 was used to form a supramolecular hydrogel in the presence of αCDs. Indeed, the components released from the system provided ROS scavenging activity already in the first 6 h (around 80%) and then throughout the hydrogel life (around 40% at 24 h and 48 h), significantly improving the CHP407-SHF68 hydrogel initially developed. A similar trend was observed for the MMPs inhibitory activity, with an inhibition above 60% in the first 6 h, that decreased in the next timepoint (around 50% at 24 h and 20% at 48 h). The CHP407-SHF68-based hydrogel also displayed limited durability in aqueous environments. Indeed, stability was maintained for the first 24 h, followed by complete dissolution. While matching the requirements of moderately to highly exudative wounds, extending the durability of the SM-gel beyond 48 h could equip the market with a solution capable of reducing the frequency of dressing changes. Therefore, Lig-SHF68 was blended with a photosensitive polymer (poly(ethylene glycol) diacrylate, PEG-DA) to extend its durability by adding light-mediated chemical crosslinks in the network. The new system presented consistent antioxidant activity throughout its life, similar to the Lig-SHF68 component, and significantly extended durability, up to 7 days with adequate mechanical properties (G’ and G’’ values of 9300 Pa and 2300 Pa), and self-healing capacity. Interestingly, the presence of chemical crosslinking did not interfere with the system injectability, indicating that the driving force of gelation is the physical supramolecular interaction. An important aspect, yet not addressed by the developed hydrogel system, is responsivity to exogenous and/or endogenous stimuli. CWs are characterized by varying levels of ROS and cytokines, depending on the healing stage or the presence of pathogens. Therefore, developing systems that could sense these changes and adapt their release accordingly is of high interest. Future developments should aim at targeting this aspect by producing PEUs with chain extenders sensitive to endogenous stimuli, for instance by incorporating enzymatically degradable sequences or redox-sensitive moieties [25], [26]. These approaches will provide the hydrogel with stimuli-response ability prompting its degradation and drug release under specific conditions.

The system designed and developed up to this point presents promising characteristics for application in CWs since it has intrinsic antioxidant properties, prolonged stability, and antibacterial and additional antioxidant activity provided by the CoLig NPs that can be loaded in the hydrogel. However, neither the hydrogel nor the CoLig NPs exhibited anti-biofilm ability, which is a desirable feature of active dressings. Indeed, biofilms represent an obstacle in the resolution of CWs, as they interfere with healing and represent a source of antibiotic-resistant bacteria [11], [27]. Thus, NPs capable of inducing biofilm dispersion and destruction were prepared through two approaches (as described in Section 4). The first involved coating the CoLig NPs with a nitric oxide

(NO) donor capable of altering the nitroxidative state to induce antibiofilm effects and promote regeneration [28]. The negatively charged CoLig NPs were successfully coated with positively charged amino cellulose (AC), which was conjugated with the NO donor S-nitroso glutathione (GSNO). The coating was successfully obtained, resulting in NO-CoLig NPs with a slightly higher diameter in comparison to CoLig NPs (from 190 nm to 210 nm) and a positive ζ potential. The surface charge changed from negative to positive values and the slight increase in diameter confirmed successful coating. Moreover, cytocompatibility was also improved, since surface coating masked the cytotoxic activity of cobalt. However, the quantity of NO released from the NO-CoLig NPs was deemed insufficient to induce antimicrobial and antibiofilm effects, probably due to a too-stable S-NO bond in the GSNO protected by AC on the NPs surface. Nevertheless, this approach remains promising since NO delivery has been used successfully to reduce bacterial burden in different works [29], [30], [31]. For instance, Lee et al. [31] used a similar approach to conjugate GSNO to poly(lactic-co-glycolic acid) (PLGA), obtaining NPs that presented antibacterial activity against *S. aureus* and promoted healing of *in vitro* infected wounds in murine models. However, few publications can be found on the use of NO delivery in antibiofilm treatments, underlining the need for further investigations to better understand the mechanism of NO action against pathogens. Future tests on NO-CoLig NPs need to focus on precisely quantifying the NO release and on developing strategies to trigger NO delivery. The second method focused on combining Lig-TA-LTH with a commercial complex between cobalt and the photo-excitable phthalocyanine (CoPc), to form NPs (CoPc-Lig NPs) exerting a dual function: antioxidant action and MMPs inhibition through the presence of polyphenols in Lig-TA-LTH, and biofilm disruption through photothermal excitation. Different formulations of CoPc-Lig NPs were tested by varying the Lig-TA-LTH and CoPc content. The optimized condition resulted in NPs of small size, around 250 nm, a low PDI of 0.14 and a negative ζ potential of -31.7 mV. For the selected CoPc-Lig NPs, the minimal concentration to have total ROS scavenging ability was 0.2 mg/mL, while 80% of MMPs inhibition was achieved at 0.8 mg/mL. These results showed that the CoPc-Lig NPs had a higher antioxidant potency as compared to CoLig NPs, probably because the phenolic groups in CoLig NPs were more involved in cobalt reduction and were, therefore, less available to exert their antioxidant activity. Cytocompatibility tests showed higher tolerance to CoPc-Lig NPs for human fibroblasts and keratinocytes, related to the low cobalt content of this formulation (15.7 µg of Co per mg of NPs, compared to 41 µg of Co per mg of NPs in CoLig NPs) and to the structure of CoPc that partially shields Co. Indeed, cell viability was above 90% for the maximum CoPc-Lig NPs concentration tested, corresponding to 60 µg/mL of Co, a concentration that in CoLig NPs presented evident cytotoxicity. This Co shielding also caused a reduction of the antibacterial activity of CoPc-Lig NPs, which could be observed only for *S. aureus* at the high concentration of 4 mg/mL (4.8 log reduction of growth), corresponding to 60 µg/mL of Co, whereas in CoLig NPs bacterial inhibition was present already at 25 µg/mL of Co. However, the high tolerability of the NPs allowed their easy internalization into bacterial biofilms, a fundamental aspect for maximizing the interaction with bacterial cells during photothermal treatment. Indeed, CoPc-Lig NPs internalized within *S. aureus* biofilm could be stimulated by external NIR laser irradiation for 2 min, resulting in a temperature increase in the biofilm mass of around 7 °C. Future tests should investigate whether this increment is capable of inducing an effect on the biofilm. Antibacterial effect through temperature increase has been reported for temperatures above 50 °C, which could also damage healthy tissue [32]. Different studies demonstrated that moderate temperature increments (at around 45 °C) coupled with antibacterial compounds promote bacteria elimination and biofilm eradication by potentiating the antimicrobial action [33], [34]. In the case of CoPc-Lig NPs, cobalt antimicrobial activity could be improved by the synergistic effect with photothermal therapy. Additionally, excitability in the NIR spectrum provided NPs photoacoustic (PA) imaging

potentiality. Indeed, NPs could be localized in *ex vivo* phantoms and within *S. aureus* biofilm with high spatial/temporal resolution. This opens the road for future applications of these NPs in the imaging field.

As further proof of concept, the CoPc-Lig NPs were encapsulated into the Lig-SHF68/PEG-DA-based hydrogel and their release was studied and compared with the release of an antioxidant compound, curcumin. These two actives differ greatly in terms of dimensions, as curcumin is a small molecule with a molecular weight of 368.38 g/mol, while CoPc-Lig NPs are large complexes with diameter of 250 nm, and in hydrophilicity, with curcumin being extremely hydrophobic, while CoPc-Lig NPs can be suspended in water at high concentrations. As expected, the different properties resulted in different release patterns from the hydrogel, with curcumin being released through a diffusion-driven mechanism, while CoPc-Lig NPs through the progressive dissolution of the hydrogel network. Future studies will investigate the release kinetics of different molecules from the system.

Overall, this PhD project developed a multi-functional system with promising features for the treatment of CWs. In literature, several hydrogels have been developed combining antimicrobial and antioxidant properties [35], [36], [37]. However, only a few studies investigate the effect of these systems on enzymes relevant to wound healing, such as MMPs and MPO. Additionally, the system here presented explored the use of components and modes of treatment not commonly investigated for wound healing. For instance, lignin is a byproduct of the paper industry that has great potential as biomass thanks to its biocompatibility and low cost. In the biotechnology field, it could be an optimal material for obtaining NPs and matrices, but it is rarely investigated in the literature due to its complex structure and poor miscibility with other polymers [38]. In this work, the use of lignin in NPs preparation and polymer functionalization sheds new light on methods to apply this material to nanomedicine. Phthalocyanines (Pc) are a class of molecules mainly used in the dye industry [39]. However, their activity in the NIR spectrum makes them interesting for photothermal and photodynamic treatments [40]. In the antibacterial and antibiofilm field, the use of Pc and photothermal therapy is poorly investigated and this project proposes a new method to exploit Pc potentialities. Additionally, PA imaging is emerging as a potent tool for *in vivo* diagnosis and the Pc-based NPs here presented could be an interesting theragnostic tool.

Although the components developed in this project are innovative and promising, additional studies are required to fully unveil their potential and translate the system into a clinical application. European and US regulations are strict on the approval of new biomaterials and treatments in the medical field. In particular, synthetic materials, such as the custom-made PEUs used in this project, require careful testing to ensure their safety. Nevertheless, the Poloxamers® used as macrodiols in the synthesis of the PEUs are both FDA-approved, which could possibly facilitate the validation process [41]. Moreover, different aspects of the system should be defined before undergoing regulatory validation. First, research should focus on finding the optimal combination between the developed NPs and hydrogels. For instance, combinations of CoLig NPs with CoPc-lig NPs could be investigated to find the optimal balance between broad-spectrum antibacterial activity and antibiofilm capacity. Additionally, their combined integration within the hydrogels could be characterized to assess the potentiality of their co-delivery. The photoacoustic properties of CoPc-Lig NPs are another aspect requiring further investigation to exploit their full potential in imaging. Finally, a crucial aspect to investigate for obtaining regulatory clearance is the regenerative effect that the system should present. For instance, *in vitro* proliferation and migration assays on cells under oxidative stress could provide important information on the system's capacity to restore oxidative balance and physiological cellular functions. Additionally,

tests on *ex vivo* wound extracts and *in vitro* or *in vivo* infected wound models are essential to better assess the therapeutic efficacy and safety of the system. I*n vitro* models would be a particularly interesting tool to use in the system's validation since they reconstruct the complexity of the biological environment, reducing the need for *in vivo* testing and the consequent costs [42], [43]. Skin models with biofilm are still in the early stages of development [11] since they require a combination of biofilms with a multilayer wound model. However, some studies have shown promising results and could be used as a base for perfecting a model applicable for testing the system developed in this PhD project [44], [45], [46], [47], [48]. After validation through *in vitro* models, *in vivo* models are an essential step to achieving approval of a system before moving into clinical trials. These types of models are particularly interesting also for their capacity to explore the interactions between the treatment and the host immune system, thus validating its safety. Murine models would be a preferential choice in this case, given their lower cost compared to other animal models and the broad literature on infected chronic wound models for this species [49], [50], [51].

6.1. References

[1] G. Han and R. Ceilley, 'Chronic Wound Healing: A Review of Current Management and Treatments', *Adv Ther*, vol. 34, no. 3, pp. 599–610, Mar. 2017, doi: 10.1007/s12325-017-0478-y.

[2] C. K. Sen, 'Human Wound and Its Burden: Updated 2020 Compendium of Estimates', *Adv Wound Care (New Rochelle)*, vol. 10, no. 5, pp. 281–292, May 2021, doi: 10.1089/wound.2021.0026.

[3] R. Zhao, H. Liang, E. Clarke, C. Jackson, and M. Xue, 'Inflammation in Chronic Wounds', *International Journal of Molecular Sciences*, vol. 17, no. 12, Art. no. 12, Dec. 2016, doi: 10.3390/ijms17122085.

[4] J. Larouche, S. Sheoran, K. Maruyama, and M. Martino, 'Immune Regulation of Skin Wound Healing: Mechanisms and Novel Therapeutic Targets', *Advances in Wound Care*, vol. 7, Feb. 2018, doi: 10.1089/wound.2017.0761.

[5] R. G. Frykberg and J. Banks, 'Challenges in the Treatment of Chronic Wounds', *Advances in Wound Care*, vol. 4, no. 9, pp. 560–582, Sep. 2015, doi: 10.1089/wound.2015.0635.

[6] J. Nève, N. Parij, and N. Moguilevsky, 'Inhibition of the myeloperoxidase chlorinating activity by non-steroidal anti-inflammatory drugs investigated with a human recombinant enzyme', *European Journal of Pharmacology*, vol. 417, no. 1, pp. 37–43, Apr. 2001, doi: 10.1016/S0014-2999(01)00895-0.

[7] X. Fu, S. Y. Kassim, W. C. Parks, and J. W. Heinecke, 'Hypochlorous Acid Oxygenates the Cysteine Switch Domain of Pro-matrilysin (MMP-7): A Mechanism For Matrix Metalloproteinase Activation And Atherosclerotic Plaque Rupture By Myeloperoxidase*', *Journal of Biological Chemistry*, vol. 276, no. 44, pp. 41279–41287, Nov. 2001, doi: 10.1074/jbc.M106958200.

[8] D. Leaper, O. Assadian, and C. E. Edmiston, 'Approach to chronic wound infections', *British Journal of Dermatology*, vol. 173, no. 2, pp. 351–358, Aug. 2015, doi: 10.1111/bjd.13677.

[9] S. Noor, M. Zubair, and J. Ahmad, 'Diabetic foot ulcer—A review on pathophysiology, classification and microbial etiology', *Diabetes & Metabolic Syndrome: Clinical Research & Reviews*, vol. 9, no. 3, pp. 192–199, Jul. 2015, doi: 10.1016/j.dsx.2015.04.007.

[10] H.-C. Flemming and J. Wingender, 'The biofilm matrix', *Nat Rev Microbiol*, vol. 8, no. 9, pp. 623–633, Sep. 2010, doi: 10.1038/nrmicro2415.

[11] G. Crivello, L. Fracchia, G. Ciardelli, M. Boffito, and C. Mattu, 'In Vitro Models of Bacterial Biofilms: Innovative Tools to Improve Understanding and Treatment of Infections', *Nanomaterials*, vol. 13, no. 5, Art. no. 5, Jan. 2023, doi: 10.3390/nano13050904.

[12] T. Liu, Y. Lu, R. Zhan, W. Qian, and G. Luo, 'Nanomaterials and nanomaterials-based drug delivery to promote cutaneous wound healing', *Advanced Drug Delivery Reviews*, vol. 193, p. 114670, Feb. 2023, doi: 10.1016/j.addr.2022.114670.

[13] Y. Liang, J. He, and B. Guo, 'Functional Hydrogels as Wound Dressing to Enhance Wound Healing', *ACS Nano*, vol. 15, no. 8, pp. 12687–12722, Aug. 2021, doi: 10.1021/acsnano.1c04206.

[14] B. Blanco-Fernandez, O. Castaño, M. Á. Mateos-Timoneda, E. Engel, and S. Pérez-Amodio, 'Nanotechnology Approaches in Chronic Wound Healing', *Advances in Wound Care*, vol. 10, no. 5, pp. 234–256, May 2021, doi: 10.1089/wound.2019.1094.

[15] A. Francesko, P. Petkova, and T. Tzanov, 'Hydrogel Dressings for Advanced Wound Management', *Current Medicinal Chemistry*, no. 25, pp. 5782–5797, 2018.

[16] J. Koehler, F. P. Brandl, and A. M. Goepferich, 'Hydrogel wound dressings for bioactive treatment of acute and chronic wounds', *European Polymer Journal*, vol. 100, pp. 1–11, Mar. 2018, doi: 10.1016/j.eurpolymj.2017.12.046.
[17] A. Torchio *et al.*, 'Injectable supramolecular hydrogels based on custom-made poly(ether urethane)s and α-cyclodextrins as efficient delivery vehicles of curcumin', *Materials Science and Engineering: C*, vol. 127, p. 112194, Aug. 2021, doi: 10.1016/j.msec.2021.112194.
[18] S. Jacob, A. B. Nair, J. Shah, N. Sreeharsha, S. Gupta, and P. Shinu, 'Emerging Role of Hydrogels in Drug Delivery Systems, Tissue Engineering and Wound Management', *Pharmaceutics*, vol. 13, no. 3, Art. no. 3, Mar. 2021, doi: 10.3390/pharmaceutics13030357.
[19] P. Zarrintaj *et al.*, 'Poloxamer: A versatile tri-block copolymer for biomedical applications', *Acta Biomaterialia*, vol. 110, pp. 37–67, Jul. 2020, doi: 10.1016/j.actbio.2020.04.028.
[20] G. S. Schultz *et al.*, 'Wound bed preparation: a systematic approach to wound management', *Wound Repair Regeneration*, vol. 11, no. s1, Mar. 2003, doi: 10.1046/j.1524-475X.11.s2.1.x.
[21] A. G. Morena, S. Pérez-Rafael, and T. Tzanov, 'Lignin-Based Nanoparticles as Both Structural and Active Elements in Self-Assembling and Self-Healing Multifunctional Hydrogels for Chronic Wound Management', *Pharmaceutics*, vol. 14, no. 12, Art. no. 12, Dec. 2022, doi: 10.3390/pharmaceutics14122658.
[22] R. P. Verma, 'Hydroxamic Acids as Matrix Metalloproteinase Inhibitors', in *Matrix Metalloproteinase Inhibitors*, vol. 103, S. P. Gupta, Ed., in Experientia Supplementum, vol. 103. , Basel: Springer Basel, 2012, pp. 137–176. doi: 10.1007/978-3-0348-0364-9_5.
[23] X.-C. Cheng, R.-L. Wang, Z.-K. Dong, J. Li, Y.-Y. Li, and R.-R. Li, 'Design, synthesis and evaluation of novel metalloproteinase inhibitors based on l-tyrosine scaffold', *Bioorganic & Medicinal Chemistry*, vol. 20, no. 19, pp. 5738–5744, Oct. 2012, doi: 10.1016/j.bmc.2012.08.014.
[24] J. J. Hurlow, G. J. Humphreys, F. L. Bowling, and A. J. McBain, 'Diabetic foot infection: A critical complication', *International Wound Journal*, vol. 15, no. 5, pp. 814–821, 2018, doi: https://doi.org/10.1111/iwj.12932.
[25] F. S. Palumbo, S. Federico, G. Pitarresi, C. Fiorica, and G. Giammona, 'Synthesis and characterization of redox-sensitive polyurethanes based on l-glutathione oxidized and poly(ether ester) triblock copolymers', *Reactive and Functional Polymers*, vol. 166, p. 104986, Sep. 2021, doi: 10.1016/j.reactfunctpolym.2021.104986.
[26] J. Guan and W. R. Wagner, 'Synthesis, Characterization and Cytocompatibility of Polyurethaneurea Elastomers with Designed Elastase Sensitivity', *Biomacromolecules*, vol. 6, no. 5, pp. 2833–2842, Sep. 2005, doi: 10.1021/bm0503322.
[27] R. D. Wolcott *et al.*, 'Chronic wounds and the medical biofilm paradigm', *Journal of Wound Care*, vol. 19, no. 2, pp. 45–53, Feb. 2010, doi: 10.12968/jowc.2010.19.2.46966.
[28] A. W. Carpenter and M. H. Schoenfisch, 'Nitric oxide release: Part II. Therapeutic applications', *Chem. Soc. Rev.*, vol. 41, no. 10, pp. 3742–3752, Apr. 2012, doi: 10.1039/C2CS15273H.
[29] H. Nurhasni *et al.*, 'Nitric oxide-releasing poly(lactic-co-glycolic acid)-polyethylenimine nanoparticles for prolonged nitric oxide release, antibacterial efficacy, and in vivo wound healing activity', *Int J Nanomedicine*, vol. 10, pp. 3065–3080, Apr. 2015, doi: 10.2147/IJN.S82199.
[30] S. P. Hlaing *et al.*, 'S-Nitrosoglutathione loaded poly(lactic-co-glycolic acid) microparticles for prolonged nitric oxide release and enhanced healing of methicillin-resistant Staphylococcus aureus-infected wounds', *European Journal of Pharmaceutics and Biopharmaceutics*, vol. 132, pp. 94–102, Nov. 2018, doi: 10.1016/j.ejpb.2018.09.009.

[31] J. Lee *et al.*, 'Nitric Oxide-Releasing S-Nitrosoglutathione-Conjugated Poly(Lactic-Co-Glycolic Acid) Nanoparticles for the Treatment of MRSA-Infected Cutaneous Wounds', *Pharmaceutics*, vol. 12, no. 7, Art. no. 7, Jul. 2020, doi: 10.3390/pharmaceutics12070618.
[32] J. Fang and Y.-C. Chen, 'Nanomaterials for Photohyperthermia: A Review', *CPD*, vol. 19, no. 37, pp. 6622–6634, Sep. 2013, doi: 10.2174/1381612811319370006.
[33] Y. Zhao *et al.*, 'Near-Infrared Light-Activated Thermosensitive Liposomes as Efficient Agents for Photothermal and Antibiotic Synergistic Therapy of Bacterial Biofilm', *ACS Appl. Mater. Interfaces*, vol. 10, no. 17, pp. 14426–14437, May 2018, doi: 10.1021/acsami.8b01327.
[34] W.-C. Huang, P.-J. Tsai, and Y.-C. Chen, 'Functional gold nanoparticles as photothermal agents for selective-killing of pathogenic bacteria', *Nanomedicine*, vol. 2, no. 6, pp. 777–787, Dec. 2007, doi: 10.2217/17435889.2.6.777.
[35] Y. Fu *et al.*, 'Reduced polydopamine nanoparticles incorporated oxidized dextran/chitosan hybrid hydrogels with enhanced antioxidative and antibacterial properties for accelerated wound healing', *Carbohydrate Polymers*, vol. 257, p. 117598, Apr. 2021, doi: 10.1016/j.carbpol.2020.117598.
[36] Z. Abdollahi, E. N. Zare, F. Salimi, I. Goudarzi, F. R. Tay, and P. Makvandi, 'Bioactive Carboxymethyl Starch-Based Hydrogels Decorated with CuO Nanoparticles: Antioxidant and Antimicrobial Properties and Accelerated Wound Healing In Vivo', *International Journal of Molecular Sciences*, vol. 22, no. 5, Art. no. 5, Jan. 2021, doi: 10.3390/ijms22052531.
[37] L. Mao *et al.*, 'In Situ Synthesized Selenium Nanoparticles-Decorated Bacterial Cellulose/Gelatin Hydrogel with Enhanced Antibacterial, Antioxidant, and Anti-Inflammatory Capabilities for Facilitating Skin Wound Healing', *Advanced Healthcare Materials*, vol. 10, no. 14, p. 2100402, 2021, doi: 10.1002/adhm.202100402.
[38] P. Figueiredo, K. Lintinen, J. T. Hirvonen, M. A. Kostiainen, and H. A. Santos, 'Properties and chemical modifications of lignin: Towards lignin-based nanomaterials for biomedical applications', *Progress in Materials Science*, vol. 93, pp. 233–269, Apr. 2018, doi: 10.1016/j.pmatsci.2017.12.001.
[39] N. Sekkat, H. van den Bergh, T. Nyokong, and N. Lange, 'Like a Bolt from the Blue: Phthalocyanines in Biomedical Optics', *Molecules*, vol. 17, no. 1, Art. no. 1, Jan. 2012, doi: 10.3390/molecules17010098.
[40] D. Li *et al.*, 'Innovative Design Strategies Advance Biomedical Applications of Phthalocyanines', *Advanced Healthcare Materials*, vol. 12, no. 22, p. 2300263, 2023, doi: 10.1002/adhm.202300263.
[41] N. U. Khaliq, J. Lee, S. Kim, D. Sung, and H. Kim, 'Pluronic F-68 and F-127 Based Nanomedicines for Advancing Combination Cancer Therapy', *Pharmaceutics*, vol. 15, no. 8, p. 2102, Aug. 2023, doi: 10.3390/pharmaceutics15082102.
[42] C.-M. Moysidou, C. Barberio, and R. M. Owens, 'Advances in Engineering Human Tissue Models', *Front. Bioeng. Biotechnol.*, vol. 8, Jan. 2021, doi: 10.3389/fbioe.2020.620962.
[43] S. Caddeo, M. Boffito, and S. Sartori, 'Tissue Engineering Approaches in the Design of Healthy and Pathological In Vitro Tissue Models', *Front. Bioeng. Biotechnol.*, vol. 5, Jul. 2017, doi: 10.3389/fbioe.2017.00040.
[44] P. F. Duckworth, R. S. Rowlands, M. E. Barbour, and S. E. Maddocks, 'A novel flow-system to establish experimental biofilms for modelling chronic wound infection and testing the efficacy of wound dressings', *Microbiological Research*, vol. 215, pp. 141–147, Oct. 2018, doi: 10.1016/j.micres.2018.07.009.
[45] E. Wright, S. Neethirajan, and X. Weng, 'Microfluidic wound model for studying the behaviors of Pseudomonas aeruginosa in polymicrobial biofilms', *Biotechnology and Bioengineering*, vol. 112, no. 11, pp. 2351–2359, 2015, doi: 10.1002/bit.25651.

[46] X. Chen *et al.*, 'A novel chronic wound biofilm model sustaining coexistence of Pseudomonas aeruginosa and Staphylococcus aureus suitable for testing of antibiofilm effect of antimicrobial solutions and wound dressings', *Wound Repair and Regeneration*, vol. 29, no. 5, pp. 820–829, 2021, doi: 10.1111/wrr.12944.

[47] I. C. Thaarup and T. Bjarnsholt, 'Current In Vitro Biofilm-Infected Chronic Wound Models for Developing New Treatment Possibilities', *Advances in Wound Care*, vol. 10, no. 2, pp. 91–102, Feb. 2021, doi: 10.1089/wound.2020.1176.

[48] E. M. Townsend *et al.*, 'Development and characterisation of a novel three-dimensional inter-kingdom wound biofilm model', *Biofouling*, vol. 32, no. 10, pp. 1259–1270, Nov. 2016, doi: 10.1080/08927014.2016.1252337.

[49] L. Sheng *et al.*, 'A novel "hot spring"-mimetic hydrogel with excellent angiogenic properties for chronic wound healing', *Biomaterials*, vol. 264, p. 120414, Jan. 2021, doi: 10.1016/j.biomaterials.2020.120414.

[50] Y. Liang, X. Zhao, T. Hu, Y. Han, and B. Guo, 'Mussel-inspired, antibacterial, conductive, antioxidant, injectable composite hydrogel wound dressing to promote the regeneration of infected skin', *Journal of Colloid and Interface Science*, vol. 556, pp. 514–528, Nov. 2019, doi: 10.1016/j.jcis.2019.08.083.

[51] X. Wu *et al.*, 'Temperature-Responsive Nanoassemblies for Self-Regulated Photothermal Therapy and Controlled Copper Release to Accelerate Chronic Wound Healing', *ACS Appl. Bio Mater.*, vol. 6, no. 5, pp. 2003–2013, May 2023, doi: 10.1021/acsabm.3c00267.